Relaxation radiative dans l’infrarouge des dérivés de benzène et de gros agrégats de carbone en phase gazeuse

Ozan Lacinbala

▶ To cite this version:

Ozan Lacinbala. Relaxation radiative dans l’infrarouge des dérivés de benzène et de gros agrégats de carbone en phase gazeuse. Atomic and Molecular Clusters [physics.atm-clus]. Université Paris-Saclay, 2021. English. ⟨NNT : 2021UPASP094⟩. ⟨tel-03577892⟩

HAL Id: tel-03577892

https://theses.hal.science/tel-03577892v1

Submitted on 16 Feb 2022

IR radiative relaxation of benzene derivatives and large carbon clusters in the gas phase

Thèse de doctorat de l'Université Paris-Saclay

École doctorale n° 572, Ondes et Matière (EDOM)
Spécialité de doctorat: Physique
Unité de recherche: Université Paris-Saclay, CNRS, Institut des Sciences Moléculaires d'Orsay, 91405, Orsay, France.
Référent: Faculté des sciences d'Orsay

Thèse présentée et soutenue à Paris-Saclay, le 30/09/2021, par

Ozan LACINBALA

Composition du jury:

Laurent VERSTRAETE Professeur, IAS, Université Paris-Saclay, Orsay	President
Jan CAMI Professeur, Western University, London, Canada	Rapporteur & Examinateur
Gert von HELDEN Professeur, Fritz Haber Institute, Berlin	Rapporteur & Examinateur
Alicja DOMARACKA Chargé de recherche, CIMAP, Normandie Université, Caen	Examinatrice
Géraldine FÉRAUD Maître de conférences, LERMA, Sorbonne University, Paris	Examinatrice
Thomas PINO Directeur de recherche, ISMO, Université Paris-Saclay, Orsay	Directeur de thèse
Louis LE SERGEANT D'HENDECOURT Chercheur émérite, PIIM, Université Aix-Marseille, Marseille	Invité

Thèse de doctorat

NNT: 2021UPASP094

Acknowledgements

Plusieurs personnes de l'Institut des Sciences Moléculaires d'Orsay ont contribué de près ou de loin à ce travail de recherche. Je tiens à remercier:

Mon directeur de thèse et directeur de l'ISMO, Thomas Pino, pour m'avoir donné l'opportunité de faire de la recherche et pour sa confiance qu'il m'a accordé malgré une courte interruption dans mon parcours académique. J'ai pu m'immerger pleinement dans la recherche fondamentale et de m'en faire rapidement une idée. Ma thèse à l'ISMO m'a donc conforté dans l'idée de continuer dans la recherche publique et Thomas y a contribué en sachant me guider dans mon travail tout en m'accordant une grande autonomie. Malgré ses responsabilités, Thomas m'a toujours donné le coup de pouce nécessaire lorsque j'étais en difficulté en salle de manip. Je le remercie d'avoir été attentif à mes affinités et de m'avoir proposé différents sujets d'études au fur et à mesure que la thèse avançait.

Laurent Verstraete, Jan Cami, Gert von Helden, Alicja Domaracka, Géraldine Féraud and Louis Le Sergeant d'Hendecourt d'avoir aimablement accepté de faire partie du jury, pour leur lectures et améliorations de ce manuscrit.

Mon ami et collègue Joffrey Fréreux pour tous ces bons moments, ces fous rires et ces échanges d'idées sur tous les plans. Je pense que je n'aurais pas pu avoir un meilleur "compagnon de thèse" que Joffrey. J'ai beaucoup appris de lui, tant humainement que scientifiquement. Quelles sont mes chances de rencontrer de nouveau un collègue comme lui ?

Nos collègues Florent Calvo, Aude Simon, Clément Dubosq, Cyril Falvo et Pascal Parneix dont les travaux ont servi de bases pour les miens. Ils ont d'ailleurs contribué à améliorer les articles à venir. Je remercie en particulier Pascal Parneix dont j'ai suivi les cours en L3, M1 et M2.

Le directeur de l'équipe SYSTEMAE Emmanuel Dartois pour les discussions astrophysiques, Bérenger Gans et Ugo Jacovella pour leur conseils, ainsi que Séverine, Daniel, Olivier, Marie, Marie-Aline, Laurent, Minh, Philippe et tous les membres de l'équipe SYSTEMAE pour leur accueil.

Mes collègues doctorants et post-doctorants de l'équipe Olivia, Zixian, Oliver, Anam et Ning avec lesquelles j'ai partagé mon bureau ou la salle de manip et d'avoir été aussi aimable, en particulier Olivia pour avoir veillé au bon fonctionnement de la transmission à distance de ma soutenance. Je remercie tous les doctorants et anciens doctorants du laboratoire, en particulier Abigail, Delphine, Jordan, Pauline, Charles, Adrien et Pierre pour toutes les soirées passées à l'intérieur et devant l'ISMO.

Bernard Bourguignon pour m'avoir accompagné les deux premières années de ma thèse en tant que directeur de l'ISMO.

Julien Vincent qui a mis au point toute la chaîne d'acquisition de données de FIREFLY, Christophe Lefumeux et Catherine Le Bris pour leurs aides précieuses sur différents laser, Farah Savina pour nous avoir guidé sur la manipulation de produits chimiques, ainsi que Hocine, Magdalena et Wutharath pour nos échanges toujours très cordiales.

Tous les membres du restaurant du plateau du Comité d'Entraide Sociale de la Faculté d'Orsay.

Et, pour finir, Malek, ma mère Dilek, mon père Bülent, ma soeur Sezen et mon frère Özgür pour leur soutien.

Table of Contents

Résumé de la thèse **4**

1 Context **20**

2 Theoretical framework **28**
Modelling of the photophysics 28
Statistical approach - microcanonical framework 29
Harmonic vibrational density of states 31
Recurrent fluorescence 34
Vibrational fluorescence 37
Formula relating spectroscopic quantities 38
Modelling of the photochemistry 40
RRK theory 40
RRKM theory 41
Dissociation and isomerization 42
Collisional energy transfer 43
Collision rate 43
Parametric model 44
Relaxation radiative computation 51
Principle of the Monte-Carlo for relaxation cascade 52
Application to radiative relaxation 53
Kinetic aspect of the Monte-Carlo 56

3 Radiative emission of large carbon clusters **59**
Radiative relaxation in large carbon clusters: recurrent fluorescence versus vibrational emission 60
Introduction 60
Methods 63
Kinetics of radiative cooling in carbon clusters: selected cases 71
Behavior over a large set 79

Concluding remarks 84
Appendix 86
Supplementary result: Exponential decay profile of emission spectra from a whole relaxation cascade 87
Infrared emission of $C_{n=24,42,60}$ carbon clusters induced by stochastic heating . 91
Introduction 95
Methods 96
Results 99
Conclusions 108
Absorption cross-section and spectral energy distribution 109
Calculation of the detected emission power density from C_{60} cages in NGC 7023109
Error estimation 111
Large carbon clusters emissivity: a molecular approach 114
Introduction 114
Theoretical methodology 115
Emission spectra 117
Emissivity 120
Appendix 122
Supplementary results 124
Conclusion 127

4 Experimental setup: FIREFLY infrared spectrometer 128

Cell and light sources 131
Cell description 132
Physical conditions monitoring inside the cell 132
Light sources 135
FIREFLY spectrometer 137
Constituting components of FIREFLY 138
Absorption configuration 145
Some manipulations for the correct operation of FIREFLY 149
Correction of the FHG angular position 149
CVF calibration 149
Response function of the apparatus 152

5 Investigation of toluene to cycloheptatriene isomerization 156

Description of the studied system 156
Raw data processing 159
Infrared emission of toluene $C_6H_5CH_3$ 162

Intensity study 162
Emission spectra as a function of time 163
Time traces as a function of wavelength 165
Simulation of the cooling cascade 166
Toluene $\longrightarrow$ cycloheptatriene isomerization 170
Evidence of isomerization 170
Long time emission spectra 173
Proportion of non-isomerized toluene-d_5^{Ar} 176
Collision parameters 178
Constraints on A and E_{iso} 180
Relaxation kinetics 180
Other constraints ? 186
k_{iso}(193 nm) determination 188
The phenylacetylene-d_1 case 189
Intensity study and absorption spectrum 189
Phenylacetylene relaxation induced by 193 nm excitation 191
Phenylacetylene-d_1 relaxation induced by 193 nm excitation 195
Conclusion 203

6 Conclusion and perspectives **206**

List of Figures

1.1 Spectral energy distribution in a typical late-type galaxy. Anomalous microwave emission (AME), aromatic infrared bands (AIBs), diffuse interstellar bands (DIBs) and extended red emission are represented. The inset graph at the bottom displays the polarization fraction of light in the ISM in terms of the wavelength. The monochromatic luminosity is expressed in solar luminosity ($\approx 3.8 \cdot 10^{28}$ W). This figure is extracted from (Galliano et al., 2018) 21

2.1 Jablonski diagram showing the radiative and radiationless processes that take place during the relaxation cascade. IC: internal conversion; IIC: inverse internal conversion; IVR: intramolecular vibrational redistribution; PD: photodissociation; VF: vibrational fluorescence; EF: electronic fluorescence and zigzag arrows represent IR photons; pink arrows represent collisional de-excitation. 32

2.2 Comparison between the density of vibrational states of naphthalene calculated by the Beyer-Swinehart algorithm, the classical (2.6) and semi-classical (2.7) relation. In the naphthalene case, $E_z \approx 60000$ cm^{-1}. 34

2.3 Ratio (2.12) in terms of the electronic energy. Except at high internal energies ($\approx 10^5$ cm^{-1}) and for very low electronic energies (< 3000 cm^{-1}), the ratio is negligible compared to 1. 36

2.4 Left panel: probability distribution of the ΓE energy transfer per collision in the exponential model with the α(E) parameterization shown in the right curve, T=300 K and degree of freedom $g = 50$. Right panel: parameterization $\alpha(E) = 30 + 0.009 \times E + 7 \cdot 10^{-9} \times E^2$ with internal energy E (in cm^{-1}) 52

3.1 Selected archetype isomers for all families and sizes 70

3.2 Normalized emission intensity spectra of the six selected carbon clusters obtained from radiative cooling with 12.4 eV initial internal energy. The spectra were obtained as histograms and convoluted by a Lorentzian distribution with a full width at half maximum of 50 cm^{-1}. 72

3.3 Left panel: Recurrent fluorescence rate constants for the six selected carbon clusters, as a function of their internal energy. Right panel: Vibrational emission rate constants for the six selected carbon clusters, as a function of their internal energy. The inset focuses on the low internal energies below 10 000 cm^{-1}. 73

3.4 Left panel: Recurrent fluorescence efficiency ξ obtained from the rate constants of figure 3.3. Right panel: Recurrent fluorescence efficiency ξ in terms of E_{internal}/g for the three sizes. 76

3.5 Temporal decay of the internal energy for the six carbon clusters. For all isomers, the initial internal energy was 18.5 eV except for the C_{24} flake for which it was 15 eV only. Main regime shifts are highlighted by vertical dashed lines. The numbering in circles for the C_{60} flake decay curve indicates the main decay regimes. Orange lines indicate the internal energy and the delay for which the RF efficiency is 0.5 (as deduced from Fig. 3.4). 78

3.6 Recurrent fluorescence intensities from dominant electronic states in terms of the internal energy for the C_{60} flake. The numbering in circles indicates relaxation regimes. 79

3.7 (a) RF rate constant at several internal energies. Pearson coefficients were calculated for data above 0.2 eV and corresponding linear fit. (b) RF rate constant from the 1st or 2nd electronic levels in terms of the electronic energy and corresponding linear fit with slope values used in the text. (c) RF rate constant for different sizes of flakes family. (d) recurrent fluorescence (RF) rate constant for two different isomer families. The data are shown for 1000 independent isomers of C_{60} cages and C_{60}, C_{42}, C_{24} flakes. 82

3.8 (a) and (b): Normalized emission intensity spectra from one thousand C_{60} cage isomers with 2.5 and 12.4 eV initial internal energy. Contribution from recurrent fluorescence and vibrational emission are also displayed. The inset highlights the exponential fit for the recurrent fluorescence component. (c) and (d): Normalized emission intensity spectra from one thousand C_{60} isomers for each family. Spectra in dashed lines (resp. solid lines) are those without (resp. with) recurrent fluorescence taken into account over the relaxation cascade. 85
3.9 Number of electronic excited states per 2000 cm^{-1} electronic energy for the six chosen isomers. 87
3.10 Recurrent fluorescence rate constant from the 1^{st} excited electronic of 1000 flake isomers of C_{24}, C_{42} and C_{60} excited at 2.48 eV (= 20000 cm^{-1}). The linear fit was performed for electronic energies above 0.2 eV (= 1500 cm^{-1}). 88
3.11 Electronic (left panel) and vibrational (right panel) density of states over a large set of C_{60} isomers for each family. 89
3.12 Electronic (left panel) and vibrational (right panel) density of states over a large set of C_{42} isomers for each family. 89
3.13 Electronic (left panel) and vibrational (right panel) density of states over a large set of C_{24} isomers for each family. There is only 11 isomers for C_{24} cages. 90
3.14 $E_2(\alpha)$ in terms of α in semi-log scale. This indicates that E_2 can be approximated to an exponential decay (at least for $\alpha > 1$). 91
3.15 Emission intensity spectra of a large set of C_{60} carbon clusters irradiated by a 20 000 K blackbody (simulating a star). The vibrational emission and recurrent fluorescence components are also shown. To obtain these emission intensity spectra, a lorentzian convolution have been done on the computed histogram emission intensity spectra with a FWMH of 50 cm^{-1}. 100
3.16 Emission intensity spectra from the four families (branched, cages, flakes and pretzels) for all sizes, irradiated by a 20 000 K blackbody and χ=1 ISRF. Each emission spectrum in full lines is associated with a dotted lines emission spectrum for which only VF is taken into account. The emission intensity spectrum from C_{24} cages is particularly different because there are only 11 isomers. 102
3.17 Same emission intensity spectra of figure 3.17 displayed here in terms of wavelength. 103

3.18 Ratios of vibrational band ratios for all families and all sizes. R represents ratio between to vibrational bands. Ratios have been deduced from emission spectra of figure 3.16. All band ratios are not defined for the cage family. 104

3.19 Emission spectrum extracted from Sellgren (1984). Near-IR continuum emission observed in NGC 7023 within 12″ aperture. 105

3.20 Emission spectra at the near-IR region. Upper panel: the four families of C_{60} are displayed. Lower panel: the interesting emission spectra of cage family is displayed for two different sizes. 107

3.21 Emission spectra of neutral C_{24} pretzel and ppa excited by a 20 000 K star. The region of the extended red emission lies between 600 and 850 nm.108

3.22 Left panel: the average electronic absorption cross-section per carbon number of C_{60} cage isomers and obtained by a FWHM= 300 cm^{-1} lorentzian convolution. Right panel: the average absorbed spectral energy power by C_{60} cages located at the surface a 20 000 K blackbody. This curves have been obtained by multiplying the 20 000 K blackbody spectral irradiance shown in figure 3.23 and the average electronic absorption cross-section of C_{60} cage isomers shown at the left panel. 110

3.23 Spectral irradiance associated with SEDs that we used in this work. Actually, we added a cutoff to take the ionization into account. This cutoff occurs at 60 000 cm^{-1} for C_{60}, 65 000 cm^{-1} for C_{42} and 70 000 cm^{-1} for C_{24}. Left panel: spectral irradiance of the $\chi = 1$ ISRF Mathis et al. (1983). Right panel: spectral irradiance at the surface of a 20 000 K blackbody. 111

3.24 Number of photons emitted via VE in terms of internal energy. At internal energies below 2 eV, this number is dependent of the initial internal energy. This is a computational artifact. (a): above 1.5 eV internal energy, VE decreases with the internal energy because it is quenched more and more by recurrent fluorescence. (b): the same plot as (a) and points represents kMC steps of the mean trajectory. There are more kMC steps for higher initial energies although the total emitted photons below 2 eV are equal. 112

3.25 K(E) factor for the C_{60} cage arbitrarily chosen in this appendix and for a 20 000 K blackbody. 113

3.26 Simulated emission intensity spectra of C_{60} and C_{42} flake carbon clusters. Panel (a): comparison of C_{60} for two temperatures. The best fit is a modified Planck's function which gives the temperature 2499.4 ± 0.4. Panel (b): comparison between two sizes. The computed histogram emission spectra have been convolved by a lorentzian function (FMWH=300 cm^{-1}). 119

3.27 Mean emissivities for C_{60} and C_{42} at different temperature and deduced from the simulated emission spectra of figure 3.26 with the ϵ_{tot} calculated from expression (3.46). The inset figure illustrates expression (3.47) with a linear fit (black line). A numerical artifact prevents us to display the emissivity above 30 000 cm^{-1}. This artifact stems from the fraction of the two exitance in the expression 3.43. Indeed, these two quantities become very low at high internal energies and the fraction increases indefinitely (physically not acceptable) with the internal energies. 121

3.28 Electronic density of states per 1000 cm^{-1} for all families of C_{60} and C_{42} carbon clusters. One thousand isomers for each family and size. 124

3.29 Normalized emission spectra of C_{60} isomer at 2500K from all families computed as described in section 3 and 3. 125

3.30 Simulation performed for an arbitrarily chosen flake. This simulation result is the same for any other carbon cluster at fixed size. (a): this figure illustrates the relation 3.68. In green, the simulated internal energy via the vibrational partition function. The zero-point energy has been added *ad hoc*. In black, the relation 3.68 obtained analytically for internal energies larger than E_z. (b): this figure illustrates the relation 3.69. In red, the ratio between the standard deviation by the internal energy. In black, $\frac{1}{\sqrt{g}}$ for g=173. 126

4.1 Side view illustration of the cell in which species of interest undergo radiative and collisional relaxation after excitation by UV photon (UV laser in violet). Species are leaked into the cell and their pressure is controlled by micrometric valve. The IR fluorescence experiment is done under stationary flow conditions. Blackbody radiation is used for absorption spectra measurements. The cell length is about 90 cm. 133

4.2 Upper image: Illustration of the UV laser pulses crossing through the cell. Blackbody beam trajectory before going through the cell. The IR spectrometer is placed inside a Faraday cage. Lower image: UV laser entrance window through which two pipes are visible. One of the pipes is used to argon flow injection in the vicinity of the UV laser entrance window and the other pipe is used for gas inlet connected to the reservoir containing the species to be investigated. 134

4.3 Schematic illustration of the acquisition data system for IR fluorescence photons detection for the emission configuration of FIREFLY. 138

4.4 Illustration of FIREFLY and the cell. 3D illustration: the optical path followed by IR photons emitted during the cooling cascade are illustrated by red beams. During scans, FIREFLY is enclosed inside Faraday cage. 2D illutration: Top view of FIREFLY and the cell. The blue beam crossing the cell illustrates the UV exciting laser pulses. The main compounds of FIREFLY are also indicated. These schemas have been drawn by Thierry Chamaillé (CNRS engineer at Institut des Sciences Moléculaires d'Orsay). 139

4.5 Upper image: The filter holder gearwheel set up in FIREFLY. Image extracted from Géraldine Féraud's PhD thesis (2012). Lower image: CVF 1 and CVF 2 are mounted on the filter holder gearwheel. Unfortunately, because of technical issues of the MCT detector, the CVF 2 could not been used. 141

4.6 Upper panel: CVF 1 transmittance measured by Thomas Pino and Emmanuel Dartois by Fourier Transform IR spectroscopy in 2004. This figure has been extracted from Géraldine Féraud's PhD thesis (2012). Lower panel: from the same measurement, CVF 1 absorption around 2432 cm^{-1} (4.11 µm), 3193 cm^{-1} (3.13 µm) and 4013 cm^{-1} (2.49 µm) with a Gaussian fit in blue and indication of the full width at half maximum (FWHM). . . . 142

4.7 Spectral detectivity of InSb detector used for CVF 1 ranging from 2.5 to 4.5 µm. Source: http://irassociates.com 144

4.8 Output signal from the preamplifier for a very short input square signal (0.008 µs rising edge, 0.050 µs width). The fitting pulse function is expressed by $y_0 + A \times (1 - e^{-t/\tau_1})^P \times e^{-t/\tau_2}$. Parameters of the pulse function are indicated for the two independent measurements. In the left panel, the output signal of the previous amplifier is also displayed for comparison (corresponding curve and parameters are in green color). 145

4.9 Schematic illustration of the acquisition data system when FIREFLY operates in absorption configuration 146

4.10 Recorded spectra with CVF 1 of a 800°C blackbody radiation by means of a lock-in detection. Two spectra for two different cell conditions: cell in contact with the atmosphere and vacuumed cell ($< 10^{-4}$ mbar). 147

4.11 (a): spectra with and without propylbenzene in the cell. The C–H aromatic (∼3.3 µm) and aliphatic (∼3.4 µm) bands are visible besides solid water and CO_2 absorptions. (b) In red, the propylbenzene absorption deduced from (a) and in blue the propylbenzene found in the NIST database. Normalization have been done at 3.4 µm. Artifact band appears around 2.85 µm. 148

4.12 Several CO_2 absorption bands irradiated by a 800 K blackbody. (a): without correction. Given that electrical noise, there is an uncertainty on the step motor position of the minimum of absorption bands. (b): The correction is done using the fitting sinusoidal function displayed in figure 4.13a. 150

4.13 Two absorption bands motor step position in terms of the rotation number of the filter holder gearwheel (FHG). The fit function is a sinus function and the period is the same for both fitting, around 5.15. Uncertainty bars are estimated from the uncertainty of the minimum of absorption bands because of electrical noise (see figure 4.12 without correction). (a): 4.27 µm of carbon dioxide and positions are deduced from figure 4.12a (b): 3.28 µm of C-H aromatics of toluene. 150

4.14 Black points are those appearing in figure 4.13a. Red points are the motor step position after the numerical correction. These positions should correspond to that of figure 4.12 b. The dispersion is reduced. 151

4.15 Calibration curve of the CVF 1. 151

4.16 Normalized absorption spectra deduced from the calibration of figure 4.15 and compared to NIST spectra. 153

4.17 Shift of carbon dioxide absorption bands from one rotation of the FHG to an another. The correction reduces these shifts. 154

4.18 (a) In red: the relative 800°C blackbody radiance obtain by the Planck function. In black: the detected signal by FIREFLY when irradiated by 800°C blackbody. In violet: the profile of the response function of the apparatus that have been obtained from the black and red spectra. . . . 154

4.19 IR fluorescence signal of toluene excited at 193 nm. For this record, pressure conditions are approximately known: argon partial pressure around 10 mbar and toluene partial pressure between 1 and 2 mbar. 155

5.1 Principle of toluene → cycloheptatriene isomerisation study via the vibrational emission process. The initially excited toluene-d_5^{Ar} isomerizes to cycloheptatriene which, before isomerizing back to toluene, undergoes hydrogens/deuteriums scrambling of 7-membered ring carbon atoms. Consequently, a toluene-d_5 isotopologue appears from the cycloheptatriene → toluene isomerisation. The goal is to detect the emission of toluene-d_5 isotopologues through the emergence of aromatic C–H bonds and their vibrational stretching mode. The emergence of aliphatic C–D bonds is not detectable because their vibrational stretching mode emission wavelength is out of the circular variable filter wavelength range (2.5 to 4.5 µm). 158

5.2 toluene absorption spectra. The figure has been taken from *The MPI-Mainz UV/VIS Spectral Atlas of Gaseous Molecules of Atmospheric Interest* website. 159

5.3 Toluene-d_5^{Ar} emission with 1.16 mbar total pressure (P_{Ar}=0.95 mbar and toluene-d_5^{Ar} partial pressure of 0.21 mbar). The laser power at the entrance window was 175 mW (repetition rate is 20 Hz). Left panel: two examples of raw time trace. The inset figure is a zoom between -20 and 100 µs. Right panel: two examples of raw emission spectra 160

5.4 Left panel: time trace correction infected with the hollow-shaped parasitic signal between 0 and 100 µs. Right panel: emission spectrum calculated after time traces processing. The sudden increase around 4.5 µm is due to the end of the interference filter and no wavelength is filtered. 161

5.5 Left panel: emission spectra corrected by the response function of the apparatus. Right panel: the same spectra of the left panel smoothed by the Savitsky-Golay algorithm (over three points by a polynome of degree 1). 162

5.6 Intensity study of toluene excited at 193 nm. Each points of the scatter plot has been deduced by integrating the undispersed vibrational emission signal (all wavelengths between 2.5 and 4.5 µm) over the whole relaxation. Left panel: log scale. Right panel: linear scale to show that between 150 and 200 mW the absorption regime is indeterminate. 163

5.7 Undispersed emission signal of toluene excited at 193 nm. 164

5.8 (a_1, a_2): two emission spectra above are from the same acquisition. (b_1, b_2): two emission spectra above are from the same acquisition but different from (a_1, a_2) acquisition. In these two acquisitions pressure conditions are identical: total pressure is P= 1.16 mbar and argon partial pressure is 0.93 mbar. The laser power upstream of the entrance UV window is 145 mW. The ultimate vacuum reached is of the order of 10^{-4} mbar. . . . 165

5.9 Left panel: emission spectra at the end of the cooling cascade of toluene excited at 193 nm. The dotted line shows the absorption spectra of toluene and cycloheptatriene (obtained as described in section 4). The emission band around 3.3 µm is due to aromatic C-H streching and the band around 3.45 µm is due to aliphatic C–H stretching. Right panel: emission spectra are narrower as the internal energy decreases. Broadening of the emission spectra in short times is due to the anharmonicity of the potential energy surface. 166

5.10 Left panel: time traces at different wavelengths from the radiative relaxation of toluene. Right panel: these same normalized temporal traces. . . 167

5.11 Upper panel: sum of the aromatic and aliphatic C–H streching IR emission. The experimental time trace are in solid lines. The simulated time trace are shown in dashed lines. Lower panel: the average energy transferred per down-step collisions (which is equal to α at high internal energies, see section 2) depending on the parameterization used. Dashed lines for Toselli & Barker's parameterization (Barker and Toselli, 1993) indicates extrapolation beyond their measurement. The plot is stopped at 52 000 cm^{-1}= 193 nm. 169

5.12 Simulated internal energy decay of toluene in terms of time, with P_{Ar}= 0.93 mbar et P_{Tol}= 0.23 mbar. The kMC trajectories were stopped at 1000 cm^{-1} internal energy. 170

5.13 Temporal evolution of normalized emission spectra for toluene excited at 193 nm 171

5.14 For all these spectra, the total pressure is 1.16 mbar with 0.93 mbar argon partial pressure. Green spectra: emission spectra recorded after excitation at 193 nm of toluene-d_5^{Ar} with laser power varying from one acquisition to another (between 140 et 190 mW). Purple spectra: emission spectra recorded after excitation at 193 nm of CH_5CH_3 toluene with laser power between 145 and 175 mW. 172

5.15 Emission spectrum profile variation after excitation at 193 nm of toluene-d_5^{Ar}. We clearly see the redshift in the short times. 173

5.16 Kinetics of the emission spectra obtained for four different acquisitions with approximately the same pressure conditions. The laser power upstream of the entry window is also indicated. From left to right and top to bottom: acquisitions n° 5, 6, 11 et 26. 174

5.17 Emission spectra with integration between 10 and 16 µs for the 4 acquisitions in the figure 5.16. From left to right and top to bottom: acquisitions n° 5, 6, 11 et 26. 175

5.18 Absorption spectra simulated by CAM-B3LYP/6-311++G(d,p) for toluene-d_5^{Ar} and the mixture of all isotopologues liable to appear after the CHT-d_5 → toluene-d_5 isomerisation. A gaussian convolution (fwhm = 70 cm^{-1}, faithful to the resolution of the interference filter) have been applied to the histogram absorption spectra. 177

5.19 Linear combinations of the absorption spectrum of all isotopologues and that of toluene-d_5^{Ar}. Non-isomerised toluene-d_5^{Ar} percentage are shown for all these combinations. Theoretical spectra are obtained by CAM-B3LYP/6-311++G(d,p). The green dotted lines delimit the aromatic C–H band and are determined by the uncertainty of the average ratio of table 5.1. Those in dark red delimit the aromatic C–D band. The aliphatic C–H band is arbitrarily fixed to unity for all spectra. 179

5.20 Mean energy transferred per down-step collision for several settings. The parameterization is expressed as a second order polynomial such as $A_0 + A_1 \cdot 10^{-3} \times E + A_2 \cdot 10^{-7} \times E^2$ for collisions between excited toluene and argon and $C_0 + C_1 \cdot 10^{-3} \times E + C_2 \cdot 10^{-7} \times E^2$ for that between excited and non-excited toluene, E is the internal energy. The time traces of aromatic + aliphatic C-H stretching modes from all settings are superimposed on that obtained by the experiment. 181

5.21 Each red dot represents the pairs (A, E_{iso}) giving a proportion of 20% ± 2% non-isomerised toluene-d_5^{Ar}. The same goes for black dots for a proportion of 50% ± 2%. The curves are fits for each set of points. . . . 182

5.22 Isomerisation rate obtained by RRK for the several (A, E_{iso}) pairs. 182

5.23 (a) et (b): Time emissions for the four bands and two (A, E_{iso}) pairs. (c): Aromatic C–H emissions for both pairs. (d): Aliphatic C–H emissions for both pairs. 184

5.24 Simulation of the number first isomerization per molecule (*i.e* first isomerization proportion) from toluene-d_5^{Ar} to CHT-d_5. The simulation is carried out for (A, E_{iso}) pairs presented in figure 5.22. 185

5.25 Sum of simulated aromatic C–H and aliphatic C–H stretching modes emission. (a): without convolution by the preamplifier response. (b): with convolution by the preamplifier response. 186

5.26 Temporal (aromatic C–H + aliphatic C–H) emission signal after excitation at 193 nm from toluene (in green) and toluene-d_5^{Ar} (in red). The resulting simulations are dotted. 187

5.27 Red curve: set of (A, E_{iso}) leaving a proportion of toluene-d_5^{Ar} at 50 %. Black curve: proportion of toluene -d_5^{Ar} at 20 %. In green: for condition 5.4 to be verified, the couple must be on the left of the curve 188

5.28 Integrated emission signal over the whole relaxation for several laser powers and wavelengths. For 266 and 213 nm excitation, more than one-photon absorption process occurs. For 193 nm, one-photon absorption process occurs up to 100 mW. At the bottom right panel, emission spectra from FIREFLY, NIST and DFT calculation (CAM-B3LYP/6-311++G(d,p)) are displayed. The histogram absorption spectra have been convolved by gaussian function with FWHM = 70 cm^{-1}. 190

5.29 (a): normalized undispersed temporal traces (undispersed IR photons between 2.5 and 4.5 µm) of the relaxing phenylacetylene excited at 193 nm for three laser powers. The inset focuses at the beginning of the relaxation. The dotted horizontal grey line indicates the zero value. There is still emission signal after 100 µs for 350 mW laser power. Panel (b): the unnormalized undispersed temporal traces. Panel (c): panel (a) in log scale. 192

5.30 Phenylacetylene emission spectra excited at 193 nm for laser power below 100 mW (one-photon absorption process). Pressure conditions and acquisition number are indicated. Temporal gates are 2 µs wide. 193

5.31 Emission spectra of the four acquisitions in figure 5.30 and all have the same emission profile. The theoretical absorption spectra (CAM-B3LYP/6-311++G(d,p), 0.955 scaling factor) is superimposed. 194

5.32 Phenylacetylene emission spectra excited at 193 nm for 370 mW laser power (more than one-photon absorption process). Pressure conditions and acquisition numbers are indicated. Temporal gates are 2 µs wide but are wider at long times to have a better signal-to-noise ratio. 196

5.33 Three absorption spectra of phenyacetylene-d1 recorded with FIREFLY (blue, green and red). For all spectra, there is systematically an artifact drifting signal growing toward short wavelength and stems from our method to obtain absorption spectra that can generate artifact signal (chapter 4 section 4). The theoretical spectra is shown in black (CAM-B3LYP/6-311++G(d,p)) with a Gaussian convolution (FWMH= 50 cm^{-1}) and 0.955 scaling factor. 197

5.34 Phenylacetylene-d_1 emission spectra excited at 193 nm at 90 mW laser power. 199

5.35 Left panel: emission spectra integrated within 13-19 µs temporal gates, at the end of the relaxation. In black line, the theoretical absorption spectra of phenylacetylene-d_1. Right panel: emission spectra integrated within 18-28 µs temporal gates. 200

5.36 Normalized total emission (between 2.5 and 4.5 µm) of phenylacetylene and phenylacetyelene-d_1 after 193 nm excitation at 90 mW laser power. The phenylacetylene-d_1 is slightly lower. The weaker signal-to-noise ratio of phenylacetyelene-d_1 signal is due to the fact that the aperture was smaller than for phenylacetylene. 200

5.37 Phenylacetylene-d_1 emission spectra excited at 193 nm for 370 and 200 mW laser power. Pressure conditions are indicated only for the acquisition n°22 because during the acquisition n°21 total pressure was cosntantly increasing (see the text). Temporal gates are 2 µs but are wider at long delay time to have a better signal-to-noise ratio. 202

5.38 Intensity emission study for each emission bands. Left panel: two-photon absorption process for the acetylenic C–H band. Right panel: one-photon process for the aromatic C–H band. The same slope is obtained for the acetylenic C–D band. 203

List of Tables

2.1 Lennard-Jones parameters for three species used for the cooling cascade simulation. Argon is used as a buffer gas. Values taken from (Barker and Toselli, 1993). 44

3.1 Main features for the six selected carbon clusters, from top to bottom: sum over the first fifty electronic oscillator strengths (for all isomers, the 50^{th} electronic state energy is less than 3 eV above that of the ground state), summed vibrational intensities, geometrical mean of vibrational wavenumbers, zero-point energies and energies of the three lowest excited electronic states. 70

3.2 Mean internal energy and standard deviation for the Gaussian distribution of internal energy of flakes carbon cluster isomer at two gas temperature and for two sizes. These quantities have been deduced from the vibrational partition function (relation 3.34). 118

4.1 Approximative vapor pressures of species studied in this work. Values for 300 K. 136

4.2 Estimation of the resolution from lower panels of figure 4.6. 140

5.1 Measured emission bands ratios for the four acquisitions. The average of these values is deduced. 178

Résumé de la thèse

Ce travail de thèse s'inscrit dans la lignée des travaux entamés depuis l'énoncé de l'hypothèse PAH stipulant que les pics d'émissions observés dans l'infrarouge moyen et omniprésents dans le milieu interstellaire seraient dus à des espèces semblables aux hydrocarbures aromatiques polycycliques (avec éventuellement une composante aliphatique). Ces espèces émettraient dans l'infrarouge moyen par désexcitation radiative vibrationnelle induite par l'absorption d'un photon UV stellaire. C'est dans ce contexte que nous avons effectué un travail expérimentale et théorique.

La relaxation radiative après excitation électronique des dérivés de benzène en phase gazeuse très excités vibrationnellement a pu être détecté via un spectromètre infrarouge (FIREFLY) développé dans l'équipe. L'analyse des spectres d'émission (entre 2.5 et 4.5 µm) en fonction du temps peuvent donner des informations sur la dynamique de relaxation. Cette analyse peut éventuellement être appronfondie si elle est appuyée par une simulation Monte Carlo cinétique de l'émission vibrationnelle en compétition avec d'autres voies lors de la cascade de relaxation (collision, photodissociation, photoisomérisation). Cette méthode a été appliquée à la dynamique d'isomérisation du toluène (partiellement deutérée) vers le cycloheptatriène (isomérisaton d'un cycle à 6 à un cycle à 7) en essayant de la caractériser (barrière d'isomérisation, préfacteur A). Bien que la dynamique d'isomérsation s'est avérée trop rapide pour être entièrement sondée, cette première étude a permis de voir les possibilités et les limites de l'analyse de la dynamique d'isomérisation via les processus de relaxation radiative. Cette méthode d'analyse a été étendu, sans simulation, à d'autres isomérisations du même type dans le cas du phénylacétylène et l'aniline (les deux partiellement deutérés). L'étude du phénylacétylène a permis une détection du caractère très anharmonique de l'émission d'étirement de la liaison acétylénique C–H avec un rapport signal sur bruit élevé.

Le phénomène de fluorescence récurrente (ou fluorescence de Poincaré) dans les agrégats de carbone C_n (n= 24, 42, 60) en compétition avec l'émission vibrationnelle a été étudié par simulation. La simulation de l'expérience décrite plus haut a été adaptée à ce contexte où seules les processus radiatifs sont en compétition. Une étude détaillée de la compétition entre la fluorescence récurrent et l'émission vibrationnelle dans ces agrégats carbonés a été effectuée en fonction de l'énergie interne des agrégats, de leur taille et de leur famille (cage, flake, pretzel, chaîne). Nous avions à notre disposition les structures vibrationnelles et électroniques de plusieurs milliers d'isomères d'agrégats carbonés, ce qui nous a permis de tirer des conclusions sur le spectre d'émission d'un grand ensemble d'agrégats de carbone. Dans ce travail, les strucutres vibrationnelles et électroniques de plusieurs milliers d'isomères d'agrégats carbonés sont au préalable connus. Ceci permet de tirer des conclusions sur le spectre d'émission d'un grand ensemble agrégats carbonés. En effet, c'est un grand nombre d'isomères qui sont susceptés d'être présents dans le milieu interstellaire et dans les milieux en combustion. Il s'est avéré que la compétition entre la fluorescence récurrente et vibrationnelle dépend de l'énergie interne, de la taille et de la famille des agrégats.

La simulation du spectre d'émission des agrégats de carbones dans les conditions du milieu interstellaire (irradiés par une étoile à 20000 K ou par le champ de radiation standard du milieu interstellaire) a montré que l'émission des cages C_{60} dans le proche IR (< 4 µm) pourrait expliquer le continuum d'émission dans le proche IR observés dans certaines sources astrophysiques. L'abondance des cages C_{60} (et dans une moindre mesure des C_{60} flakes) qui en découlerait a été estimé dans la nébuleuse en réflexion NGC 7023.

L'émission d'un grand nombre d'agrégats de carbone à température fixée a aussi été simulée (toujours par une approche moléculaire) et indique que le spectre d'émission est de type corps noir. L'émissivité moyenne des agrégats de carbone a alors été déduite.

Dans ce travail, les processus de relaxation radiative dans l'infrarouge ont été employé en tant qu'observable pour l'étude expérimentale du mécanisme d'isomérisation dans les dérivés du benzène. Sur le plan théorique, la fluorescence récurrente et l'émission vibrationnelle dans les gros agrégats de carbone C_n (n = 24, 42, 60) ont été étudiées dans le contexte du milieu interstellaire et dans un contexte d'environnement à température fixe.

1. Context

The interstellar medium of a galaxy is the matter and radiation contained outside all stellar systems. The sole interstellar medium to which we have access in detail is that of the Milky Way. The interstellar matter contains gas and dust intimately mixed and represents about 5 % of the total mass of stars (Lequeux, 2012). The interstellar matter consists of 70 % of hydrogen, 28 % of helium and 2 % of heavy elements such as carbon, nitrogen, oxygen, silicon, sulfur or iron (Lequeux, 2012; Tielens, 2005). The origin of the matter in the interstellar medium (ISM) comes mainly from supernova ejections or stellar winds of low-to-intermediate mass stars (< 10 $M_\odot$) at the end of their life. Nevertheless, the ISM is also the birthplace of stars in very cold regions (molecular clouds) where gravitational collapses can occur. Therefore, the lifecycle of matter in a galaxy obeys the following pattern: *interstellar medium → star formation → stellar nucleosynthesis → stellar winds or supernovae → interstellar medium* (Lequeux, 2012). This lifecycle has the effect to increase the abundance of heavy elements in galaxies over time.

The physics and chemistry of the ISM is strongly determined by the energy sources passing through it. We list them in the following points.

- The electromagnetic radiation mainly includes FUV-UV-visible photons coming from hot stars, millimeter photons coming from the cosmic background (but which interact only very little with the interstellar matter) and the mid- and far- infrared photons partly emitted by the interstellar dust absorbing stellar UV-visible photons. X and γ photons originates from supernovae. The extragalactic radiation is negligible. Figure 1.1 shows a typical spectral energy distribution.

- Cosmic rays consist of relativistic atomic nuclei of galactic origin (10^{10}-10^{20} eV), are mainly protons and are probably emitted by stars and, for the most energetic ones, by supernovae.

- The magnetic field, detected for instance by the Zeeman effect, is supposed to be created by the motion of charged matter over the whole galaxy (Terral, 2016). It has an influence on the dynamics of the ISM (e.g. gravitational collapse), on the polarization of photons and charged particles, and is at the origin of synchroton radiation (Beck, 2009).

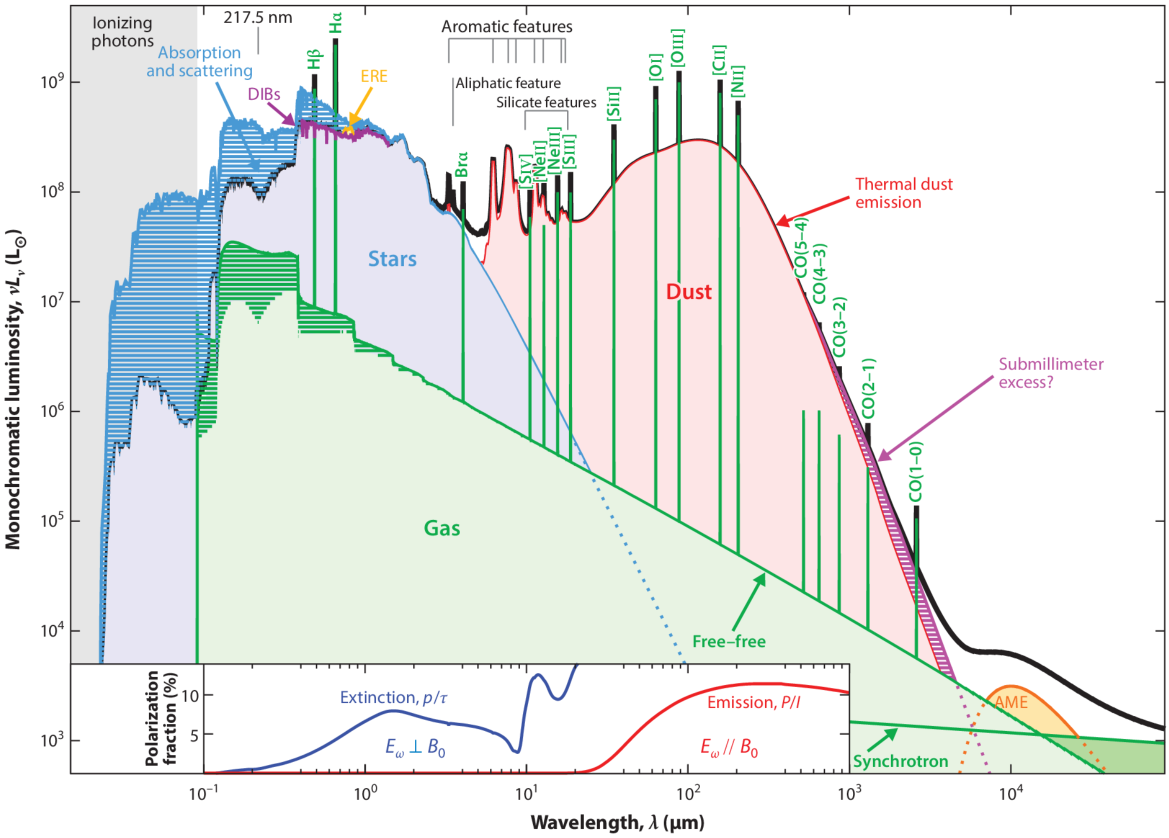

Figure 1.1: Spectral energy distribution in a typical late-type galaxy. Anomalous microwave emission (AME), aromatic infrared bands (AIBs), diffuse interstellar bands (DIBs) and extended red emission are represented. The inset graph at the bottom displays the polarization fraction of light in the ISM in terms of the wavelength. The monochromatic luminosity is expressed in solar luminosity ($\approx 3.8 \cdot 10^{28}$ W). This figure is extracted from (Galliano et al., 2018)

Macroscopic kinetic energy stems mainly from shocks vigorously created by a pressure increase and causes supersonic macroscopic motions. Shocks includes supernovae remnants, bubbles, HII regions. Stellar winds, which are not considered as shocks, are also mechanical energy sources. Shocks can influence the chemistry of the ISM via strong thermodynamic conditions variations (Lequeux, 2012). The interstellar turbulence is also a vector of kinetic energy transfer toward the ISM (Elmegreen and Scalo, 2004). All energy sources have, on average, similar energy density (≈ 1 eV/cm^3 in the neighborhood of our solar system). This testifies to the efficient coupling between all the components of the ISM and to the complexity of modeling the physics and chemistry of the ISM.

Besides solid or gaseous phase, the interstellar matter is also in neutral, ionized or molecular state. This matter has constantly a macroscopic motion and does not reach thermodynamic equilibrium. To give an indication of the state of matter, it is usual to refer to the state of the most abundant element, hydrogen. We talk about neutral interstellar gas when hydrogen is mainly in its non-ionized state. This neutral gas is called molecular in regions where molecular hydrogen is abundant (molecular clouds). This neutral gas is called atomic in regions where atomic hydrogen is abundant (cold neutral medium, CNW; warm neutral medium, WNM). We talk about ionized interstellar gas when hydrogen is mostly ionized (warm ionized medium, WIM; hot ionized gas; HII regions). The state of matter is determined by the radiation and local conditions (temperature, density, degree of ionization, density of photons, etc) which are determined, in turn, by surrounding interstellar objects (O and B stars, AGB stars, post-AGB stars, supernovae, planetary nebulae) and the heating/cooling of the interstellar gas which is determined by radiation and species constituting the gas.

Several interstellar gas heating mechanisms take place, with more or less importance according to the region. The general mechanism of heating of the interstellar gas is that of electrons releasing by neutral or ionized grains and the transfer of their excess kinetic energy to the surrounding gas via coulombic collisions. These electrons can be released by photoelectric effect on grains, ionization of atoms and molecules upon harsh radiation (wavelength < 10 nm) and cosmic particles of low energy. The photoelectric effect on grains is the dominant process because the extraction of electrons requires less energy. To a lesser extent, X-ray photons (from the hot gas, 10^5-10^6 K) release such energetical electrons from the inner layers of atoms and molecules that these electrons can in turn ionize other atoms and molecules to give secondary electrons that will heat the surrounding gas (secondary electrons can also be released by cosmic particles irradiations). Chemical reactions can also participate to the gas heating via exothermic reactions. H_2 formation via heterogeneous catalysis on dust grains is particularly exothermic (4.48 eV)(Wakelam et al., 2017). Stellar winds and supernova explosions release a large amount of energy by radiation and kinetic energy of atoms and molecules (neutral, ions) which contribute to the heating of interstellar gas. Also, magnetohydrodynamic heating takes place via viscous dissipation of the magnetic field motion driving the ionized gas. Then, the neutral gas is insensitive to magnetic lines (ambipolar diffusion) but is heated by collisions with the ionized component.

Interstellar gas cooling takes place mainly by radiative de-excitation. Indeed, atoms and molecules are easily excited by collision to their lowest excited levels (fine structure), hence cooled by spontaneous emission. Even at low temperatures, rotational levels of small molecules are populated (Roueff and Lique, 2013).

Radiation, cosmic particles, shocks, heating and cooling of the interstellar gas will strongly influence the physics and chemistry in the interstellar medium. Since external perturbations (radiation, cosmic particles, etc) vary faster than the energy transfer within and between gas and dust grains, the ISM is constantly out of thermodynamic equilibrium. This results in kinetically-driven chemistry. The chemistry takes place in the gas phase and on dust grains surface. In the gas phase, molecules are formed by ion-molecule reactions, radiative association, dissociative recombination, neutral-neutral reactions and can be destroyed by photodissociation and photoionization. Reactions that could not take place in the gas phase take place at grain surfaces such as the H_2 formation in molecular clouds or the formation of CO_2, H_2O, H_2CO, CH_3OH and many others (Tielens, 2013; Snow and Bierbaum, 2008). Molecules are usually first detected by rotational spectroscopy, rovibrational spectroscopy, electronic fluorescence and chemical reaction models are built to explain their formation according to local conditions (via theoretical and experimental estimates of reaction or destruction rates (Wakelam et al., 2010)). To date, nearly 230 molecules have been detected in the interstellar medium, ranging from diatomic molecules to indene with 17 atoms. The largest molecules detected are the buckminsterfullerene C_{60}, its cation (C_{60}^+) and the C_{70} (the most stable fullerenes) (Tielens, 2013).

Interstellar dust is composed of carbonaceous and silicate grains of size ranging from about 0.3 nm to about 0.3 µm (Galliano et al., 2018). They are formed in envelopes of stars at the end of their life depending on whether they are carbon-rich or oxygen-rich. Carbon-rich stars (containing more carbon than oxygen, $C/O>1$) eject carbonaceous grains (Duley, 2019) while cold oxygen-rich stars eject amorphous or crystalline silicate grains (Galliano et al., 2018). Grains have relevant influence on the physics and chemistry of the ISM. They are largely responsible for the extinction of UV/visible radiation stemming from stars, its scattering (the reddening of the transmitted light and blueshifted diffused light) and its absorption. Grain absorption is sometimes at the origin of photoelectron ejection which participates, as mentioned above, in the interstellar gas heating and leaves grains electrically charged. Then, grains with anisotropic shape are spatially oriented by the surrounding magnetic field and are thus, partly, responsible for the partial polarization of the interstellar radiation (Andersson et al., 2015) (figure 1.1). In cold regions, the interstellar gas adsorbs on grains surface to form ice mantles where chemical reactions can take place, whereas they are prohibited in the gas phase. These reactions give rise to interstellar complex organic molecules that are interesting for prebiotic chemistry in ISM (Zamirri et al., 2019). These molecules produced on grain surfaces are then restored in the gas if the grain is heated.

The heated grains also cool down through radiative cooling in the mid and far IR. After UV photon absorption, the smaller the grains are, the higher the temperature peak will be and emit at shorter wavelengths, up to the near-IR (typically 1000 K and emit below 5 µm, (Sellgren et al., 1983; Sellgren, 1984)). The size of grains cooling by radiative emission in the near and mid-IR are likely of the order of 1 nm (Sellgren, 1984). At this scale, we can talk about very large molecules (benzene diameter is 0.5 nm and buckminsterfullerene is around 1 nm). However, detected near and mid-IR emission signal from plethora of interstellar environments are usually composed of very particular emission features.

Figure 1.1 shows typical emission spectra detected in the interstellar medium in the mid-IR (between 3 µm and 20 µm). This set of emission features are called Aromatic Infrared Bands (AIB) and major features are around 3.3, 6.2, 7.7, 8.6, 11.3 and 12.7 µm (Gillett et al., 1973, 1975; Russell et al., 1977; Willner et al., 1979). The proposed explanation of the carriers and photophysics mechanism at the origin of AIBs is called the PAH hypothesis. It states that, upon UV-visible photon absorption, electronically excited neutral or cationic polycyclic aromatic hydrocarbon molecules, PAH (Clar and Schoental, 1964)), convert rapidly electronic energy into vibrational energy (via internal conversion or intersystem crossing) and the highly vibrationally excited PAH emits spontaneously via vibrational radiative de-excitation (or vibrational fluorescence) to reach the ground state (radiative relaxation). The resulting emission spectra contain major AIB features (Leger and Puget, 1984; Allamandola et al., 1985). The development of the PAH hypothesis started actually in 1956 with Platt's work (Sellgren, 1984; Platt, 1956; Donn, 1968; Duley and Williams, 1981). The 217.5 nm UV-bump absorption is suspected to be a collective feature of PAHs (Steglich et al., 2011, 2010; Pino et al., 2021) and can also be due to aromatic/aliphatic carbonaceous grain with diverse degree of hydrogenation (Gavilan et al., 2017; Kwok and Zhang, 2011). The UV absorption and subsequent IR emission of PAHs would then contribute to the conversion of UV radiation into IR radiation in the ISM. Besides IR emission induced by UV stellar photon absorption, PAHs could emit by electronic radiative de-excitation although internal conversion is very efficient (Medvedev and Osherov, 1995). Indeed, in the isolated conditions of the ISM, vibrational radiative relaxation of PAHs is slow enough to convert a part of their vibrational energy into electronic energy (electronic excitation) and undergo electronic fluorescence. This mechanism is called recurrent fluorescence or Poincaré fluorescence (Léger et al., 1988) and is at the core of our thesis work.

Very recently, indene has been detected by its rotational emission spectrum in TMC-1 (Cernicharo et al., 2021; Burkhardt et al., 2021). Benzonitrile has also been detected in TMC-1 (McGuire et al., 2018), its presence was predicted and its formation via barrierless reactions of benzene was discussed in (Jones et al., 2011). The detection of these species strenghten the assumption that PAH-like molecules are abundant in the ISM. Only PAHs containing more than 50 carbon atoms are expected to survive to radiation (Allain et al., 1996a,b) and PAHs contain around 10 % of interstellar carbon (Puget and Léger, 1989; Allamandola et al., 1989) and would have consequently important contribution in chemistry (ionization, dissociation, ion-neutral recombination, etc) and physics (heating via electron release, cooling via radiative relaxation, etc) in the ISM (Tielens, 2005, 2008, 2021). AIBs are also detected in the envelopes of evolved C-rich stars in which PAHs formation is suspected to take place by the HACA mechanism (H-abstraction C_2H_2-addition) such as in flames (Joblin et al., 2011; Frenklach and Feigelson, 1989; Frenklach and Mebel, 2020) although HAVA mechanism (H-abstraction vinylacetylene-addition) have been recently to explain large plane PAH molecules formation (Zhao et al., 2018). Other PAH formation mechanism have been suggested in cold regions (bottom-up approach, (Jones et al., 2011; Zhang et al., 2011)) or from soot particles (top-down approach via grain-grain collisions (Jones et al., 1996) or PAH release upon energetic processing (Pino et al., 2019)). Large PAH molecules are a good starting point to relate molecules and small carbonaceous grains (diameter around 1 nm) discussed above. To this aim, C_n (n $\gtrsim$ 20) large carbon clusters turn out to be of interest.

Cage-like large carbon clusters include the fullerenes subset which are the most stable carbon clusters. The most stable fullerene is the C_{60} buckminsterfullerene and its presence in ISM was suspected (Kroto et al., 1985; Kroto and Jura, 1992) on account of the high dissociation threshold ($\approx$ 10 eV, (Lifshitz, 2000b)). The C_{60} buckminsterfullerene vibrational emission spectra have been detected in several ISM environments (reflection nebulae, diffuse medium, planetary nebulae, protoplanetary nebulae) (Sellgren et al., 2010; Cami et al., 2010; Roberts et al., 2012; Zhang and Kwok, 2011a; Otsuka et al., 2013; Berne et al., 2013). Its vibrational emission is supposed to occur in the same framework than PAH hypothesis (vibrational emission induced by UV stellar electronic excitation). The C_{60}^+ cation has also been detected in absorption (Cordiner et al., 2019) and five DIBs have been attributed to it (Campbell et al., 2015; Maier and Campbell, 2017; Lykhin et al., 2018). The C_{70} has also been detected in the Tc1 planetary nebulae (Cami et al., 2010) and C_{24} fullerene or its most stable planar isomer may have been detected (Bernstein et al., 2017; García-Hernández et al., 2011).

Although PAH and fullerene formation has been explored in carbon rich flames (Homann, 1998), interstellar regions in which PAHs and the buckminsterfullerene have been detected are H abundant relative to helium and trace amounts of carbon, oxygen, nitrogen, etc (Otsuka et al., 2014; García-Hernández et al., 2011, 2010, 2012). The coexistence or correlation of AIBs et buckminsterfullerene emission indicates the C_{60} formation route could involve PAHs (Sellgren et al., 2010; Castellanos et al., 2014). The likely fullerene formation route in ISM is the so-called top-down mechanism (Berné and Tielens, 2012). This mechanism states that fullerenes are formed by photolysis of large PAHs (dehydrogenation and/or fragmentation) with subsequent isomerization. Experiments supporting this mechanism has been carried out (Zhen et al., 2014) and we think this mechanism could also lead to carbon chains, rings or smaller hydrocarbons. A similar mechanism is suspected to occur for fullerene formation from hydrogenated amorphous carbon nanoparticles (García-Hernández et al., 2010; Micelotta et al., 2012). The closed network mechanism (CNG) could explain fullerene growth (endohedral fullerenes as well) in carbon vapour environment by C or C_2 incorporation into the growing fullerene via carbon-catalysed bond rearrangement (Dunk et al., 2012b,a). This is interesting for fullerene formation in outflows of evolved C-rich stars or circumstellar environments (Bernard-Salas et al., 2012; Cami et al., 2011; Gielen et al., 2011; Dunk et al., 2013). Besides top-down formation routes, bottom-up approaches have been suggested to proceed in envelopes of old C-rich rich stars. Actually, on Earth, fullerenes are products of incomplete combustion (flames with $C/O > 1$, (Gerhardt et al., 1989; Howard, 1992)). Originally, fullerenes have been discovered in laser evaporating graphite experiments (Kroto et al., 1985; Krätschmer et al., 1990). Two main formation routes of fullerenes are still under discussion. One involving aromers (aromatic oligomeres) which are formed via PAH agglomeration linked to each other covalently by C-C bonds and the fullerene appears by the formation of other C-C bonds by unimolecular reaction (zip mechanism, (Ahrens et al., 1994; Homann, 1998)). The other mechanism involves PAHs containing five-membered rings (mainly similar to corannulene but larger size) with acetylene addition and H_2 loss (Pope et al., 1993; Homann, 1998) (similar to HACA mechanism for PAHs formation in flames). Thus, like PAH formation in the envelopes of C-rich stars, these mechanisms could take place given that the buckminstefullerene has been detected in a few post-AGB stars (Gielen et al., 2011; Bernard-Salas et al., 2012).

Our work is focused on the radiative relaxation of C_n (n= 24, 42, 60) large carbon clusters and benzene derivatives. This work is in line with the photophysics mechanism of the PAH hypothesis in which molecules undergo, in isolated conditions, radiative relaxation subsequent to photon absorption. After several buckminsterfullerene detections in space, it is plausible that large carbon clusters are present in abundance in the ISM. In that context, our colleagues generated and investigated the structural properties of hundreds of thousands of C_{24}, C_{42}, C_{60} isomers (Bonnin et al., 2019) as well as their

vibrational and electronic structures (Dubosq et al., 2019, 2020). We used several thousand of these isomers to study the radiative relaxation of C_{24}, C_{42}, C_{60} in order to simulate the IR emission spectra from a large set of isomers in the ISM irradiated by a star or the interstellar radiation field. The two radiative relaxation that we took into account in the simulation is vibrational emission and recurrent fluorescence (or Poincaré fluorescence). In this study, we were led to investigate in detail the competition between vibrational emission and recurrent fluorescence in large carbon clusters.
As mentioned above, fullerene and carbon clusters have been detected in flames. We then also simulated the emission spectra of a large set of carbon clusters in temperature fixed context, potentially useful for laser-induced fluorescence experiments.
Still within the same photophysics framework (vibrational emission induced by UV-excitation), we experimentally investigated the way vibrational emission could be applied to unimolecular reaction studies such as six to seven-membered ring isomerization for toluene → cycloheptatriene.

The thesis is organized as follows. The second chapter introduces the photophysics and photochemistry processes taking place and theoretical models to describe them. The third chapter shows the simulation results on the competition between recurrent and vibrational fluorescence in large carbon clusters, the emission spectra of large set of carbon clusters irradiated by a 20 000 K star or the average interstellar radiation field and the emission spectra of a large set of carbon clusters at fixed temperature (1500 K and 2500 K). In the fourth chapter, we present the home-made IR spectrometer FIREFLY for UV-laser induced IR fluorescence experiments and the fifth chapter is dedicated to experimental results on toluene to cycloheptatriene isomerization study by analyzing toluene IR emission spectrum during the relaxation. The same investigation did with phenylacetylene and aniline is also briefly shown. Then a conclusion terminates the thesis with some perspectives.

2. Theoretical framework

In this chapter, we briefly introduce the photophysical and photochemical processes considered in our work. We simulated the radiative relaxation of large species (between 10 and 60 atoms) in isolated and non-isolated conditions. In our work, *isolated* means that the molecules do not undergo external interaction during the relaxation time. These simulations requires all rates (spontaneous emission, dissociation, collision and isomerization) occurring during the relaxation. In the following sections, we present the theoretical models that we have used in this work.

In our models, the fundamental assumption is that the species studied are sufficiently large for a statistical approach to be adopted in describing their internal energy distribution. This is what we try to justify in the first section of this chapter before applying this assumption to the calculation of the recurrent and vibrational fluorescence rates. The second section introduces the ideas of RRK and RRKM theories to calculate dissociation and isomerization rates. The third section introduces the model to describe the collisional energy transfer between excited species and their environment. Given the difficulty to describe the radiative relaxation analytically, we introduce in the fourth and last section the kinetic Monte-Carlo method to simulate the kinetics of the radiative relaxation as well as the resulting emission spectra.

Modelling of the photophysics

The photophysicalprocesses within a molecular edifice include all the phenomena other than ionization or chemical bonds alteration. We divide them into three categories (Birks, 1970b):

• Radiative excitations for which the molecule, after absorption of photon, reaches a higher electronic state. This definition can be transposed to transitions involving vibrational or rotational states. In the molecular systems we studied, the internal energy is very often provided by electronic excitation induced by the absorption of UV photon.

• Radiative de-excitations are the reverse path of radiative excitations. When photon emission occurs between two states of the same spin multiplicity, we talk about fluorescence. Between states with different spin multiplicity, the term phosphorescence is used. In our work, we studied two types of radiative de-excitation: the *recurrent fluorescence* and the *vibrational fluorescence*. We are aware that the term vibrational fluorescence may disturb some readers who would prefer the name *vibrational emission*. We will nevertheless also use the term *vibrational fluorescence* because it is very often used in the astrophysics community.

• Radiationless transitions involve processes in which there is no photon emission 2.1. Under isolated conditions, radiationless transitions take place at fixed internal energy. They include all interactions that take place between the different degrees of freedom of the molecule (electronic, vibrational or rotational). The internal conversion, the reverse internal conversion, the inter-system crossing and the intramolecular vibrational redistribution are part of radiationless transitions which are going to play a very important role in our model (Bixon and Jortner, 1968; Itoh, 2012). Under non-isolated conditions, the molecular species can also exchange energy with its environment through collisional excitations or de-excitations.

In this first section we will define recurrent fluorescence and vibrational fluorescence and present the theoretical model from which we calculate their emission rates. This model involves statistical mechanics arguments because of the very high density of vibrational states in the molecule.

Statistical approach - microcanonical framework

We consider the case in which the molecule is in an excited electronic state (excited vibronic state) and in isolated conditions. We neglect the rotational degrees of freedom. First of all, the vibrational states will interact with each other via anharmonic couplings and Coriolis interactions (Medvedev and Osherov, 1995). These couplings will cause a vibrational energy flow among all the vibrational degrees of freedom. This is called the intramolecular vibrational redistribution (IVR) (Quack, 1990; Medvedev and Osherov, 1995; Nesbitt and Field, 1996; Parmenter, 1982). In addition to the coupling, the efficiency of IVR increases with the size of the molecule (i.e. its density of rovibrational states) and takes place on τ timescales of the order of 10^{-13}-10^{-9}s for organic molecules such as polycyclic aromatic hydrocarbons (Nesbitt and Field, 1996; Bondybey, 1984; Kim et al., 1987).

At the same time, the excited electronic state undergoes a coupling with vibrational states of an electronic state of lower energy. We talk about *internal conversion* (IC) in the case where the two electronic states have the same multiplicity ($\tau \sim 10^{-13}$-10^{-10} s) and we talk about *intersystem crossing* (intersystem crossing, ISC) in the case with different multiplicities ($\tau \sim 10^{-10}$-10^{0} s for hydrocarbons) (Birks, 1970b; Medvedev and Osherov, 1995; Ermolaev, 2001). This interaction originates from the fact that the electronic wave functions are sensitive to nuclear motion. It is neglected in the Born-Oppenheimer approximation and treated by the perturbation theory. The internal conversion rate can then be obtained by the Fermi golden rule which involves the density of vibrational states. Since the density of vibrational states increases very rapidly with size and internal energy ($10^{15}/\mathrm{cm}^{-1}$ for naphthalene at 20 000 cm^{-1} internal energy, (Cook and Saykally, 1998)), internal conversion and intersystem crossing are actually very fast processes.

Coupling terms between the upper electronic state and the vibronic states of a lower electronic state appear also (via Fermi's golden rule) in this internal conversion rate. Thanks to the separability of the Hamiltonian (one of the consequences of the Born-Oppenheimer approximation), these coupling terms give rise to vibrational overlap terms between the two electronic states called *Frank-Condon factors.* It turns out in the statistical limit that the Franck-Condon factors decrease (approximately) as the exponential of the electronic energy gap. This result is called *Energy Gap Law.* The exponential dependence comes from the Hermite polynomials (vibrational wavefunction in the harmonic approximation). Then, the Energy Gap Law implies that the internal conversion operates most often via the transitions $\mathrm{S}_n \rightarrow \mathrm{S}_{n-1}$ (Pino et al., 2021). This conversion is considered irreversible because the density of vibrational states increases very rapidly with energy. Indeed, the duration to explore the whole phase space of the vibrational states associated to S_{n-1} is so large that we can consider that the transition $\mathrm{S}_n \rightarrow \mathrm{S}_{n-1}$ is irreversible (Freed and Jortner, 1970). The return will not take place, at this stage, because the transition $\mathrm{S}_{n-1} \rightarrow \mathrm{S}_{n-2}$ takes over very quickly.

To summarize: after electronic excitation, a sufficiently large molecule (more than 10 atoms) will undergo a succession of internal conversion $\mathrm{S}_n \rightarrow \mathrm{S}_{n-1}$ at the same time as the IVR within each electronic state. Thus, the molecule moves irreversibly towards the fundamental electronic state by converting continuously its electronic energy into vibrational energy (the internal energy remains constant). The large amount of energy distributed in the vibrational degrees of freedom of the lower electronic states will give rise to a very large number of accessible rovibrational states. Then, it is quite legitimate to make a statistical treatment to model the distribution of the internal energy.

Of course, after the ground electronic state is reached, the molecule starts to relaxe slowly by vibrational de-excitation (slow compared to the IC, IVR and ISC). However, in the electronic ground state, there is neither internal conversion nor inter-system crossing. Moreover, under isolated conditions, the recurrence time in the S_0 state can be comparable to (or even shorter than) the radiative relaxation time. This implies that, during radiative vibrational relaxation, the molecule can explore vibrational states of higher electronic states. This is called *inverse internal conversion* (or possibly *inverse inter-system crossing*) and admits a rate three or four magnitudes below the internal conversion (Itoh, 2012; Baba et al., 1971; Chihara and Baba, 1977; Nitzan and Jortner, 1978, 1979). The inverse internal conversion rate is still very fast compared to radiative transition rates. All radiationless transitions listed so far are therefore very fast compared to radiation transitions. We can then say that, under isolated conditions, internal energy is statistically distributed among all accessible vibronic states. Between two successive radiative transitions, the IVR, the internal conversion and the inverse internal conversion will allow the system to maximize its entropy very rapidly. We believe that these radiationless transitions ensure the ergodicity of polyatomic molecules.

Fluorescence rates will be calculated in the microcanonical framework (internal energy fixed and at statistical equilibrium). In this framework, the fundamental quantity is the density of vibrational states because it is through the vibrational degrees of freedom that the internal energy is mostly distributed. In our work, we have neglected the rotational degrees of freedom. The figure (2.1) represent the processes occurring after electronic excitation.

Harmonic vibrational density of states

We would like to exactly calculate the harmonic vibrational density of states (VDOS) at fixed internal energy for a molecule described by a set of vibrational normal modes. We shall briefly present the Beyer-Swinehart algorithm principle which exactly calculate the harmonic VDOS by a recurrence relation (Beyer and Swinehart, 1973).
We suppose the harmonic approximation of the vibrational states is valid. Suppose that $\rho(E,n)$ is, at internal energy E, the VDOS of a set of n vibrational modes. The i$^{\text{th}}$ vibrational mode has a frequency ν_i. By adding an $(n+1)^{\text{th}}$ vibrational mode of frequency ν_{n+1}, the VDOS $\rho(E,n+1)$ is then expressed in terms of $\rho(E,n)$ by

$$\rho(E,\, n+1) = \sum_{k=0}^{[E/h\nu_{n+1}]} \rho(E - kh\nu_{n+1},\, n) \tag{2.1}$$

Indeed, the term $\rho(E - kh\nu_{n+1},\, n)$ gives the density of states on the set of n vibrational modes at internal energy $E - kh\nu_{n+1}$ knowing that k quanta are contained in the $(n+1)^{\text{th}}$ mode. The sum represents then all the states that the (n+1)$^{\text{th}}$ mode can take. $[E/h\nu_n]$ represents the integer part of $E/h\nu_n$. We can write the relation (2.1) for an internal energy of $E - h\nu_{n+1}$

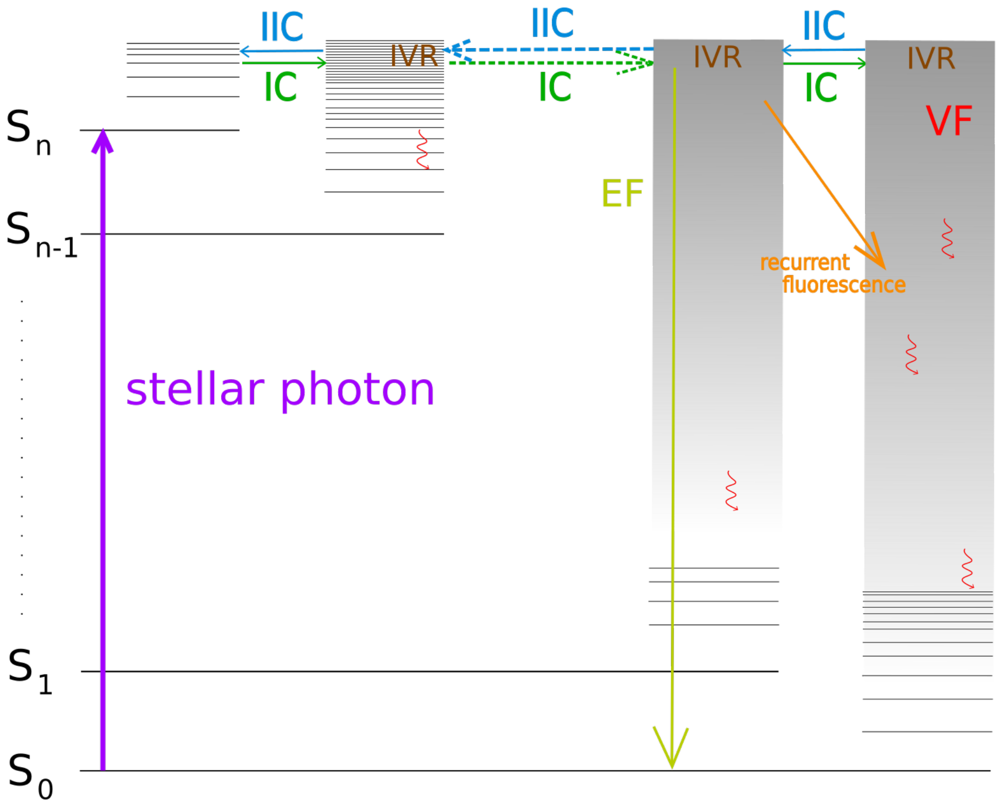

Figure 2.1: Jablonski diagram showing the radiative and radiationless processes that take place during the relaxation cascade. IC: internal conversion; IIC: inverse internal conversion; IVR: intramolecular vibrational redistribution; PD: photodissociation; VF: vibrational fluorescence; EF: electronic fluorescence and zigzag arrows represent IR photons; pink arrows represent collisional de-excitation.

$$\rho(E - h\nu_{n+1},\, n+1) = \sum_{k=0}^{[(E-h\nu_{n+1})/h\nu_{n+1}]} \rho(E - (k+1)h\nu_{n+1},\, n) \tag{2.2}$$

$$= \sum_{k=1}^{[E/h\nu_{n+1}]} \rho(E - kh\nu_{n+1},\, n) \tag{2.3}$$

$$\tag{2.4}$$

This last equality, subtracted from (2.1), gives the recurrence relation

$$\rho(E,\, n) = \rho(E - h\nu_n,\, n) + \rho(E,\, n-1) \tag{2.5}$$

Then, it is sufficient to know ρ for a single mode, at a given energy, to then deduce via the recurrence relation (2.5) the density of vibrational states over all modes at that energy. The initialization calculation, *i.e.* the VDOS for a single mode, is elementary. For all our calculations, we have used this relation.
It is possible to give an analytical relation to the VDOS, in the approximation of a set of classical harmonic oscillator. It is written,

$$\rho(E) = \frac{E^{\,g-1}}{(g-1)!\prod_{i=1}^{g} h\nu_i} \tag{2.6}$$

with E the internal energy, g the number of vibrational modes and ν_i their frequency. This relation can be demonstrated by a recurrence relation on the number of vibrational modes (Robinson and Holbrook, 1972). This expression is far from the result of the exact quantum calculation (Beyer-Swinehart algorithm) when the internal energy is of the order of the zero-point energy and underestimates its value. To limit the error, Marcus and Rice proposed to add empirically the zero-point energy E_z to the internal energy in the relation (2.6), to obtain the semi-classical expression

$$\rho(E) = \frac{(E+E_z)^{g-1}}{(g-1)!\prod_{i=1}^{g} h\nu_i} \tag{2.7}$$

Figure (2.2) shows the VDOS obtained by Beyer-Swinehart and the two expressions (2.6) and (2.7).

The semi-classical expression of Marcus and Rice is close to reality when the internal energy is large compared to the zero-point energy. In our work, we systematically used the expression (2.7) when it was necessary to do analytical developments.

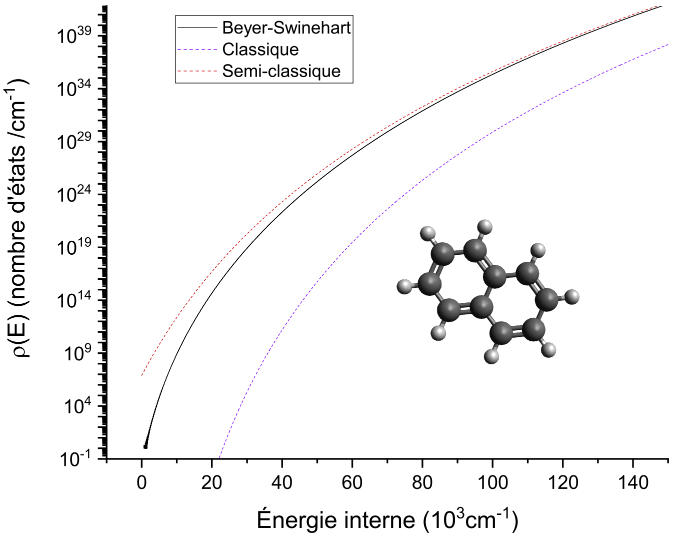

Figure 2.2: Comparison between the density of vibrational states of naphthalene calculated by the Beyer-Swinehart algorithm, the classical (2.6) and semi-classical (2.7) relation. In the naphthalene case, $E_z \approx 60000$ cm^{-1}.

Recurrent fluorescence

Recurrent fluorescence (also called *Poincaré fluorescence*) was predicted in 1988 in the interstellar medium context (Léger et al., 1988). The central idea of the article is that a polycyclic aromatic hydrocarbon in the interstellar medium (thus in isolated conditions) takes several seconds to relax via vibrational emission. This duration gives isolated PAHs (in fact, any other species) enough time to explore higher electronic states during the radiative relaxation. During the vibrational relaxation, the molecule can then be recurrently electronically excited by inverse internal conversion and undergo electronic fluorescence. Thus, we talk about *recurrent fluorescence* (figure (2.1)). Several experimental studies have detected the recurrent fluorescence. By studying the internal energy decay of cationic anthracene $(C_{14}H_{10})^+$ placed in a storage ring, Martin *et al.* noticed that the cooling rate was too fast to be explained by vibrational fluorescence and attributed it to recurrent fluorescence (Martin et al., 2013, 2015). Still in a storage ring, recurrent fluorescence was also detected in the case of C_6^- and C_6^-H by discriminating it from electron fluorescence through its emission time profile (Ito et al., 2014; Ebara et al., 2016).

At a fixed internal energy E a molecule can occupy a vibrational state associated with the i$^{\text{th}}$ excited electronic state of energy E_i. In this case, the vibronic density of states $\rho(E)$ at internal energy E is given by

$$\rho(E) = \rho_0(E) + \rho_1(E - E_1) + \rho_2(E - E_2) + ... + \rho_n(E - E_n) \tag{2.8}$$

$\rho_i(E - E_i)$ is the VDOS in the i^{th} excited electronic state of energy E_i. In the i^{th} excited electronic state, the vibrational energy is equal to $E - E_i$. ρ_0 is the VDOS in the ground electronic state and we have $E_n < E < E_{n+1}$. The (microcanonical) probability that the molecule occupies the i^{th} electronic state is then given by

$$\frac{\rho_i(E - E_i)}{\rho_0(E) + \rho_1(E - E_1) + \rho_2(E - E_2) + ... + \rho_n(E - E_n)} \tag{2.9}$$

Let us assume that ρ_i functions are approximately equal for internal energies high compared to vibrational mode frequencies. This is justified by the fact that the vibrational mode frequencies do not change much with the electronic state for large hydrocarbons and large carbon clusters. The probability is then written as

$$\frac{\rho_0(E - E_i)}{\rho_0(E) + \rho_0(E - E_1) + \rho_0(E - E_2) + ... + \rho_0(E - E_n)} \tag{2.10}$$

which can be written as

$$\frac{\rho_0(E - E_i)}{\rho_0(E)} \times (1 + \sum_{i=1}^{n} \frac{\rho_0(E - E_i)}{\rho_0(E)})^{-1} \tag{2.11}$$

From the semi-classical expression (2.7), we write

$$\frac{\rho_0(E - E_i)}{\rho_0(E)} = (1 - \frac{E_i}{E + E_z})^{g-1} \tag{2.12}$$

In our work, we studied recurrent fluorescence for molecules with 24 to 60 atoms. For carbon species containing 60 atoms, $E_1 \approx 3000$ cm^{-1} (=0.4 eV) (Dubosq et al., 2020). For 10^5 cm^{-1} (12.4 eV) internal energy, the ratio (2.12) is of the order of 10^{-2}. The result is even weaker when the electronic energy increases. Indeed, figure (2.3) shows the exponential decrease of the ratio (2.12) in terms of the internal energy and the size. Generally, we have to simulate the emission from a set of carbon clusters (some thousands). We shall see later (chapter 3, section 3) that the electronic density of states of a carbon cluster set increases almost linearly with the electronic energy. Except, for the first electronic states of C$_{60}$, the ratio (2.12) is at most of the order of 10^{-2}.

The electronic density of states does not increase exponentially. Then, we can assume that the ratios of the fraction in the the right hand side of (2.12) are negligible compared to 1. We consider the occupation probability of the i$^{\text{th}}$ electronic state as

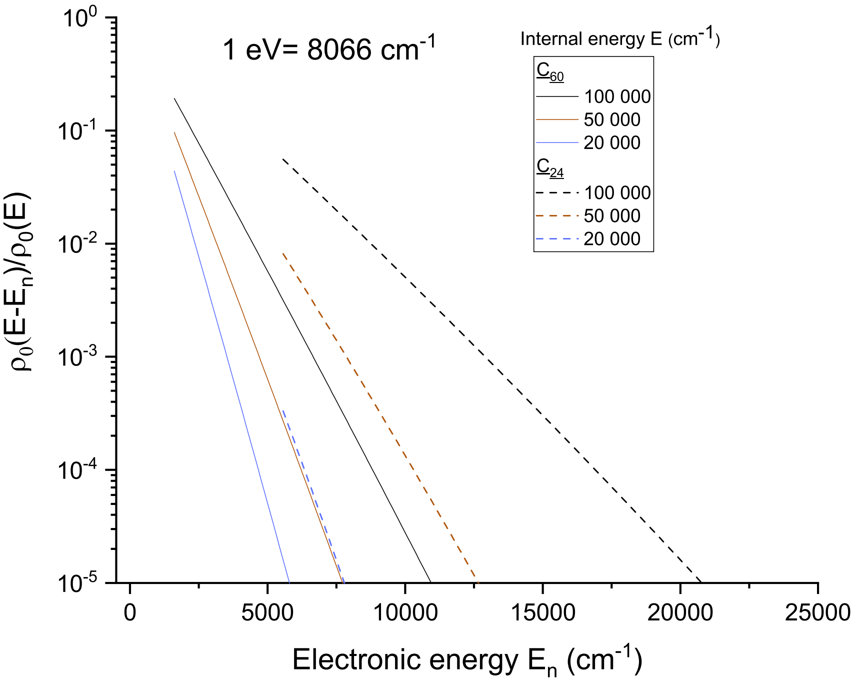

Figure 2.3: Ratio (2.12) in terms of the electronic energy. Except at high internal energies ($\approx 10^5$ cm^{-1}) and for very low electronic energies (< 3000 cm^{-1}), the ratio is negligible compared to 1.

$$\frac{\rho_0(E-E_i)}{\rho_0(E)} \tag{2.13}$$

In this excited electronic state, the molecule undergoes spontaneous emission at rate A_{f}^i. We also know that the probability (2.13) reflects the proportion of time spent in the i^{th} electronic state. This implies that recurrent fluorescence rate from the i^{th} electronic state is expressed by

$$A_{\mathrm{rec}}^i = A_{\mathrm{f}}^i \frac{\rho_0(E-E_i)}{\rho_0(E)} \tag{2.14}$$

However, electronic fluorescence A_{f}^i from the i^{th} electronic state are still to calculate. We shall see the calculation of A_{f}^i in section 2.

Vibrational fluorescence

During radiative relaxation, a vibrationally excited molecule is spontaneously emitting via vibrational emission (figure (2.1)). As before, the internal energy is fixed and statistical equilibrium is supposed to be reached. We follow the model introduced in (Durana and McDonald, 1976).
We represent by $\rho_0(E)$ the VDOS in the ground electronic state at internal energy E. The probability that the vibrational mode i contains v vibrational quanta is written

$$P_{i,v}(E) = \frac{\rho_{0/i}(E-vh\nu_i)}{\rho_0(E)} \tag{2.15}$$

with $\rho_{0/i}$ representing the VDOS without taking into account the i^{th} mode. At internal energy E, i^{th} mode can contain up to $[E/h\nu_i]$ vibrational quanta. We then write the vibrational emission rate from i^{th} mode

$$A_i(E) = \sum_{v=1}^{[E/h\nu_i]} \frac{\rho_{0/i}(E-vh\nu_i)}{\rho_0(E)} A_i^{v\to v-1} \tag{2.16}$$

with $A_i^{v\to v-1}$ the spontaneous emission rate via the $v \to v-1$ transition. In the harmonic approximation of vibrations, it is shown via the creation and annihilation operators applied to the dipolar transition moment of the $v \to v-1$ spontaneous emission that $A_i^{v\to v-1} = v \times A_i^{1\to 0}$. Then, the previous relation of the emission rate $A_i(E)$ becomes

$$A_i(E) = A_i^{1\to\ 0} \sum_{v=1}^{[E/h\nu_i]} v \times \frac{\rho_{0/i}(E-vh\nu_i)}{\rho_0(E)} \tag{2.17}$$

This relation was confirmed experimentally by the study of the infrared emission of azulene at 3.3 µm (Shi and Barker, 1988). In our work, we made the approximation that the overtones and the combination bands are negligible compared to the transitions $v \rightarrow\ v-1$. If we want to calculate the vibrational fluorescence rates from an excited electronic state i, we just have to multiply the expression (2.17) at $E-E_i$ internal energy by the probability to occupy the electronic state i, $\rho_0(E-E_i)/\rho_0(E)$ (equation 2.13). As for the recurrent fluorescence, spontaneous emission rates $A_i^{1\rightarrow 0}$ from the i^{th} vibrational mode are still to be calculated. This is what we present in the next section.

Formula relating spectroscopic quantities

In recurrent and vibrational fluorescence rates, spontaneous emission rates are involved. These spontaneous emission rates are written in terms of quantities calculated via *ab initio* calculations. Indeed, the recurrent fluorescence rate (relation (2.14)) involves the electronic fluorescence rate A_f^i of the i^{th} electronic state which is proportional to the electronic oscillator strength (no unit). Similarly, in the relation (2.17) of the vibrational emission rate, the $A_i^{1\rightarrow 0}$ involve IR intensities strengths (often expressed in km/mol in quantum chemical calculations). In the next two subsections, we try to show the relations used between the spontaneous emission rate involving relations (2.14) and (2.17) and the electronic dimensionless oscillator strength (no unit) or the IR intensity strength (in km/mol) which are obtained by ab initio calculations.

Relationship between spontaneous emission rate and oscillator strength

In (Cohen-Tannoudji et al., 2021), the oscillator strength of a radiative transition between the $|\varphi_i\rangle$ initial state to the $|\varphi_j\rangle$ final state is defined by

$$f_{ij} = \frac{4\pi m_e}{\hbar}\nu_{ij}|\left\langle\varphi_i\right|\widehat{Z}\left|\varphi_j\right\rangle|^2 \tag{2.18}$$

with m_{e} the mass of the electron, $\hbar$ the reduced Planck constant, $\widehat{Z}$ the position operator along the z axis (this operator comes from the electric dipole hamiltonian) and $h\nu_{ij}$ is the energy gap between $|\varphi_i\rangle$ and $|\varphi_j\rangle$ states. Moreover, in the framework of quantum electrodynamics, it is possible to give an interpretation of the spontaneous emission in terms of coupling between the excited state of a molecule (or atom) and the ground state of the electromagnetic field in vacuum. This approach gives then a relation between the spontaneous emission rate A_{ij} and the transition moment $\left\langle\varphi_i\right|\widehat{Z}\left|\varphi_j\right\rangle|$,

$$A_{ij} = \frac{16\pi^3 e^2 \nu_{ij}^3}{\epsilon_0 h c^3}|\left\langle\varphi_i\right|\widehat{Z}\left|\varphi_j\right\rangle| \tag{2.19}$$

with e the elementary charge, ϵ_0 the vacuum permittivity and c the speed of light in the vacuum. Combining the last two relations, we obtain

$$A_{ij} = \frac{2\pi e^2 \nu_{ij}^2}{\epsilon_0 m_e c^3} \times f_{ij} \tag{2.20}$$

From the numerical values of the fundamental constants, we find

$$A_{ij} = 0.665 \times f_{ij} \widetilde{\nu}_{ij}^2 \tag{2.21}$$

with f_{ij} the electronic oscillator strength (no unit) between the state i and the state j, $\widetilde{\nu}_{ij} = \frac{|E_i - E_j|}{hc}$ in cm^{-1} and A_{ij} in s^{-1}. This relation will be used for recurrent fluorescence. Since no assumption has been made on the nature of the $|\varphi_i\rangle$ and $|\varphi_j\rangle$ states, the relation (2.21) is also valid for the $A_i^{1\to 0}$ appearing in the vibrational fluorescence rates. However, for the vibrational fluorescence we have to use the infrared intensity strength in km/mol. Indeed, this quantity is computed by Gaussian and DeMon softwares for vibrational structure calculations (Dubosq et al., 2019).

Relationship between spontaneous emission rate and IR strength in km/mol

According to (Hilborn, 1982, 2002), the cross section (dimension: surface) for a transition of energy $\widetilde{\nu}$ is given by:

$$\sigma(\widetilde{\nu}) = \frac{e^2}{4\epsilon_0 m_e c^2} f \times g(\widetilde{\nu}) \tag{2.22}$$

g is a Lorentzian distribution centered around the considered frequency and f the oscillator strength of the radiative transition. $g(\widetilde{\nu})$ has the dimensionality of length. The cross section $\sigma(\widetilde{\nu})$ is also expressed in the following form

$$\sigma(\widetilde{\nu}) = \frac{1}{NL} \ln\left(\frac{I_o(\widetilde{\nu})}{I(\widetilde{\nu})}\right) \tag{2.23}$$

with N the absorbing species density (dimension: inverse of volume), L the optical path traveled (dimension: length), I_o the incident intensity and I the transmitted intensity. The intensity strength is the cross section integrated over the entire absorption band. When expressed in contexts where the molar concentration is known, we have

$$S(\widetilde{\nu}) = \frac{1}{CL} \int \ln\left(\frac{I_o(\widetilde{\nu})}{I(\widetilde{\nu})}\right) d\widetilde{\nu} \qquad \text{en} \tag{2.24}$$

with C the molar concentration (Douin et al., 2015). Given that $N/C = \mathrm{N_A}$, the Avogadro number, and combining the last three relations, we obtain

$$S_{ij}(\widetilde{\nu}) = \mathrm{N_A} \times \frac{e^2}{4\epsilon_0 m_e c^2} f_{ij} \times \int g(\widetilde{\nu}) d\widetilde{\nu} \tag{2.25}$$

The integral being equal to unity, we conclude that

$$S_{ij} = \mathrm{N_A} \times \frac{e^2}{4\epsilon_0 m_e c^2} f_{ij} \tag{2.26}$$

From the relation (2.20), we obtain

$$A_{ij}(\mathrm{s}^{-1}) = 1.25 \cdot 10^{-7} \times \widetilde{\nu}_{ij}^2(\mathrm{cm}^{-1}) \times S_{ij}(\mathrm{km/mol}) \tag{2.27}$$

This last relation will be used for our vibrational fluorescence rate calculations. Thus, we think we proved the relation given, without any demonstration, in (Cook and Saykally, 1998).

Modelling of the photochemistry

In the previous section, we have discussed processes (other than ionization or chemical reactions) induced by photon absorption. In our work, we had to calculate unimolecular reactions rates such as isomerization and dissociation. In this section, we will present very briefly the two theories that we had the opportunity to use. The ultimate goal of these theories is to give a framework to predict the unimolecular reaction rates.

The mechanism explaining unimolecular reactions involves two steps: a first one for the species to reach enough energy by collision (collisional excitation by the buffer gas) and allow the second reaction which is a chemical reaction. When the pressure of the buffer gas is high enough, the second reaction becomes the limiting step of the whole reaction (high-pressure limit). Since in our work the unimolecular reactions are systematically induced by photon absorption, the first step has de facto already taken place. We will therefore focus only on the second step. For more details on unimolecular reactions, we refer the reader to the books (Robinson and Holbrook, 1972; Forst, 2012).

RRK theory

This theory was independently developed by Rice and Ramsperger on the one hand (1927) and Kassel on the other (1928) Robinson and Holbrook (1972). The starting point of the theory is to describe the unimolecular reaction rate as depending only on the internal energy of the reactant species.

It is assumed (long before the advent of the RRK theory) that a unimolecular reaction takes place only via a single vibrational mode (or combination of modes). This translates then, in this theory,to the fact that a minimal amount of energy E_0 must be contained in this mode (for example, C–H stretching mode for the dissociation of a hydrogen in the case of benzene). The unimolecular reaction considered here is then written

$$\mathrm{A}^* \xrightarrow{\mathrm{k(E)}} \mathrm{A}^\ddagger \xrightarrow{\mathrm{k}^\ddagger} \mathrm{B} \tag{2.28}$$

A^* is the reactant with internal energy E, B the product, $k(E)$ the reaction rate from A to its transition state $A^\ddagger$ and $k^\ddagger$ the reaction rate from the transition state $A^\ddagger$ to the product B.

To use a statistical treatment, it is necessary to assume that the internal energy distribution among all degrees of freedom has reached statistical equilibrium. This assumes an effective interaction between normal modes (at that time, IVR was still an assumption). The reaction rate $k(E)$ is assumed to be proportional to the probability of finding an energy greater than E_0 in the vibrational mode involved in the reaction. By doing some combinatorics with the vibrational quanta among all the vibrational degrees of freedom g , the result reads

$$k(E) = A \times (1 - E_0/E)^{g-1} \tag{2.29}$$

with E_0 the energy threshold for the unimolecular reaction to take place and A as the constant of proportionality homogeneous to a frequency. This probability can be seen, in the steady state approximation, as the ratio of the concentrations (or partial pressures) $[A^\ddagger]/[A^*]$. In a slightly more elaborate model, Eyring *et al.* (Giddings and Eyring, 1954) showed that the prefactor A is expressed by

$$A = \prod_{j=1}^{g} \nu_j / \prod_{j=1}^{g-1} \nu_j^\ddagger \tag{2.30}$$

the ν_j are the vibrational frequencies of reactant A and the $\nu_j^\ddagger$ are those of the $A^\ddagger$ transition state. Thus, the prefactor A should be of the order of one vibrational frequency, i.e., 10^{13}-10^{14} s^{-1}.

RRKM theory

The RRKM (Rice-Ramsperger-Kassel-Marcus) theory developed by Marcus and Rice (1952) is an improvement of the RRK theory in the sense that the transition state theory is used for the calculation of the $k^\ddagger$ rate and in which the rotational motion can eventually be taken into account.

The internal energy of the transition state is then defined by $E^{\ddagger} = E - E_0$, with E the internal energy of the reactant and E_0 the reaction threshold. The calculation of rate $k^{\ddagger}(E - E_0)$ (mechanism (2.28)) involves the reaction coordinate called ξ. In this case, we can express the transition state energy $E^{\ddagger}$ as the sum of the energy E_ξ associated with the reaction coordinate and the energy E_v associated to the rest of the vibrational degrees of freedom (*i.e.* $E^{\ddagger} = E_v + E_\xi$). The rate expression given by RRK (relation (2.29)) is then replaced in RRKM by

$$k(E) = \frac{\alpha}{h\rho^*(E)} \sum_{E_v=0}^{E^{\ddagger}} P(E_v) \tag{2.31}$$

h is Planck's constant, $\rho^*(E)$ represents the VDOS of the reactant at internal energy E, $P(E_v)$ represents the number of possible states of the transition state $A^{\ddagger}$ at an internal energy of E_v (the reaction coordinate ξ being frozen and containing the energy $E_\xi = E^{\ddagger} - E_v$). Actually, the sum contains all possible states of the complex for which the energy E_ξ contained in the reaction coordinate is lower or equal to $E^{\ddagger} - E_0$. α is the degeneracy due to the symmetry of the molecule and represents the equivalent path number for the reaction (for example, $\alpha = 6$ for C–H bond breaking in benzene). The terms involved in the relation (2.31) involve quantities that are calculated via the VDOS. We discuss, in the next section, in which context we use RRK and RRKM theories.

Dissociation and isomerization

RRK and RRKM theory apply to dissociation and isomerization reactions (with or without activation energy). When it is possible to estimate the transition state of a complex then RRKM theory is used. For example, for the dissociation of toluene in which a C–H bond breakage takes place, we assumed the transition state as being toluene with a frozen aliphatic C–H bond (which assumes that the dissociation takes place via the stretching mode). We can then obtain the vibrational structure of this transition state by DFT methods using the Gaussian software and calculate the sum appearing in relation (2.31). In this case, the degeneracy factor α is equal to 3 (three methyl hydrogens). Another case is that of toluene forming a phenyl and a methyl group via the breaking of the C–C bond that connects the two radicals. In the same way, we have frozen the distance between these two carbons and obtained the vibrational structure of the transition state. The reaction barriers are systematically searched in the literature. In the absence of a transition state, we performed an RRK calculation. In addition to the reaction barrier, the prefactor A must be estimated. We noticed that it was not systematically of the order of 10^{13}-10^{14} s^{-1}. Indeed, in the case of the dissociation of a C_2 from C_{60} buckminsterfullerene, the prefactor A is of the order of 10^{20} s^{-1} (Lifshitz, 2000b). Theoretical calculation of the prefactor A is generally complicated (Klots, 1991). Another way to estimate A is to deduce it from the reaction threshold and an experimental value of the rate at a given excitation energy. This is what we did for the isomerization from cycloheptatriene to toluene. Moreover, we have also used RRK to make order of magnitude calculations. In the context of our work, the absorption of a photon induces dissociation and isomerization via the conversion of electronic energy into vibrational energy. It is therefore appropriate to speak of photo-thermodissociation and photo-thermoisomerization.

Collisional energy transfer

The experiments we conducted consist in detecting the vibrational emission of benzene derivatives (called M) during the entire relaxation. This cooling is dominated by collisions, *i.e.* most of the internal energy of the excited species M^* is yielded by collisional de-excitation with the buffer gas (argon) or with other non-excited species M. Therefore, simulate the collisional cooling of M^* implies to know collision rates M^*-M and M^*-Ar and the energy transferred during a collision.

Collision rate

We know that the collision rate τ_c (dimensionality: volume per time unit)undergone by a species constituting the gas in the model of hard spheres is written by

$$\tau_c = \pi b^2 \sqrt{\frac{8k_B T}{\pi\mu}} \tag{2.32}$$

with b the species radius, μ the reduced mass of the system formed by two colliding species, T the temperature of the gas and k_B the Boltzmann constant. Actually, neutral molecules interact via intermolecular forces (dipole forces) which implies a collision rate different than (2.32). In the non-equilibrium statistical mechanics framework, it is possible to introduce into the Boltzmann equation quantities related to the intermolecular interaction potential. These quantities, called *collision integrals* relate the interaction potential and the energy or momentum transport quantities (thermal diffusion, viscosity). In this very general framework, the collision rate is expressed by

$$\tau_c = \pi\sigma^2 \sqrt{\frac{8k_B T}{\pi\mu}} \varOmega^{(2,2)*} \tag{2.33}$$

	σ_{LJ} ($\mathring{A}$)	$\epsilon_{\mathrm{LJ}}/k_B$ (K)
Toluene	5.92	410
Toluene-d_8	5.92	410
Argon	3.47	114

Table 2.1: Lennard-Jones parameters for three species used for the cooling cascade simulation. Argon is used as a buffer gas. Values taken from (Barker and Toselli, 1993).

with σ the collision cross section and $\Omega^{(2,2)*}$ the reduced collision integral related to the potential of intermolecular forces (dimensionless quantity). Note that in the case of the hard sphere model, the reduced collision integral is equal to unity and σ is equal to b, then we find again the expression (2.32).

We use the Lennard-Jones potential because intermolecular forces have been mainly studied in this framework. This potential is defined only by two parameters: the effective cross section σ_{LJ} and the depth of the well ϵ_{LJ}. These two parameters are tabulated for the species of interest (table 2.1) (Troe, 1977; Matsugi, 2018; Barker and Toselli, 1993). The collision integral, on the other hand, is expressed approximately as (Reid and Sherwood, 1966)

$$\Omega^{(2,2)*} \approx (0.697 + 0.567 \log\left(\frac{k_B T}{\epsilon_{\mathrm{LJ}}}\right)) \tag{2.34}$$

ϵ_{LJ} is the well of the Lennard-Jones potential. In the case where the collision is between two different species A and B, the two parameters are then expressed by

$$\sigma_{A-B} = \frac{\sigma_A + \sigma_B}{2} \tag{2.35}$$

$$\epsilon_{A-B} = (\epsilon_A \epsilon_B)^{1/2} \tag{2.36}$$

To obtain the collision rate, we simply multiply the expression (2.33) by the volume density of the species.

Parametric model

Several authors have experimentally studied collisional relaxation of vibrationally excited M^* species. Collisions take place mainly between M^*-M and M^*-Ar pairs. From these studies, it is possible to deduce the average energy transferred by collision and it turns out that this average energy depends on the vibrational internal energy. The aim is to find the probability distribution of transferring a certain amount of energy during a collision. These probability distribution are defined from an empirical parametrization and depend on the internal energy. We are going to list techniques on which we based on our parametrization.

Some experimental studies

One of the experimental techniques, used since the 1980s, consists in detecting the vibrational emission induced by electronic excitation (Barker and Toselli, 1993) (IR fluorescence, IRF). The photophysical path is similar to the one explained at the beginning of this chapter: after electronic excitation, the internal conversion brings the molecule to its ground electronic state with a high vibrational excitation level. The theoretical model used to make the correspondence between the detected fluorescence signal and the internal energy is similar to the one described at the beginning of this chapter (Durana and McDonald, 1976). This model allows to plot the temporal evolution of the internal energy. Moreover, knowing the pressure and the temperature in the cell, it is possible to plot the collision rate and to make a correspondence between the time elapsed during the relaxation and the average total collision number undergone by the excited species during this duration. The average total collision number and the internal energy being known at each time, it is possible to obtain the average energy transferred per collision as a function of the internal energy of M^*. We can find IRF studies for species like azulene (Shi and Barker, 1988; Rossi and Barker, 1982a; Rossi et al., 1983; Barker and Golden, 1984), benzene (Yerram et al., 1990) and toluene (Toselli et al., 1991; Toselli and Barker, 1991).

Another method is the study of the kinetics of the relaxation by UV absorption (UVA for UV absorption). It was noticed that for certain molecules (like toluene or derivatives of cyloheptatriene) that the molar extinction (absorption coefficient) at a wavelength depends on the internal energy. To trace the internal energy, it is then sufficient to see the time evolution of the absorption of the relaxing species. By a process similar to that of the previous paragraph, they obtain the average energy transferred by collisions as a function of the internal energy. This technique has been used in particular in the case of toluene and cycloheptatriene derivatives (Hippler et al., 1983d,b,a).

The KCSI (Kinetically controlled selective ionization) technique consists, by a pump-probe technique, to see the temporal evolution of the internal energy by REMPI in two colors (Hold et al., 2000). The Resonance-Enhanced Multiphoton Ionization (REMPI) is used when the molecule has already started its collisional relaxation. By fixing the duration between the pump and the probe, we define an observation window in the relaxation that is to say an internal energy whose value must be determined. The probe is defined by the first excitation of the two color REMPI. During the collisional relaxation, M^* is in S_0 electronic state. Then, the two-color REMPI consists of exciting M^* to its S_1 electronic state and the second photon causing the ionization. The photon energy of the probe laser is fixed in such a way that M^* is in the ground vibrational state of S_1. Indeed, in higher vibrational states, the internal conversion to S_0 becomes efficient and faster than the absorption of the second photon which is supposed to ionize the molecule from S_1. In this way, it is possible to plot the internal energy in terms of the duration between the pump laser pulse (excitation towards S_1) and the probe laser pulse (ionization from S_1). The average energy transferred per collision in terms of the internal energy is determined in the same way as before.

Theoretical generalities

First of all, we want to highlight required quantities for the description of the collisional energy transfer model. Let us assume a population $\gamma(E,t)$ of species with internal energy E at time t and which can yield or receive energy via inelastic collisions. The inelastic collision rate, denoted k, is assumed to be constant with internal energy. We assume that there is no gain or loss of thermal, chemical or radiative energy. The master equation is then written (Barker, 2009)

$$\frac{d\gamma(E,t)}{dt} = k\int_0^\infty P(x,E)\gamma(x,t)dx - k\int_0^\infty P(E,x)\gamma(E,t)dx \tag{2.37}$$

$P(x,E)$ represents the probability that a species with initial internal energy x is left with the internal energy E after undergoing an inelastic collision. Thus, the first integral represents a source term for the population $\gamma(E,t)$. Conversely, $P(E,x)$ represents the probability that a species with initial internal energy E is left with the internal energy x after undergoing an inelastic collision. In the following, the "inelastic collision" is called "collision" for simplicity. For a fixed internal energy E, we have the following condition on P

$$\int_0^\infty P(E,x)dx = 1 \tag{2.38}$$

Note that the probability distribution P contains the energy losses and gains per collision. The convention we take in the notation $P(x,y)$ is that the initial energy x is placed as the first variable while the internal energy y after collision is placed as the second variable. At thermal equilibrium, the master equation becomes $P(x,E)\gamma(x) = P(E,x)\gamma(E)$ (γ is no more time-dependent). Moreover, at thermal equilibrium, the population ratio is written

$$\frac{\gamma(E)}{\gamma(x)} = \frac{\rho(E)}{\rho(x)}e^{-\beta(E-x)} \tag{2.39}$$

Here, $\rho(E)$ the density of states of the species at E internal energy. This reads, in terms of probability, as

$$\frac{P(x,E)}{P(E,x)} = \frac{\rho(E)}{\rho(x)} e^{-\beta(E-x)} \tag{2.40}$$

This relation expresses the collisional de-excitation proportion in both directions $E \rightarrow x$ and the $x \rightarrow E$. From the probability distribution of energy transferred during a collision, we would like to define two other probability distributions: one for the energy losses during a collision and the other for the energy gains during a collision. Indeed, as noted above, the P distribution contains energy losses and energy gains. At an initial internal energy E, the probability that the species ends up with internal energy x after one collision is given by $P(E,x)$ with the condition

$$1 = \int_0^E P(E,x)dx + \int_E^\infty P(E,x)dx \tag{2.41}$$

The first integral contains collision events where energy is yielded (down-steps) while the second integral contains collision events where energy is received during the collision (up-steps). It will be useful to define a dimensionless quantity $f(E,x)$ proportional to the probability distribution,

$$P(E,x) = \frac{f(E,x)}{N(E)} \tag{2.42}$$

with $N(E)$ defined as following

$$N(E) = \int_0^E f(E,x)dx + \int_E^\infty f(E,x)dx \tag{2.43}$$

We note $N_{\mathrm{d}}(E)$ the first integral (d for *down* because $x < E$) and $N_{\mathrm{u}}(E)$ the second integral (u for *up* because $E < x$). $N(E)$ is then written

$$N(E) = N_{\mathrm{d}}(E) + N_{\mathrm{u}}(E) \tag{2.44}$$

$N_{\mathrm{d}}(E)/N(E)$ (resp. $N_{\mathrm{u}}(E)/N(E)$) represents the probability that, during a collision, the system yields (resp. receives) energy.

By symmetry, we also have $P(x,E) = f(x,E)/N(x)$ and the equilibrium relation (2.40) reads

$$\frac{f(x,E)}{f(E,x)} = \frac{N(x)}{N(E)} \frac{\rho(E)}{\rho(x)} e^{-\beta(E-x)} \tag{2.45}$$

In order to simplify the treatment we will define a single function f_{d} which will allow us to determine all the other quantities and thus, will define the empirical model of collisional energy transfer. We define $f_\mathrm{d}(E,x)$ by

$$f_\mathrm{d}(E,x) = f(E,x) \qquad \text{with } x < E \tag{2.46}$$

$N_\mathrm{d}(E)$ is then defined by

$$N_\mathrm{d}(E) = \int_0^E f_\mathrm{d}(E,x)dx \tag{2.47}$$

Also, from (2.44),

$$N_\mathrm{u}(E) = \int_E^\infty f(E,x)dE \qquad \text{with } E < x \tag{2.48}$$

Given that $E < x$, we have $f(E,x) \neq f_\mathrm{d}(E,x)$. Now, according to relation (2.45) and given that $E < x$, we write

$$N_\mathrm{u}(E) = \int_E^\infty f_d(x,E)\frac{N(E)}{N(x)}\frac{\rho(x)}{\rho(E)}e^{-\beta(x-E)}dx \tag{2.49}$$

We see that it is not necessary to define f_u because it would be related to f_d via relation (2.45). However, to calculate $N_\mathrm{u}(E)$ we still have to determine $N(E)$. We proceed as follows:

$$N(E) = N_\mathrm{d}(E) + N_\mathrm{u}(E) \tag{2.50}$$

$$N(E) = N_\mathrm{d}(E) + \int_E^\infty f_\mathrm{d}(x,E)\frac{N(E)}{N(x)}\frac{\rho(E)}{\rho(x)}e^{-\beta(E-x)}dx \tag{2.51}$$

$$\tag{2.52}$$

We deduce that

$$N(E) - N(E)\int_E^\infty f_\mathrm{d}(x,E)\frac{1}{N(x)}\frac{\rho(E)}{\rho(x)}e^{-\beta(E-x)}dx = N_\mathrm{d}(E) \tag{2.53}$$

thus we obtain (Barker, 2009; Gilbert and King, 1980):

$$N(E) = \frac{\int_0^E f_\mathrm{d}(E,x)dx}{1 - \int_E^\infty f_d(x,E)\frac{1}{N(x)}\frac{\rho(E)}{\rho(x)}e^{-\beta(E-x)}dx} \tag{2.54}$$

Thus, the normalization constant $N(E)$ can be determined by an iterative process as we will see in the next section.

The purpose of all these definitions and algebraic manipulations was to prove that the mere knowledge of f_d allows us to entirely model the collisional energy transfer (given, of course, the temperature and the density of vibrational states ρ). Indeed, the relation (2.54) allows to calculate $N(E)$ which gives $N_\mathrm{u}(E)$ (relation 2.49). The relation 2.47

gives directly $N_{\mathrm{d}}(E)$. The f_{d} distribution and the three constants allow us to find the distribution probability of the energy transferred during a collision. This distribution probability may depend on the internal energy. Therefore, it is necessary to define f_{d}.

Exponential model

To date, the KCSI experiments provide the most reliable results in terms of empirical data for the collisional energy transfer between two species (King and Barker, 2019). The probability distribution model ($\propto f_{\mathrm{d}}$) used for KCSI experiments is a linear combination of exponential and bi-exponential with proportions according to species considered. The problem is that no empirical KCSI data is provided for the Toluene*-Toluene collisions, although there are measurements for Toluene*-Argon collisions. We carefully compared their results for other species to see if any extrapolation can be made for Toluene*-Toluene collisions case. A reliable extrapolation is not possible. This is the reason why we turned to results obtained by IRF. The empirical results obtained by IRF and UVA are earlier than those of the KCSI technique. These two techniques are the first studies that deduce relevant quantities for the collisional energy transfer probability distribution, such as the mean transferred energy per collision (which is actually the first order of the probability distribution). However, both techniques often show discrepancies in their results, attributed to their calibration. The Toluene*-Argon and Toluene*-Toluene collisions were studied by (Barker and Toselli, 1993; Toselli and Barker, 1991) within the framework of a decreasing exponential model and is still used (Robertson, 2019). We therefore use a decreasing exponential model for the probability distribution of energy transferred during a collisional energy loss. The function $f_{\mathrm{d}}(E,x)$ is then written

$$f_{\mathrm{d}}(E,x) = e^{-(E-x)/\alpha(E)} \qquad \text{with } x < E \tag{2.55}$$

with $\alpha(E)$ a polynomial function of E whose the physical meaning will be given later. The normalization constant $N_{\mathrm{d}}(E)$ is written

$$N_{\mathrm{d}}(E) = \int_0^E e^{-(E-x)/\alpha(E)} dx \tag{2.56}$$

We can give analytical expressions of the average energy transferred per collision which is defined by

$$< \mathit{\Delta} E > (E) =< \mathit{\Delta} E >_{\mathrm{u}} (E) - < \mathit{\Delta} E >_{\mathrm{d}} (E) \tag{2.57}$$

with $< \mathit{\Delta} E >_{\mathrm{d}}$ (resp. $< \mathit{\Delta} E >_{\mathrm{u}}$) the average energy transferred during a down-step (resp. up-step) collision. The calculation of $< \mathit{\Delta} E >_{\mathrm{d}}$ is defined by

$$< \mathit{\Delta} E >_{\mathrm{d}} (E) = \frac{1}{N_{\mathrm{d}}(E)} \int_0^E (E - x) \times e^{-\frac{E-x}{\alpha(E)}} dx \tag{2.58}$$

$N_{\mathrm{d}}(E)$ is given by the relation 2.47. These integrals can be calculated in an elementary way and we obtain

$$< \mathit{\Delta} E >_{\mathrm{d}} (E) = -\alpha(1 - \frac{E}{\alpha} \times \frac{e^{-E/\alpha}}{1 - e^{-E/\alpha}}) \tag{2.59}$$

and we notice that

$$< \mathit{\Delta} E >_{\mathrm{d}} (E) \xrightarrow{E \ll \alpha(E)} 0 \tag{2.60}$$

$$< \mathit{\Delta} E >_{\mathrm{d}} (E) \xrightarrow{\alpha(E) \ll E} -\alpha(E) \tag{2.61}$$

The physical meaning of $\alpha(E)$ appears at internal energies higher than α(E) (*i.e.* higher than $\approx$ 1000 cm^{-1}). Indeed, it turns out that $\alpha(E)$ corresponds to the average energy transferred per collision (King and Barker, 2019). We insist that this results from an empirical model and has no theoretical basis.

In the same way, we can calculate $< E >_{\mathrm{u}} (E)$. As mentioned above, we should no longer use $f_{\mathrm{d}}(E,x)$ but rather the relation (2.45).

$$< \mathit{\Delta} E >_{\mathrm{u}} (E) = \frac{1}{N_{\mathrm{u}}(E)} \int_E^{\infty} (x - E) \times f_{\mathrm{d}}(x,E) \frac{N(E)}{N(x)} \frac{\rho(x)}{\rho(E)} e^{-\beta(x-E)} dx \tag{2.62}$$

We can simplify this expression to integrate it and give an analytical expression. For E and x very large, we make the approximation $N(E) \approx N(x)$ (Barker and Golden, 1984). We did a few calculations of $N(E)$ and it turns out that this approximation holds true as long as the internal energy is not very small. We make the approximation

$$\frac{d \ln \rho(E)}{dE} \approx B \tag{2.63}$$

As we shall see later in the chapter 3, this quantity is related to $1/k_B T^*$, with T^* the microcanonical temperature. Then, the VDOS reads

$$\rho(E) = \mathrm{cste} \times e^{BE} \tag{2.64}$$

Hence,

$$\frac{\rho(E)}{\rho(x)} = e^{B(E-x)} \tag{2.65}$$

We find this relation in (Barker and Toselli, 1993; Troe, 1973; Barker, 1983) and it allows us to give an analytical expression of $< \Delta E >_{\rm u}$. Using the semi-classical expression of the VDOS (2.7), it turns out that $B(E) = \frac{g-1}{E+E_z}$ with g the number of degree of freedom of the species M*. According to the approximation $N(E) \approx N(x)$ and the relation (2.65), the normalization constant (2.49) then becomes

$$N_{\rm u}(E) = \int_E^\infty e^{-\frac{x-E}{\alpha(E)}} e^{B(E)(x-E)} e^{-\beta(x-E)} dx = \int_E^\infty e^{-C(E)\times(x-E)} dx \tag{2.66}$$

with $C = 1/\alpha + \beta - B$. We write the average energy received by a collision increasing the internal energy as

$$< \Delta E >_{\rm u} (E) = \frac{1}{N_{\rm u}(E)} \int_E^\infty (x - E) \times e^{-C(E)\times(x-E)} dx \tag{2.67}$$

The calculation is immediate and we obtain, $< \Delta E >_{\rm u} (E) = 1/C(E)$. We can then write that the average energy $< \Delta E >$ transferred is written

$$< \Delta E >= (1/\alpha + \beta - B)^{-1} - \alpha \tag{2.68}$$

For $\alpha \approx 1000$ cm^{-1}, at room temperature (300 K) and a species with 50 degrees of freedom ($g = 50$, arbitrary choice), we obtain

$$< E >_{\rm d} \approx 1000 \text{ cm}^{-1} \tag{2.69}$$

$$< E >_{\rm u} \approx 200 \text{ cm}^{-1} \tag{2.70}$$

In this rough calculation, the species M* yields, on average, 5 times more energy than it receives. These orders of magnitude are corroborated by figure (2.4) in which we show an example of the probability distribution of collisional energy transferred during a collision with its parameterization $\alpha(E)$ for the exponential model.

Relaxation radiative computation

In this last section, we shall present the computational method used to describe a relaxation cascade. We have shown so far models and theories used for the calculation of relaxation pathway rates. Among these rates, we find all recurrent fluorescence rates, vibrational fluorescence rates associated with all normal vibrational modes, collision rate and unimolecular reaction rates (dissociation and isomerization). All these rates are therefore known whatever the internal energy. From all these rates, it is difficult to find an analytical solution of the relaxation path. This is why we used a numerical

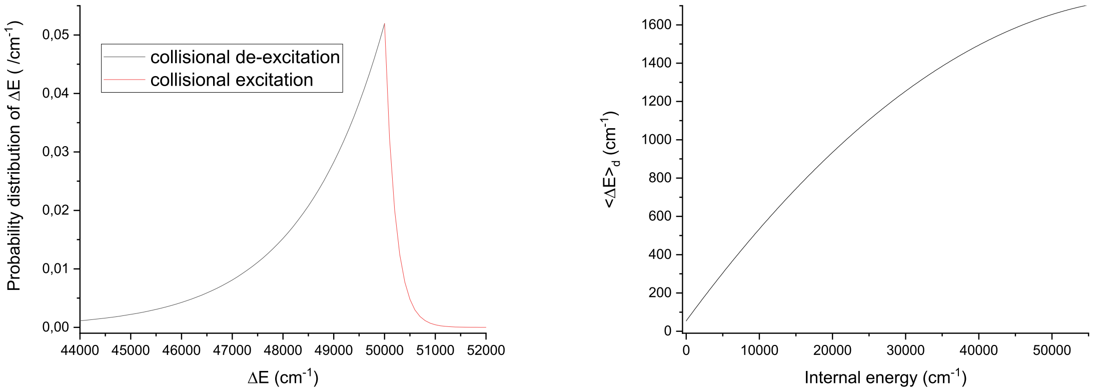

Figure 2.4: Left panel: probability distribution of the ΔE energy transfer per collision in the exponential model with the α(E) parameterization shown in the right curve, T=300 K and degree of freedom $g = 50$. Right panel: parameterization $\alpha(E) = 30 + 0.009 \times E + 7 \cdot 10^{-9} \times E^2$ with internal energy E (in cm^{-1})

calculation to simulate the relaxation of an excited species. In this section, we present the way we have implemented a kinetic Monte-Carlo type simulation (Gillespie, 2007).

Principle of the Monte-Carlo for relaxation cascade

Monte-Carlo type methods consist in computing values by means of a probabilistic calculation. In our simulation, we know the species at internal energy E as well as the rates $k_i(E)$ of all relaxation pathways at E. Since the internal energy is statistically distributed (statistical equilibrium is supposed to be achieved), we can say that the probability of the excited species taking the i^{th} pathway with rate $k_i(E)$ at internal energy E is given by

$$\frac{k_i(E)}{\sum_i k_i(E)} \tag{2.71}$$

the sum is over all possible relaxation pathways at internal energy E. Since probabilities are known, we can randomly (according to probabilities) select a pathway, denoted j_1, through which the species will relax and then end up with the internal energy $E - E_{j_1}$.

All relaxation pathways rates are also known for this new internal energy $E - E_{j_1}$. As explained at the beginning of this chapter, statistical equilibrium is very quickly reached before the next relaxation pathway is taken by the relaxing species. This still allows us to randomly select a relaxation pathway in the same way as the previous step since probabilities are still written

$$\frac{k_i(E - E_{j_1})}{\sum_i k_i(E - E_{j_1})} \tag{2.72}$$

Again, a relaxation path j_2 is selected randomly. After this second step, the species ends up with internal energy $E - E_{j_1} - E_{j_2}$. We continue in this way until we reach the minimum of the internal energy. We call *trajectory* the set of relaxation paths taken by the species and write it as $(j_1^1, j_2^1, \ldots, j_{N_1}^1)$. The superscript 1 refers to the first path of the algorithm. Indeed, given the probabilistic nature of the algorithm, a single trajectory does not represent the reality. The observed or measured spectra come from innumerable species that follow different trajectories. Actually, the observed or measured emission spectra reflect the average of these trajectories. This is why we calculate a large number of trajectories

$$\begin{array}{c}(j_1^1, j_2^1, \ldots, j_{N_1}^1)\\ (j_1^2, j_2^2, \ldots, j_{N_2}^2)\\ \vdots \\ (j_1^m, j_2^m, \ldots, j_{N_m}^m)\\ \vdots\end{array}$$

To obtain the relevant trajectory for our experiments or astrophysical observations, we average all these trajectories. In this way, we can simulate the emission spectrum resulting from the entire relaxation cascade and eventually the proportion of dissociated or isomerized species during the cooling. The number of trajectories depends on the signal we want to simulate. The lower the probabilities of the simulated signals, the more trajectories will be needed to approach the reality. The number of trajectories we used is between 10^5 (isolated species) and 10^9 (with collisions).

Application to radiative relaxation

The principle of the implementation is very simple (Barker, 1983). At the n^{th} stage of the relaxation, the species has an internal energy E_n and the probability that the i^{th} relaxation pathway takes place is written

$$P_i(E_n) = \frac{k_i(E_n)}{\sum_i k_i(E_n)} \tag{2.73}$$

At this n^{th} step, we randomly select a number $0 \leq \texttt{ran} \leq 1$ (random). Then, starting with i=0, we sum the $P_i(E_n)$ in ascending order of i as long as the sum is less than `ran`. As soon as the sum becomes greater than or equal to `ran` then the relaxation path is identified. In other words, we locate the relaxation path j to select randomly if the following condition is verified

$$P_1(E_n) + P_2(E_n) + \ldots + P_j(E_n) < \texttt{ran} \tag{2.74}$$

and

$$\texttt{ran} < \mathtt{P_1(E_n) + P_2(E_n) + \ldots + P_j(E_n) + P_{j+1}(E_n)} \tag{2.75}$$

After any random selection, we proceed as follows according to the nature of the pathway:

• If this relaxation pathway is a radiative de-excitation, then we count the emitted photon. The photon energy is subtracted from the internal energy E_n which will give the internal energy of the $(n+1)^{\text{th}}$ step. Then, the photon counting emitted at each step allows to simulate the emission spectrum.

• If the selected relaxation pathway is a dissociation pathway, then we stop the implementation. Indeed, in our work we did not consider the emission of fragments (see chapter 5)

• If the selected relaxation pathway is an isomerization pathway, then another isomer appears with the internal energy unchanged.

• If the selected relaxation pathway is a collision, then internal energy must be removed or added to the species. In this case, it is necessary to proceed by another Monte-Carlo to calculate the collisional energy transfer.

Application to collisional energy transfer

We now assume that the selected pathway at the n^{th} step of the trajectory is a collision. The internal energy of the species is E_n.
Previously, we saw that if a collisional energy transfer model is defined (via f_{d}), then relation 2.44 allows to calculate the collisional excitation and de-excitation probabilities. In this case, it is enough to select another number $0 \leq \texttt{ran} \leq 1$ and check if

$$\frac{N_d(E_n)}{N(E_n)} \leq \texttt{ran} \tag{2.76}$$

If this inequality is true, then we are dealing with collisional de-excitation, otherwise we are dealing with collisional excitation. For the calculation of $N(E)$, the implementation of the recurrence relation 2.54 is initialized at sufficiently high internal energies to consider $N(E)$ as constant with the internal energy E.

For collisional de-excitation, we define the collisional energy transfer probability

$\mathit{\Delta} E_{\rm d} = E - x$ (with $x < E$) by

$$P_{\rm d}(E,x) = \frac{1}{\int_0^E f_{\rm d}(E,x)dx} \int_x^E f_{\rm d}(E,x)dx \tag{2.77}$$

The idea is then to select randomly a number $0 \leq \texttt{ran} \leq 1$ and to relate it to the yielded energy $\mathit{\Delta} E_{\rm d}$. We have the following equality:

$$\texttt{ran} = \frac{1}{\int_0^E f_{\rm d}(E,x)dx} \int_x^E f_{\rm d}(E,x)dx \tag{2.78}$$

Yet,

$$\int_x^E f_{\rm d}(E,x)dx = \alpha(E) \times (1 - \exp\left(-\frac{\mathit{\Delta} E_{\rm d}}{\alpha(E)}\right)) \tag{2.79}$$

$$\int_0^E f_{\rm d}(E,x)dx = \alpha(E) \times (1 - \exp\left(-\frac{E}{\alpha(E)}\right)) \tag{2.80}$$

from which we deduce

$$\texttt{ran} = \frac{1 - \exp\left(-\frac{\mathit{\Delta} E_{\rm d}}{\alpha(E)}\right)}{1 - \exp\left(-\frac{E}{\alpha(E)}\right)} \tag{2.81}$$

After some algebraic manipulations (Barker, 1983), we end up with the sought-after relation

$$\mathit{\Delta} E_{\rm d} = -\alpha(E) \ln[1 - (1 - e^{-E/\alpha(E)}) \times \texttt{ran}] \tag{2.82}$$

For the collisional excitation, we define the collisional energy transfer probability $\mathit{\Delta} E_{\rm u} = x - E$ (with $E < x$) by

$$P_{\rm u}(E,x) = \frac{1}{N_{\rm u}(E)} \int_E^x e^{-C(E)\times(x-E)}dx \tag{2.83}$$

and assuming that the energy is large enough to the normalization constant $N(E)$ be constant and relation 2.65 be valid

$$\mathit{\Delta} E_u = -\frac{ln(\texttt{ran})}{\beta + \frac{1}{\alpha(E)} - B(E)} \tag{2.84}$$

Up to now, we have seen how to simulate the emission spectrum of the whole relaxation cascade. But the Monte-Carlo method presented here does not inform us about the relaxation kinetics.

Kinetic aspect of the Monte-Carlo

We know how to select a relaxation path at a given internal energy. However, we do not know the time between two successive steps of the Monte-Carlo presented in the previous section. Here we will look for the probability distribution of the time interval between two successive Monte-Carlo steps.

Let us take the hypothetical case where there is only one relaxation path (whatever its nature). Let k be the rate associated with the relaxation pathway and $P(\tau)$ the probability that the species has not yet taken the relaxation pathway after the duration τ. The probability that the species has still not relaxed during the infinitesimal time $d\tau$ is written

$$P(\tau + d\tau) = P(\tau) \times P(d\tau) \tag{2.85}$$

We know that there is, on average, one occurrence during the duration $T = 1/k$. As long as the system is complex enough to be described statistically, we can write the probability that the relaxation path is taken during the infinitesimal time $d\tau$ as $d\tau/T$. We can then write that the probability that the relaxation takes place during $d\tau$ is $kd\tau$ the probability that the relaxation has not taken place during $d\tau$ is $(1 - kd\tau)$, hence

$$P(\tau + d\tau) = P(\tau) \times (1 - kd\tau) \tag{2.86}$$

After integration, we obtain

$$P(\tau) = Ae^{-k\tau} \tag{2.87}$$

k is the occurrence rate associated with the relaxation path. We must add the normalization condition which is expressed by

$$\int_0^\infty P(\tau)d\tau = 1 \tag{2.88}$$

We see that P is a temporal probability distribution. We obtain

$$P(\tau) = ke^{-k\tau} \tag{2.89}$$

The probability of not emitting decreases exponentially with the duration t separating the last emission.

We can transpose this proof to the case we are interested in (several relaxation pathways). We also have to keep in mind that at each step of the relaxation (i.e of the Monte-Carlo), the internal energy E is fixed and so we have $k(E)$. Moreover, we have a multitude of relaxation pathways with $k_i(E)$ rates. The reasoning is exactly the same if we replace relation 2.86 by

$$P(\tau + d\tau) = P(\tau) \times (1 - (\sum_i k_i)d\tau) \tag{2.90}$$

The sum $\sum_i k_i$ simply comes from the sum of the probabilities of the different relaxation paths. In this case, the duration probability distribution of an occurrence at internal energy E is written by

$$P(\tau; E) = \mathit{\Gamma} \exp(-\mathit{\Gamma} t) \qquad \mathit{\Gamma} = \mathit{\Gamma}(E) = \sum_i k_i(E) \tag{2.91}$$

Thus, at each step of the Monte-Carlo and in addition to randomly selecting a relaxation path, we must also randomly select a duration after which this relaxation takes place. If we note `ran` a number chosen randomly between 0 and 1, we write that

$$\mathit{\Gamma} \exp(-\mathit{\Gamma} \mathit{\Delta} \tau) = \texttt{ran} \tag{2.92}$$

$\mathit{\Delta}\tau$ represents the duration that has elapsed between the occurrence of the current and previous step. This gives (Barker, 1983)

$$\mathit{\Delta}\tau = \frac{-\ln(\texttt{ran})}{\mathit{\Gamma}(E)} \tag{2.93}$$

In this way, it is also possible to simulate and visualize the temporal evolution of the emission spectrum.

Conclusion

In this chapter, we presented models implemented to simulate photophysical processes (recurrent and vibrational fluorescence), photochemical processes (dissociation and isomerization) and collisional de-excitation/excitation during relaxation cascades after UV photon absorption. The fundamental hypothesis that appears in all models is that the species contains so many accessible vibrational states that its time evolution is independent of its history and, then, observable quantities can be calculated by statistical methods (ergodic hypothesis). This allows us to simulate the relaxation cascade and the emission spectrum by a kinetic Monte-Carlo method. However, we have to keep in mind the approximations we have made: i) for the calculation of the electronic states occupation probability with fixed internal energy, we neglected the ratios of densities of states ratios in the expression 2.11; ii) the collisional energy transfer model is an empirical result and can only be approximated; iii) to find an analytical solution of $< \mathit{\Delta} E >_u (E)$, we approximated the VDOS ratio to an exponential (relation 2.65).

3. Radiative emission of large carbon clusters

Contents

Modelling of the photophysics **28**
  Statistical approach - microcanonical framework 29
  Harmonic vibrational density of states 31
  Recurrent fluorescence 34
  Vibrational fluorescence 37
  Formula relating spectroscopic quantities 38
Modelling of the photochemistry **40**
  RRK theory 40
  RRKM theory 41
  Dissociation and isomerization 42
Collisional energy transfer **43**
  Collision rate 43
  Parametric model 44
Relaxation radiative computation **51**
  Principle of the Monte-Carlo for relaxation cascade 52
  Application to radiative relaxation 53
  Kinetic aspect of the Monte-Carlo 56

We present in this chapter the theoretical work we have done on $\mathrm{C}_{n=24,42,60}$ carbon clusters emission in two different environments: in the interstellar medium where carbon clusters are in isolated conditions and in combustion context where carbon clusters are in thermal equilibrium. We present these results of our research in the form of three papers in preparation (to be submitted very soon). The first paper deals with the photophysics

of C_{24}, C_{42} and C_{60} carbon clusters. The second paper deals with the emission spectra of these clusters obtained from radiative relaxation induced by a 20 000 K black body irradiation or by the interstellar radiation field. In the third article, we are interested in the emission spectrum that would be obtained when these carbon clusters are brought to temperatures similar to flame temperature ($\approx$ 3000 K).
Except in the first part of the first paper, all these studies are performed over a large set of carbon clusters (thousands of isomers). Indeed, the emission signal coming from the interstellar medium or from a flame should involve a very large number of isomers.
The first section (*i.e* first paper) has been corrected and improved by Florent Calvo, Cyril Falvo and Aude Simon but all the research work has been done by Thomas and I.

Radiative relaxation in large carbon clusters: recurrent fluorescence versus vibrational emission

Hundreds of thousands of carbon clusters for each C_{24}, C_{42} and C_{60} sizes have been generated and their vibrational and electronic structures calculated by Maëlle Bonnin, Florent Calvo, Clément Dubosq, Cyril Falvo, Pascal Parneix, Mathias Rapacioli and Aude Simon. I did not participate to this work. Thomas Pino proposed me to study the emission induced by photon absorption of these carbon clusters in the interstellar medium context. During this study, we noticed that the competition between recurrent fluorescence and vibrational fluorescence was slightly more complicated than we supposed. This led to a work in which we only focused on the photophysics of carbon clusters.

In this first theoretical work, the competition between recurrent fluorescence and vibrational fluorescence of C_{24}, C_{42} and C_{60} carbon clusters is studied as a function of their internal energy, their size and their structural properties. We calculated with a kinetic Monte Carlo method the radiative relaxation kinetics and the resulting emission spectra. Fluorescence rates (recurrent and vibrational) were calculated in a microcanonical framework. We assumed that the harmonic approximation of vibrational modes is valid. It turns out that in our carbon clusters the recurrent fluorescence is highly competitive with the vibrational emission. We also noted that the recurrent fluorescence rates follow an Energy Gap Law-type evolution.

Introduction

The sp, sp^2 and sp^3 hybridizations exhibited by the carbon element are a central component of organic chemistry and explain the various allotropic forms of carbon, including its various crystalline phases of diamond, lonsdaleite and graphite, as well as the amorphous phase. At the nanoscale, structural diversity is manifested by the existence of nanotubes, graphene, but also a great variety of carbon clusters (Handschuh et al., 1995; Van Orden and Saykally, 1998; Lai et al., 2016; Bonnin et al., 2019). Recently, motivated by astrophysical issues, the structural diversity of carbon clusters was also explored from the perspective of their infrared and electronic spectra (Bonnin et al., 2019; Dubosq et al., 2019, 2020). A systematic exploration of the structures themselves (Bonnin et al., 2019), carried out by means of molecular simulation and a systematic sampling based on the REBO potential (Brenner et al., 2002), revealed that in the range between 24 and 60 atoms, carbon clusters can be classified into four main families depending essentially on their aromatic content and overall shape: cages, that include fullerenes; flakes, that can be defined as mostly planar polycyclic aromatic compounds, pretzel-like structures (Kim and Tománek, 1994), with a more open character and long carbon chains, and finally branched structures with terminating sp^1 carbons. From the knowledge of these structures, both the vibrational (Dubosq et al., 2019) and optical (Dubosq et al., 2020) spectra were subsequently determined using an efficient electronic structure method, namely self-consistent charge density-functional based tight-binding (SCC-DFTB) (Elstner et al., 1998) and its time dependent version (Niehaus et al., 2001).

Such compounds are notably found as products of incomplete combustion (Anacleto et al., 1992; Rotello et al., 1993; Zhang et al., 1986), and several of them have been detected in the interstellar medium (ISM). Owing to combined efforts from observation, experiments and simulations, it is now known that a large fraction of carbon in space is included in large carbonaceous molecules and dust grains. The former could be (nano-)diamonds, fullerenes, polycyclic aromatic structures, amorphous carbon and their hydrogenated amorphous carbon forms (Dartois, 2019). In particular, C_{60} buckminsterfullerene and C_{70} have been identified through their infrared emission spectra in several ISM environments (reflection nebulae, planetary nebulae, protoplanetary nebulae, diffuse medium) (Sellgren et al., 2010; Cami et al., 2010; Otsuka et al., 2013; Zhang and Kwok, 2011b; Roberts et al., 2012; Berné et al., 2017) and the C_{70} in Tc 1 planetary nebulae (Cami et al., 2010). The C_{60} buckminsterfullerene cation has also been detected in absorption (Cordiner et al., 2019), and likely in emission too Berne et al. (2013) and five diffuse interstellar bands have been attributed to it (Campbell et al., 2015; Maier and Campbell, 2017; Lykhin et al., 2018). Interestingly, smaller clusters such as C_2 (Federman et al., 1994) C_3 (Maier et al., 2001) or C_5 (Bernath et al., 1989) have also been detected.

From the point of view of interstellar absorption spectroscopy, carbon clusters with a high aromatic content such as fullerenes or flakes may contribute to the UV-bump at 217.5 nm (Dubosq et al., 2020). Two main models have been proposed to explain the presence of fullerenes in the ISM. In the so-called top-down model, large polycyclic aromatic hydrocarbons (PAHs) experience UV irradiation and consequently undergo dehydrogenation, fragmentation and then isomerization to form pentagon rings until they reach a cage shape (Berné and Tielens, 2012; Zhen et al., 2014). In the alternative bottom-up scenario, the growth of fullerenes is explained by the successive incorporation of individual carbon atoms or C_2, a mechanism known as closed network growth (Dunk et al., 2012a).

Owing to their reasonably large size and great structural diversity, these clusters often have low-lying electronic states, of magnitude comparable to some vibrational excited states. This proximity makes the photophysics of carbon clusters particularly interesting. In the present work, we further exploit the large database of structures made available from the previous efforts in the context of photophysical evolution Bonnin et al. (2019); Dubosq et al. (2019, 2020), and address their relaxation kinetics upon absorption of a UV photon.

Upon excitation, which may be electronic or vibrational, a large molecule can undergo various relaxation processes acting on the different degrees of freedom and operating over different time scales, and which include electronic fluorescence, internal conversion or intersystem crossing, isomerization, ionization or fragmentation. One typical situation is that of internal conversion or intersystem crossing, in which the initial electronic energy is entirely converted into nuclear motion, leading the system in the electronic ground state but with a high vibrational energy, relaxation proceeding subsequently through emission of IR photons (vibrational emission)(Leger and Puget, 1984; Allamandola et al., 1985), in competition with fragmentation and isomerisation if these pathways are open at the current internal energy.

However, it is also possible that a part of the vibrational energy flows back into the electronic degrees of freedom, especially if there are some low-lying electronic excited states as in the case of carbon clusters. In this process called inverse internal conversion, the internal energy is sufficient to possibly induce spontaneous electronic excitation, after which the molecule can again relax through electronic fluorescence or non-radiative processes. When electronic fluorescence occurs after such inverse internal conversion, it is usually referred to as recurrent or Poincaré fluorescence (Léger et al., 1988).

In the context of photophysics in the ISM, recurrent fluorescence (RF) has been suggested as a likely relaxation pathway for PAH emission (Léger et al., 1988), and RF of large carbon clusters is suspected to be a possible cause for the extended red emission detected in several interstellar environments (reflection nebulae, HII regions, carbon-rich planetary nebulae, diffuse interstellar medium, galactic cirrus clouds and in other galaxies) and particularly in the Red Rectangle (Duley, 2009; Lai et al., 2020, 2017). RF is also suspected to contribute to the continuum of the near-IR emission (Sellgren, 1984). In very hot environments such as flames, carbon clusters are so highly vibrationally excited that RF may extend over the near-IR and visible wavelength ranges (Mitzner and Campbell, 1995; Rohlfing, 1988). Recently, evidence for RF taking place in (hydro)carbon clusters such as PAH cations, anthracene (Martin et al., 2013) and naphthalene (Saito et al., 2020a) and the C_6^- anion (Ito et al., 2014; Chandrasekaran et al., 2014) was provided in experiments in which the relaxation could be monitored over long times in electrostatic storage rings.

The purpose of the present work is to get further insight into the possible competition between recurrent fluorescence and vibrational emission occurring in large carbon clusters and the dependence of both processes on the internal energy, the size and the structural features of these clusters. We have chosen to focus on archetypal isomers of C_{60} that belong to the four structural families (cags, flakes, pretzels, branched) identified in our earlier contribution (Bonnin et al., 2019), and to selected structures of the smaller C_{42} and C_{24} clusters, both taken from the sample of flakes isomers.

To quantify the relative efficiencies of recurrent fluorescence and vibrational emission, we employ a kinetic Monte Carlo model that uses static vibrational and electronic data obtained from electronic structure calculations and assumes an harmonic approximation for the level densities. Using appropriate expressions for the various rate constants associated to the different relaxation pathways, the time evolution of the internal energy of the system can be monitored and the radiative cooling mechanisms can be addressed in detail.

The article is organized as follows. The theoretical and computational details of our approach are detailed in Sec.3, while Sec.3 is devoted to its application to several carbon clusters of selected size and shape. In Sec.3 we discuss the dependence of the RF rate on the electronic state energy and find some connection with the energy gap law in the context of radiationless transitions. We also elaborate further on the relation between RF efficiency and structural features, extending much beyond our reduced selection of archetypal isomers, by considering now thousands of them. Finally, Sec.3 summarizes the main findings of our work and draws some conclusions and perspectives.

Methods

Before laying out the general theoretical framework, it is useful to recall the typical time scales associated with the various elementary radiative processes taking place in carbon clusters. Upon an electronic excitation, large molecules such as carbon clusters or carbonaceous aromatic compounds undergo internal conversion over $\sim 10^{-14}$–10^{-8} s, intersystem crossing occuring over $\sim 10^{-10}$–10^{-7} s and usually involving neighboring electronic states, until the electronic ground state is reached (Birks, 1970a) with the excess energy being converted mainly into vibrational motion. Concomitantly, intramolecular vibrational redistribution (IVR) typically proceeds over $\sim 10^{-13}$–10^{-10} s (Nesbitt and Field, 1996; Quack, 1990), the vibrational energy being thus redistributed among all vibrational states so that the system reaches statistical equilibrium.

In contrast, the typical time scales for vibrational emission (VE) and recurrent fluorescence are $\sim 10^{1}$–10^{-2} s and $\sim 10^{1}$–10^{-4} s, respectively, much slower than internal conversion, intersystem crossing and IVR. We will thus safely assume as a statistical hypothesis that the vibrational energy in the ground electronic state is ergodically distributed between two successive emissions. In doing so, we neglect the contribution of rotational degrees of freedom to the total system energy (Mulas, 1998). However, for the present relatively large clusters, the rotational energy is negligible compared to the vibrational contribution and we further ignore it in our modeling. Various relaxation channels are a priori in competition for carbon clusters. These include radiative pathways, which are RF and VE mentionned hereabove, but also direct electronic fluorescence, and non radiative relaxation channels such as dissociation and ionisation (Lifshitz, 2000a).

Our aim is to compute the emission spectra originating from the various radiative relaxation channels and their dynamical features. Here we follow a methodology already laid out in earlier contributions (Basire et al., 2011; Parneix et al., 2013) which relies on an event-driven kinetic Monte Carlo (kMC) approach where all possible relaxation events are enumerated for a given state of the system, the next state being stochastically advanced from the knowledge of the corresponding rate constants. The kMC simulation requires evaluating the rate constants associated with the various relaxation mechanisms, at the current internal state of the system. It is intrinsically microcanonical, as we do not consider the additional interaction between the system and the environment once the initial excitation has driven it out of equilibrium.

The emission spectrum is obtained from the accumulation of photons emitted over many independent realizations of the simulations, for a fixed observation time or until the system has reached its ground state or, in practice, a very low internal energy sufficient to make it stable over extremely long times.

Vibrational emission and recurrent fluorescence rate constants

We first discuss the case of vibrational emission, starting with the decay of vibrational energy on the ground electronic state by successive emission of IR photons.

In the harmonic approximation, the vibrational state of the system can be described from the knowledge of its vibrational frequencies $\{\omega_i, i = 1, \cdots, g\}$ where g denotes the number of vibrational modes. For a given internal energy E, the microcanonical probability $P_{i,v}$ that a specific mode i is occupied by v vibrational quanta reads

$$P_{i,v}(E) = \frac{\rho_{/i}(E - v\hbar\omega_i)}{\rho(E)}, \tag{3.1}$$

where $\rho(E)$ is the total ground state vibrational density of states at the internal energy E, $\rho_{/i}(E - v\hbar\omega_i)$ is the ground state vibrational density of states at the internal energy $E - v\hbar\omega_i$ without taking into account the i^{th} vibrational mode. This is made possible because we use the harmonic approximation for the vibrational density of states. From this probability, the emission rate constant from the i^{th} mode occupied by all possible v vibrational quanta is obtained as

$$A_i(E) = \sum_{v=1}^{v_{\max}} \frac{\rho_{/i}(E - v\hbar\omega_i)}{\rho(E)} A_i^{v \to v-1}, \tag{3.2}$$

where $A_i^{v \to v-1}$ is the one-photon emission rate from v upper level to the next lower level $v - 1$ from the i^{th} mode, and $v_{\max}$ the maximum number of quanta that this mode can sustain at the current total energy, given by the integer part of $E/\hbar\omega_i$. Note that the total emission rate constant $A_i(E)$ is a weighted sum of all possible rate constants $A_i^{v \to v-1}$, individual weights being related to the occupation of the respective vibrational levels. In addition, we do not take into account overtones or combination bands which we assume to be negligible compared to the direct $v \to v - 1$ emissions. For harmonic oscillators we can further use the relation $A_i^{v \to v-1} = vA_i^{1 \to 0}$, where $A_i^{1 \to 0}$ is the Einstein coefficient of the fundamental transition of mode i. This allows the emission rate constant from the i^{th} vibrational mode to be rewritten as Durana and McDonald (1976); Cook and Saykally (1998)

$$A_i(E) = A_i^{1 \to 0} \sum_{v=1}^{v_{max}} \frac{\rho_{/i}(E - v\hbar\omega_i)}{\rho(E)} \times v. \tag{3.3}$$

The emission rate constant $A_i(E)$ can be viewed as resulting from two different contributions, namely a quantum contribution through the Einstein coefficient $A_i^{1 \to 0}$, and a statistical contribution which expresses the occupation of the vibrational levels and gives rise to a dependency of the emission rate on the internal energy. The Einstein coefficients are directly related to the frequency ω_i and the vibrational oscillator strength f_i of the mode through (Cohen-Tannoudji et al., 2021)

$$A_i^{1 \to 0} = \frac{8\pi^3 e^2 \omega_i^2}{\epsilon_0 m_e c^3} \times f_i \tag{3.4}$$

Turning now to recurrent fluorescence, we again assume that owing to the much faster time for vibrational redistribution, the distribution of vibronic states is entirely statistical, not only on the ground electronic state but also for all accessible electronic excited states. The occupation probability of any n^{th} electronic state of energy E_n is proportional to $\rho_n(E-E_n)$ where $\rho_n(E)$ is the density of vibrational states on the corresponding electronic state at energy E_n relative to the ground electronic state. Here we introduce two additional approximations. First, we assume that for relatively large systems as those under scrutiny in the present work, the vibrational structure is similar between the low-lying electronic states and the ground state, allowing us to assume that $\rho_n(E) \approx \rho_0(E) = \rho(E)$. The probability of the n^{th} electronic state at thermal equilibrium thus reads

$$\gamma_n = \frac{\rho(E-E_n)}{\sum_k \rho(E-E_k)},$$

where the denominator is a normalizing factor. In addition, the densities of states grow very fast with increasing energy, hence we approximate the sum in this denominator as its first, dominant term:

$$\frac{\rho(E-E_n)}{\rho(E)}, \tag{3.5}$$

The RF rate constant, which can be considered as an effective electronic fluorescence rate, is then written as

$$A_{\mathrm{RF}}^{n \to 0}(E) = A_{\mathrm{f}}^{n0} \frac{\rho(E-E_n)}{\rho(E)}. \tag{3.6}$$

For this process too the rate constant contains one quantum contribution in the prefactor, and a statistical contribution involving the densities of vibronic states. Moreover, the electronic fluorescence rate A_f^{n0} is expressed from Eq. (3.4) in which f_i is the electronic oscillator strength and $\hbar\omega_i$ the electronic energy of the i^{th} excited electronic state. For the sake of computational simplicity, we further neglect fluorescence between different excited electronic states and assume that only the $n \to 0$ transitions are efficient.

Vibrational emission from electronically excited states can also be accounted for, using a similar expression as Eq. (3.3) above for the ground state but involving now the correctly shifted densities of states (still assuming $\rho_n \approx \rho_0 = \rho$):

$$A_i^n(E) = \frac{\rho(E-E_n)}{\rho(E)} A_i(E-E_n). \tag{3.7}$$

VE from electronically excited states is usually negligible compared to those from the ground electronic states and RF. Expressions (3.3), (3.6) and (3.7) are implemented for the simulation.

Approximate analytical expressions for the rate constants

For both RF and VE mechanisms, simple expressions can be obtained for the corresponding rate constants by considering specific approximations and limiting forms. The total rate constant for RF processes and its dependence on internal energy can be determined at high internal energy using a semiclassical expression for the harmonic vibrational density of states Robinson and Holbrook (1972)

$$\rho(E) \approx \frac{(E+E_z)^{g-1}}{(g-1)! \prod_{i=1}^{g} \hbar\omega_i}, \tag{3.8}$$

where E is the internal energy and E_z the zero-point energy. Incorporating the latter expression inside Eq. (3.6) and assuming that $E + E_z \gg E_n$, the total RF rate constant can be expressed as

$$A_{\mathrm{RF}}^{\mathrm{tot}}(E) = \sum_{n=1}^{n_{\max}} A_{\mathrm{f}}^{n0} \times \exp(-\frac{(g-1)E_n}{E+E_z}), \tag{3.9}$$

in which $n_{\max}$ is the highest electronic quantum number that is accessible at the internal energy E. Likewise, an analytical approximation can be obtained for the VE rate constant from the i^{th} vibrational mode using a continuous approximation for the discrete sum of Eq. (3.3). This approximation is also valid at high internal energies $E/\hbar\omega_i = v_{\max} \gg 1$, and yields:

$$A_i(E) \simeq A_i^{1\to 0}(g-1) \int_0^{v_{\max}} \mathrm{d}v \; \frac{v}{v_{\max}} \left(1 - \frac{v}{v_{\max}}\right)^{g-2}$$

This integral can be solved exactly as

$$A_i(E) = A_i^{1\to 0} \frac{E}{g\hbar\omega_i} \tag{3.10}$$

in which we further neglected the zero-point contribution to the internal energy E, assumed to be high. Summing over all VE rate constants eventually leads to

$$A_{\mathrm{vib}}^{\mathrm{tot}}(E) = \frac{E}{g} \sum_{i=0}^{n_{\max}} \frac{A_i^{1\to 0}}{\hbar\omega_i}.$$

Equations (3.8), (3.9) and (3.10) will be used for interpreting simulation results.

Other processes: C_2 dissociation and delayed ionisation

When modeling the long-time relaxation decay of carbon clusters it is important to also consider the possible contribution of other non-radiative pathways. At high energies, thermal dissociation or fragmentation could be activated, and we have evaluated the propensity for such events through the traditional unimolecular reaction theories based on the Rice-Ramsperger-Kassel (RRK) framework (Robinson and Holbrook, 1972). More precisely, the dissociation rate constant can be expressed within this approach simply as

$$k_{\mathrm{diss}}(E) = A(1 - D/E)^{g-1},$$

where D is the dissociation energy and A is a prefactor. For C_{60}, accepted values for $A = 10^{20}$ s^{-1} and $D = 12$ eV (Lifshitz, 2000b) yield a dissociation rate constant of 10^{-38} s^{-1} at the excess energy of 18.5 eV, which is the maximum value considered in the present work. For C_{42}, a similar prefactor and a dissociation energy of 7.5 eV (Chang et al., 2005) lead to a much higher dissociation rate constant of about 10^{-7} s^{-1}, although, and as seen below, still much faster than the processes we are focusing on.

To the best of our knowledge, no such data are available for C_{24}. The dissociation rate constant for this cluster can be estimated at 15 eV ($\approx 120\,000$ cm^{-1}) excess energy if we assume a prefactor $A = 3 \cdot 10^{13}$ s^{-1} (~ 1000 cm^{-1}) and a modest dissociation energy D of 6 eV only (Chang et al., 2005). Such values lead to a dissociation rate constant of 0.1 s^{-1}. For this cluster, the neglect of thermal dissociation could be a more stringent approximation than for the two larger systems, for which dissociation is unlikely to occur at all under the conditions of our modeling.

However, in all cases we note that the actual dissociation process is a highly complex function of the isomer too, which further involves strong anharmonicities, making the rate constant determination quite difficult. Additionally, the RRK modeling used here for crude evaluation of the rate constants ignores the possibility of fragmentation on electronic excited states, which for carbon clusters was shown to be also a realistic event (Montagnon and Spiegelmann, 2007). Similarly, we also rule out the possibility of delayed (thermo)ionisation, which is essentially described by similar laws, prefactors and energy factors (Lifshitz, 2000a).

Kinetic Monte Carlo modeling of emission cascades

We now incorporate the previously determined rates for vibrational and recurrent relaxations into an integrated framework in which the evolution of the system and its internal energy can be monitored as a function of time. The main idea is to enumerate all possible events for a given internal energy and calculate their absolute rates, then select one of them randomly based on a probability proportional to its rate.

In practice, owing to complete IVR between successive events, memory loss allows us to assume a Markovian process for the kMC procedure, and a time duration for the current state that follows Poissonian statistics (Fichthorn and Weinberg, 1991). From the knowledge of all individual rate constants, their sum $\mathit{\Gamma}$ is determined and the duration δt of the current state is taken as $\delta t = -\log(\mathtt{ran})/\mathit{\Gamma}$, where `ran` is a uniform random number in the range $0 < \mathtt{ran} \leq 1$. Alternatively, a simple constant $\delta t = 1/\mathit{\Gamma}$ was found sufficient to describe the overall kinetics.

By repeating the kMC simulations over a large number of independent trajectories, the results can be averaged to yield a statistical description of the complete relaxation pathway as a function of time. The total emission spectra are notably obtained by integrating the trajectory until no more relaxation step is possible.

Computational details and structural selection

All ingredients needed for the above calculations were provided by dedicated electronic structure calculations based on the self-consistent charge density-functional based tight-binding (SCC-DFTB) method (Elstner et al., 1998) for ground state vibrational energies and intensities of normal modes. Its Time Dependent version (Niehaus et al., 2001) was used to determine vertical electronic states energies and oscillator strengths, computed for transitions from the ground electronic state exclusively. This approach was found to be able to determine both vibrational (Dubosq et al., 2019) and electronic (Dubosq et al., 2020) spectra of chemically diverse carbon clusters, and is thus found to be appropriate here for evaluating the intensity strengths and the vibrational densities of states, which were numerically calculated using the Beyer-Swinehart algorithm (Beyer and Swinehart, 1973). SCC-DFTB vibrational frequencies and TD-DFTB excitation energies were scaled (Dubosq et al., 2019, 2020) and 10^5 kMC trajectories were computed.

Our objective is to unravel the relative efficiencies of RF and VE mechanisms in the radiative cooling of carbon clusters. Of special interest are the combined influences of size and structural features. In the present work, we considered sets of isomers for C_n (n=60, 42, 24) belonging to the four families mentioned in the introduction (cages, flakes, pretzels, branched). About 100 000 isomers per family were optimized at the SCC-DFTB level for C_{60}. Among those, we determined a subset of 1000 isomers per family for which the root mean square deviation (RMSD) of the families' order parameters (%sp^2 and asphericity parameter β) were the closest to the average value for the given family. The full sets of isomers will be considered in section 4. However, our first study is dedicated to individual isomers. We therefore first selected four isomers of C_{60} belonging to the

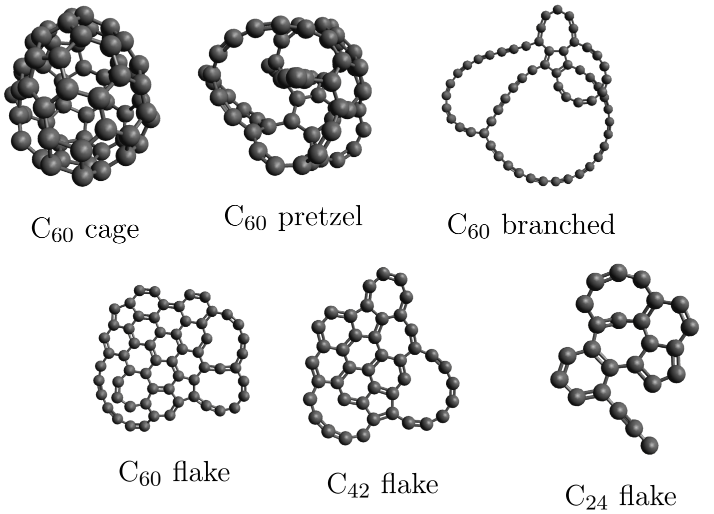
C_{60} cage C_{60} pretzel C_{60} branched

C_{60} flake C_{42} flake C_{24} flake

Figure 3.1: Selected archetype isomers for all families and sizes

	C_{60}				C_{42}	C_{24}
Property	cage	pretzel	branched	flake	flake	flake
$\sum^{50} f_{\text{elec}}$	0.14	0.22	1.34	0.26	0.31	0.23
$\sum I_{\text{vib}}$ (km/mol)	990	3300	7424	5600	3530	3260
$\overline{\omega}$ (cm^{-1})	754	537	372	559	557	557
ZPE (eV)	9.4	8.1	7.3	8.4	5.8	3.1
E_1 (eV)	0.25	0.33	0.27	0.21	0.26	0.60
E_2 (eV)	0.53	0.48	0.36	0.31	0.39	0.83
E_3 (eV)	0.58	0.76	0.66	0.35	0.50	0.95

Table 3.1: Main features for the six selected carbon clusters, from top to bottom: sum over the first fifty electronic oscillator strengths (for all isomers, the 50^{th} electronic state energy is less than 3 eV above that of the ground state), summed vibrational intensities, geometrical mean of vibrational wavenumbers, zero-point energies and energies of the three lowest excited electronic states.

cages, flakes, pretzel, and branched families, respectively, as well as two other members of the flakes family but having 24 or 42 atoms only. These specific isomers, depicted in Fig. 3.1, were selected so that their average electronic and vibrational oscillator strengths are the closest to the average of the same quantities among the entire family set.

These properties are reported in Table 3.1. Here we should emphasize that we purposedly did not choose the buckminsterfullerene isomer of the cage family, which owing to its very particular symmetry is actually poorly representative of its own family. For instance, its lowest allowed electronic excited state lies more than 3 eV above the ground electronic state (Heath et al., 1987), yielding essentially no recurrent fluorescence under the conditions where the other, less ordered isomers contribute to a much greater extent.

Kinetics of radiative cooling in carbon clusters: selected cases

Emission spectra

The total emission spectra of the six selected species were computed for a radiative cascade initiated from an excitation at 100 000 cm^{-1} internal energy (arbitrarily fixed). These spectra are shown in Fig. 3.2. In the following, we discuss the influence of the different parameters on the competition between RF and VE. Regarding RF from an electronic excited state, its intensity depends on the electronic state energy, but also on the oscillator strengths of the involved transitions. The sum of oscillator strengths over the fifty electronic states for all considered isomers is reported in Table 3.1. The reported values for C_{60} illustrate the dependence on structure. More insight is provided by considering size effects. Comparing the RF from the C_{24}, C_{42} and C_{60} flake isomers, interesting variations can be noticed, that can be related to the density of electronic states. For such aromatic isomers, the density of electronic states increases with size (see appendix 3 Fig. 3.9), which expectedly leads to more efficient and low energy RF emission.

First, the larger is the isomer, the larger is the density of electronic states and the lower in energy are the first excited states. This behavior can be rationalized by noting that in such mostly aromatic species, the π electrons can be approximately considered as free in a spatially limited constant potential. By analogy with a particle in an infinite well, the more extended is the cluster, the broader is the well and the lower are the electronic energies (Robertson and O'reilly, 1987; Platt, 1949). In contrast, and while the number of vibrational modes also increases, they are limited on the high-frequency side by the carbon-carbon bond strength, which does not scale significantly with cluster size. Thus, RF appears to be increasingly competitive with VE when the size of the isomer increases. It should also be noticed that C_{24} exhibits a particularly intense peak in the mid-IR region near 2000 cm^{-1}, which is a consequence of this structure having a terminating C_3 dangling chain (see Fig. 1) with a strongly varying dipole moment, leading to a particularly active IR response for this specific system, as seen in Table I on the summed IR intensity strength, which competes with that of the larger C_{42} cluster.

The dependence on structural type for a given size can also be examined by considering the four isomers chosen for C_{60}, assisted by the data reported in Table 3.1. However, unlike size effects for the chemically similar flake isomers, the effects of structural type are not as clear. Still, it is worth noting that the RF and VE contributions to the emission spectrum are the most distinguishable from one another for the more disordered pretzel and branched isomers, the spectrum obtained for the cage structure presenting the same extent of overlapping between its electronic and vibrational parts.

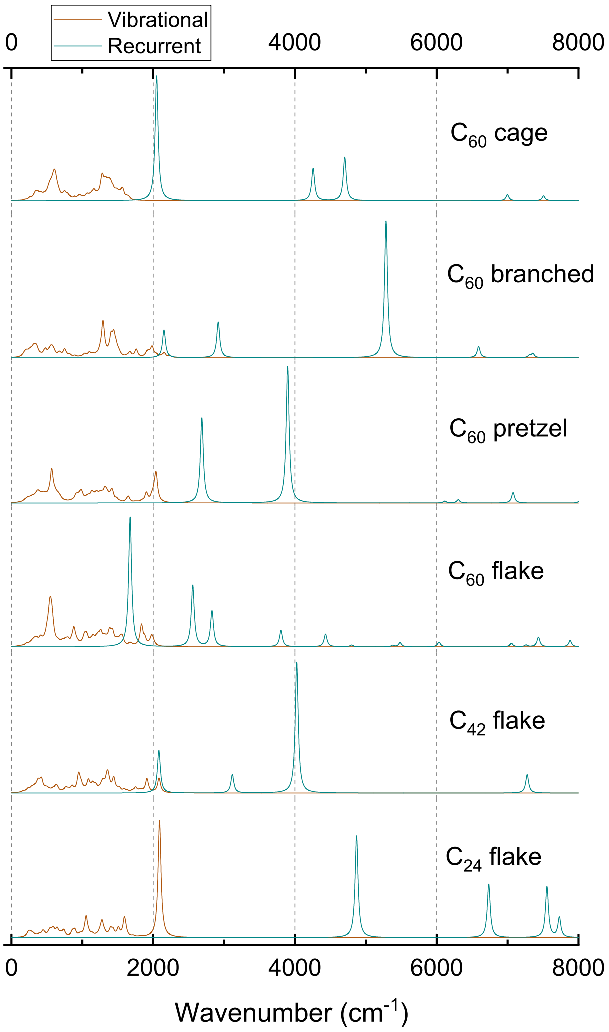

Figure 3.2: Normalized emission intensity spectra of the six selected carbon clusters obtained from radiative cooling with 12.4 eV initial internal energy. The spectra were obtained as histograms and convoluted by a Lorentzian distribution with a full width at half maximum of 50 cm^{-1}.

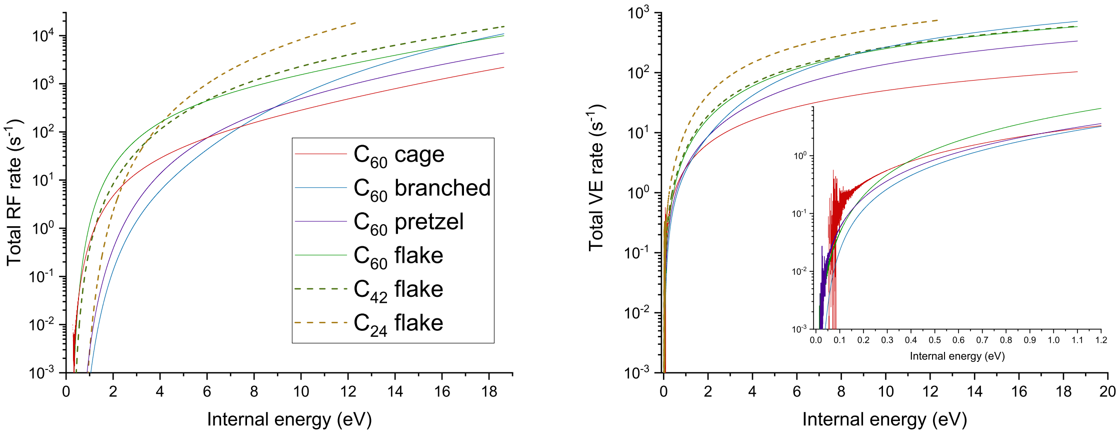

Figure 3.3: Left panel: Recurrent fluorescence rate constants for the six selected carbon clusters, as a function of their internal energy. Right panel: Vibrational emission rate constants for the six selected carbon clusters, as a function of their internal energy. The inset focuses on the low internal energies below 10 000 cm^{-1}.

Recurrent fluorescence and vibrational emission rate constants

Fig. 3.3 shows the variations of the total RF and VE rate constants, respectively for the 6 selected clusters, as a function of their internal energy.

At low internal energies $E < 2.5$ eV the relative values of the RF constants for the 6 chosen clusters can be rationalized by both their relative density of electronic states below this energy and their oscillator strengths. At high energy, $E > 12.5$ eV, the density of states being similar for all clusters (Fig. 3.9), the relative rate constants can be accounted for by the oscillator strengths only. More details are provided in this section.

Below 2.5 eV (=20 000 cm^{-1}) excess energy, the total RF rate constant is particularly high for the cage and flake isomers of C_{60}, which is due to these isomers having their first electronic states lower in energy than the other two pretzel and branched isomers (see Table 3.1). The particularly low total RF rate constant of the branched isomer of C_{60}, despite the first excited electronic state being as low as 0.27 eV, is explained by its very low vibrational frequencies as well (the lowest at 7 cm^{-1}), which makes the vibrational density of states increase very rapidly and leads to a very slow increase of the probability ratio [see Eq. (3.5)], hence a lower RF rate constant than for the cage isomer of C_{60}.

We can then speculate at this stage that the positions of the first electronic states drive the evolution of the total RF rate at low internal energies. However, in some isomers the electronic oscillator strength of these first electronic states may be decisive for the value of the total RF rate constant at low internal energies. An example of this behavior is provided by comparing the total RF rate constant of the branched and the pretzel isomers. At low internal energies, the pretzel conformer has a total RF rate constant slightly higher than the rate constant of the branched conformer despite its first electronic levels being much higher. This particular situation is explained by the relative electronic oscillator strengths involved in the process. According to our SCC-DFTB calculations, the oscillator strengths associated with the first and second electronic states of the pretzel and branched isomers are in the approximate ratios 1.1:0.4 and 4.9:1. This explains why RF is more efficient for the pretzel isomer.

At high internal energies E > 12.4 eV, the electronic oscillator strengths dictate the total RF rate constant because the energy of all electronic states is essentially the same for all clusters, whichever the family they belong to. At occupied excited electronic states of C_{60} isomers that lie below 2 eV above the ground state, the electronic density of states is approximately the same for all of them (see Fig. 3.9), only being the lowest for the cage structure.

In particular, the higher are electronic oscillator strengths, the higher is the total RF rate constant. The branched isomer has higher electronic oscillator strengths than isomers from other families, further supporting this view. Conversely, the cage isomer is associated with a relatively low total RF rate constant that concurs with a relatively low electronic oscillator strength (see figure (3.3) and table 3.1 for the selected species) and also with a slightly lower electronic density of states (fig.3.9)

Size effects are also important on the magnitude of the total RF rate constant and its variations with increasing internal energy. For the specific flake family, from which members were selected for C_{24}, C_{42} and C_{60}, Fig. 3.3 shows that below 2.5 eV internal energy, the total RF rate constant of C_{60} exceeds that of C_{24} (and that of C_{42}). However, the rate of variations is also much steeper for the smaller cluster. This is a consequence of its lesser ability for storing energy, which is intimately related to the fewer degrees of freedom of C_{24}. Moreover, RF is efficient only if the electronic states are appreciably occupied and this occurs only if the quantity $\gamma = \rho(E - E_n)/\rho(E)$ is not negligible. Such a condition implies that vibrational excitation has to be high enough for the upper electronic states to be populated as well.

At high internal energies, the number of degrees of freedom also affects the total RF rate constant but in a much smoother way. The analysis of Sec.3 shows that the main dependence on the number of degrees of freedom g occurs through the exponential term in the right hand side of Eq. (3.9), the total RF rate constant decreasing for increasing g at fixed internal energy. As the internal energy becomes very high, this term becomes negligible against the first term involving the electronic fluorescence rate constants. At this stage, the electronic levels are so easily occupied that the total RF rate constant is dominated by pure electronic fluorescence.

Fig. 3.3 also shows the variations of the total VE rate constants with increasing internal energy for the same 6 clusters. The vibrational activity is mostly sensitive to the set of frequencies, which for simplicity we sum up in their geometric average, and the set of vibrational intensity strengths.

Fig. 3.3 shows that the cage and the branched isomers of C_{60} are associated with the lowest and the highest VE rate constants for this stoichiometry, respectively. These differences can be understood from looking at the properties of the isomers in Table 3.1: the intensity strength appears to be the lowest for the cage, while the average vibrational frequency is the highest, implying fewer quanta at a given internal energy. The same arguments can be used to explain the opposite behavior of the branched isomer and its particularly high VE rate constant.

Size effects are also marked for VE processes, and remain the manifestation of fewer quanta being distributed in the various vibrational modes at fixed internal energy. As expressed by Eq. (3.10), the VE rate constant is expected to decrease with increasing g, at fixed E. In Fig. 3.3 the VE rate constant for the C_{42} flake isomer indeed lies between the corresponding rate constants for the two other flake isomers C_{24} and C_{60} at low energies, but crosses that of C_{60} at high energies. As seen in Table 3.1, this specific behavior results from the unexpectedly low average intensity strength for this system, very close to the value in C_{24}.

Quantifying the competition between RF and VE processes

Having neglected electronic fluorescence, thermal dissociation and delayed ionisation, the competition between RF and VE mechanisms can be directly quantified from the ratio of their rate constants:

$$\xi(E) = \frac{A_{\rm rec}^{\rm tot}}{A_{\rm rec}^{\rm tot} + A_{\rm vib}^{\rm tot}}.$$

The variations of this quantity with increasing energy are shown in Fig. 3.4 for the 6 selected clusters. At low energy, VE is the main mechanism for all systems. Then ξ increases monotonically with internal energy and ranges from 0 at low energies and eventually exceeds 90% above 140 000 cm^{-1}, indicating that RF becomes the increasingly dominant process at very high energies.

The value of the RF efficiency ξ and its variation from an isomer to another can be rationalized again from the electronic oscillator strengths and the vibrational activities. The particularly low electronic levels of the C_{60} cage and flake isomers make their RF efficiency increase as early as below 10 000 cm^{-1} internal energy. Their increase is steeper than that of the two other isomers of this size, but this is due to two distinct effects.

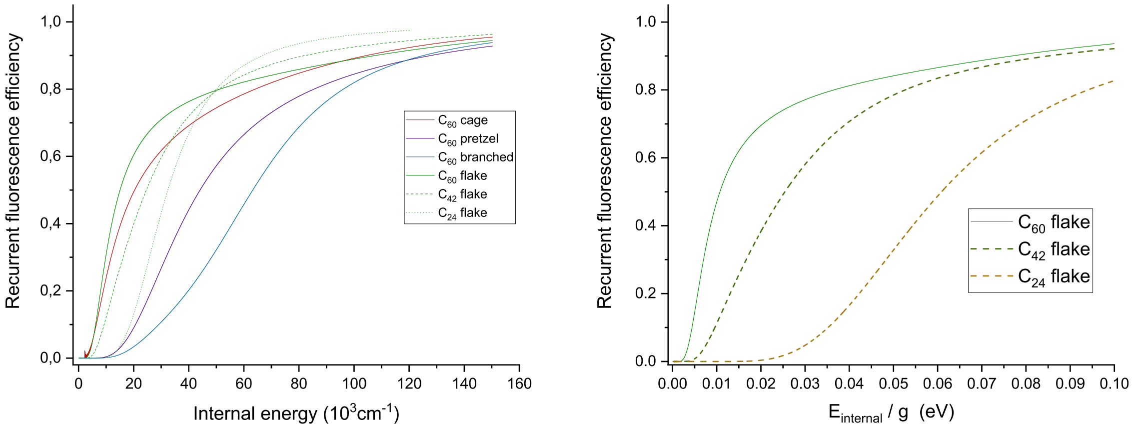

Figure 3.4: Left panel: Recurrent fluorescence efficiency ξ obtained from the rate constants of figure 3.3. Right panel: Recurrent fluorescence efficiency ξ in terms of E_{internal}/g for the three sizes.

In the case of the flake isomer, RF is particularly strong, while VE is very inefficient for the cage. For the branched isomer, vibrational frequencies are particularly low (22 vibrational frequencies below 100 cm^{-1} and the lowest is at 7 cm^{-1}) as shown by the value of the geometrical mean of vibrational frequencies (Table 3.1), making the RF rate constant lower despite its first electronic state being similar to that of the cage isomer: low vibrational frequencies imply higher vibrational densities of states and thus a higher ability to store energy in vibrational degrees of freedom.

In general, the isomer size also has an effect on the overall evolution of the RF efficiency. At low energy, larger isomers are associated with lower electronic states energies, leading to higher total RF rate constants. The RF efficiency then increases and reaches a maximum value at lower internal energies. Even though the RF efficiency for C_{24} increases at higher internal energies, it reaches its maximum value earlier than for both C_{42} and C_{60}, the three efficiencies crossing each other near approximately 50 000 cm^{-1}. The reason behind this size effect is again to be found in noticing that, for a fixed internal energy, smaller clusters are warmer because of the fewer number of degrees of freedom in which this excess energy must be shared. At low internal energy, smaller clusters thus have a higher fraction of this energy available for recurrent fluorescence, hence a lower associated rate constant. At high internal energy, where electronic and vibrational components can flow both ways more easily, RF efficiency becomes stronger for smaller clusters because the vibrational degrees of freedom play a relatively less important role.

Kinetics of radiative cooling

We turn now to the kinetics of radiative cooling processes in more detail, discussing the decay of the internal energy initially deposited into the system.

Using the kinetic Monte Carlo procedure described in Sec.3, the flow of energy in the system between the various electronic and vibrational degrees of freedom can be monitored as a function of time. Fig. 3.5 displays the variations of the total energy in the six clusters as a function of time, for an excess energy of 18.5 eV in all systems. These results were obtained by repeating the kMC trajectories a number of 10^5 independent times.

From this graph, it appears that for some isomers the internal energy decays, once plotted in log-log scale, in a piecewise linear fashion. If we arbitrarily define a relaxation time as the duration needed for the internal energy to decrease by a factor of 10, we find values between 0.1 and 1 s depending on the size and isomer type.

The different slopes in the various curves are the manifestations of different relaxation regimes in which the dominant mechanism varies along the relaxation path. A more detailed example is discussed in Fig. 3.5 for the flake isomer of C_{60}, in relation with Fig. 3.6 where the four main relaxation regimes are highlighted. The first relaxation regime, occurring at short times and for energies still located above 12.4 eV, is correlated with the presence of five competing relaxation pathways involving recurrent fluorescence (first, second, third, twelfth and thirteenth electronic states) and also depicted in Fig. 3.6. Once the energy reaches 8.7 eV, recurrent fluorescence from the twelfth and thirteenth electronic levels become negligible and this corresponds to another decay regime, denoted as the second regime, located between 7.4 and 3.1 eV. As the internal energy becomes lower than 3.1 eV, RF becomes efficient when the first electronic state is involved, which is associated with yet another decay regime (third regime) between 2.5 and 1 eV. Finally, below 0.75 eV, RF from the first electronic excited state becomes negligible compared to VF processes, leading to another, fourth regime change. The time-dependence of RF and VE competition can be analyzed by putting together Figs. 3.4 and 3.5. For the C_{60} flake, the RF efficiency is less than 0.5 for internal energies under 1.9 eV and for times beyond 0.2 s during which RF occurs only from the first excited electronic state (Fig. 3.6).

Comparing now the behaviors for the various isomers, and keeping in mind that RF is the dominant process at high energies, relaxation in the branched isomer is slightly faster than in the 60-atom flake, although this is not immediately obvious in Fig. 3.5. This is concomitant with the higher RF rate for the branched isomer. However, below 10 eV relaxation in the C_{60} flake is faster because its RF rate constant is much higher than others while the RF rate constant of the C_{60} branched isomer falls down owing to

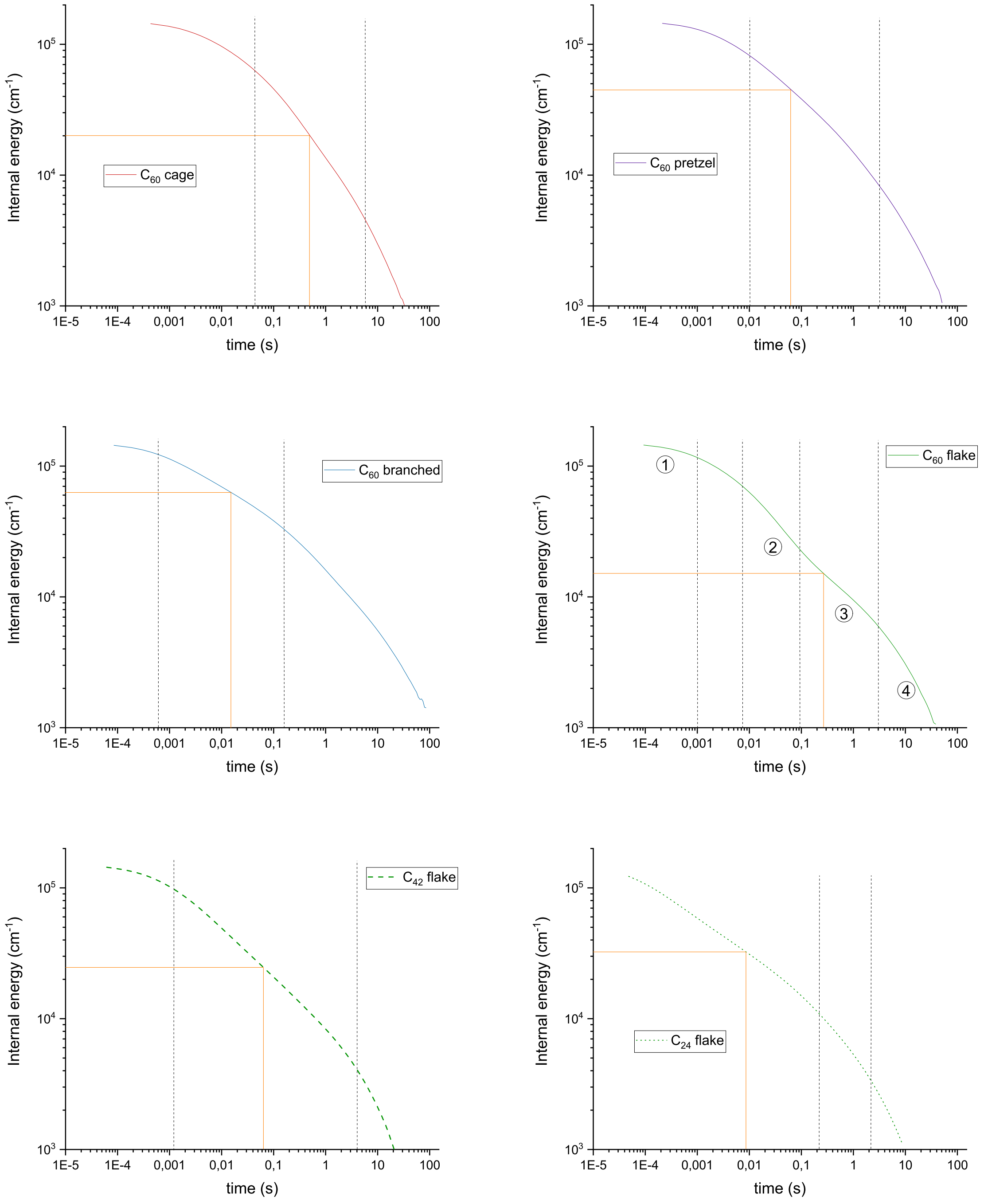

Figure 3.5: Temporal decay of the internal energy for the six carbon clusters. For all isomers, the initial internal energy was 18.5 eV except for the C_{24} flake for which it was 15 eV only. Main regime shifts are highlighted by vertical dashed lines. The numbering in circles for the C_{60} flake decay curve indicates the main decay regimes. Orange lines indicate the internal energy and the delay for which the RF efficiency is 0.5 (as deduced from Fig. 3.4).

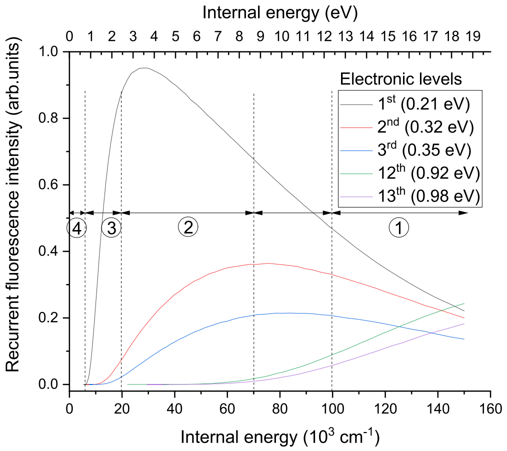

Figure 3.6: Recurrent fluorescence intensities from dominant electronic states in terms of the internal energy for the C_{60} flake. The numbering in circles indicates relaxation regimes.

its high first electronic levels (see Fig. 3.3).

Below 2.5 eV, the cage isomer relaxes faster than the branched and pretzel isomers because their RF rate constants are particularly low. This is not the case for the flake and cage isomers owing to their low-lying electronic states. The faster decrease obtained for the cage isomer compared to the flake compound is due to the VE process being dominant at energies lower than 0.4 eV, and which is further favored for the cage isomer relative to the flake (see inset in Fig. 4).

As shown in the previous section, the RF efficiency increases with internal energy whatever the size and the family of the isomer. Fig 3.2 shows that RF emits usually higher energetic photons. Smaller isomers have higher RF efficiency at high internal energies and thus their radiative relaxation is faster for smaller isomers (Fig. 3.5). Even at low internal energy, where RF is poorly efficient, radiative relaxation is faster for smaller isomers because, at fixed energy, vibrational quantum numbers are higher and thus the VE rate constant is higher. As far as structural dependence is concerned, our study also indicates that there is no clear general tendency but, conversely, that relaxation processes depend significantly on the isomers details. More insight into these aspects can be gained from looking at broader sets of structures.

Behavior over a large set

We now extend our scope by attempting to correlate the fluorescence rate constants with the structural features of the carbon clusters beyond the limited examples scrutinized in the previous section.

Electronic gap law decay type for RF rate constants

For simplicity, we assume that a single excited electronic state is available for all clusters. Its recurrent fluorescence rate constant in Eq. (3.6) can be expressed more explicitly by employing the semiclassical harmonic approximation of Eq. (3.8). The corresponding rate constant is straightforwardly obtained by applying Eq. (3.9) with $n_{\max} = 1$:

$$A^1_{\text{rec}} = A^1_f e^{-\frac{g-1}{E+E_z}E_1}, \tag{3.11}$$

where, consistent with the semiclassical approximation, we have further used $E_1 \ll E + E_z$. In Eq. (3.11), the internal energy E can be viewed as a parameter of the RF rate constant.

We have determined the corresponding quantity for much larger sets of structures for which the low-lying electronic excited states are available (Dubosq et al., 2020), namely one thousand isomers for each of the four families of C_{60}, as well as one thousand flake isomers for the smaller C_{24} and C_{42} systems. The RF rate constants obtained through the kMC simulation for these six sets of isomers and for different values of the internal energy are shown in Fig. 3.7 as scattered plots.

For each system, the logarithm of the RF rate constant roughly varies linearly with the first electronic excited state energy at sufficiently high energies, confirming the exponential relation of Eq. (3.11). This exponential behavior is particularly clear in the case of C_{60} cage isomers, for which the RF rate constant was determined at four internal energies, the results being shown in the upper right part of Fig. 3.7. In this case, the linear part in the logarithmic RF rate constant is well established once the electronic energy lies above 0.2 eV. We can correlate the quality of the exponential dependence by performing a linear regression of the logarithmic rate constant for electronic energies in the above range and estimating the corresponding Pearson correlation factor R. At internal energies below 12.4 eV this factor is the range of 53–96%, while it drops to 6% at the higher internal energy considered (Pearson's factor have been computed for data above 0.2 eV).

The slopes of the linear fits of the scatter plots tend to 0 (rates tend to 0) with increasing internal energy, which is explained by the exponential in Eq. (3.11) approaching unity in this regime. Thus, the scatter plots tend to the electronic fluorescence values for very high internal energies.

At lower electronic energies, the strong increase in the RF rate constant reflects the concomitant increase in the electronic oscillator strength. A similar dependence is also predicted for the other electronic states of all isomers, with comparable exponential variations since the slope in logarithmic scale only depends on the size of the system and its internal energy. This behavior is illustrated in the Fig. 3.7b where the RF rate constants obtained for C_{60} cage isomers and excitations on the first or second electronic states are represented against the corresponding energy, at the two internal energies of 0.62 and 6.2 eV: the exponential rate of variations does not depend on the electronic state from which fluorescence originates, but only on internal energy.

The size dependence is better examined by comparing the RF rate constants obtained for the various flake isomers of the three different clusters, for a fixed electronic excitation state and a fixed internal energy. The resulting total RF rate constants determined for such samples of C_{24}, C_{42} and C_{60} are shown in Fig. 3.7(c). From this figure the slope in logarithmic scale is found to decrease with decreasing size (see Eq. (3.11)). However, these slopes do not scale linearly with the term $\frac{g-1}{E+E_z}$, as Eq. (3.11) would suggest. From Fig. 3.7c and Eq. (3.11), the ratios between the slope and the corresponding term $\frac{g-1}{E+E_z}$ vary as 1.14(C_{24}):1.11(C_{42}):1(C_{60}). We interpret this discrepancy as due to the condition $E+E_z \gg E_1$ necessary for Eq. (3.11) but not completely valid for all C_{24} and C_{42} isomers at 1.24 eV internal energy. These ratios tend to unity with the internal energy and at 2.5 eV internal energy they read as 1.08(C_{24}):1.07(C_{42}):1(C_{60}) (see appendix 3 fig. 3.10).

The exponential decay dependence of the RF rate constant from a given electronic level is similar to the energy gap law decay (EGL) encountered in radiationless transitions, which states that the non-radiative (internal conversion or intersystem crossing) rate constant from an upper electronic level to a lower decreases as $e^{-\beta \Delta E}$ with ΔE the energy gap between the two electronic states (Medvedev and Osherov, 1995). Such an exponential dependence originates from the fact that the couplings between the electronic state and the vibronic state of other electronic states are proportional to Franck-Condon factors, which present an exponential decay with the electronic gap (Englman and Jortner, 1970), itself determined by the accepting modes of the vibrational energy reservoir. Here, the origin of the term $e^{-\frac{g-1}{E+E_z}E_1}$ is exactly the same as that of the Boltzmann factor in the canonical framework. The overall internal energy can there be viewed as an energy reservoir by the electronic level being occupied, as long as it is negligible against internal energy. In this case, there is an analogy between the quantity $\frac{E+E_z}{g-1}$ appearing in the exponential decay and the well-known quantity $k_B T$.

Global emission spectra

The effects of isomer diversity can also be examined on their emission spectra resulting from a cascade of successively emitted photons, as modeled using the kinetic Monte Carlo approach described in Sec.3. Following a similar approach as in our previous work (Falvo et al., 2013, 2012) we determined the emission spectra of entire samples of isomers by summing the individual contributions of all their members (independent to

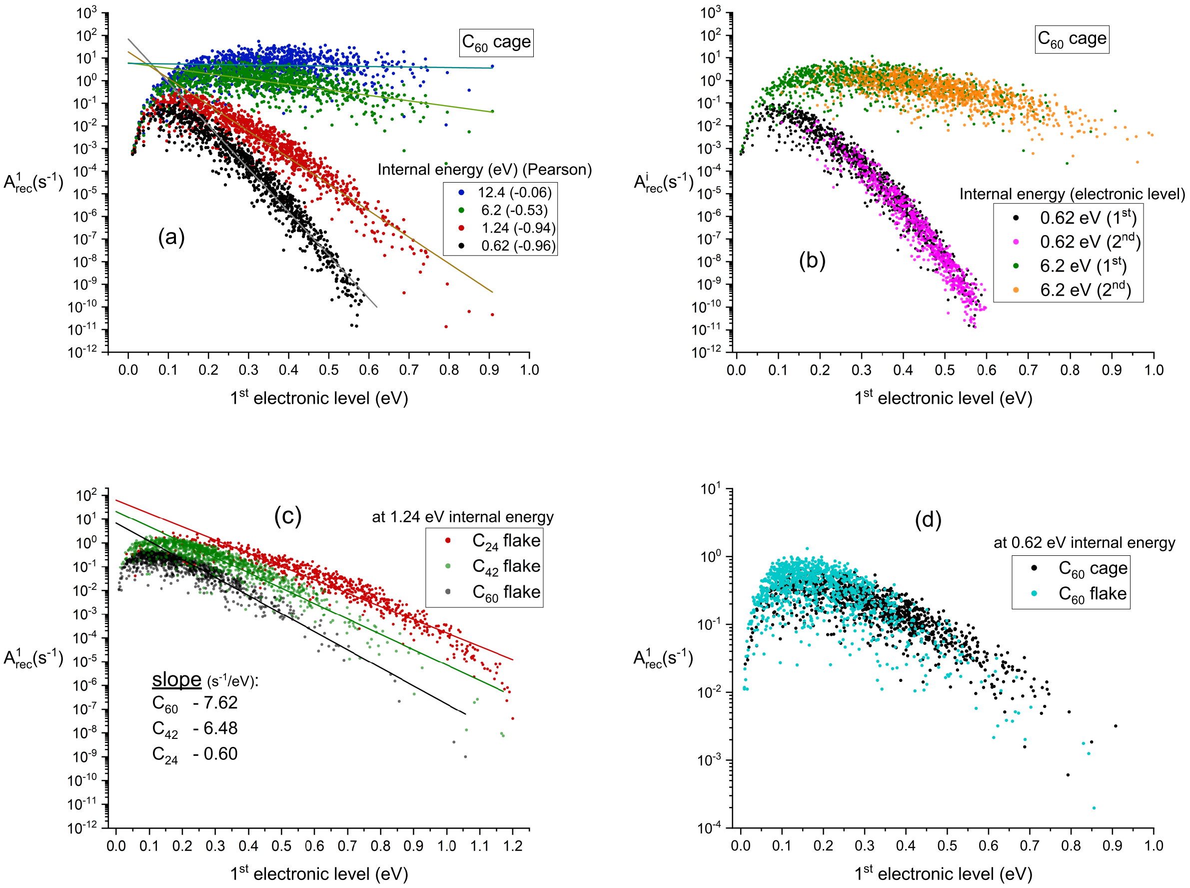

Figure 3.7: (a) RF rate constant at several internal energies. Pearson coefficients were calculated for data above 0.2 eV and corresponding linear fit. (b) RF rate constant from the 1st or 2nd electronic levels in terms of the electronic energy and corresponding linear fit with slope values used in the text. (c) RF rate constant for different sizes of flakes family. (d) recurrent fluorescence (RF) rate constant for two different isomer families. The data are shown for 1000 independent isomers of C_{60} cages and C_{60}, C_{42}, C_{24} flakes.

each other as in gas phase), with uniform weighting. The initial internal energy is the same for each isomer. The emission spectra were determined assuming only vibrational emission, or including also the contribution of recurrent fluorescence.

The upper panels of Fig. 3.8 show the emission spectrum resulting from the sample of 1000 cage isomers of C_{60} excited at 20 000 and 100 000 cm^{-1} energies, respectively. The RF spectra span a broad range of wavenumbers, usually starting around 500 cm^{-1}, and overlap with the VE spectra. RF seems also rather weak compared to VE in the region where VE dominates (below 2000 cm^{-1}), which could seem somewhat contradictory with our earlier conclusion that RF efficiency is significant, especially at the higher internal energy considered. However, it is important to recognize that the density of vibrational states is much higher than the corresponding density of electronic states in the overlap region, and this effect is further magnified by the statistical averaging over the 1000 isomers (Figs. 3.11, 3.12, and 3.13), which leads to a nearly continuous distribution of vibrational modes in the 0–2000 cm^{-1} range, while the electronic states are much fewer and fall into much narrower distributions. Moreover, once VE becomes significant it quickly drains internal energy away from the system and quenches the possibility of RF, making it even less likely.

These processes contribute to partitioning the overall emission spectra into showing a rather narrow overlapping region between the two ranges in which either of the two processes is clearly dominant. At both internal energies, the overall RF spectral profile shows a bell shaped profile with an extended high frequency wing. The sharp increase at low electronic energy is due to the square dependence of electronic fluorescence rate constant on electronic energy expressed in Eq. (3.4) and to the increase of the electronic density of states (Figs. 3.11, 3.12, and 3.13). The decrease at high energies is found to be exponential, and can be essentially understood from the EGP law type behavior of the RF rates, even though the global spectrum obtained here results from an emission cascade and the contribution from multiple isomers.

The global emission spectra obtained for the other structural families of C_{60} are depicted in the lower part of Fig. 3.8, at the same two internal energies of 2.5 and 12.4 eV, and together with the spectra discussed above for the cages isomers. For the other three families, a vibrational emission band is seen above 2000 cm^{-1}, as originating from chains of sp^1 carbon atoms that are mostly absent in the cages. Broad bands found between 1600 cm^{-1} and 1000 cm^{-1} are essentially due to CC stretching modes possibly overlapping with CCC bending modes near 1000 cm^{-1} (Dubosq et al., 2019). Broad bands around 600 cm^{-1} involve CCC in-plane and out-of-plane bending modes associated with stronger deformation of the overall structures (Dubosq et al., 2019).

At 2.5 eV initial internal energy, the RF component of the global emission spectrum is not very strong for all the four structural families, especially for pretzels and branched isomers. This is consistent with our earlier observation in Fig. 3.4 that these structures have a particularly low RF efficiency. At 12.4 eV, the contribution of RF to the global spectrum is much stronger and affects the entire spectral range for all families. As the internal energy increases, the band ratios thus also vary as the result of the increasing importance of recurrent fluorescence. This effect is more pronounced for high frequency modes, which can be interpreted by the high energy approximation of Eq. (3.10):

$$A_i(E) = A_i^{1\to 0}\frac{E}{g\hbar\omega_i} \propto \omega_i I_i \frac{E}{g}.$$

The influence of RF processes on the VE emission spectra thus amounts to inhibitting emission from high vibrational frequency modes, where the competition with the low-lying electronic states is the strongest. High frequency vibrational modes are therefore less likely to emit photons when RF is accounted for, which precisely matches our computational results.

Concluding remarks

Upon their initial excitation, large carbon clusters may relax through recurrent fluorescence and vibrational emission processes, whose relative efficiency was found here to depend on a number of factors. The present work aimed at elucidating this dependence by means of dedicated modeling, systematically addressing the roles of cluster size, structural features, and the excess energy itself.

For the present clusters containing several tens of carbon atoms, recurrent fluorescence was generally found to become of importance as soon as the internal energy exceeds about 10 000 cm^{-1}, even dominating over vibrational emission above 100 000 cm^{-1}. The very high efficiency of recurrent fluorescence identified at high internal energies is not only due to the appreciable occupation of excited electronic states but also to their significant electronic oscillator strength, which is typically two or three orders of magnitude larger than vibrational intensities.

At low or moderate internal energies, a significant dependence of recurrent fluorescence efficiency on the structural family was also found, such electronic processes being more exacerbated for flakes owing to their low-lying electronic states. Cages also show a higher RF efficiency, but as the result of their lower vibrational activity. The size dependence of recurrent fluorescence is also substantial at low internal energies (below 7.4 eV), in relation with their lesser ability to store vibrational energy.

From the spectral viewpoint, the recurrent fluorescence spectra obtained from an emission cascade is constituted of a main emission band that becomes increasingly broad

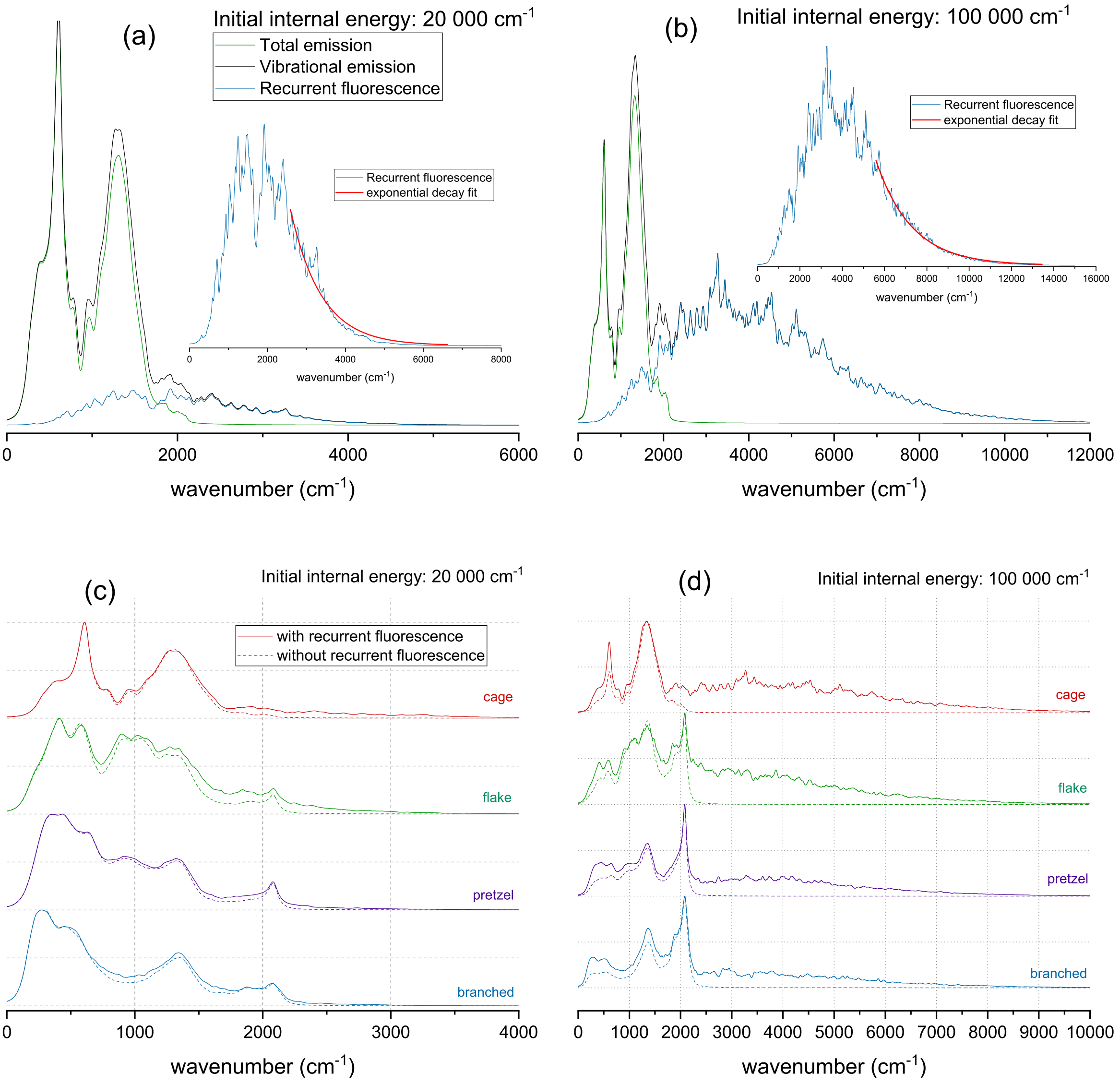

Figure 3.8: (a) and (b): Normalized emission intensity spectra from one thousand C_{60} cage isomers with 2.5 and 12.4 eV initial internal energy. Contribution from recurrent fluorescence and vibrational emission are also displayed. The inset highlights the exponential fit for the recurrent fluorescence component. (c) and (d): Normalized emission intensity spectra from one thousand C_{60} isomers for each family. Spectra in dashed lines (resp. solid lines) are those without (resp. with) recurrent fluorescence taken into account over the relaxation cascade.

with increasing internal energy. The intensity increase in the RF spectrum at low energies originates from the concomitant increase in the spontaneous emission propensity with electronic transition energy, given that these states are appreciably occupied. Similarly, the decrease at high energies results from the exponentially decaying occupation probabilities.

When considering populations of isomers, the recurrent fluorescence rate constant from a given electronic state was found to follow a behavior similar to the energy gap law decay in radiationless transitions. This was interpreted as resulting from the numerous degrees of freedom in the present clusters, whose vibrational energy distribution is perceived as a statistical reservoir from the perspective of an electronic excitation. Recurrent fluorescence has also a noticeable influence on vibrational emission spectra by inhibiting high vibrational frequency modes. In this spectral region, recurrent fluorescence tends to attenuate the band ratio between high and low frequency vibrational mode.

Expanding the scope of this work, we expect that recurrent fluorescence could be detected in environments where large carbon clusters are known to be highly vibrationally excited, as in hot environments or when exposed to UV irradiation. In the interstellar medium, UV irradiation is sufficiently harsh to induce recurrent fluorescence on neighboring large carbon clusters and make them emit in the near-IR/visible range. Recurrent fluorescence could then have an influence on the vibrational emission spectra, especially on the continuum emission lying below the Aromatic Infrared Bands. In flames or soot-formation environments, where temperatures reach or exceed 2000 K and recurrent fluorescence originating from such highly excited systems could be detected in the visible range by techniques such as laser-induced incandescence.

Acknowledgements

This work has been supported by ANR project PACHYNO (ANR-16-CE29-0025).

Appendix

Electronic density of states for the six chosen isomers

Fig. 3.9 shows the electronic density of states of the six selected isomers. At considered internal energies (< 18.5 eV), the energy of the occupied electronic states does not exceed 2 eV ($\approx 16\,000$ cm^{-1}). Below 2 eV, it is reasonable to consider that the electronic density of states is similar for all C_{60} isomers, except for cages beyond 10 000 cm^{-1} (1.24 eV). As expected, the electronic density of states is lower for smaller isomers.

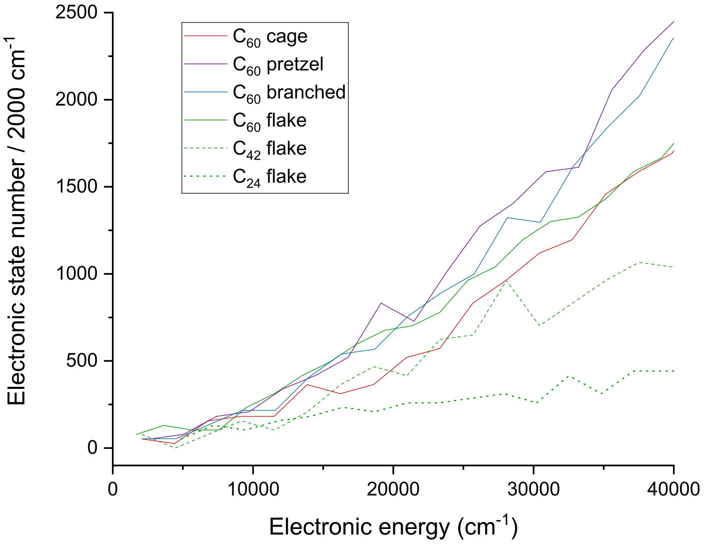

Figure 3.9: Number of electronic excited states per 2000 cm^{-1} electronic energy for the six chosen isomers.

A^1_{rec} at 20 000 cm^{-1} for flake isomers

Figure 3.10 displays recurrent fluorescence from the first excited electronic states for C_{24}, C_{42} and C_{60} flake isomers at 20 000 cm^{-1} internal energy. The ratio between linear fit slopes and the corresponding quantity $\frac{g-1}{E+E_z}$ are in the ratios 1.08 (C_{24}):1.07 (C_{42}):1 (C_{60}).

Electronic and vibrational density of states

Figures 3.11, 3.12 and 3.13 show electronic and vibrational density of states over a large set of isomers (about 1000 thousand) for cage, flake, pretzel and branched families and C_{24}, C_{42} and C_{60}. Occupied electronic states do not appreciably exceed 30th electronic excited states which is usually below 2 eV.

Supplementary result: Exponential decay profile of emission spectra from a whole relaxation cascade

We saw in the previous work that an exponential decay appears in the emission spectrum obtained from a whole radiative relaxation cascade. The exponential decay is explicitly shown in panel a and b of figure 3.8 but it actually also appears in all spectra of panel c and d. This result does not seem intuitive and we proposed here to justify this emission profile. Here, the part of emission spectrum that we are interested in involves only the

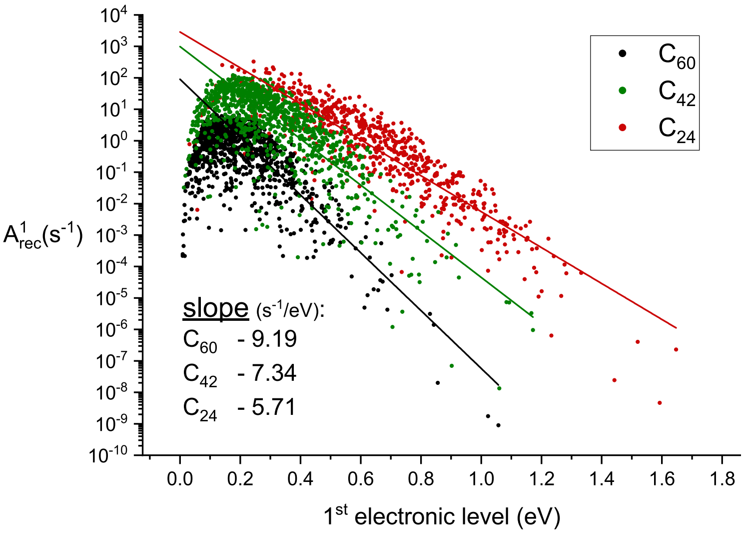

Figure 3.10: Recurrent fluorescence rate constant from the 1st excited electronic of 1000 flake isomers of C_{24}, C_{42} and C_{60} excited at 2.48 eV ($= 20000\ \text{cm}^{-1}$). The linear fit was performed for electronic energies above 0.2 eV ($= 1500\ \text{cm}^{-1}$).

recurrent fluorescence which is written, for $E + E_z \gg h\nu$, by

$$A_{rec}(\nu) = K\nu^3 e^{-\frac{g-1}{E}\nu} \tag{3.12}$$

g is the vibrational degree of freedom, E the internal energy, ν the emitted photon frequency and K a proportionality constant. The $K\nu^3$ term is related to the spontaneous emission and the exponential term is the probability to occupy an electronic state of energy $h\nu$. The interesting quantity for our purpose is the emission intensity $\mathscr{I}$ obtained after integration over the whole radiative relaxation. We know that

$$\mathscr{I}(\nu) \propto h\nu \int_0^{E_{\text{ini}}} A_{rec}(\nu) dE \tag{3.13}$$

with E_{ini} the initial internal energy (exciting photon energy). Thus, we have to calculate the following integral

$$\int_0^{E_{\text{ini}}} e^{-\frac{g-1}{E}\nu} dE \tag{3.14}$$

which is also written as (by means of three integration by parts)

$$\mathscr{I}(\nu) \propto h\nu \times K\nu^3 E_{\text{ini}} \times E_2(\alpha) \tag{3.15}$$

$$\text{with } E_2(\alpha) = \int_1^{\infty} \frac{e^{-\alpha x}}{x^2} dx$$

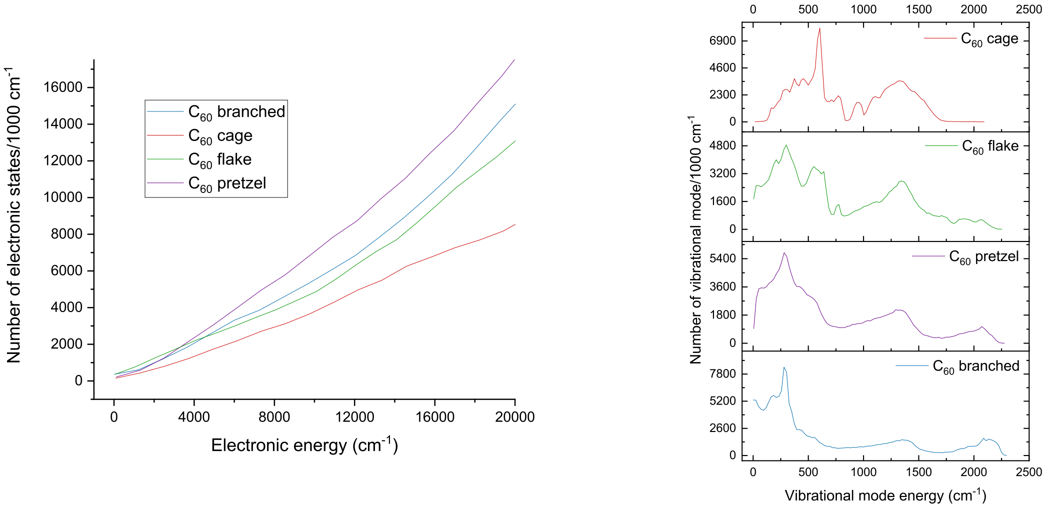

Figure 3.11: Electronic (left panel) and vibrational (right panel) density of states over a large set of C_{60} isomers for each family.

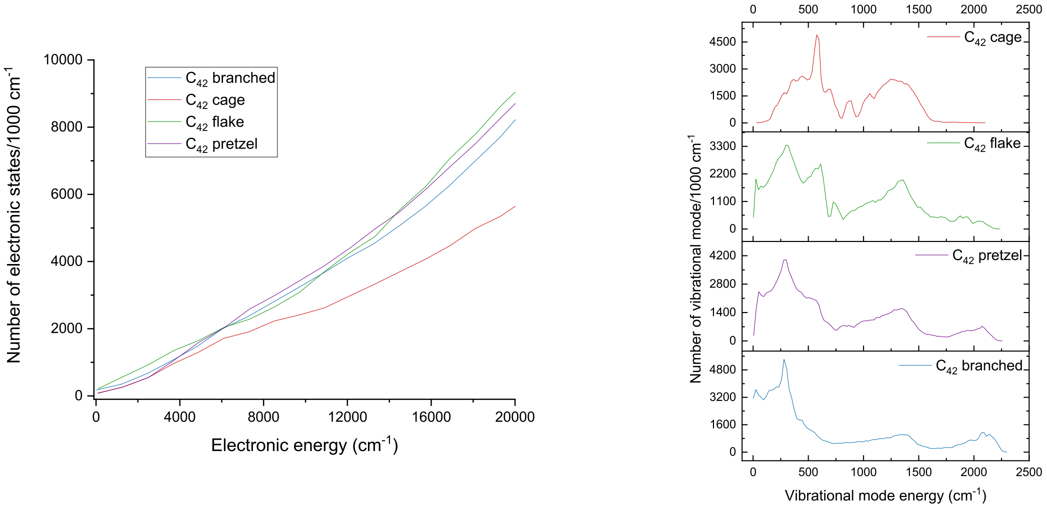

Figure 3.12: Electronic (left panel) and vibrational (right panel) density of states over a large set of C_{42} isomers for each family.

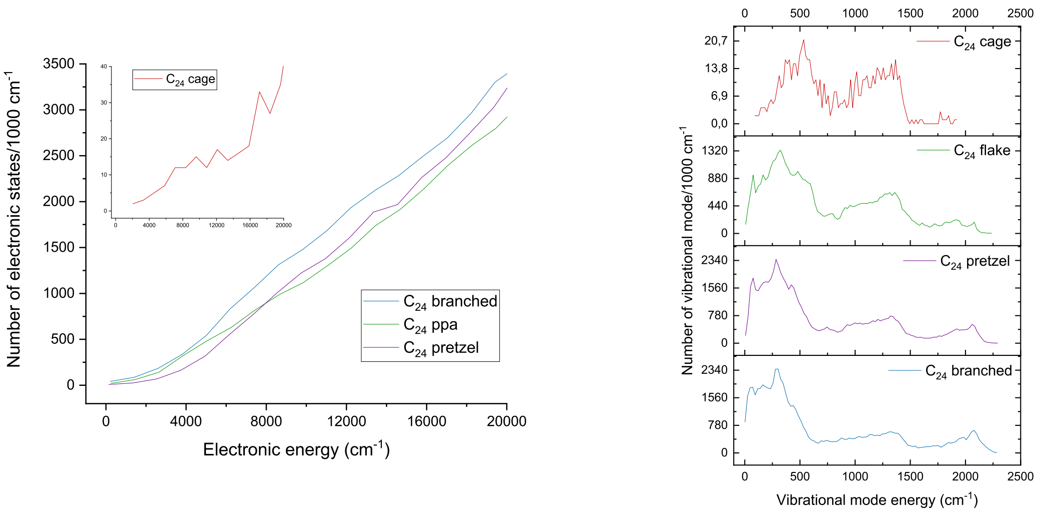

Figure 3.13: Electronic (left panel) and vibrational (right panel) density of states over a large set of C$_{24}$ isomers for each family. There is only 11 isomers for C$_{24}$ cages.

with $\alpha = \frac{(g-1)}{E_{\text{ini}}}\nu$. The integral E_2 is a function of α and there is no analytical solution. This is why we drew the E$_2$ function thanks to tables of values in Abramowitz and Stegun (1964). We see in figure (3.14) that we can approximate the E$_2$ decreasing to an exponential decay, which would justify the exponential decay of the emission spectra (figure 3.8). These emission spectra decays as the exponential of (g-1)ν/E.

Emission spectra decrease as ν because the occupation probability decreases with the electronic state energy. Emission spectra decrease with the number of vibrational modes g. Indeed, the more the molecule can contain internal energy in vibrational degrees of freedom, the less there will be energy in electronic excitation. Emission spectra increases when the initial energy is higher because the occupation probability of excited electronic states increases with the internal energy. Moreover, the E$_{\text{ini}}$ term also appears in $\mathscr{I}(\nu)$ expression which increases proportionally to E$_{\text{ini}}$.

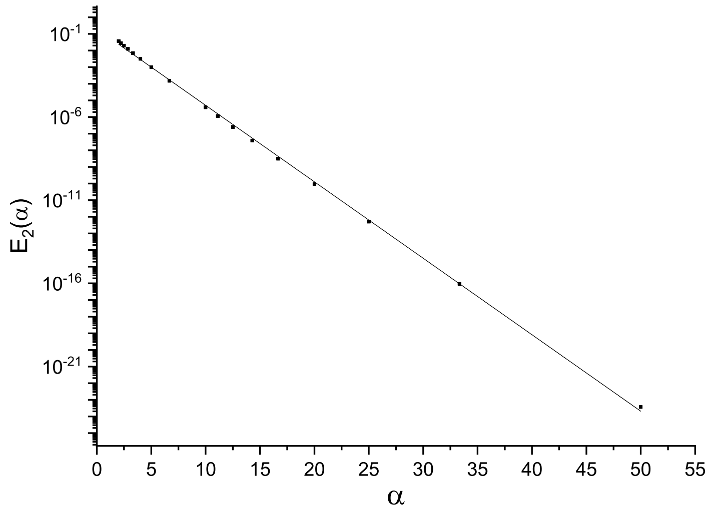

Figure 3.14: $E_2(\alpha)$ in terms of α in semi-log scale. This indicates that E_2 can be approximated to an exponential decay (at least for $\alpha > 1$).

Infrared emission of $C_{n=24,42,60}$ carbon clusters induced by stochastic heating

In this second work, we are interested in the first goal of the theoretical part of the thesis. What would be the emission of the carbon clusters C_{24}, C_{42} and C_{60} when they are irradiated by a 20 000 K stellar-like spectral energy distribution or by the interstellar radiation field ? By means of a computational trick, it has been possible to simulate the emission spectrum obtained from radiative cooling of a large set of carbon clusters. The modeling is the same as in the previous work. These emission spectra have been simulated for each size and each family of carbon clusters. We were particularly interested in the emission in the near infrared (between 1 and 5 µm). To our knowledge, only K.Sellgren's observations Sellgren (1984) present emission spectra in this wavelength range. We found in Onaka et al. (2018) spectra up to 3 µm but useless for our work. From K.Sellgren's observations, we deduced that mainly cage-form carbon clusters could be at the origin of near-IR emission. Among the three investigated sizes, C_{60} emission best matches the observed spectra. We therefore conclude that if the emission observed between 1 and 5 µm in NGC 7023 (reflection nebula) is due to recurrent fluorescence of C_{60} cages, then 0.1% of the carbon in the region must be contained in these C_{60} cages (in other words, their volume density should be around 10^{-3} cm^{-3}). We also came to the conclusion that C_{24} could not explain the extended red emission (ERE) observed in several interstellar regions. Although the near-IR and visible emission profile of C_{24}

shows a profile similar to the ERE, it is clearly redshifted and much broader.

Our guest member of the jury, Dr. Louis Le Sergeant D'Hendecourt, has very kindly written a short historical review on the astrophysical part of this PhD work. Dr. Louis Le Sergeant d'Hendecourt has been one of the co-authors (along with Dr. Alain Léger and Prof. Pierre Boissel) to introduced the Poincaré fluorescence as a new emission mechanism from PAHs molecules (Léger et al., 1988). With his kind permission, we incorporated its historical review in this thesis.

Short historical review from Louis Le Sergeant d'Hendecourt

The 1984 paper by Léger and Puget in A&A Letters, **137**, L5 is reaching now almost 1500 citations, quite a record for such a paper on one property of the ISM, namely the widespread observations of the so-called unidentified infrared emission bands (UIR). Remember that in 1983, and confirmed in 84, K. Sellgren (ApJ. Letters **271**, 13 (1983) and ApJ. **277**, 623 (1984)) had shown that these UIR bands were recorded on top of a strong 1000 K blackbody-like emission of unknown origin.

This rather complete and, visionary and prophetic Léger and Puget's paper does identify the UIR bands with vibrational fundamental bands of Polycyclic Aromatic Molecules taking the coronene molecule ($C_{24}H_{12}$) as a model. Note that, to the first order, each band of this set (3.3, 6.2, 7.7, 8.6 and 11.3 µm) are identified with a particular fundamental vibrational mode (stretching, bending, wagging) of a collection of Polycyclic Aromatic Molecules, the famous PAHs.

Stochastic heating of very small grains (actually large carbon molecules), up to 600 – 1000 K from a single ultraviolet photon does provide the excitation mechanism.

Relaxation via vibrational infrared fluorescence from the ground electronic state (when molecules are considered) provides for the observed UIR bands with the relatively correct expected position as well as an explanation for the bands position in terms of molecular motions (fundamentals vibrations).

Partial hydrogen coverage is deduced from the band position of the 11.3 micron bending mode that lies precisely at 11.9 in coronene where hydrogen atoms are grouped two by two at the periphery of the molecule. Where other geometry can be considered for other molecules, trios-H give rise to a 12.3 µm band when solos-H gives correctly a 11.3 µm position.

Approaching the problem from the grain sizes side, as any astronomer at this time was doing (graphitic grains and C–H peripheral bonds), as well as C=C sp^2 stretch (a well-known vibration of graphite), classical graphitic grain sizes are not transparent (are opaque) to IR radiation rendering these transitions impossible to be observed. Thus,

much tinier grains are necessary (i) to attain very high temperatures and excite the vibrational bands (ii) to render these grains "transparent" to radiation. Thus such tiny grains should be no larger than molecules (actually, much larger than the ones currently observed in radio astronomy).
The concept of photo-thermo stability is introduced leading to minimal sizes in the ISM compatible with coronene or slightly larger molecules (a typical order of magnitude is given to be around 40 atoms).
The number of carbon atoms in the carriers is calculated to be at most 50 carbon atoms per molecule (by equating the heat capacity of a typical carrier with the absorbed UV photon energy and the need for an emission T of around 1000 K).
In the objects of interest (mostly a planetary nebula, NGC 7027) a tentative abundance for such molecules is calculated to be between 1.5 and 6 % of the cosmic carbon (by comparing the plausible UV absorption of such molecules with the IR emission energy emitted in the bands, assuming an approximate band strength from existing molecular data) as well as scaling to the total IR emission in different objects.
It is speculated that pre-graphitic molecules (PAHs) might be rather abundant in the diffuse ISM and thus account for many "unrelated" observations such as the well-known 2200 Å absorption band in the UV (usually attributed to graphite), the extent of the objects in which the UIR are observed and even the Extended Red Emission (often associated with the UIR bands).
The next paper in 1985 by Puget, Léger and Boulanger (in A&A Letters, **142**, L19) will propose that Cirrus clouds just discovered by IRAS at 100 microns in the diffuse ISM may also emit at 12 µm (and possibly 25) because of the 11.3 µm band possibly present in the diffuse ISM as well as the presence of other PAH emission bands further in the spectra of PAHs. This emission at 12 and 25 microns will be indeed discovered by Boulanger, Baud and van Albada at the end of 1985 (again in A&A letters **144**, 9). The detection of the 3.3 µm emission line in the diffuse ISM will be discovered 3 years later from a dedicated balloon observation (the Arome experiment) by Giard et al (A&A Letters, **201**, 1).

All this making a very coherent story starting in the 1984 paper by Léger and Puget. But, the Sellgren's continuum (a blackbody at 1000 K) has never been explained by this model to the notable despair of Alain Léger. Molecular description of excited states of molecules where absorption of a UV photon is treated as an absorption by discrete molecular levels and within different states of different multiplicities (S_n or D_n) finally prompted the paper by Léger, d'Hendecourt and Boissel in 1988 in Phys. Rev. Letters, **60**, 921, where the inverse fluorescence or Poincaré fluorescence (or also recurrent fluorescence) was proposed on the basis of calculations, less developed than the ones presented by Ozan Lacinbala and colleagues in this thesis but nevertheless considering the correct mechanism for this inverse fluorescence mechanism: in a collisionless medium (such as in the ISM), the de-excitation in the lowest electronic state is done only by the slow process of infrared emission. Therefore the molecule may retransfer this energy to the first electronic state and then cools by an electronic transition, thus an inverse fluorescence mechanism.

However, the Poincaré fluorescence was mostly proposed to account for the ERE (Extended Red Emission) particularly observed in the Red Rectangle where UIBs are easily observed. This is thanks to the Jablonski's diagram (Figure 2.1 in the thesis), which somewhat wrongly puts the Poincaré fluorescence (because of the representation of the excited levels) much more in the visible part of the spectrum (as well as because classical fluorescence and phosphorescence of some PAHs was known to be in the visible part of the spectrum). So from the idea of the Poincaré fluorescence, the authors did not go further on this activity from a lack of experiment and returning to more astrophysical significance of the UIR bands that later would be called.

To my opinion the major and most fundamental result of Lacinbala's thesis, especially for astronomical observations, is to use the Poincaré fluorescence to provide for the continuum at 1000 K blackbody emission from Sellgren which still remains a complete mystery in the community. Not only is this hypothesis well sounded in this present work (and the paper proposed to be submitted to A&A) but its description implies (to my modest knowledge), that, following IVR within the lower electronic state and inverse system crossing to the first upper electronic state, these many levels (in both states S_0 and S_1) should be occupied according to a Boltzmann distribution, thus the re-emission from the electronic excited state is logically one of a blackbody emission. If this is correct then, Poincaré fluorescence might explain the Sellgren's continuum but evidently not the ERE in the visible because the spectrum of the ERE is not the one of a blackbody. Thus another explanation for the ERE should be found. Note that, on the contrary to the main ideas on the ERE, this phenomenon is indeed present on the extinction curve in the form of the VBBS (Very Broad Band Structure) interpreted as a reduction in extinction curve by Mayo Greenberg in the 70's. If the ERE is indeed an emission within the diffuse ISM such as the 12 micron emission from Cirrus is... then it is of prime importance to obtain some explanation for its origin. But again, the origin of Sellgren's continuum seems finally understood by a phenomenon first described in a paper in 1988 where the lead is again... Alain Léger himself. Congrats for this piece of work which may deserve more recognition soon, for example by changing the title of the present would be paper to A&A Letters (again !) accordingly to something like "A plausible explanation for the strong infrared emission continuum in reflexion nebulae: the Poincaré fluorescence". I would also suggest to try to submit this paper (with this title in a high impact journal like Nature Astronomy because it could be a major breakthrough in our understanding of a key observation of the interstellar medium, linked to a very specific molecular phenomenon, probably unique in the ISM, the Poincaré fluorescence.

Louis Le Sergeant d'Hendecourt , Marseille, 5th October 2021

Introduction

Insight in spectroscopy and chemistry of interstellar matter allows to better understand the lifecyle of matter in galaxies and ultimately galaxies themselves. In that sense, carbonaceous and silicate dust grains, very small grains and PAH-like molecules are among the key features to understand emission in the visible, near, mid and far-IR wavelength range. From such observations, valuable information about the local interstellar medium (ISM) can be extracted via diagnostic tools such as the correlation between the star formation rate and the mid-IR emission of PAHs Peeters et al. (2004); Shipley et al. (2016). We can also infer physical conditions from certain aromatic infrared bands ratios Berné et al. (2009a,b); Pilleri et al. (2012); Stock et al. (2016). An interesting subset of carbonaceous interstellar matter are large carbon clusters for which there is growing interest since the detection of the C_{60} buckminsterfullerene in interstellar and circumstellar environments Cami et al. (2010); Sellgren et al. (2010); Zhang and Kwok (2011b); Berné et al. (2017), although presence of fullerenes was suggested 30 years ago Kroto et al. (1985). The formation mechanism of these large molecules in the ISM is the so-called top-down mechanism in which they are formed by shrinking of dehydrogenated PAHs Berné and Tielens (2012); Berné et al. (2015). A bottom-up mechanism has been suggested (closed network growth mechanism), more suitable in carbon stars or supernovae environments Dunk et al. (2012a). From a spectroscopical viewpoint, fullerenes (also fulleranes) are highly suspected to contribute to the well-known 2175 Å UV-bump Malloci et al. (2008); Dubosq et al. (2020) and diffuse interstellar bands Cami (2014).

In our study, we are interested in the fluorescence induced by photon absorption of C_n (n= 60, 42, 24) carbon clusters (fullerenes are a subset of carbon clusters). Our study relies on a large set of carbon clusters and the general idea is to compute the emission spectra under ISM conditions, namely the overall radiative relaxation of each isolated carbon cluster irradiated by a 20 000 K star-like spectrum or by the standard interstellar radiation field (ISRF, χ=1). We have extracted carbon cluster isomers from Bonnin et al. (2019) in which carbon clusters have been generated by exploring the conformational landscapes, using molecular dynamics methods and quenching system.

Carbon clusters are classified according to their overall shape: branched, cage, flake and pretzels. We have around one thousand isomers for each family and each size (C_{60}, C_{42}, C_{24}). Vibrational and electronic structures of all these isomers have been computed by SCC-DFTB method Dubosq et al. (2019, 2020).
After getting electronically excited by a stellar photon, carbon clusters undergo very rapidly several internal conversions (IC, $\sim 10^{-14} - 10^{-8}$ s) or intersystem crossing (ISC, $\sim 10^{-10} - 10^{-7}$ s) Birks (1970b); Medvedev and Osherov (1995); Ermolaev (2001) to finally reach the ground electronic state. Electronic fluorescence is considered to be quenched by IC and ISC. the exciting photon energy is then entirely converted into vibrational motion in the ground electronic state (we neglect rotational energy in our study) and then radiative cooling starts via vibrational emission (VE, $\sim 10^{1} - 10^{-2}$ s). In addition to VE, we also have another radiative relaxation pathway due to highly isolated conditions of large carbon clusters in the ISM and their particularly low-lying excited electronic states ($\sim$ 0.3 eV for the first ones Dubosq et al. (2020)). Indeed, large carbon clusters undergo also inverse internal conversion (IIC, $\sim 10^{-10} - 10^{-4}$ s) Baba et al. (1971); Chihara and Baba (1977); Nitzan and Jortner (1978, 1979); Itoh (2012) which is much faster than VE. Then, during the radiative cooling (via VE), electrons can be excited and large carbon clusters can undergo electronic de-excitation. However, this process is different from electronic fluorescence because the electronic excited states occupation probabilities are dependent on the internal energy. We talk about *recurrent fluorescence* (RF, also named *Poincaré fluorescence*) Léger et al. (1988) and several experiments have reported its observation for small species such as C_6^- Ebara et al. (2016); Ito et al. (2014), C_6H^- Ito et al. (2014), naphthalene cation Saito et al. (2020b) and anthracene cation Martin et al. (2013). C_6H^-).

Methods

Because intramolecular vibrational redistribution (IVR,$\sim 10^{-10} - 10^{-7}$ s) Parmenter (1982); Quack (1990); Medvedev and Osherov (1995); Nesbitt and Field (1996), IC/IIC ($\sim 10^{-14} - 10^{-8}$ s) and ISC ($\sim 10^{-10} - 10^{-7}$ s) are considered as very rapid compared to other relaxation pathways (vibrational and recurrent fluorescence, isomerisation, dissociation), we can assume that the vibrational energy is statistically distributed among all states of all accessible electronic states at every moment of the radiative relaxation. After each spontaneous emission (VE or RF), statistical equilibrium is always reached very quickly. That allows us to compute RF and VE rates in the microcanonical framework (isolated and equilibrium conditions). We calculate probabilities by an exact calculation of the vibrational density of states Beyer and Swinehart (1973). Then, by a kinetic Monte-Carlo method, the emission spectrum from the overall radiative cooling is com-

puted.
In this work, large carbon clusters are irradiated by two spectral energy distribution (SED), a 20 000 K blackbody (simulating a 20 000 K star) and the standard ISRF. Exciting and computing the cooling relaxation for all photon excitation of the SED is very CPU time consuming. Instead, we compute only the radiative relaxation induced by the maximum energy photon excitation of the SED and from that we can deduce, as described below, carbon clusters emission spectra irradiated by a given SED. In this work, we take 20 000 K blackbody or the $\chi = 1$ ISRF as SEDs (see appendix).

Defining $n_{\mathrm{E}_{max}}(\nu,E)$ as the photon number of frequency ν emitted by a carbon cluster isomer at internal energy E given that the exciting photon energy is E_{max}, the total emitted photon number of frequency ν during all the radiative cooling is

$$N_{\mathrm{E}_{max}}(\nu) = \int_0^{\mathrm{E}_{max}} n_{\mathrm{E}_{max}}(\nu,E)dE \tag{3.16}$$

From this quantity, we obtain the emission spectrum of the overall radiative cooling process after excitation of carbon clusters by a E_{max} energy photon.
Considering IVR implies that emission (both vibrational and recurrent) at a given internal energy is independent of the previous photon emission during the radiative cooling cascade. By computing the emission spectra of the radiative cooling induced by the maximum photon energy E_{max} of the SED, we actually also calculate the emission at all internal energies E lower than E_{max}. Thus, by means of a specific sum, we may determine the emission spectrum obtained by the SED excitation from the known emission spectra at all E. All we have to do is to compute, by a kinetic Monte-Carlo method, the photon number emission $n_{\mathrm{E_{max}}}(\nu,E)$ at internal energy E when excited by a $\mathrm{E_{max}}$ photon and then deduce the $N(\nu)$ photon number emitted for each frequency ν when excited by a SED.
If we take a SED containing two photon energy $\mathrm{E}_1 > \mathrm{E}_2$ (with their respective electronic cross-section σ_1 and σ_2) and respectively α_1 and α_2 photon number density per unit volume, the emitted $\mathrm{N}(\nu)$ relative photon number is expressed as:

$$N(\nu) \propto \int_0^{E_1} n_{\mathrm{E}_1}(\nu,E)\alpha_1\sigma_1 dE + \int_0^{E_2} n_{\mathrm{E}_1}(\nu,E)\alpha_2\sigma_2 dE \tag{3.17}$$

We underline that n_{E_1} is involve in both integrals. Then,

$$N(\nu) \propto \int_0^{E_1} n_{\mathrm{E}_1}(\nu,E)K(E)dE \tag{3.18}$$

with

$$K(E) = \begin{cases} \alpha_1\sigma_1 & \text{for } E > E_1, \qquad (3.19) \\ \alpha_1\sigma_1 + \alpha_2\sigma_2 & \text{for } E \leq E_2. \qquad (3.20) \end{cases}$$

For a more complicated SED $u(E';T)$ (with E' the photon energy and T the temperature of the exciting source), we generalize the relation (3.18) by

$$N(\nu) \propto \int_0^{E_{max}} n_{\mathrm{E}_{max}}(\nu{,}E) K(E) dE \qquad (3.21)$$

$$\text{with } K(E) = \int_E^{E_{max}} \frac{u(E';T)}{\nu} \sigma(E') dE' \qquad (3.22)$$

The quantity $\frac{u(\nu;E)}{h\nu}$ is the spectral photon number density per unit volume and $\sigma(E)$ the electronic absorption cross section of the large set of carbon clusters. The product of these two quantities gives the relative abundance of effectively exciting photons of frequency ν. See the appendix for a typical internal energy dependence of the $K(E)$ quantity.

However, the expression (3.21) leads to errors in the $N(\nu)$ emission spectra at low internal energy because of computational artifacts. In principle, the radiative cooling does not depend on its history and this property is at the origin of our calculation trick. But, from a computational viewpoint, this is not entirely true because there is a slight difference in the emission at low internal energies ($<$ 15 000 cm^{-1}) depending on the initial internal energy. Indeed, the mean kMC trajectory is obtained by calculating the mean step of the kinetic Monte-Carlo over the 10^5 trajectories. Yet, the kMC step number (wide of energy bins) below 15 000 cm^{-1} internal energy is highly dependent of the initial internal energy and there are less kMC step numbers (wider energy bins) for lower initial internal energies. We estimated that the relative error on the photon number for recurrent and vibrational fluorescence is less than 5 % (see the appendix for more details and the error estimation).

Electronically excited carbon clusters can also dissociate, isomerize and ionize. Given that we take a flat population distribution within each cluster family, we put aside isomerization. We do not have any information about ionization of each individual carbon clusters. This is why we suppose that ionization occurs at 7.5 eV for C_{60} isomers (that of C_{60} buckminsterfullerene) De Vries et al. (1992) and we arbitrarily choose slightly larger ionization barrier for smaller isomers, namely 8 eV for C_{42} and 8.5 eV for C_{24}. Thus, we add a cutoff in the SED to encode the ionization process in our simulation. We do not take into account emission from cation carbon clusters. C_2 dissociation for C_{60} is negligible at internal energies below 7.5 eV internal energy Lifshitz (2000b). A crude RRK calculation show that dissociation is also negligible for C_{42} and C_{24} below 8.5 eV internal energy.

Results

Emission spectra from C_{60} cage carbon clusters irradiated by a 20 000 K blackbody stellar-like spectrum are displayed in figure 3.15. The emission broad bands below 2000 cm^{-1} are essentially due to VE whereas decreasing emission above 2000 cm^{-1} is exclusively due to RF. During the radiative cooling, there is a competition between these two main relaxation pathways and the RF efficiency increases with internal energy, decreases with the isomer size and is dependent of carbon clusters families. This competition has been extensively studied in our previous work. Usually, RF is prevailing above 20 000 cm^{-1} internal energy but it appears from figure 3.15 that VE is more intense than RF. The vibrational emission bands are more intense because of the smaller dispersion of the vibrational bands compared to the electronic transitions over the large set of C_{60} cage carbon clusters. Indeed, for each isomers, the 174 vibrational normal modes are localized below 2000 cm^{-1} in constrast to electronic states. That makes vibrational broad bands stronger than the RF part of the spectra because of the overlapping of all vibrational lorentzian peaks. The VE part is also stronger for other families (figure 3.16) and the VE spectrum are usually dependent of the family (figure 3.16), however the RF spectra have always the overall shape of a blackbody-like emission.

Figure 3.16 and 3.17 display emission spectra from the four families of C_{60}, C_{42} and C_{24} carbon clusters irradiated by a 20 000 K star or the standard interstellar radiation field (χ=1). In order to see the RF influence on vibrational band ratios, emission spectra computed without RF during the relaxation (only VE has been taken into account) are displayed in dotted lines. As shown figure 3.17, the maximum of the RF part ($< 5\ \mu$m) is blueshifted when the isomers are smaller. We unambiguously see the size effect in C_{24} pretzel and flakes isomers emission spectra for which the maximum of the RF part of the spectra is below 2 μm (figure 3.17). Indeed, at the same initial internal energy (absorbed photon energy), the energy per vibrational degree of freedom reached is higher for smaller carbon clusters.

In figure 3.16, we see there are noticeable differences in the relative intensity of VE bands according to the SED. These variations are important for C_{60} carbon clusters and are weaker for smaller clusters (C_{42}). There is no difference for C_{24} carbon clusters. For irradiation by the standard ISRF, the relative intensity of low-frequency bands are stronger than in the case of 20 000 K blackbody irradiation. Indeed, the blackbody radiation at 20 000 K is more extended from a spectral viewpoint than that of the standard ISRF (χ = 1) (see appendix). Namely, the average ISRF has a maximum

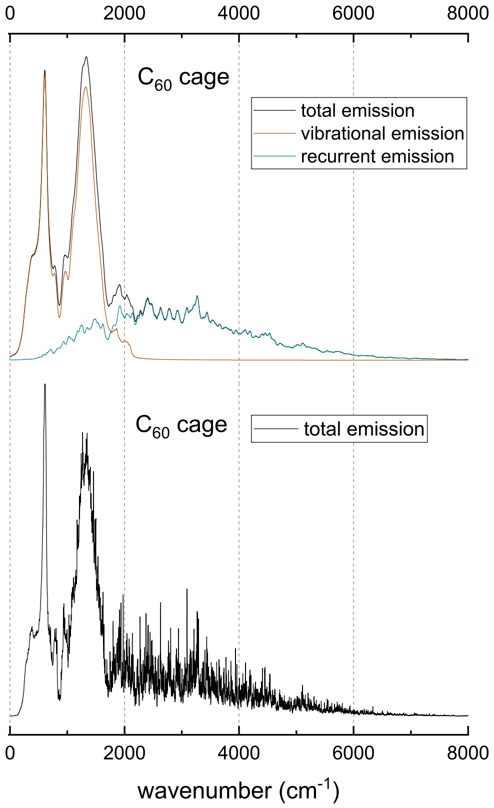

Figure 3.15: Emission intensity spectra of a large set of C_{60} carbon clusters irradiated by a 20 000 K blackbody (simulating a star). The vibrational emission and recurrent fluorescence components are also shown. To obtain these emission intensity spectra, a lorentzian convolution have been done on the computed histogram emission intensity spectra with a FWMH of 50 cm^{-1}.

around 10 000 cm^{-1} and is negligible beyond 40 000 cm^{-1} ($< 1\%$ of the maximum) whereas the 20 000 K blackbody has a maximum emission at around 20 000 cm^{-1} and is negligible beyond 100 000 cm^{-1}. Thus, when irradiated by a 20 000 K star, carbon clusters have higher internal energies. At higher internal energy, emission from high-frequency modes is more likely and this is translated in the emission spectra in terms of stronger (resp. lower) relative intensity for high-frequency modes (resp. low-frequency modes).

Figure 3.18 displays the evolution of emission band ratios in terms of the size, the family and the RF influence. R represents the ratio between vibrational bands called 500 (for the emission band around 500 cm^{-1}), 1300 (around 1300 cm^{-1}) and 2000 (around 2200 cm^{-1}). For example, $R_{500/1300}$ represents the ratio of the band around 500 cm^{-1} over that of around 1300 cm^{-1}. In figure 3.18, we display the ratio of two R ratios: R^{RF} deduced from an emission spectrum in which we took RF into account and R^{NOTRF} in which RF has not been taken into account. In panel (a) of figure 3.18, the ratios are always greater than 1. This means that RF makes the relative intensity emission of low-frequency modes stronger (around 500 cm^{-1}) and this effect is more important for smaller clusters. We explain these evolutions as follows. RF mainly occurs at high internal energies ($>$ 20 000 cm^{-1}). As mentioned above, at high internal energy VE mainly occurs via high-frequency modes. Then, at high internal energy, RF is in competition with emission from high-frequency vibrational modes. Consequently, RF should predominantly reduce the relative intensity of high-frequency modes. That explains why all ratios in panel (a) are greater to unity. Some ratios in panel (b) are less than unity, we assign them to the fact that RF can considerably emit around 2000 cm^{-1} which complicates the analysis of panel (b). Nevertheless, the explanation given for ratios of panel (a) are also valid for those of panel (b).

We also notice that these ratios are generally greater for smaller isomers. A possible explanation is that smaller isomers have higher RF efficiency. Indeed, high RF efficiency implies that the high-frequency VE quenching from RF is more important, hence higher values for $R_{500/1300}$ ratio.

Figure 3.20 displays the near-IR emission for C_{60} families and C_{42} cages. The near-IR emission below 4 μm is mainly due to RF and the emission broad band at 4.8 μm stems from VE. We know that the VE band appearing at 4.8 μm (panel a of figure 3.20) for all families except cages is not astrophysically observed which urge us to consider only cage isomers from now Flagey et al. (2006); Onaka et al. (2018). Emission spectra of panel (b) (figure 3.20) are very similar to the near-IR emission spectra observed by Sellgren in 1983 (figure 3.19), namely a flat emission signal from 5 to 2.5 μm (in log scale) and a steep decrease below 2 μm reflects the exponential decay of the blackbody-

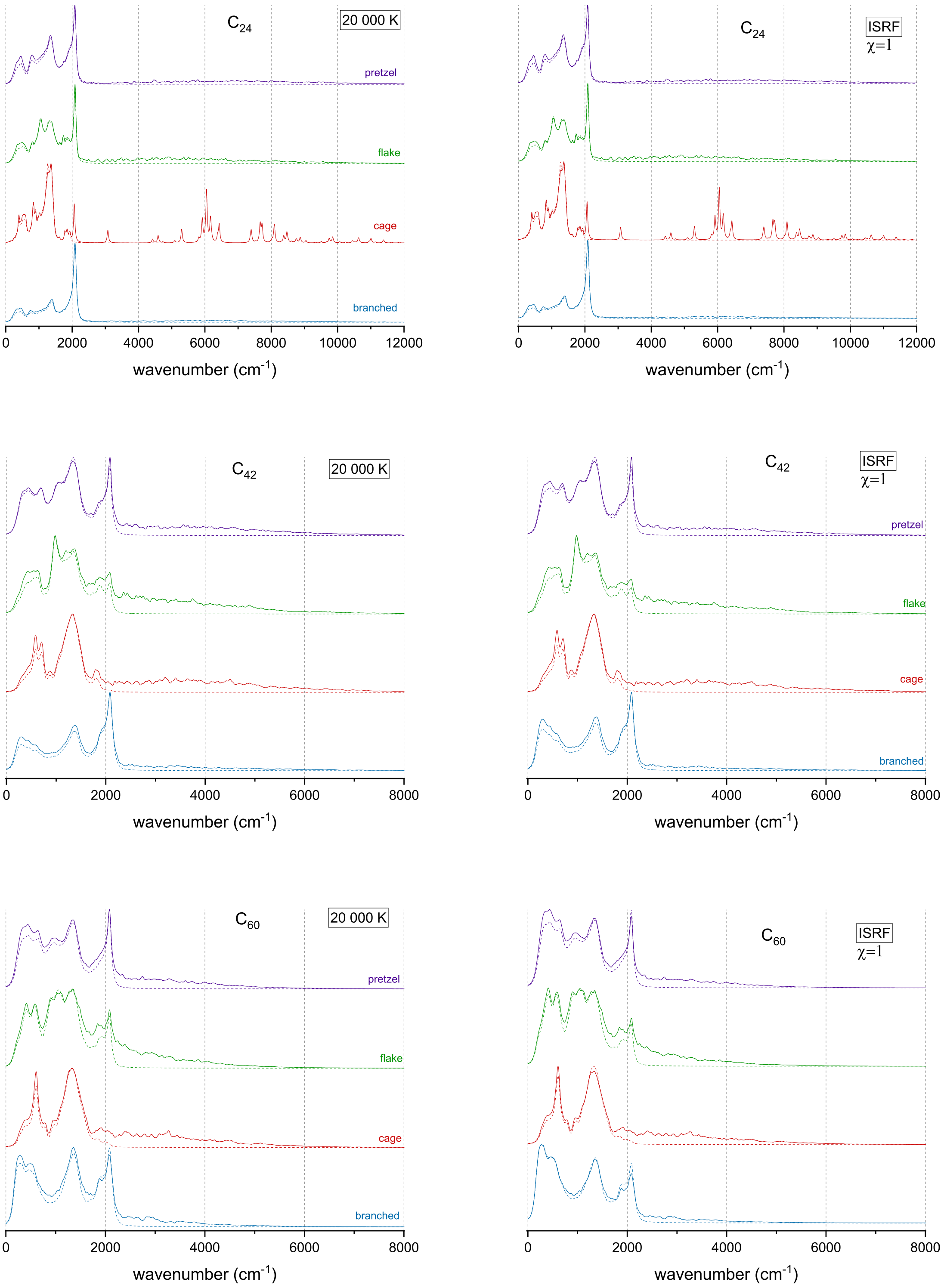

Figure 3.16: Emission intensity spectra from the four families (branched, cages, flakes and pretzels) for all sizes, irradiated by a 20 000 K blackbody and χ=1 ISRF. Each emission spectrum in full lines is associated with a dotted lines emission spectrum for which only VF is taken into account. The emission intensity spectrum from C_{24} cages is particularly different because there are only 11 isomers.

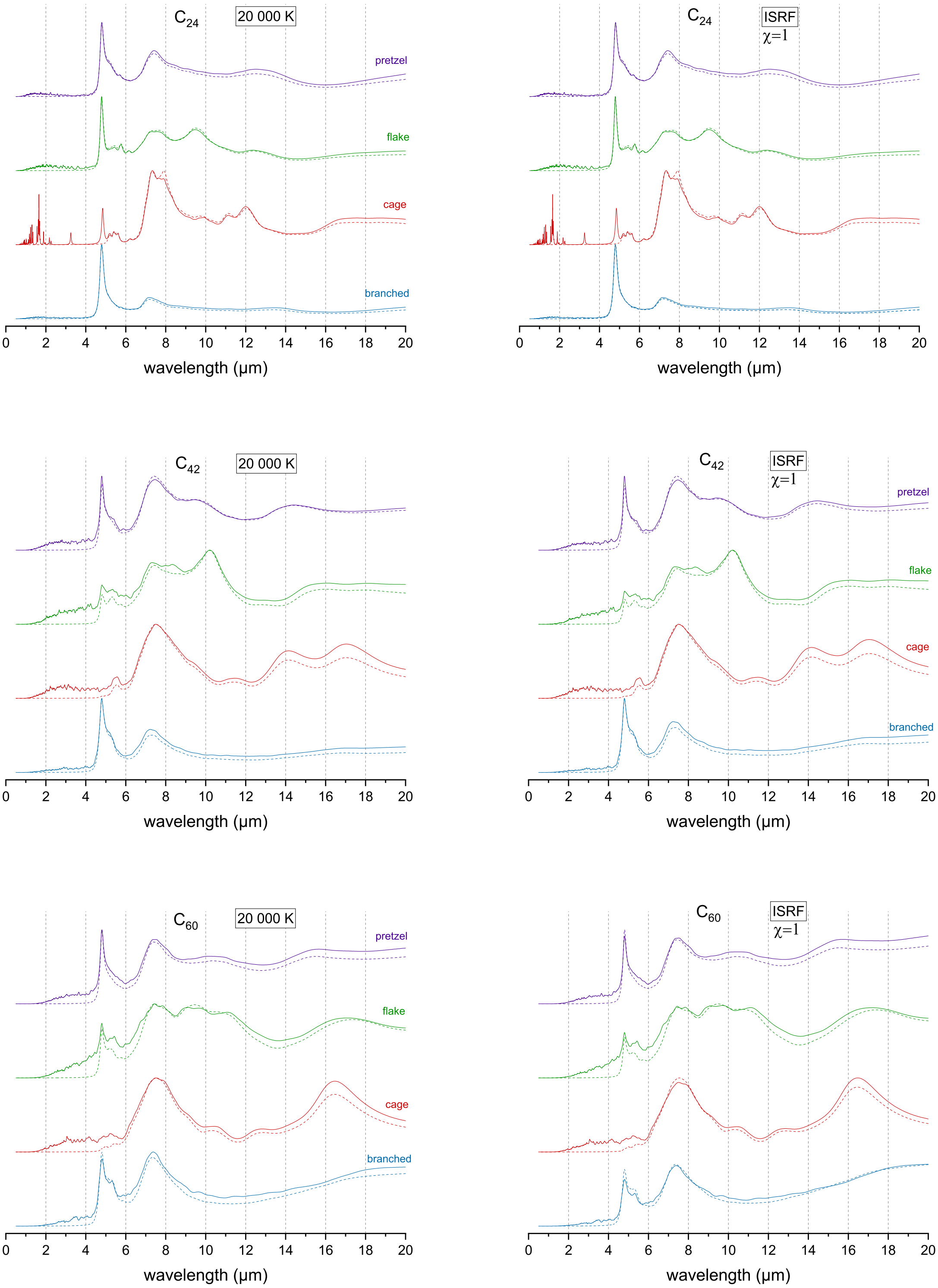

Figure 3.17: Same emission intensity spectra of figure 3.17 displayed here in terms of wavelength.

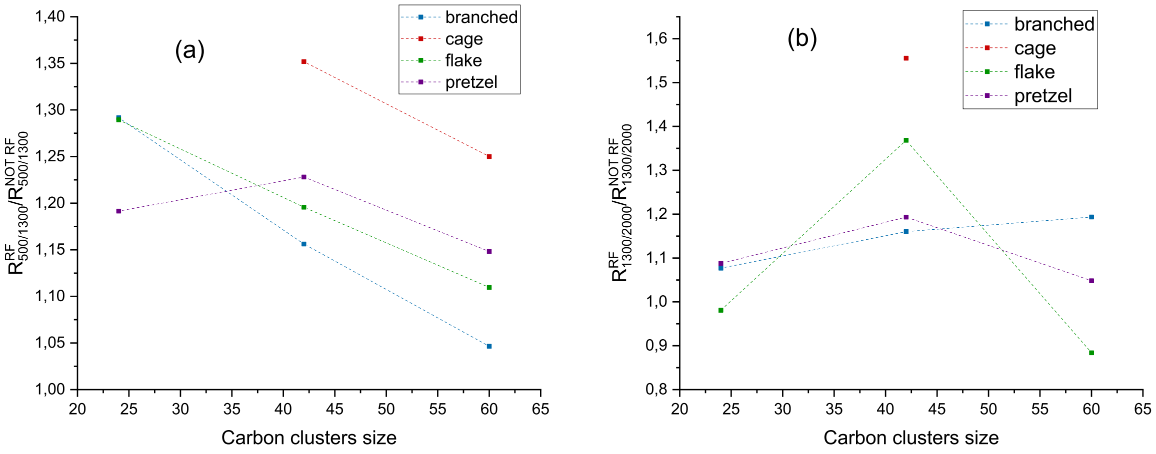

Figure 3.18: Ratios of vibrational band ratios for all families and all sizes. R represents ratio between to vibrational bands. Ratios have been deduced from emission spectra of figure 3.16. All band ratios are not defined for the cage family.

like emission due to RF (figure 3.15). From figure 3.19, we notice that the ratio between the continuum emission at 4.8 μm and 1.25 μm is around 5 for the NGC 7023 reflection nebulae and 6 for the NGC 2023. In this work, by taking a 20 000 K blackbody as a SED, this ratio is around 70 for C_{60} cages and 10 for C_{42} cages. Actually, the size of cage carbon clusters should be smaller than C_{60}. In addition, our exact calculation of the vibrational density of states for each isomers allow us to determine the temperature at which near-IR photons are emitted: by supposing that emission below 2 μm stems from isomers with the highest internal energies (60 000 cm^{-1} for C_{60} and 65 000 cm^{-1} for C_{42}), we estimate the mean reached temperature as being around 1000 K for C_{60} isomers and 1300 K for C_{42} isomers.

Emission spectra displayed in figure 3.20 have been normalized in order to make the integrated spectra equal to unity. The radiated energy between 1 μm and 3 μm after UV-excitation is around 16 % of the total emission intensity for C_{60} cage isomers (around 8% for ppa, 8.7% for pretzels, 5% for branched). This percentage is slightly lower for illumination from the χ=1 ISRF which is around 14% for C_{60} cage isomers. For C_{42} cages, we have 27% for 20 000 K and 24% for ISRF.

Observations from Sellgren (1984) indicate that the near-IR emission around 2 μm is around 20 mJy within 12″ diaphragm. Supposing that, over the large set of C_{60} cage carbon clusters, the total absorbed power density (W/m^2) is equal to the total emitted power density, the integrated emission spectrum over frequencies that we computed is equal to the integrated absorbed power density over frequencies. The emitted emission spectra in the near-IR wavelength range is shown in figure 3.20 (b) in such a way that

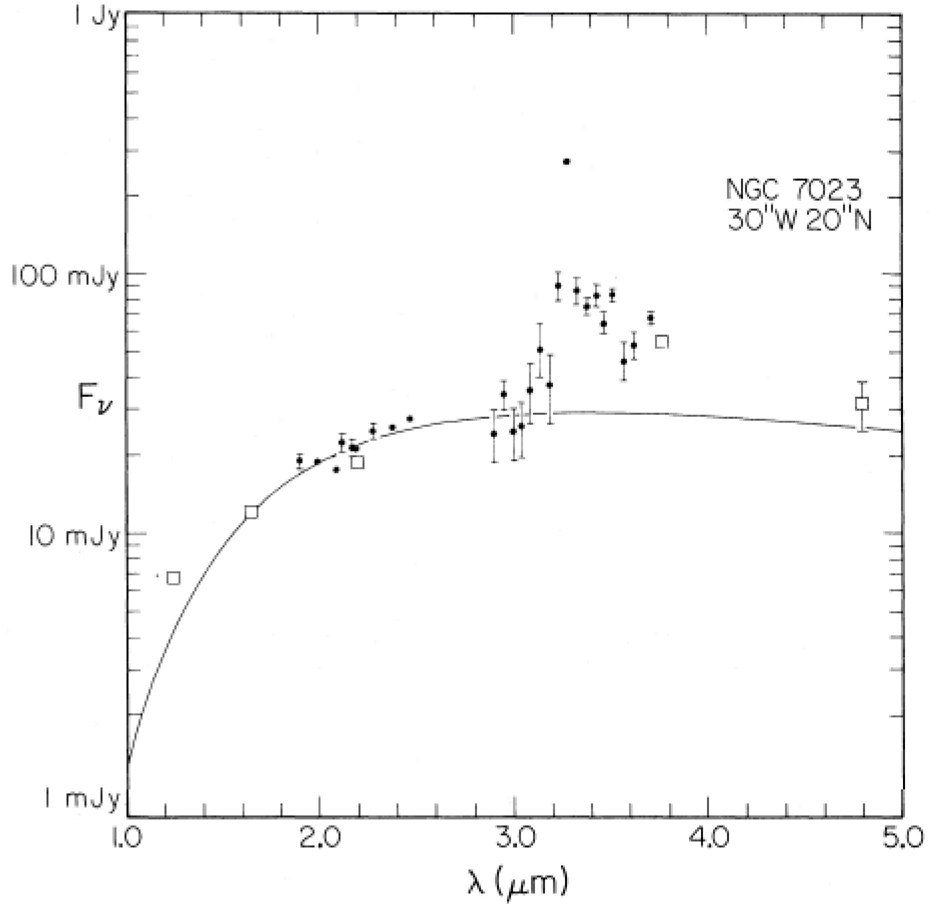

Figure 3.19: Emission spectrum extracted from Sellgren (1984). Near-IR continuum emission observed in NGC 7023 within 12″ aperture.

the integral over the frequency is set to unity. We can also estimate the absorbed power flux density because we know the electronic absorption cross-section of the large set of C_{60} cage carbon clusters (see the appendix).

The exciting power density per frequency in the observed region is given by the following quantity

$$(\frac{R_\bullet}{D_\bullet})^2 \times M^o(\nu;T) \tag{3.23}$$

with M^o ($\mathrm{W{\cdot}m^{-2}{\cdot}Hz^{-1}}$) the spectral exitance of the blackbody (star) at temperature $T = 20000K$ (actually, the temperature is around 20 400 K Van den Ancker et al. (1997)), $R_\bullet$ the radius of the illuminating source, $D_\bullet$ the distance between the illuminating source and NGC 7023. The absorbed power density per frequency is then given by

$$(\frac{R_\bullet}{D_\bullet})^2 \times M^o(\nu;T) \times \mathrm{C_{abs}}(\nu) n_{\mathrm{C}}^{2/3} \tag{3.24}$$

with $\mathrm{C_{abs}}$ ($\mathrm{m^2}$) the electronic absorption cross section of the set of C_{60} cage carbon clusters and n_{C} ($\mathrm{m^{-3}}$) the C_{60} cages volume density in the region. Then, the total absorbed power density is written as

$$(\frac{R_\bullet}{D_\bullet})^2 \times \left(\int_0^{E_{ion}} M^o(\nu;T) \mathrm{C_{abs}}(\nu) d\nu \right) \times n_{\mathrm{C}}^{2/3} \tag{3.25}$$

with E_{ion} the mean ionization threshold of C_{60} cages (set to 7.5 eV as mentioned in the previous section). To obtain the power density detected on Earth, we have to multiply the quantity (3.25) by

$$\frac{1}{4\pi}(\frac{R_\triangle}{D_\triangle})^2 \tag{3.26}$$

with $R_\triangle$ the spatial extension of the observed NGC 7023 region, $D_\triangle$ the distance between Earth and NGC 7023. Thus, keeping in mind that the integral of the emission spectrum shown in figure 3.20 (b) is equal to unity, we can deduce the spectral power density that should be detected on Earth by multiplying the y-axis of figure 3.20 (b) by the following quantity

$$(\frac{R_\bullet}{D_\bullet})^2 \times \left(\int_0^{E_{ion}} M^o(\nu;T) \mathrm{C_{abs}}(\nu) d\nu \right) \times n_{\mathrm{C}}^{2/3} \times \frac{1}{4\pi}(\frac{R_\triangle}{D_\triangle})^2 \tag{3.27}$$

For C_{60} cage carbon clusters, this latter quantity is equal to $2.3 \cdot 10^{-25} \times n_{\mathrm{C}}^{2/3}$ $\mathrm{W{\cdot}m^{-2}{\cdot}}$ $\mathrm{ste^{-1}}$ (see the appendix for details) or $3 \cdot 10^{-24} \times n_{\mathrm{C}}^{2/3}$ $\mathrm{W{\cdot}m^{-2}}$. In figure 3.20 (b), we indicate that emission value around 2 μm is a fraction of $4{\cdot}10^{-5}$ of the total emission. Thus, the detected spectral power density on Earth is equal to

$$4 \cdot 10^{-5} \times 3 \cdot 10^{-24} \times n_{\mathrm{C}}^{2/3} = 1 \cdot 10^{-28} \times n_{\mathrm{C}}^{2/3} \ \mathrm{W \cdot m^{-2} \cdot Hz^{-1}} = 10 \times n_{\mathrm{C}}^{2/3} \ \mathrm{mJy} \tag{3.28}$$

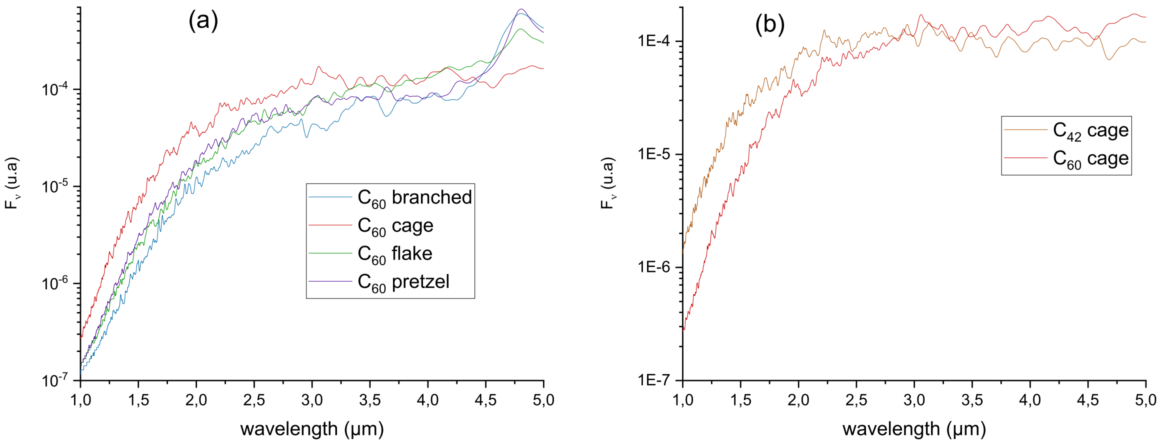

Figure 3.20: Emission spectra at the near-IR region. Upper panel: the four families of C_{60} are displayed. Lower panel: the interesting emission spectra of cage family is displayed for two different sizes.

Thus, the detected power density per frequency within 12″ solid angle is $\frac{12}{3600}\times 10\times n_{\mathrm{C}}^{2/3} = \frac{1}{30}n_{\mathrm{C}}^{2/3}$ mJy. K.Sellgren detected 20 mJy at 2 μm Sellgren (1984), then we deduce that $n_{\mathrm{C}} = 1.5\cdot 10^{-2}$ cm^{-3}. Hydrogen abundance in that region is around 10^5 cm^{-3} Martini et al. (1999) and carbon abundance is $2.4\cdot 10^{-4}$ of the hydrogen abundance **?**, we deduce that 4 % of the carbon is locked up in C_{60} cages. The same calculation for C_{42} cages gives a percentage of 2.5 %. The percentage of interstellar carbon locked up in C_{60} buckminsterfullerene have been estimated to 0.1-0.6 % Sellgren et al. (2010) and this would mean the percentage of buckminsterfullerene among C_{60} cages and larger carbon clusters (up to C_{70}) should be 2.5-15 %. We stress that C_{60} buckminsterfullerene contribute in the near-IR emission because the recurrent fluorescence is negligible (the first excited electronic state is too high, $\sim$ 3 eV).

Carbon clusters are also suspected to contribute to the extended red emission via recurrent fluorescence induced by absorption of photon energies between 10 and 13.6 eV. Extended red emission is a broad emission band peaking between 600 and 850 nm and the FMHW spans between 60 and 120 nm Witt and Lai (2020); Lai et al. (2020). From figure 3.17, we deduce that only C_{24} ppa and pretzel isomers could emit in the ERE region (below 0.8 μm). The explanation is that they are sufficiently small to reach high temperature and emit in the visible region when excited by photons between 11 and 13.6 eV. The blackbody-like emission appears around 2 μm for these isomers and we stress this blackbody-like emission comes from a large set of isomers and does not come from individual carbon clusters. We have computed the emission spectra after UV-excitation by a 12.4 eV photon for a very qualitative study of neutral carbon clusters in the ERE

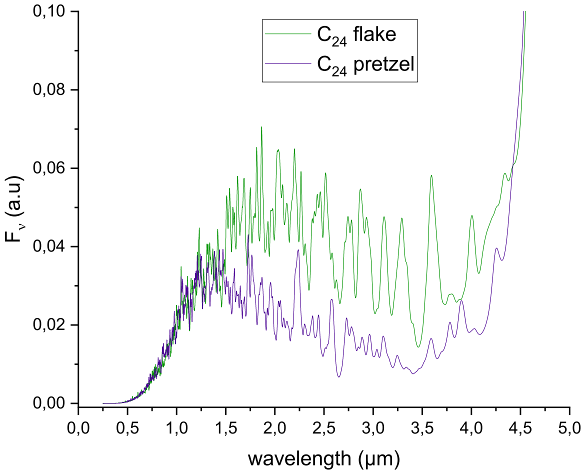

Figure 3.21: Emission spectra of neutral C_{24} pretzel and ppa excited by a 20 000 K star. The region of the extended red emission lies between 600 and 850 nm.

context. This is very qualitative because we take the neutral species which should be ionized at this excitation energy. But the electronic structure over a large set of neutral C_{24} is representative of the ionic spectra of a large set of C_{24} cations which should better survive upon ionization at 12.4 eV excitation energy. Figure 3.21 displays emission spectra below 5 μm from C_{24} pretzel and ppa. This is actually the RF part of the spectra. Even excitated by 12.4 eV photon, the RF part does not reach the ERE region and would not be sufficiently blueshifted by 13.6 eV photon excitation. Also, the RF part is too large (FWHM $\simeq$ 1000 nm) to be identified to the ERE. These results suggest that RF induced by photon absorption from C_{24} carbon clusters (or comparable size) does not contribute to the ERE.

Conclusions

Our study revealed that emission spectra induced by a spectral energy distribution (20 000 K star or χ=1 ISRF) of carbon clusters spreads from the far-IR to near-IR wavelength region. It turns out that recurrent fluorescence of carbon clusters has an influence on the vibrational part of the spectra by inhibiting the emission from high-frequency vibrational modes. The recurrent fluorescence part of the emission spectra has a blackbody-like shape. The observed near-IR emission in certain reflection nebulae could be explained by recurrent fluorescence of C_{60} cage carbon clusters as suspected earlier Sellgren (1984). If so, we estimate the f_C abundance of carbon locked up in C_{60} cage relative to H nuclei to be about 0.1 ppm (or 0.1 % of the carbon is locked up in

C_{60} cages).
In that sense, it could be useful to investigate how recurrent fluorescence near-IR continuum supports the 3.3 and 3.4 µm emission features in large PAHs-like molecules ($N_C \sim$ 30-50) because, as underlined in Sellgren (1984), the feature-to-continuum ratio of the 3.3 µm emission feature is about 6. Actually, recurrent fluorescence from large PAH-like molecule should not be as high as that of carbon clusters because of their higher electronic states Malloci et al. (2007).
Recurrent fluorescence spectra of C_{24} are found to be redshifted compared to extended red emission. This suggest that the mechanism at the origin of extended red emission is not as simple as recurrent fluorescence of C_{24} (or similar size carbon cluster) induced by photon stellar with energies between 11 and 13.6 eV.

Acknowledgements

This work has been supported by ANR project PACHYNO (ANR-16-CE29-0025).

Absorption cross-section and spectral energy distribution

From Dubosq et al. (2020), it has been possible to derive the electronic oscillator strength of all $S_n \rightarrow S_0$ transitions from which we deduced the absorption cross-section displayed in figure 3.22 (right panel) for C_{60} cage isomers.
Actually, electronic oscillator strength extracted from Dubosq et al. (2020) are not reliable above 8.2 eV ($\simeq$ 66 000 cm^{-1}). This is why we fitted the absorption cross-section from the well-known Draine & Li's model Li and Draine (2001) above 8.2 eV. The discontinuity around 66 000 cm^{-1} is a computational artifact and does not influence the results and discussions of this work. The two spectral irradiances used in this work are shown in figure 3.23.

Calculation of the detected emission power density from C_{60} cages in NGC 7023

Several distances are involved in (3.27). The distance $D_\triangle$ between Earth and the NGC 7023 has been estimated to 430 pc Van den Ancker et al. (1997). The spatial extension $R_\triangle$ of the observed region inside NGC 7023 has been determined by the information that the diaphragm size is 12″ angle solid Sellgren (1984). Thus, we have

$$R_\triangle = D_\triangle \arctan\left(6'' \times \frac{2\pi}{3600''}\right) = 4.5 \text{ pc} \tag{3.29}$$

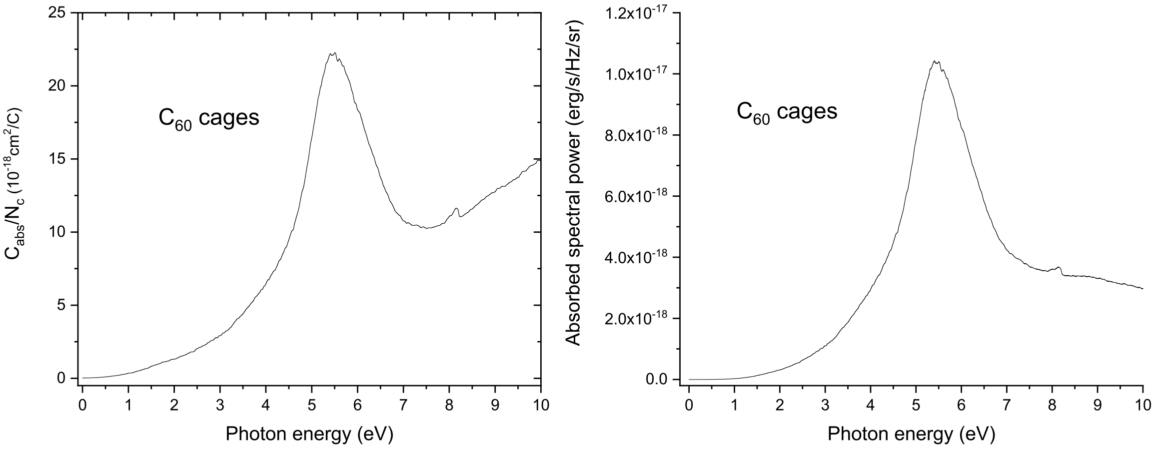

Figure 3.22: Left panel: the average electronic absorption cross-section per carbon number of C_{60} cage isomers and obtained by a FWHM= 300 cm^{-1} lorentzian convolution. Right panel: the average absorbed spectral energy power by C_{60} cages located at the surface a 20 000 K blackbody. This curves have been obtained by multiplying the 20 000 K blackbody spectral irradiance shown in figure 3.23 and the average electronic absorption cross-section of C_{60} cage isomers shown at the left panel.

Hence,

$$\frac{1}{4\pi}\left(\frac{R_\triangle}{D_\triangle}\right)^2 = 8.7 \cdot 10^{-6}\ \mathrm{ste}^{-1} \tag{3.30}$$

The distance $D_\bullet$ between the observed region and the exciting binary star has been estimated from Sellgren (1984). Indeed, it is indicated that the observed region position is localized at 30″W 20″N relative to the exciting binary star. Supposing that the exciting star and the observed region are in a plane perpendicular to the line of sight, the distance $D_\bullet$ is expressed as

$$D_\bullet = D_\triangle \sqrt{\sin^2(30'' \times \frac{\pi}{3600''}) + \sin^2(20'' \times \frac{\pi}{3600''})} = 27\ \mathrm{pc} \tag{3.31}$$

From Pogodin et al. (2004), we know that the exciting source is a binary star composed of a 10 $M_\odot$ mass and 8 $R_\odot$ radius star and a smaller companion with 3.5 $M_\odot$ mass. Thus, we assume that the total radius $R_\bullet$ is around 10 $R_\odot = 2.3 \cdot 10^{-7}$ pc. Hence,

$$\left(\frac{R_\bullet}{D_\bullet}\right)^2 = \left(\frac{2.3 \cdot 10^{-7}\ \mathrm{pc}}{27\ \mathrm{pc}}\right)^2 = 7.3 \cdot 10^{-17} \tag{3.32}$$

The integral involved in brackets in the quantity (3.27) has been computed via the

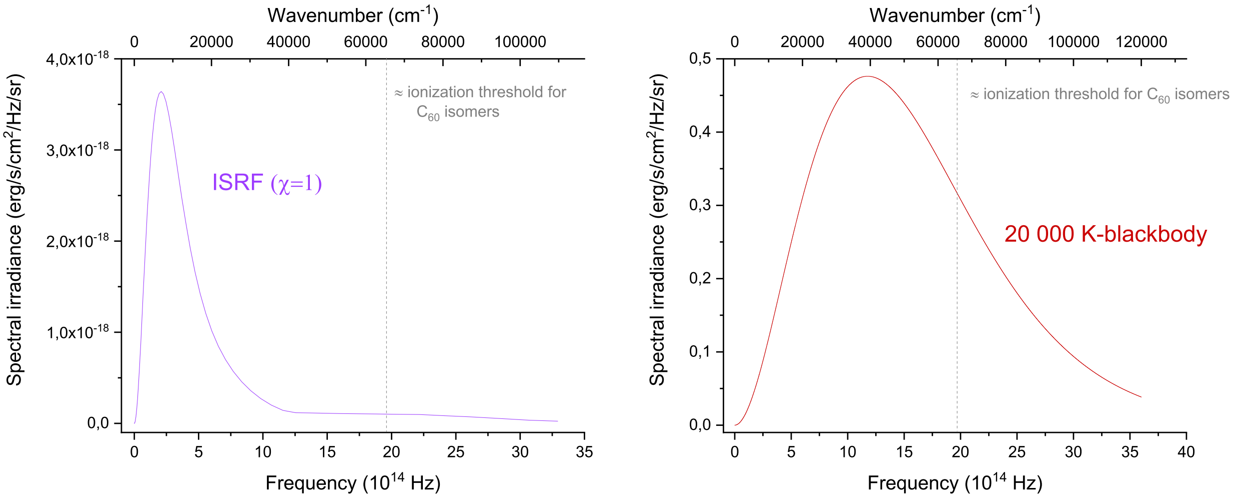

Figure 3.23: Spectral irradiance associated with SEDs that we used in this work. Actually, we added a cutoff to take the ionization into account. This cutoff occurs at 60 000 cm^{-1} for C_{60}, 65 000 cm^{-1} for C_{42} and 70 000 cm^{-1} for C_{24}. Left panel: spectral irradiance of the $\chi = 1$ ISRF Mathis et al. (1983). Right panel: spectral irradiance at the surface of a 20 000 K blackbody.

electronic cross-section shown in the left panel of figure (3.22). For a blackbody at 20 000 K, this integral is equal to $3.6 \cdot 10^{-4} \times n_{\mathrm{C}}^{2/3}$ W·m^{-2}.
Then, the quantity (3.27) is given by

$$7.3 \cdot 10^{-17} \times 3.6 \cdot 10^{-4} \times n_{\mathrm{C}}^{2/3} \times 8.7 \cdot 10^{-6} = 2.3 \cdot 10^{-25} \times n_{\mathrm{C}}^{2/3}\ \mathrm{W} \cdot \mathrm{m}^{-2} \cdot \mathrm{ste}^{-1} \qquad (3.33)$$

This value represents the power density per solid angle detected on Earth and stemming from recurrent fluorescence of C_{60} cage carbon clusters illuminated by the binary star HD 200775 at 20 000 K.

Error estimation

The biased value of the total number of emitted photons N_9^{tot} (electronic excitation at 9 eV, i.e initial internal energy) in our computation occurs because, as shown in figure 3.24, the emitted photon number at each internal energy depends on the initial internal energy. This is an artifact of our kinetic Monte Carlo (kMC) computation. The mean trajectory is constituted of kMC steps obtained by calculating the mean of each kMC steps over 10^5 trajectories. In other words, we did not define energy bins in our algorithm and these vary with the internal energy. Yet, as illustrated in figure 3.24, energy bins are also dependent of the initial internal energy. Below 2 eV internal energy, energy bins are narrower for higher initial internal energy curves. On the other hand, below 2 eV,

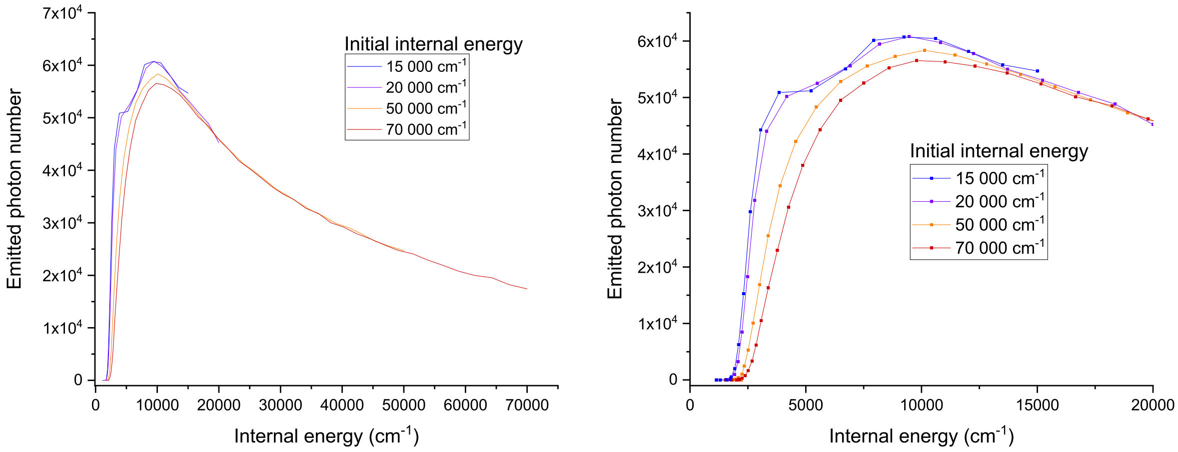

Figure 3.24: Number of photons emitted via VE in terms of internal energy. At internal energies below 2 eV, this number is dependent of the initial internal energy. This is a computational artifact. (a): above 1.5 eV internal energy, VE decreases with the internal energy because it is quenched more and more by recurrent fluorescence. (b): the same plot as (a) and points represents kMC steps of the mean trajectory. There are more kMC steps for higher initial energies although the total emitted photons below 2 eV are equal.

emitted photon number at a given internal energy is lower for higher initial energies. These two facts compensate each other when we calculate the total emitted photon number below 2 eV internal energy.

Thus, the vibrational emission (VE) of the red curve (excitation at 9 eV) will be necessarily lower at each step of the mean trajectory than the blue one (excitation at 2 eV) at lower internal energies. Thus, even if, the total emitted photon number below 2.5 eV is the same ($\approx 6{\cdot}10^5$ for each initial energies with relative difference below 0.5% to each other), its repartition in terms of the internal energy is not the same because the kMC energy bins are different. To estimate the error on N_9^{tot}, we have to calculate the following quantities

$$N_9^{tot} \propto \int_0^9 N_9(\nu)K(E)dE$$
$$N_{1.9}^{tot} \propto \int_0^{1.9} N_{1.9}(\nu)K(E)dE + \int_{1.9}^9 N_9(\nu)K(E)dE$$

K(E) is shown in figure 3.25 for the arbitrarily chosen isomer here (there is no difference with other carbon cluster isomers). The difference between N_9^{tot} and $N_{1.9}^{tot}$ gives us an indication about the relative error. We obtained 3.5% for recurrent fluorescence and

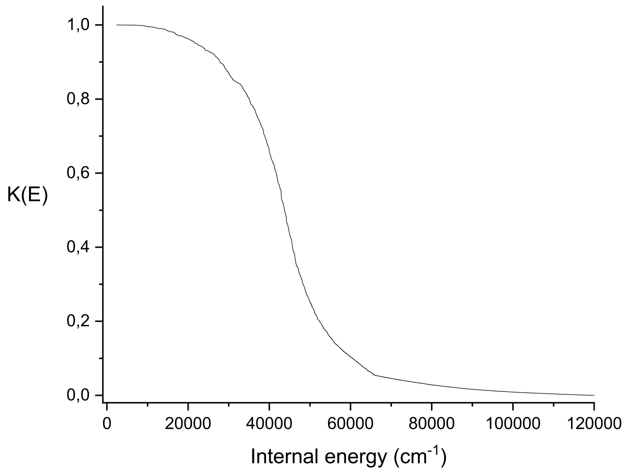

Figure 3.25: K(E) factor for the C_{60} cage arbitrarily chosen in this appendix and for a 20 000 K blackbody.

vibrational emission. This estimation has been deduced for the isomer chosen in this appendix but it should be the same for other isomers.

Large carbon clusters emissivity: a molecular approach

In flames, large carbon clusters are products of incomplete combustion. In that case, there is not enough oxygen (oxidant) to consume all the fuel. Then, the remaining fuel is at the origin of chain reactions made possible by the exothermicity of combustion reactions. These chain reactions produce hydrocarbons and carbon clusters. By laser diagnostic techniques, such as laser-induced fluorescence or laser-induced incandescence, it is possible to increase the temperature to study the carbonaceous particles in the flame.

In this theoretical work, we investigate the emission of C_{42} and C_{60} carbon clusters at fixed temperature. Temperatures have been chosen in such a way that dissociation and thermoionization are negligible. We made our calculations for the flake family on a large number of isomers (a thousand for both sizes). Resulting emission spectra are modified blackbody emission spectra. The quantity usually determined in laser-induced fluorescence or incandescence experiments is the emissivity. We then deduced the average emissivity of C_{42} and C_{60} flakes and their total emissivity.

Introduction

In 1917, Einstein has found Planck's distribution for thermal emission from quantum and statistical arguments and by introducing stimulated emission in addition to absorption and spontaneous emission Einstein (2016). Then, as long as the statistical approach is justified, thermal emission from a set of very small particles (radius ≈ 5 Å) could be explained. In this work, we are interested in the emission spectra of a large set of carbon cluster isomers (C_{60} and C_{42}) at fixed high temperature. In combustion environments, carbon clusters are products of incomplete combustion Siegmann et al. (2002); Ebert (1990). A widely used in-situ optical diagnostic of soot particles is laser-induced incandescence (LII). The basic principle of this technique is to heat the soot particle to high temperature (around vaporization temperature) by energetic laser irradiation and detect the thermal emission and its decay Dreier and Ewart (2002). Thus, we wonder what would be emission spectra of C_{42} and C_{60} carbon clusters arising in LII context via electronic and vibrational emission. Indeed, several experiments have reported thermal emission from particles as small as C_{60} carbon clusters or 5 nm-sized nanoparticles Mitzner and Campbell (1995); Rohlfing (1988); Long et al. (2019); Hansen and Campbell (1998).

To this end, we used one thousand flake carbon clusters (namely PPA, planar polycyclic aromatic) for each size (C_{60} and C_{42}) that have been generated by exploring the conformational landscapes and using advanced molecular dynamics Bonnin et al. (2019).

Actually, the electronic density of states over a large set of carbon clusters (see section 3 in the appendix) is the relevant quantity and our starting point. This is why we deliberately choose flake carbon clusters (cage carbon clusters contains a very stable isomer, the buckminsterfullerene), whatever their vibrational structure because, as we shall see, in this work vibrational emission is negligible compared to electronic emission. The emission processes detected from hot carbon cluster gas are vibrational and electronic radiative de-excitation. Indeed, at fixed temperature, carbon clusters contain internal energy distributed among accessible vibronic states. To calculate these emission rates, information about the electronic and vibrational structures of all carbon cluster isomers are needed and these have already been calculated by SCC-DFTB method Dubosq et al. (2020, 2019).

Theoretical methodology

To obtain the emission spectra of carbon clusters gas at fixed temperature, first of all we need electronic and vibrational emission rates at fixed internal energy for each flake isomer. Indeed, we computed radiative emission rates at fixed internal energy (chapter 2) and we did a weighted sum of emission rates over all internal energies. The weighting is defined for a given temperature T and approximated by a Gaussian function and its two parameters (mean internal energy and standard deviation, table 3.2) are computed from the partition function. By means of this sommation, we obtain emission rates at temperature T. The partition function Z_{vib} is computed by using the following relation

$$Z_{\text{vib}} = \int_0^\infty \rho_{\text{vib}}(E) e^{-\beta E} dE \tag{3.34}$$

with $\beta = (k_B T)^{-1}$, $\rho_{\text{vib}}(E)$ the harmonic vibrational density of states (VDOS) at E internal energy computed by exact counting (section 2 in chapter 2). In this computation, we went through microcanonical calculation (emission rates at fixed internal energy) to finally calculate emission rates at fixed temperature. We proceeded in this way because the computer program of previous simulation work was already done and uses the microcanonical framework.

In this work, we analytically calculated emission rates to have a better understanding of computed emission spectra. However, this calculation has been naturally done in the canonical framework. In this subsection, we present, on one hand, the details of the computation of emission rates at fixed temperature and, on the other hand, its analytical derivation. In the appendix (section 3), we show the equivalence of these two approches.

In the case of carbon clusters, excited electronic states are relatively low (around 0.3 eV $\simeq$ 2500 cm^{-1} for the first one for C_{60} and C_{42} flakes) and make notable the occupation probability of excited electronic states via inverse internal conversion and then make electronic emission possible (see recurrent fluorescence in chapter 2). The main hypothesis is that the fixed internal energy is statistically distributed among all vibrational normal modes of all electronic states (intramolecular vibrational redistribution, $\sim 10^{-12}$-10^{-10}s). This assumption is justified by the fact that internal conversion and inverse internal conversion ($\sim 10^{-14}$-10^{-8}s) are very rapid compared to all radiative relaxation pathways. At fixed internal energy E, the microcanonical probability to occupy the n^{th} electronic state of energy $h\nu_n$ is given by

$$\frac{\rho_0(E - h\nu_n)}{\sum_i \rho_0(E - h\nu_i)} \tag{3.35}$$

with $\rho_0(E)$ the harmonic vibrational density of states in the ground electronic states which is calculated by an exact counting (see section 2 in chapter 2). From that probability, the electronic fluorescence of the transition n $\rightarrow$ 0 (from the n^{th} electronic state to the ground electronic state) and energy $h\nu_n$, it is possible to obtain the electronic radiative de-excitation rates $A_{rec}(\nu_n; E)$. Electronic emission rates are obtained from two quantities: electronic energy levels and electronic oscillator strengths of n $\rightarrow$ 0 transitions. Given that, at fixed temperature the internal energy distribution follows approximately a Gaussian distribution, it is then possible from Gaussian weighting of all $A_{rec}(\nu_n; E)$ (E ranging from 0 to ∞) to determine the electronic emission rate $A_{rec}(\nu_n; T)$ from n^{th} electronic level of a given flake isomer at a fixed temperature (table 3.2). Thus, the emission spectrum of the flake isomer set is obtained by summing all individual emission spectra. We took a flat distribution over the C_{60} and C_{42} flake isomer population because, as stressed above, the electronic density of states over the set of flake isomers is the relevant quantity and their vibrational structure is irrelevant.

Calculating emission rates $A_{elec}(\nu_n; T)$ in the canonical framework is easier. The emission rate from the n^{th} electronic state of energy $h\nu_n$ reads as

$$A_{elec}(\nu_n; T) = A_n \times p(h\nu_n) \tag{3.36}$$

with $p(h\nu_n)$ the canonical probability to occupy the n^{th} electronic state. Given that, the electronic states are independent of vibrational states (this is an approximation), the probability $p(h\nu_n)$ is written by

$$p(h\nu_n) = \frac{e^{-\beta h\nu_n}}{1 + e^{-\beta h\nu_1} + e^{-\beta h\nu_2} + ... + e^{-\beta h\nu_n} + ...} \tag{3.37}$$

Thus, the analytical expression of the spontaneous electronic radiative de-excitation rate of an isomer from the nth electronic state is

$$A_{elec}(\nu_n;T) = A_n \frac{e^{-\beta h\nu_n}}{Z_{elec}} \tag{3.38}$$

with Z_{elec} the electronic partition function computed from the vibrational density of states. The electronic fluorescence rate for n → 0 transitions are calculated from

$$A_n = \frac{2\pi e^2 \nu_{n0}^3}{m_e \epsilon_0 c^3} \times \frac{f_{n0}}{\nu_{n0}} \tag{3.39}$$

with e the elementary charge, m_e the electron mass, ϵ_0 the vacuum permittivity, c the speed of light, $h\nu_{n0}$ the electronic energy gap of the nth electronic excited state and f_{n0} the electronic oscillator strengths for n → 0 electronic transitions. As a first approximation, we neglect n → m electronic transitions (m $\neq$ 0). The analytical expression of vibrational emission rates is not necessary for the discussion but they have been taken into account in the simulation anyway. Vibrational emission rates are calculated within the same framework than electronic emission rates (see section 2 in chapter 2).

We fixed temperatures of carbon clusters gas in such a way to have radiative emission processes as the main relaxation pathways (much more likely than dissociation or thermionic emission). To our knowledge, there is no work on dissociation of flake carbon clusters. Thus, we suppose C_2 channel with a dissociation energy similar to the cage ones, which are supposed to be slightly lower ($\sim$ 10 eV) to that of C_{60} buckminsterfullerene ($\sim$ 11 eV Tomita et al. (2003); Hansen and Echt (1997)). A crude RRK calculation indicates that C_2 dissociation from C_{60} flake carbon clusters is negligible compared to radiative relaxation (total vibrational emission rate $\approx$ 20 s^{-1} and total electronic emission rate $\approx$ 20 000 s^{-1} at 240 000 cm^{-1} of internal energy) below 3000 K Lifshitz (2000b). Furthermore, supposing that C_2 dissociation energy from C_{42} is about 7 eV (7.5 eV for the more stable of them Chang et al. (2005)), C_2 dissociation is negligible compared to radiative relaxation at 2500 K. Thermoionic emission rate is even weaker than dissociation rate Lifshitz (2000b) and can also be neglected.

Emission spectra

Normalized emission spectra from a set of flakes carbon clusters at different temperatures are shown in panel (a) of figure 3.26. The emission spectra behave like a Planck function in that the temperature increase has a blueshift effect on the spectra and makes it broader. From C_{60} to C_{42}, the overall shape of the emission spectrum does not change at fixed temperatures as shown on panel (b) of figure 3.26. The slight differences between C_{60} and C_{42} emission spectra are explained from fluctuations of electronic oscillator

			2500 K	1500 K
C_{60}:	$\langle E\rangle$	(10^3cm^{-1})	240	124
	ΔE	(10^3cm^{-1})	22	13
C_{42}:	$\langle E\rangle$	(10^3cm^{-1})	165	85
	ΔE	(10^3cm^{-1})	26	10

Table 3.2: Mean internal energy and standard deviation for the Gaussian distribution of internal energy of flakes carbon cluster isomer at two gas temperature and for two sizes. These quantities have been deduced from the vibrational partition function (relation 3.34).

strengths from one electronic state to another. The displacement of the maximum of the spectrum with the temperature does not coincide with the Wien's displacement law. Indeed, the $\lambda_{max}T$ product corresponding the peak of the fitting function (left panel of figure 3.26) indicates the values 3060 µm· K (for 1500 K) and 2950 µm· K (for 2500 K) wheareas, for Wien's displacement law, $\lambda_{max}T = 2898$ µm· K. The vibrational contributions in the emission spectra are localized below 2200 cm^{-1}, and are hidden in the electronic contribution.

Emission spectra displayed in figure 3.26 can be viewed as the spectral exitance for which the best fit is a modified Planck function with a ν^5-dependence at the numerator instead of the ν^3-dependence for the Planck's function. An analytical expression of the spectral exitance is obtained by taking into account not only the spontaneous electronic emission but also the stimulated electronic emission from the photon gas in thermodynamical equilibrium with the carbon cluster gas. Then, the spectral exitance $M_{rec}(\nu{,}T)$ (W/Hz/m^2), in the approximation of continuous spectral density of electronic states over the isomer set, is expressed by

$$M_{elec}(\nu;T) = \frac{1}{S} \times h\nu[A_{elec}(\nu;T) + A^{sti}_{elec}(\nu;T)]\rho_{elec}(\nu) \tag{3.40}$$

with $h\nu$ the emitted photon energy, $S = 4\pi < R_g >^2$ the surface of flake carbon clusters, $< R_g >^2$ the mean gyration radius of flake carbon clusters (5.2 Å for C_{60} and 4.3Å for C_{42}) and ρ_{elec} the spectral density of electronic states over the flake isomer set which is approximately linear-dependent with ν below 40 000 cm^{-1} ($\rho_{elec} \propto \nu$). $A_{elec}(\nu;T)$ is the spontaneous electronic emission and $A^{sti}_{elec}(\nu;T)$ is the stimulated electronic emission related to $A_{elec}(\nu;T)$ by means of Einstein's relations:

$$A^{sti}_{elec}(\nu;T) = \frac{A_{elec}(\nu;T)}{e^{\beta h\nu} - 1} \tag{3.41}$$

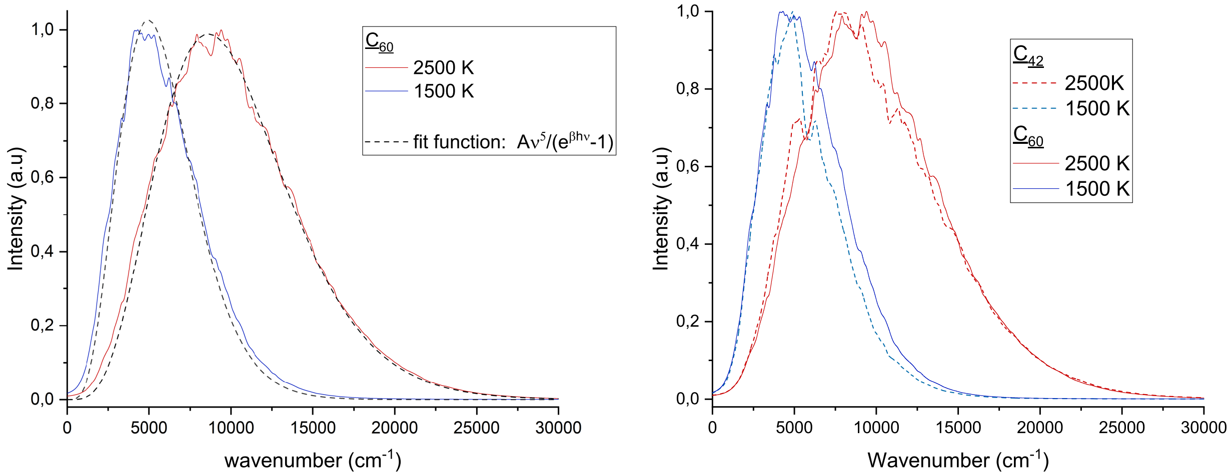

Figure 3.26: Simulated emission intensity spectra of C_{60} and C_{42} flake carbon clusters. Panel (a): comparison of C_{60} for two temperatures. The best fit is a modified Planck's function which gives the temperature 2499.4 ± 0.4. Panel (b): comparison between two sizes. The computed histogram emission spectra have been convolved by a lorentzian function (FMWH=300 cm^{-1}).

From expressions 3.39, 3.40 and 3.41, we obtain

$$M_{elec}(\nu;T) = \frac{eh^4\beta^2}{8\pi m_e\epsilon_0 c^3} \times \frac{<\frac{f(\nu)}{\nu(\text{eV})}>}{<R_g>^2} \times \frac{\nu^5}{e^{\beta h\nu}-1} \tag{3.42}$$

with $\beta^{-1} = k_B T$, $<\frac{f(\nu)}{\nu(\text{eV})}>$ a mean quantity (over the flake isomer set) which is not ν dependent (equals to 3.4 $\cdot 10^{-3}$ eV^{-1} for C_{60} and C_{42}) and $f(\nu)$ the electronic oscillator strength from electronic state with $h\nu$ energy to the ground electronic state. The ν^5-dependence of the exitance is understood as follows: 1) a linear contribution comes from the spectral density of electronic states 2) a linear contribution comes from the hν energy of emitted photons (this contribution take also place in Planck's function) 3) a ν^3-dependence stems from the spontaneous emission of excited electrons originating from two contributions, one linear dependence coming from the electric dipole transition moment and a ν^2-dependence from the spectral density of electromagnetic modes (also taking place in Planck's function).

Another difference with the blackbody exitance is the fact that at low frequencies ($h\nu \ll k_B T$) the carbon clusters exitance decreases like T^{-1} (equation 3.42) which is in contradiction with Rayleigh-Jeans law. The explanation is that, when the temperature increases, low electronic states are depopulated in favor of higher electronic states. Indeed, there cannot be more than one electron per electronic state (two with spin degree of freedom). This depopulation does not occurs for photon modes (purely blackbody radiation). The β^2 term in equation 3.42 comes from the electronic partition function.

Emissivity

The emissivity $\epsilon(\beta h\nu)$ is defined as follows

$$\epsilon(\beta h\nu) = \frac{M_{elec}(\beta h\nu)}{M^o_{elec}(\beta h\nu)} \tag{3.43}$$

with M_{elec} the spectral exitance emitted by our flake carbon cluster gas, M^o_{elec} the blackbody spectral exitance and $\beta^{-1} = k_B T$. The mean total emissivity ϵ_{tot} is defined as following

$$\epsilon_{tot} = \frac{\int_0^\infty M_{elec}(\nu;T)d\nu}{\int_0^\infty M^o_{elec}(\nu;T)d\nu} \tag{3.44}$$

From the simulated spectra, we obtained the relative spectral exitance. Thus, it has been possible to draw the ratio $\epsilon(\beta h\nu)/\epsilon_{tot}$ (figure 3.27). However ϵ_{tot} has to be determined analytically. We see on figure 3.27 that the emissivity of C_{42} and C_{60} flakes increases quadratically with the frequency and decreases with temperature. By integrating (3.42) over frequencies and all directions, Stefan-Boltzmann law and supposing that the spectral density of electronic levels over all the isomer set ρ_{elec} is ν^n-dependent, we obtain

$$\epsilon(\beta h\nu) = \epsilon_{tot} \times \frac{\pi^4}{15} \frac{1}{\mathit{\Gamma}(n+5)\zeta(n+5)} \times (\beta h\nu)^{n+1} \tag{3.45}$$

with

$$\epsilon_{tot} = \frac{15}{\pi^4} \frac{\mathit{\Gamma}(n+5)\zeta(n+5)}{\mathit{\Gamma}(n+1)} \frac{eh}{4\pi\epsilon_0 c m_e} \times \frac{< \frac{f(\nu)}{\nu(eV)} >}{< R_g >^2} \tag{3.46}$$

$\mathit{\Gamma}$ and ζ are respectively gamma and Riemann's zeta function. According to the inset of figure (3.27), we can state that n=1 which allow to reduce the two latter expressions as follows

$$\epsilon(\beta h\nu) = 0.053 \times \epsilon_{tot} \times (\beta h\nu)^2 \tag{3.47}$$

with

$$\begin{cases} \epsilon_{tot} = 4.1 \cdot 10^{-4} \text{ for } C_{60} \text{ flakes} \\ \epsilon_{tot} = 6.0 \cdot 10^{-4} \text{ for } C_{42} \text{ flakes} \end{cases}$$

The ν^2-dependence of emissivity is explained by two independent quantities which are linearly increasing with ν : the spectral density of electronic levels ρ_{elec} over thousands of flakes and the electric dipole moment transition between an excited electronic state and the ground electronic state. Of course, in the case of our flake carbon clusters, ρ_{elec} is no more linearly increasing above 50 000 cm^{-1} (see the appendix). Nevertheless, very high internal energies (and temperatures) are needed to detect any emission at energies

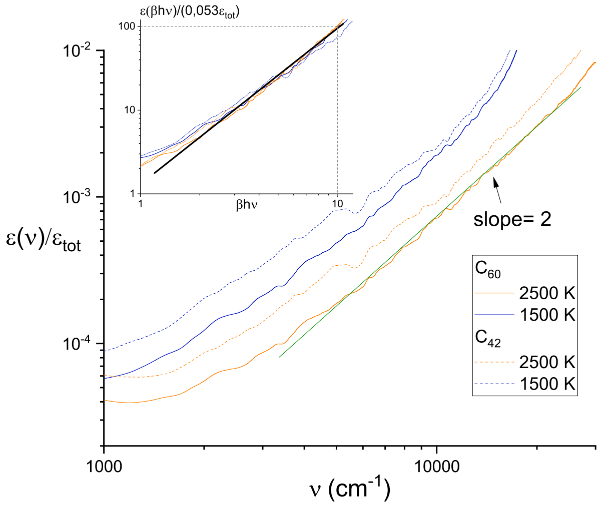

Figure 3.27: Mean emissivities for C_{60} and C_{42} at different temperature and deduced from the simulated emission spectra of figure 3.26 with the ϵ_{tot} calculated from expression (3.46). The inset figure illustrates expression (3.47) with a linear fit (black line). A numerical artifact prevents us to display the emissivity above 30 000 cm^{-1}. This artifact stems from the fraction of the two exitance in the expression 3.43. Indeed, these two quantities become very low at high internal energies and the fraction increases indefinitely (physically not acceptable) with the internal energies.

above 50 000 cm^{-1} for which dissociation becomes highly competitive with electronic deexcitation rates and emission above 30 000 cm^{-1} is negligible for temperatures we considered in this work. This is why, in our analytical calculation, we supposed $\rho_{elec} \propto \nu$ over all the frequency range (0 to ∞). It should be noted that relation 3.47 is not available when $\beta h\nu$ is lower than 2 (as shown in figure 3.27) because the vibrational deexcitation rate have not been taken into account in relation 3.42, and it is no more negligible below 2500 cm^{-1} (see the previous work).

By simulating the emission spectra of flake carbon cluster gas at fixed temperature, in addition to finding a blackbodylike emission, we unambiguously determined the quadratic frequency dependence and the temperature dependence of the mean emissivity for C_{60} and C_{42} flake carbon clusters. The total emissivity seems to be around 10^{-4}. There is no conclusion on the size-dependence of the emissivity.

Several works indicate that carbon clusters total emissivity should be around 10^{-5}-10^{-3} Barran et al. (1997); Hedén et al. (2005); Nakai et al. (2001); Kolodney et al. (1995). However these studies derive total emissivities by investigating either buckminsterfullerene radiative cooling or radiative cooling of C_{60}, C_{70} and C_{84} fragments. To our knowledge, no experiments have been done over a large set of C_{60} or C_{42} isomers. Nevertheless, as highlighted above, we considered only the electronic density of states over the large set and ignored vibrational structure of isomers. Thus, this study is valuable if a large set of carbon clusters of several sizes, say C_{30}-C_{100}, have a quadratically increasing electronic density of states.

Appendix

Electronic spontaneous emission rate calculation

We show the equivalence between the analytical expression of the spontaneous electronic radiative de-excitation rate and the way we computed it. Spontaneous electronic emission rates (section 3 equation 3.38) for the $n \to 0$ transition at internal energy E for an isomer is given by

$$A_{elec}(\nu_n; E) = A_n \times \frac{\rho_0(E - h\nu_n)}{\sum_i \rho_0(E - h\nu_i)} \tag{3.48}$$

with A_n the electronic fluorescence rate for the n $\to$ 0 transition, $h\nu_i$ the electronic energy level of the i^{th} state and $\rho_0(E)$ the harmonic VDOS in the electronic ground state. The sum is done over all accessible electronic excited states (equation 2.9 in chapter 2). By defining the electronic density of states ρ_{elec}, we write the previous relation as

$$A_{elec}(\nu_n; E) = A_n \times \frac{\rho_0(E - h\nu_n)}{\int_0^E \rho_0(E - \xi)\rho_{\text{elec}}(\xi)d\xi} \tag{3.49}$$

By the way, $\rho_0(E - \xi) = 0$ for $E < \xi$, thus we rewrite relation 3.49 as

$$A_{elec}(\nu_n; E) = A_n \times \frac{\rho_0(E - h\nu_n)}{\int_0^\infty \rho_0(E - \xi)\rho_{\text{elec}}(\xi)d\xi} \tag{3.50}$$

From all $A_{elec}(\nu_n; E)$, it is possible to find an expression of the spontaneous electronic emission rate at temperature T:

$$A_{elec}(\nu_n; T) = \int_0^\infty P(E; T) \times A_{elec}(\nu_n; E)dE \tag{3.51}$$

with E the internal energy, $P(E; T)$ the probability of an isomer to have the internal energy E at temperature T. $P(E; T)$ is defined by

$$P(E; T) = \frac{ge^{-\beta E}}{Z} \tag{3.52}$$

with $\beta = (k_B T)^{-1}$, E the internal energy, g the degeneracy at E and Z the partition function. The degeneracy is written as

$$g = \rho_0(E) + \rho_0(E - E_1) + ... + \rho_0(E - E_n) \text{ with } E_n < E < E_{n+1} \tag{3.53}$$

which is also written by

$$g = \int_0^E \rho_0(E-\xi)\rho_{\text{elec}}(\xi)d\xi = \int_0^\infty \rho_0(E-\xi)\rho_{\text{elec}}(\xi)d\xi \tag{3.54}$$

Thus, the partition function Z reads as

$$\begin{aligned}
Z &= \int_0^\infty (\int_0^\infty \rho_0(E-\xi)\rho_{elec}(\xi)d\xi)e^{-\beta E}dE && (3.55)\\
&= \int_0^\infty (\int_0^\infty \rho_0(E-\xi)\rho_{elec}(\xi)e^{-\beta E}dE)d\xi && (3.56)\\
&= \int_0^\infty (\int_0^\infty \rho_0(x)\rho_{elec}(\xi)e^{-\beta(x+\xi)}dx)d\xi && (3.57)
\end{aligned}$$

Thus,

$$\begin{aligned}
Z &= \int_0^\infty \rho_0(x)e^{-\beta x}dx \times \int_0^\infty \rho_{elec}(\xi)e^{-\beta\xi}d\xi && (3.58)\\
Z &= Z_{vib} \times Z_{elec} && (3.59)
\end{aligned}$$

Finally, we deduce the expression of the probability for an isomer to have internal energy E located in a thermal bath at temperature T as follows

$$P(E;T) = \frac{\int_0^\infty \rho_0(E-\xi)\rho_{elec}(\xi)d\xi}{Z_{\text{vib}}Z_{elec}}e^{-\beta E} \tag{3.60}$$

From relations 3.60 and 3.49, we rewrite the emission rate 3.51 at fixed temperature as follows

$$\begin{aligned}
A_{elec}(\nu_n,T) &= \int_0^\infty \frac{\cancel{\int_0^\infty \rho_0(E-\xi)\rho_{elec}(\xi)d\xi}}{Z_{vib}Z_{\text{elec}}}e^{-\beta E} \times \frac{A_n \times \rho_0(E-h\nu_n)}{\cancel{\int_0^\infty \rho_0(E-\xi)\rho_{\text{elec}}(\xi)d\xi}}dE && (3.61)\\
&= \frac{A_n}{Z_{vib}Z_{\text{elec}}}\int_0^\infty \rho_0(E-h\nu_n)e^{-\beta E}dE && (3.62)\\
&= \frac{A_n}{Z_{vib}Z_{\text{elec}}}\int_0^\infty \rho_0(E)e^{-\beta E}e^{-\beta h\nu_n}dE && (3.63)\\
&= \frac{A_n}{\cancel{Z_{vib}}Z_{\text{elec}}}e^{-\beta h\nu_n} \times \cancel{Z_{vib}} && (3.64)\\
A_{elec}(\nu_n,T) &= A_n\frac{e^{-\beta h\nu_n}}{Z_{elec}} && (3.65)
\end{aligned}$$

The emission rates at fixed temperature T obtained in the canonical framework in section 3 (equation 3.38) is recovered here.

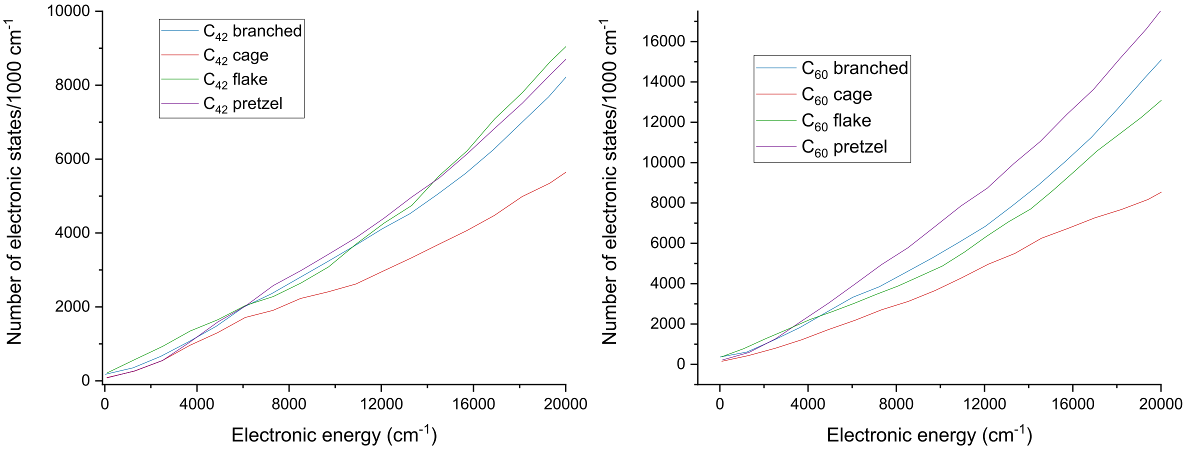

Figure 3.28: Electronic density of states per 1000 cm^{-1} for all families of C$_{60}$ and C$_{42}$ carbon clusters. One thousand isomers for each family and size.

Electronic density of states of C$_{60}$ and C$_{42}$ carbon clusters

Figure 3.28 shows the electronic density of states for each family of C$_{42}$ and C$_{60}$ carbon clusters. The linear dependence of electronic density of states below 40 000 cm^{-1} internal energy that we assumed in section 3 for analytical calculation seems to be a good approximation.

Emission spectra from other C$_{60}$ carbon cluster family

Carbon clusters are classified among four families: cages, flakes, pretzel and branched. We simulated the emission spectra of all C_{60} carbon clusters as we did for flakes (see 3) and we show in figure 3.29 emission spectra from a set of one thousand C$_{60}$ isomers for each family at 2500 K. Mean total emissivity ϵ_{tot} of the four families are found to be around 10^{-4}. All emission spectra are superimposed which reveals that the emission spectra profile of a large set of carbon clusters isomers does not on the geometrical structure of carbon clusters.

Supplementary results

Relationship between $< E >$, ΔE and T in carbon clusters

We can check, for our carbonaceous clusters, the relation between the average internal energy $< E >$ and the temperature T. We know that the average internal energy is

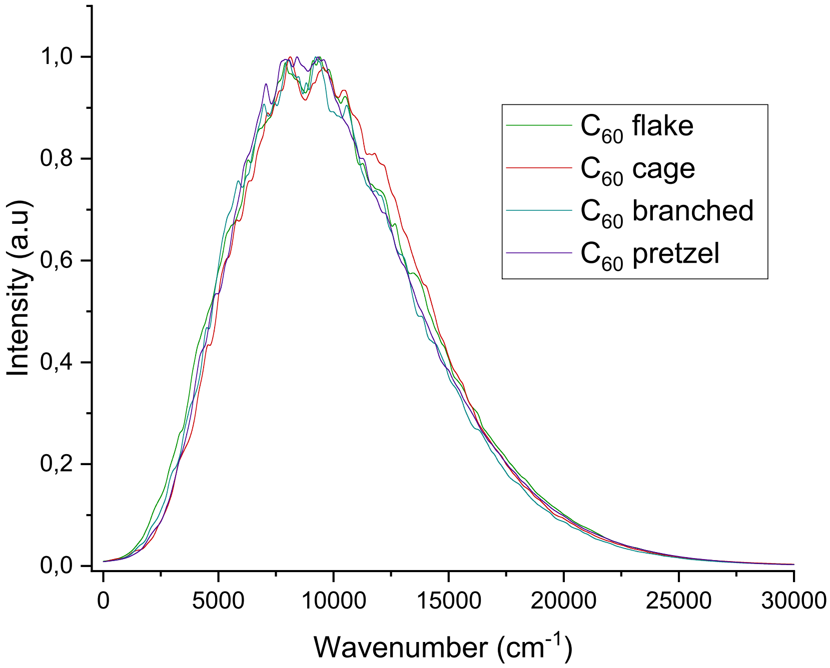

Figure 3.29: Normalized emission spectra of C_{60} isomer at 2500K from all families computed as described in section 3 and 3.

given by

$$< E >= \frac{\int_0^\infty E\rho_{vib}(E)e^{-\beta E}dE}{\int_0^\infty \rho_{vib}(E)e^{-\beta E}dE} \tag{3.66}$$

with E the internal energy and ρ_{vib} the vibrational density of states that we calculate in the semi-classical approximation. ρ_{vib} is expressed as (chapitre 2, equation 2.7):

$$\rho_{vib}(E) = \frac{(E + E_z)^{g-1}}{(g-1)!\prod_{i=1}^{g} h\nu_i} \tag{3.67}$$

From relations 3.66 and 3.67, the result is $< E >= gk_BT$, with g the vibrational degree of freedom. However, we must also take into account the zero-point energy that we add in an *ad hoc* way, which gives

$$< E > +E_z = gk_BT \tag{3.68}$$

Figure 3.30 shows the internal energy calculated by the simulation (green dotted), namely computation of relation 3.66 by an exact counting of $\rho(E)$ (Beyer-swinehart algorithm, section 2 of chapter 2) and the values of gk_BT (black dotted). When the internal energy is sufficiently large (large compared to E_z) then the relation (3.68) is

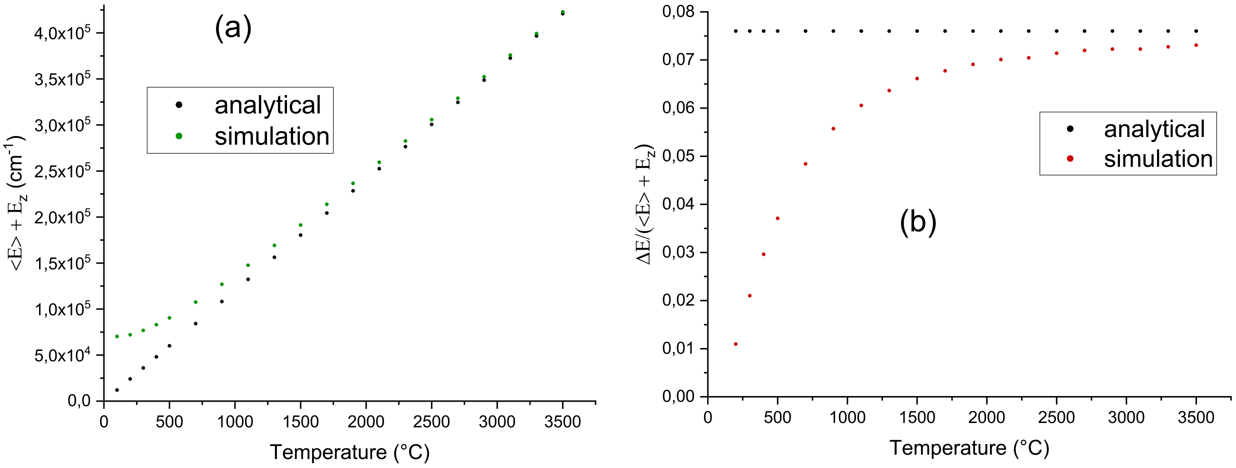

Figure 3.30: Simulation performed for an arbitrarily chosen flake. This simulation result is the same for any other carbon cluster at fixed size. (a): this figure illustrates the relation 3.68. In green, the simulated internal energy via the vibrational partition function. The zero-point energy has been added *ad hoc*. In black, the relation 3.68 obtained analytically for internal energies larger than E_z. (b): this figure illustrates the relation 3.69. In red, the ratio between the standard deviation by the internal energy. In black, $\frac{1}{\sqrt{g}}$ for g=173.

recovered by the simulation. At internal energies similar to E_z, the relation (3.68) is not valid anymore. The standard deviation of the internal energy is defined as

$$\varDelta E = \sqrt{< E^2 > - < E >^2}$$

The calculation in the semi-classical approximation of the harmonic vibrational density of states gives $\varDelta E = \sqrt{g} \times k_B T$. Using the relation (3.68), we obtain

$$\frac{\varDelta E}{< E > + E_z} = \frac{1}{\sqrt{g}} \tag{3.69}$$

In textbooks dealing with statistical mechanics, we are used to see the relation between $< E >$ mean energy and its standard deviation $\varDelta E$ of a system composed of N particles expressed by $\frac{\varDelta E}{E} \approx \frac{1}{\sqrt{N}}$ to translate the fact we can neglect the energy distribution for large systems. It is remarkable that a strict equality is obtained in our case (with $g = 3N - 6$, N the number of atoms in the cluster).

Conclusion

Even if it has not been explicitly said above, these three parts are related to each other. We tried to better understand recurrent fluorescence occuring in large carbon clusters and we investigated, in isolated conditions, the competition between recurrent and vibrational fluorescence during the cooling cascade in terms of internal energy, size and shape of carbon clusters (section 3). This study was necessary to interprete simulated emission spectra of a large set of carbon clusters illuminated by a 20 000 K star or interstellar radiation field (section 3). Indeed, the very interesting result of section 3 is the profile and the intensity of the emission spectra in the near-IR region which has an exponential-like profile. This is explained by the "EGL-type" dependence of the recurrent fluorescence (from an electronic state) with the electronic energy. The "EGL-type" dependence explains also the exponential decrease of the emission spectra profile of a large set of carbon clusters at fixed temperature. The difference between the emission spectra in interstellar conditions and that of temperature fixed conditions is that for the first the emission spectra is the result of the whole radiative relaxation. Nevertheless, we checked analytically that the emission spectra in the near-IR region obtained from the overall cooling cascade has approximately an exponential-like profile. We gave some observable and measurable quantities. We calculated that the mean total emissivity of large carbon clusters should be around 10^{-4}. The emissivity is ν^2 and T^{-2}-dependent, at least for optical wavelength above 500 nm (but it should be the case up to 400 nm). We found these results from a molecular approach and that allowed us to bridge a macroscopic quantity (emissivity) to microscopic quantities (electronic levels, oscillator strengths). We are particularly excited by the idea to make the bridge between condensed matter properties and clusters properties. In interstellar medium context, we compared large carbon clusters emission spectra in the near-IR to Sellgren's 1983 observation between 1 and 5 µm in some reflection nebulae. As suspected by K.Sellgren, C_{60} carbon clusters (or similar sizes) could be at the origin of the observed profile. We concluded that C_{60} cages (or species of similar sizes but still cages) could be the main carriers in the observed near-IR emission spectra and that implies C_{60} cages abundance in these reflection nebulae is of the order of 0.1 % of the available carbon.

4. Experimental setup: FIREFLY infrared spectrometer

Contents

Radiative relaxation in large carbon clusters: recurrent fluorescence versus vibrational emission 60

Introduction 60

Methods 63

Kinetics of radiative cooling in carbon clusters: selected cases 71

Behavior over a large set 79

Concluding remarks 84

Appendix 86

Supplementary result: Exponential decay profile of emission spectra from a whole relaxation cascade 87

Infrared emission of $C_{n=24,42,60}$ carbon clusters induced by stochastic heating 91

Introduction 95

Methods 96

Results 99

Conclusions 108

Absorption cross-section and spectral energy distribution 109

Calculation of the detected emission power density from C_{60} cages in NGC 7023 109

Error estimation 111

Large carbon clusters emissivity: a molecular approach 114

Introduction 114

Theoretical methodology 115

Emission spectra 117
Emissivity 120
Appendix 122
Supplementary results 124
Conclusion 127

Experiments that have been carried out in this thesis consist in detecting the vibrational fluorescence induced by UV excitation of benzene derivatives in the gas phase. One strength of this detection is the possibility to follow the relaxation dynamics via a careful analysis of the time-dependent emission spectra. Besides relaxation dynamics, it is also possible to study the radiationless processes depending on the presence or not of vibrational emission, as it has been done by G. Féraud *et al.* (Féraud et al., 2014) with FIREFLY for the “Channel three” of benzene. Additionally, vibrational emission can be an observable for internal energy of emitters (Durana and McDonald, 1976).

UV laser induced infrared fluorescence experiments have been done by means of a homemade IR spectrometer called FIREFLY (Fluorescence in the InfraRed from Excited FLYing molecules). Originally FIREFLY was developed as an add-module to existing experimental setup known as NANOGRAINS, from which a molecular beam of PAHs and large carbon clusters mixture is produced by a low-pressure flat flame (combined with a laval nozzle).

My first task in the laboratory was to install NANOGRAINS in the building we just moved in (with Joffrey Fréreux). Once this task was successfully achieved, I could re-assemble and optimize FIREFLY. Since Joffrey Fréreux implemented several modifications to the NANOGRAINS setup in an attempt to reach a temperature of 50 K in the molecular beam, the idea was to couple these two experimental setups to generate a 50 K molecular beam of PAHs and carbon clusters and analyze emission spectra after UV excitation. Unfortunately, despite Joffrey Fréreux efforts, the goal reaching a temperature of 50 K has proven to be very challenging because of several technical issues. This is why my experimental works were entirely focused on FIREFLY and the coupling of the two experimental setups could not be performed in the time-frame of my PhD thesis.

Before describing the FIREFLY setup, a short review of previous UV laser induced IR fluorescence (UV-LIIRF) experiments will be given

Previous IR fluorescence experiments

Here, we only talk about UV-LIIRF experiments which can be considered as a subset of laser-induced fluorescence experiments. To our knowledge, UV-LIIRF experiments have been first used for studying the collisional energy transfer between highly vibrationally excited and non-excited large molecules (> 10 atoms) and between highly vibrationally excited large molecules and buffer gas atoms. Smith & Barker transposed to the azulene case the vibrational energy transfer experiments for small molecules (such as OCS) pumped by CO_2 laser (≈ 10 µm) (Mandich and Flynn, 1980b,a; Smith and Barker, 1981). The idea was to get insight in energy transfer per collision by detecting the time-resolved emission signal of C-H stretching mode around 3.3 µm by excitation at 337, 600, and 670 nm and using theoretical models that we showed in chapter 2. This study has been done using several buffer gases for azulene (Rossi and Barker, 1982b; Rossi et al., 1983), benzene (Yerram et al., 1990), and benzene derivatives (Yerram et al., 1990; Barker and Toselli, 1993). These experiments contributed to the understanding of collisional energy transfer between highly vibrationally excited large molecules and non excited ones or rare gas atoms.

Experiments addressing the PAH hypothesis (1984-1985, (Leger and Puget, 1984; Allamandola et al., 1985)) started from 1989 with Cherchneff & Barker's work in which a wavelength-resolved and time-resolved detection of the IR emission of highly vibrationnally excited azulene induced by 308 nm excitation has been done. This was the first measurement of the 3.3 µm emission band of a PAH and its anharmonicity (Cherchneff and Barker, 1989). They used a circular variable filter (resolution power around 0.01). The same study has been extended to benzene and naphthalene (Brenner and Barker, 1992) (both excited at 248 and 193 nm) and they observed overtones from C-H stretching modes at 1.67 µm. These studies revealed also that the 3.3 µm emission feature should appear in all neutral PAH molecule and that it will be complicated to identify an individual PAH molecule from the Unidentified Infrared Bands (UIB). Shan *et al.* detected the IR emission of benzene and benzene with several methyl groups (toluene, xylenes, mesitylene, and durene after excitation at 193 nm) by means of a monochromator and a dispersion system (Shan et al., 1991) (resolution= 0.025 µm= 23 cm^{-1}). For all these species, besides the 3.3 µm feature they also detected the 3.4 µm emission feature. Williams & Leone detected the time-dependent emission spectra of naphthalene excited at 193 and 248 nm (Williams and Leone, 1995). A time-resolved Fourier transform infrared emission technique was used (resolution 10 cm^{-1}). They observed that the 3.3 µm emission band is redshifted compared to the 3.3 µm absorption band and the redshift is highly dependent of the internal energy. They erroneously attributed the redshift to sequence bands of highly vibrationally excited naphthalene. Nowadays, we know that this kind of redshift observed in emission spectra is due to anharmonicity.

A big step forward has been done in the comprehension of UIB carriers when Schlemmer *et al.* confirmed experimentally that small neutral PAHs cannot be the carriers of UIB

(Schlemmer et al., 1994). Indeed, by UV-laser induced desorption with subsequent 248 nm excitation, they detected emission spectra (ranging from 3 to 8 µm) of naphthalene and pyrene using a Czerny-Turner monochromator cooled to 4 K and an IR photon counting detector (Single Photon InfraRed Emission Spectroscopy, SPIRES). They noticed that the measured wavelengths of emission features and their relative intensities do not match those of astrophysically observed (UIBs). Following this study, the same experimental setup has been used to detect emission from different classes of PAHs suspected, at that time, to contribute to UIBs (unsubstituted, methyl-substituted, hetero-substitued PAHs) (Cook et al., 1996). The wavelength was ranging from 3 to 15 µm, the 4K-cooled IR detector allowing wavelengths beyond 10 µm (Cook et al., 1998). They found discrepancies on relative intensities of UIBs and those of PAHs that they measured. The conclusion was that PAH cations could be the major contributor of UIBs. Saykally went further by investigating the emission spectra of pyrene cation (Kim et al., 2001). The experimental setup is the SPIRES setup interfaced with an ion beam apparatus. The relative intensities of pyrene cation emission spectra turn out to be consistent with those of UIBs and this experiment confirmed that PAH cations can be the major carriers of UIBs.
These UV-LIIRF experiments are part of results in the 1990's that support the PAH hypothesis and, nowadays, Unidentified Infrared Bands are called Aromatic Infrared Bands. To our knowledge, since Saykally's work, there is no more UV-LIIRF experiments of large species. The idea to interface FIREFLY with NANOGRAINS is actually in line with UV-LIIRF experiments in interstellar context conducted since Cherchneff & Barker's work.

Our work with FIREFLY is quite far from the astrophysical context. Indeed, in the astrophysical context, the ultimate goal is to study the emission spectra. In our work, we use the IR fluorescence to get insight in isomerisation reactions. Thus, we can assert that the experimental work in this thesis is aligned with earlier UV-LIIRF experiments in Barker's group about collisional energy transfer.

Cell and light sources

The gas phase dispersed UV-LIIRF experiment has been done by introducing the species of interest in a gas cell. We shall give in the first subsection the general description of the cell. In the second subsection, the physical conditions in the cell and the species inlet in the cell before UV-excitation are developed. The last subsection is dedicated to laser sources and blackbody used in our studies.

Cell description

A schematic representation of the cell that we used is shown in figure 4.1 and some pictures of the cell taken from different angles are shown in figure 4.2. The cell contains six branches of different lengths and directed along the three spatial directions. The UV laser beam axis is perpendicular to the IR detection axis and both are perpendicular to the pumping system and gas inlet axis (figure 4.1). Another cell branch is used for blackbody radiation when absorption spectra are recorded. The isotropic IR fluorescence region is located at the cell center and the volume of this region is around 30 cm^3. A 5 cm diameter KBr window between the emission region and FIREFLY has been used. There is also a KBr window (4 cm diameter) at the entrance of the blackbody radiation. The entrance window of the UV laser beam absorbs between 15% and 20% of the incident energy. In the upper panel of figure 4.2, we see that the arm containing the UV laser entrance window is longer than others. Indeed, it has been required to take the entrance window away from the emission region because of the pollution caused by the species on the UV laser entrance window, which could not be prevented only by the use of an argon flow at its vicinity. The deposited quantity is dependent on the species studies and on the UV irradiation time. The deposit is more important for highly substituted benzene (such as propylbenzene and ethylbenzene) and we cannot indefinitely increase argon flow as we shall see in the next subsection.

Argon is the buffer gas that we used for all the experiments. It is introduced by two paths at the same time: in the vicinity of the UV laser entrance window to protect it and by crossing the reservoir (not illustrated in figure 4.1) and mixing with the species of interest inside the reservoir before being introduced in the cell just above the UV-excitation region (figure 4.1 and 4.2). The cooling process is so fast ($\approx$ 10-100 µs) that the UV-excitation region and IR fluorescence region are considered to be the same.

Physical conditions monitoring inside the cell

The main physical parameter that is relevant for our experiment is the buffer gas (argon) partial pressure and studied species partial pressure (benzene derivatives). To have a close control of pressure conditions, we used a secondary pump. Indeed, our primary pump has a large pumping speed (Adixen Pfeiffer Vacuum PASCAL 2021SD, 300 L/min) and requires a bottleneck (valve) to limit the pumping speed. However, even the minimum valve aperture was sometimes not enough and therefore an important quantity of species were consumed. This is why we used a secondary pump (Pfeiffer Vacuum, HiCube 80 Eco, 15 L/s pumping speed for N_2) with lower pumping speed. Because the pressure in the cell is usually around 1 mbar, it is necessary to set a valve (bottleneck) upstream on the secondary pump and ensure there is high vacuum at its entrance (<

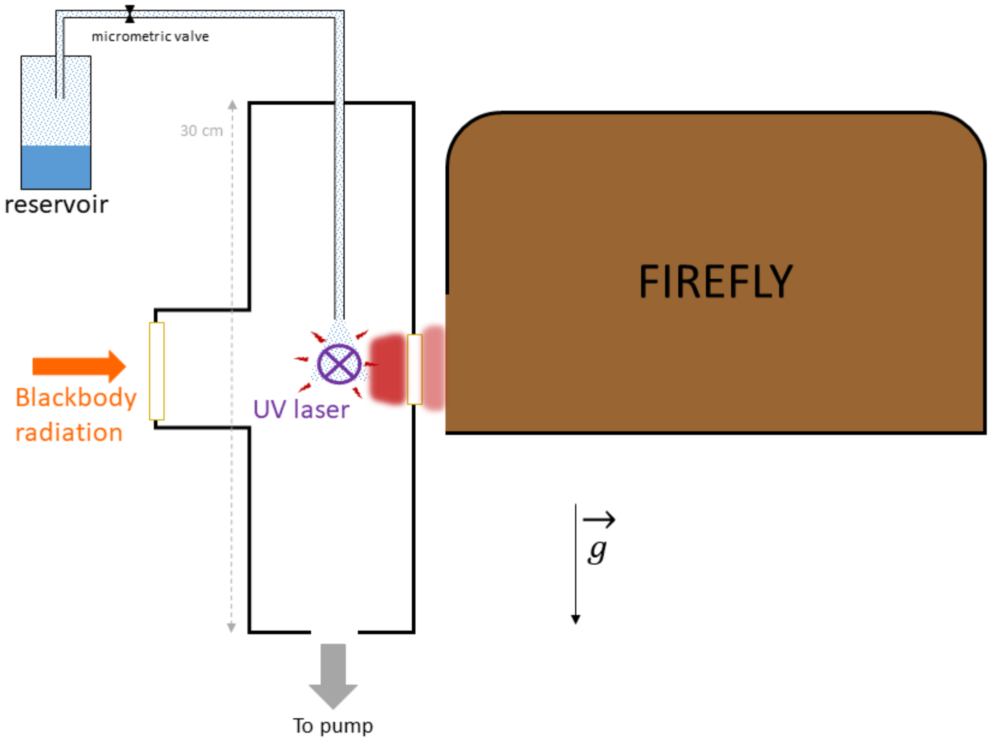

Figure 4.1: Side view illustration of the cell in which species of interest undergo radiative and collisional relaxation after excitation by UV photon (UV laser in violet). Species are leaked into the cell and their pressure is controlled by micrometric valve. The IR fluorescence experiment is done under stationary flow conditions. Blackbody radiation is used for absorption spectra measurements. The cell length is about 90 cm.

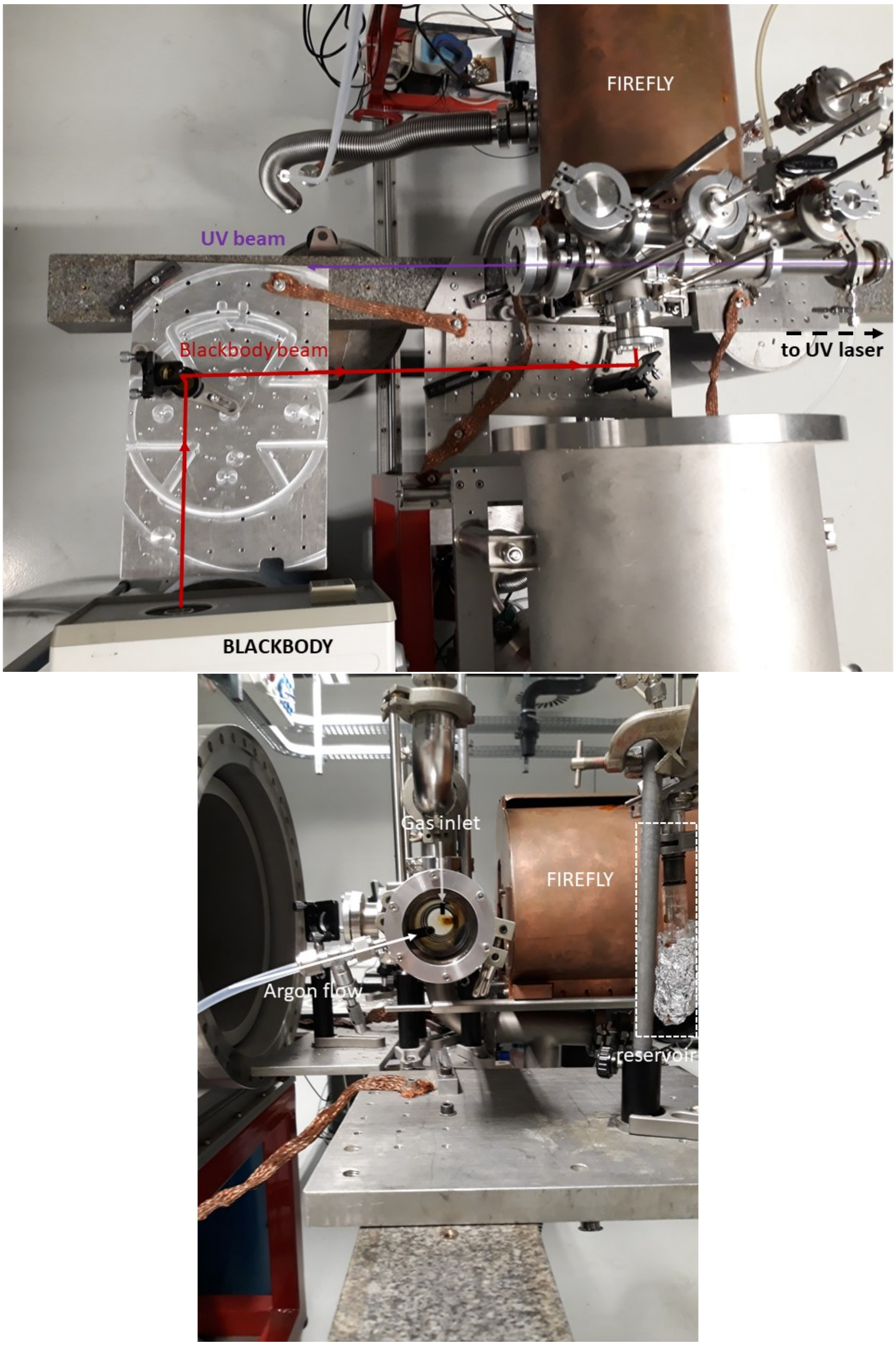

Figure 4.2: Upper image: Illustration of the UV laser pulses crossing through the cell. Blackbody beam trajectory before going through the cell. The IR spectrometer is placed inside a Faraday cage. Lower image: UV laser entrance window through which two pipes are visible. One of the pipes is used to argon flow injection in the vicinity of the UV laser entrance window and the other pipe is used for gas inlet connected to the reservoir containing the species to be investigated.

10^{-3}). Thus, with a careful control of the upstream valve of the secondary pump, it is possible to pump the cell with low pumping speed.
The two partial pressures were fixed as follows. First of all, we fix the argon flow going inside the cell thanks to a flowmeter (1 bar argon upstream on the flowmeter, Brooks 5850S, 50 NmL/min Ar). Then, we can adjust the upstream bottleneck of the secondary pump to have the desired argon partial pressure (usually about 1 mbar) which is equal, at this stage, to the total cell pressure. After that, we open the species reservoir with a micrometric valve without varying the upstream bottleneck of the secondary pump. The entrance flow of species is imposed by the valve opening and the species equilibrium vapor pressure. The subsequent total cell pressure increase is due to the partial pressure of the species. If the pressure in the cell is 1.1 mbar, that means the species partial pressure is 0.1 mbar because the argon entrance flow and the pumping flow remain unchanged. Actually, the accessible partial pressure of a species in the cell is dependent of its vapor pressure. Vapor pressures of investigated species are summarized in table 4.1. We could only detect IR emission of species with vapor pressures higher than 1 mbar. For benzonitrile and aniline, recorded emission spectra (and also absorption spectra) were very weak. Usually, in our experiments, the total pressure in the cell is around 1 mbar and this imply that the collision rate is much higher than IR fluorescence rate of highly vibrationally excited species. Thus, relaxation of our species after UV excitation is dominated by collisional cooling, except at very short times (< 1 µs) when dissociation or isomerisation rates are similar to collisional rate.

As explained in the previous subsection, a deposit of species is formed on the entrance window. In principle, the increase of argon flow on the entrance window should reduce the rate of deposit process. However, that increases the total cell pressure and, to maintain the prior pressure, we have to open the upstream valve of the secondary pump and ensure a secondary vacuum. This constraint prevents us from indefinitely increasing the argon flow at the vicinity of UV laser entrance window. This is why it has been useful to move the UV laser entrance window away from the gas inlet region by extending the branch (upper panel of figure 4.2).

Light sources

In our work, we used nanosecond pulsed lasers with wavelengths of 266, 213, and 193 nm. To generate the 266 nm and 213 nm wavelength pulses, we used a SURELITE Nd:YAG laser. 1064 nm photons from a Nd:YAG are doubled to obtain 532 nm and another frequency doubling is made to obtain 266 nm. The 1064 nm photons are added to 266 nm photons to generate 213 nm. The repetition rate of the laser was 20 Hz and the power was between 300 mW and 1300 mW with a beam diameter around 0.25 cm^2 just

Species	P_{vap} (mbar)
Benzene	130
Toluene	28
Cycloheptatriene	30
Phenylacetylene	2.6
Styrene	7
Propylbenzene	4.5
Ethylbenzene	9
Cumene	4
Aniline	< 1
Benzonitrile	1

Table 4.1: Approximative vapor pressures of species studied in this work. Values for 300 K.

before the entrance window(for which the absorption is estimated to be around 15–20% of the incident beam). Thus, the surface energy per pulse is estimated to span between 60 and 260 mJ/cm^2. We measured the emission signal of all species appearing in table 4.1 at 266 and 213 nm. Our intensity study (see chapter 5) revealed that many of these species displayed more than one-photon absorption processes for laser wavelengths we used.

For several months, we used a small ArF excimer to generate 193 nm laser photons (Neweks). We encountered several technical issues such as a strong parasitic signal induced by discharge inside the excimer laser with varying intensity from one pulse to the other. We highly reduced that parasitic signal by building a Faraday cage around the excimer laser and connecting it very carefully to the electrical ground. Because of a power cut, the thyratron of the excimer broke down and since its reparation we were unable to find again the laser power that we had before the breakdown (the power was almost 2 times weaker than before the breakdown). We suspected the impurities in the ArF bottle gas (we bought another one) or in the gas pipes (over several meters), the mirror alignment inside the laser and we even replaced the two mirrors inside the excimer. We concluded that the thyratron still causes malfunctions and has not been completely repaired. Thus, we borrowed for a few weeks another ArF excimer (Compex Pro 50 F) to finish our experiments. The laser was also operating at 20 Hz repetition rate. An estimation of the flux intensity was not possible because the spot of this excimer was very extended ($\sim$ 5 cm^2) and inhomogeneous.

For absorption spectra measurements, we used a blackbody source used at 800°C (OMEGA BB400, maximum temperature: 900 °C).

FIREFLY spectrometer

The emitted IR fluorescence photons are detected by a homemade IR spectrometer (FIREFLY). During our experiments, we noticed that the signal-to-noise ratio of recorded spectra is low because the IR fluorescence is, *de facto*, very weak. Thus, first of all, the preliminary work has been to reduce electrical noise with a very careful connection to the electrical ground of all components of the data acquisition system (computer, wires, supporting rails, etc). As shown in figure 4.2, FIREFLY is also placed in a Faraday cage to limit the surrounding electromagnetically induced noise. FIREFLY need also to be very close to the cell to detect maximum photons but without being in contact with it because of vibrations due to the pumping system.

Figure 4.3 illustrates the IR fluorescence acquisition system and the link between the main constituting components of FIREFLY. These are the circular variable filter which allows us to select wavelengths between 2.5 and 4.5 µm, the InSb IR detector with the

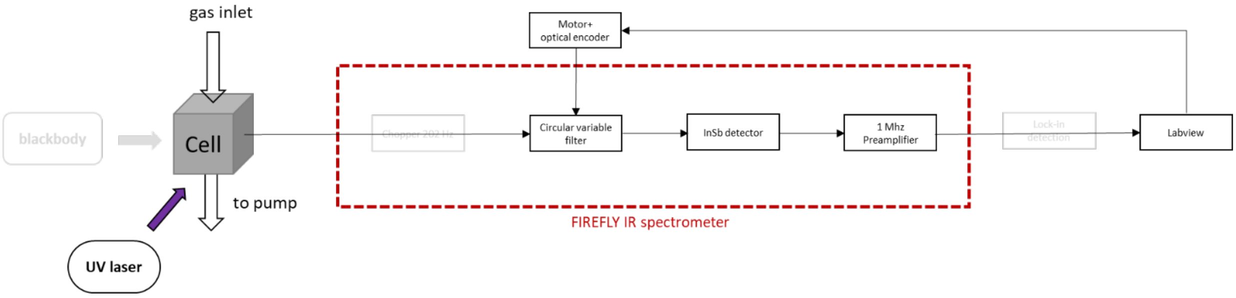

Figure 4.3: Schematic illustration of the acquisition data system for IR fluorescence photons detection for the emission configuration of FIREFLY.

associated preamplifier, a Labview programming used to record data and monitor the circular variable angular position. The data acquisition system is triggered externally by a photodiode signal detecting UV laser pulses.

FIREFLY can be used to record emission and absorption spectra. For these two cases, the setup is slightly different and the schematic illustration of data acquisition system is shown in figure 4.3 (for the emission configuration of FIREFLY) and figure 4.9 (for the absorption configuration). A detailed description of all components is given in the first subsection. In the second subsection, we shall introduce the absorption configuration of FIREFLY required for the calibration of the circular variable filter, the correction of the circular variable filter position non-reproducibility, and the estimation of the response function of FIREFLY, which are presented in the last subsection.

Constituting components of FIREFLY

As shown in figure (4.4), FIREFLY is constituted of mirrors, circular variable filters set on a filter holder mounted on a gearwheel and infrared detector. We describe them in the following subsections.

Circular variable filter

The radiative emission during the cooling is studied via time-resolved and wavelength-resolved signals. Emission spectra are obtained thanks to a band-pass circular variable filter (CVF).

We own three CVFs ranging from 2.45 to 14.5 µm and a replica of that of the ISOCAM spectrometer inside the ISO satellite (Cesarsky and Sargent, 1996). The CVF 1 ranges from 2.45 to 4.55 µm, CVF 2 from 4.26 µm to 7.72 µm and CVF 3 from 7.69 µm to 14.5 µm. To use CVF 3, a N_2-cooling system is required to limit blackbody radiation at 300 K (the maximum emission is at 9.5 µm) which was not the aim of our work. A technical problem prevented us from using CVF 2. Thus, we were led to use only the

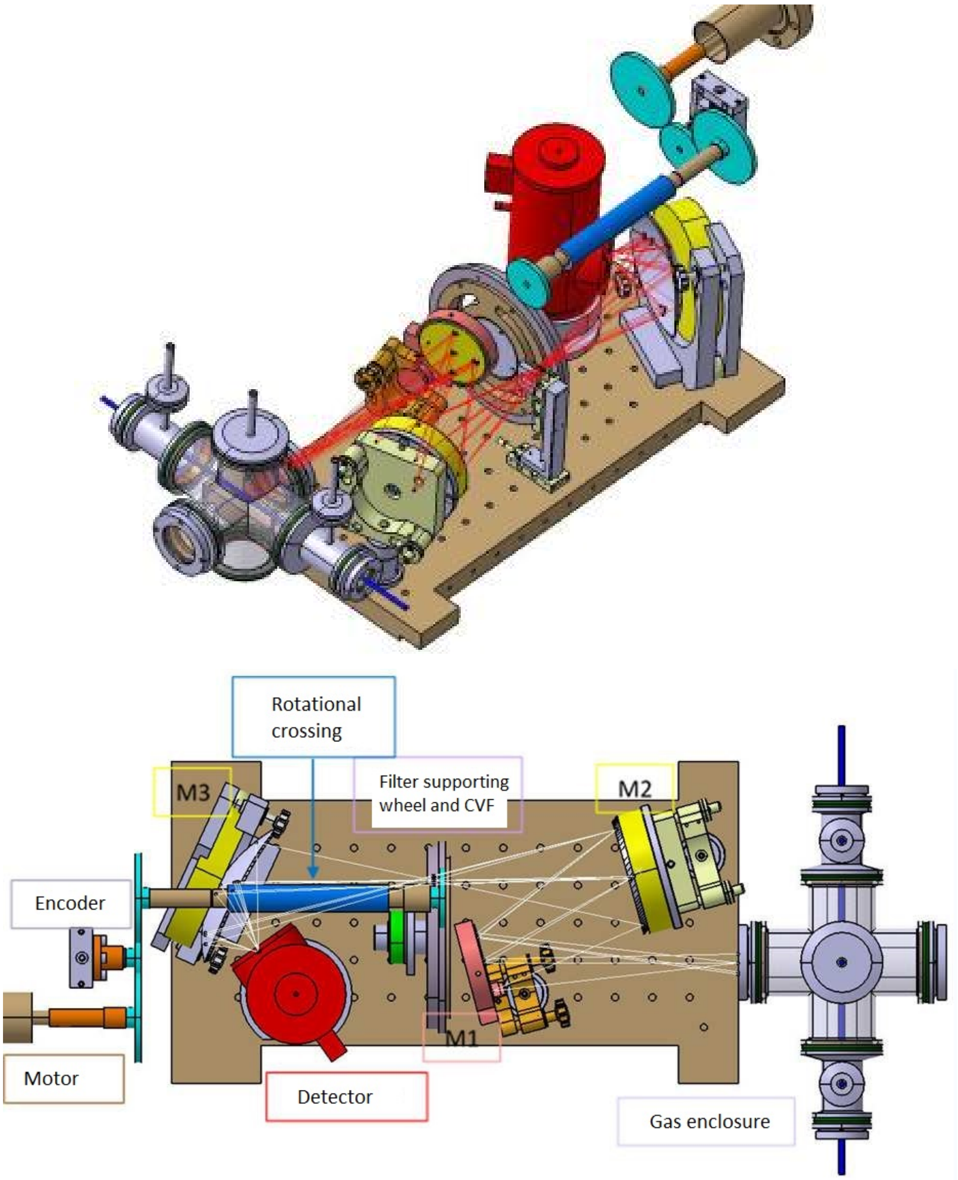

Figure 4.4: Illustration of FIREFLY and the cell. 3D illustration: the optical path followed by IR photons emitted during the cooling cascade are illustrated by red beams. During scans, FIREFLY is enclosed inside Faraday cage. 2D illutration: Top view of FIREFLY and the cell. The blue beam crossing the cell illustrates the UV exciting laser pulses. The main compounds of FIREFLY are also indicated. These schemas have been drawn by Thierry Chamaillé (CNRS engineer at Institut des Sciences Moléculaires d'Orsay).

Wavenumber (cm^{-1})		Wavelength (µm)		Angular resolution
σ	$\delta\sigma$	λ	$\delta\lambda$	$\mathcal{R}$
2432	42.5	4.11	0.07	57
3193	85	3.13	0.08	38
4013	113	2.49	0.07	35

Table 4.2: Estimation of the resolution from lower panels of figure 4.6.

CVF 1 (figure 4.5) and we limited our analysis between 2.5 and 4.5 µm.
Figure 4.6 shows the wavelength-dependence of the CVF 1 transmittance and some measured absorption profiles. From the lower panels of figure 4.6, we deduced estimations on the angular resolution (table 4.2) which is related to the spectral resolution. Given that the value of angular resolution of CVF 1, we cannot do high-resolution spectroscopic studies with FIREFLY. Indeed, we are unable to distinguish rotational structures and even hardly Fermi resonances.
These CVFs have been constructed in such a way to have a linear relationship between the angular position and the filtered wavelength. The calibration of CVF 1 is detailed in section 4. Emission spectra are recorded by rotating CVF 1 to sweep the wavelength range.

Angular position monitoring of the CVF

To monitor the CVF 1 angular position, we set it in a filter holder mounted on a gearwheel (FHG) composed of 255 teeth. A gear train is used to rotate the FHG by means of a stepper motor (figure 4.4). The stepper motor (Vacuum Generators RD6MGI with 9:1 gear reduction) is monitored by a programming interface (Labview) developed by Julien Vincent (CNRS engineer) and 3600 steps are needed so that the stepper motor makes a 360 degrees rotation. Also, the final gearwheel of the gear train and in contact with FHG is composed of 80 teeth, which implies that a FHG full rotation requires 255/80 rotation of the final gear. Thus, FHG full rotation requires $\frac{255}{80} \times 3600 = 11475$ motor steps. An optical encoder (Vacuum Generators XMOT34) has been connected to the stepper motor to position control and count the motor step.
Actually, there is a slight shift in angular position from one motor turn to the next. This effect is shown in figure 4.12. We shall see in more details (section 4) that this shift has a periodic dependence with the number of FHG full turns. These variations are partly explained by the fact that the teeth number of the FGH (255) is not a multiple of the teeth number of the gearwheel in contact with the FHG 80). The consequence is that from one motor turn to the next the contact point is not exactly the same. It turned out that this angular position shifting can be numerically corrected via Labview (see section

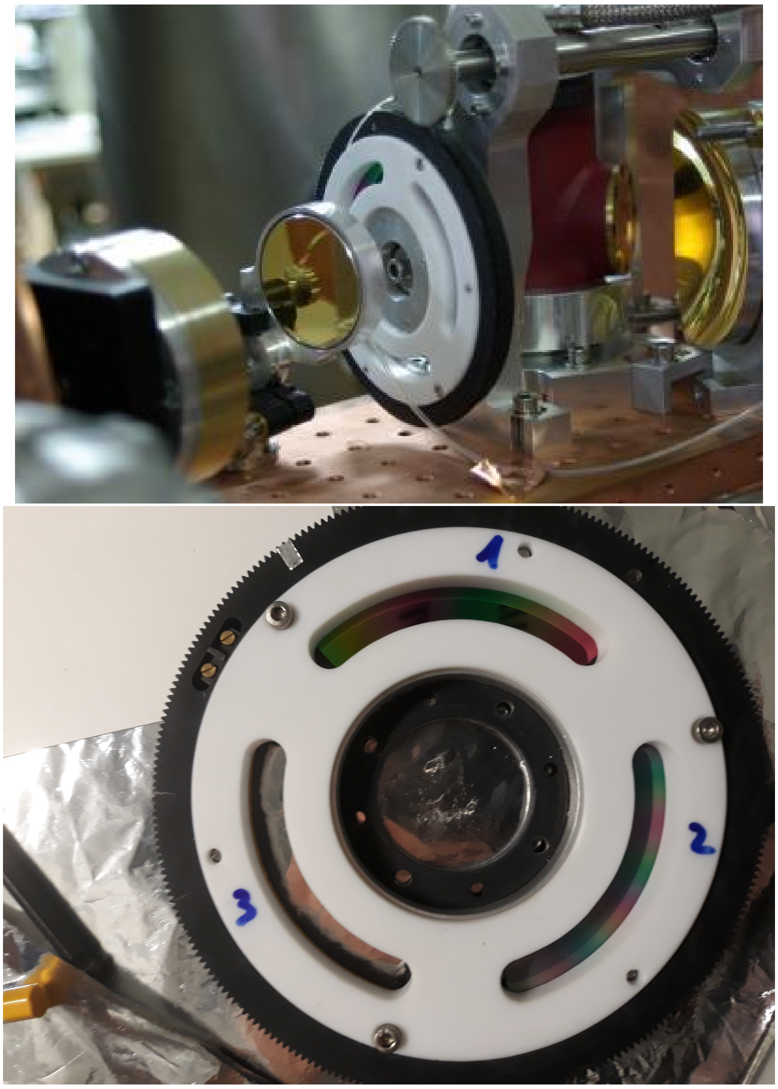

Figure 4.5: Upper image: The filter holder gearwheel set up in FIREFLY. Image extracted from Géraldine Féraud's PhD thesis (2012). Lower image: CVF 1 and CVF 2 are mounted on the filter holder gearwheel. Unfortunately, because of technical issues of the MCT detector, the CVF 2 could not been used.

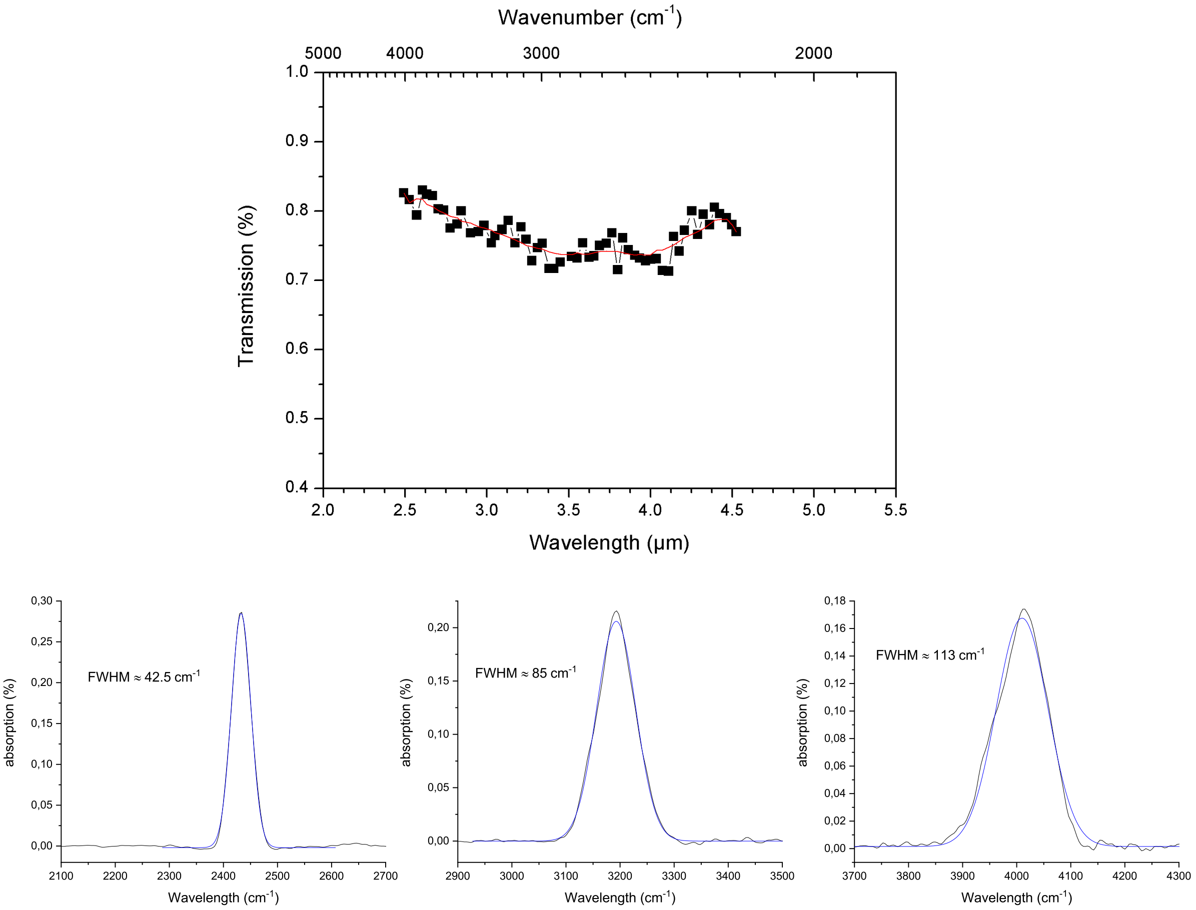

Figure 4.6: Upper panel: CVF 1 transmittance measured by Thomas Pino and Emmanuel Dartois by Fourier Transform IR spectroscopy in 2004. This figure has been extracted from Géraldine Féraud's PhD thesis (2012). Lower panel: from the same measurement, CVF 1 absorption around 2432 cm^{-1} (4.11 µm), 3193 cm^{-1} (3.13 µm) and 4013 cm^{-1} (2.49 µm) with a Gaussian fit in blue and indication of the full width at half maximum (FWHM).

4 for more details).

Mirrors

FIREFLY spectrometer contains three golden mirrors to converge IR emitted photons at the CVF 1 and subsequently at the IR detector. A gold layer has been deposited on these mirrors for a better reflection in the IR range. In the 2D representation (figure 4.4), mirrors denoted M1 (plane mirror) and M2 (ellipsoidal mirror) are used to make IR photons converge through the CVF 1, which is located between M2 and M3. The last M3 mirror (ellipsoidal mirror) makes IR photons converge into the IR detector. We oriented M1 and M2 to have a very localized spot on the interferential filter. Indeed, the more the spot is localized the better is the emission spectra resolution (up to reach the resolution of the CVF). The spot on the CVF is a disk of about 4 mm^2.

IR detector

The infrared InSb detector (Indium-Antimony) that we used for CVF 1 is based on photovoltaic effect. This effect consists in the creation of an electron-hole pair in a p-n junction by an incident photon with energy exceeding the forbidden gap energy of the semi-conductor (for InSb, the energy gap is around 0.23 eV = 1850 cm^{-1} at 80 K). The InSb detector is sensitive along the CVF 1 wavelength range (figure 4.7). Actually, we also planned to use the MCT detector (Mercury-Cadmium-Tellure), which is sensitive from 6 to 12 µm and allows to use CVF 2. InSb and MCT have the same focal point (two-color detector). Unfortunately, the MCT did not work. Indeed, before sending it to its manufacturer (IR associates), we ensured that the problem comes from the IR detector. Thus, we restricted our work in the 2.5 – 4.5 µm wavelength range by using the InSb detector only.

The InSb detector is a photodetector and has a better sensitivity and response time than thermodetectors. However, it has to be cooled to 77 K (liquid nitrogen) to lower thermal noise which induces low-lying transitions in the semiconductor material. The detecting element has to be vacuumed, otherwise water condensation occurs on its surface and results on a very strong absorption around 2.9 µm (figure 4.10).

The detector responsivity is more than 3 A/W. From that, we can estimate the photocurrent induced in the detector by the incident IR photons. The radiance at 3 µm of a 800 K blackbody from 1 cm^2 emission area is around 10^{-2} W $\cdot$ sr^{-1} $\cdot$ μm^{-1}. Because the detector is 2 m away from the detector, we have multiplied this quantity by the factor $(\frac{1\text{cm}}{2\text{m}})^2$ to obtain the radiance detected by the detector. Thus, by supposing there is 100 % transmission through all optical components, we estimate that the photocurrent

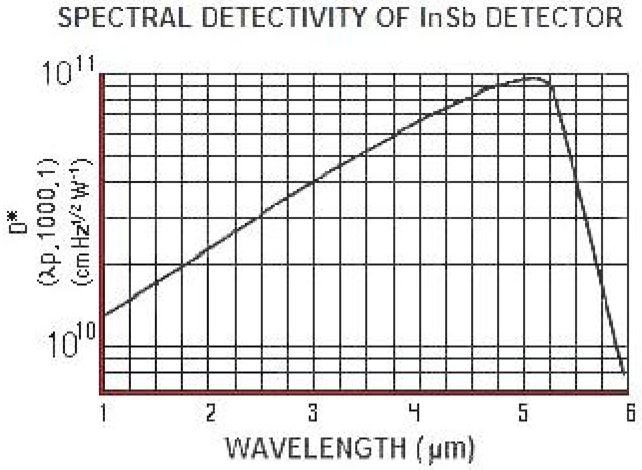

Figure 4.7: Spectral detectivity of InSb detector used for CVF 1 ranging from 2.5 to 4.5 µm. Source: http://irassociates.com

should be less than 1 µA. Actually, the infrared fluorescence radiance from vibrationally excited species is much weaker than that of blackbody at 2 meter distance away. This is the reason why (or one of the reasons) IR detectors are usually assembled with matched preamplifiers.

Preamplifier

The preamplifier provided with the InSb detector (bandwidth 1.5 Hz - 20 kHz) has been replaced by another preamplifier with bandwidth from 1.5 Hz to 1 MHz (gain $\sim 10^3$). To limit surrounding electromagnetic disturbances, the new amplifier and its power supply are set inside two different enclosures and are linked to each other via LEMO connectors and connected to the electrical ground of FIREFLY. This setup has been done by Julien Vincent.

The preamplifier rising and falling time response have been measured with a very short input square signal (0.008 µs rising edge, 0.050 µs width). Two output signals are shown in figure 4.8. From the fitting pulse function, we deduce that the rising response time τ_1 is between 0.20 and 0.25 µs which is in accordance with the maximum frequency of the bandwidth (1 MHz). The falling response time τ_1 is estimated to be around 3.6 µs. This preamplifier is used for the first time on FIREFLY because of electrical ground issues in the commercial design. All previous works were performed with the former 20 kHz-preamplifier (left panel of figure 4.8).

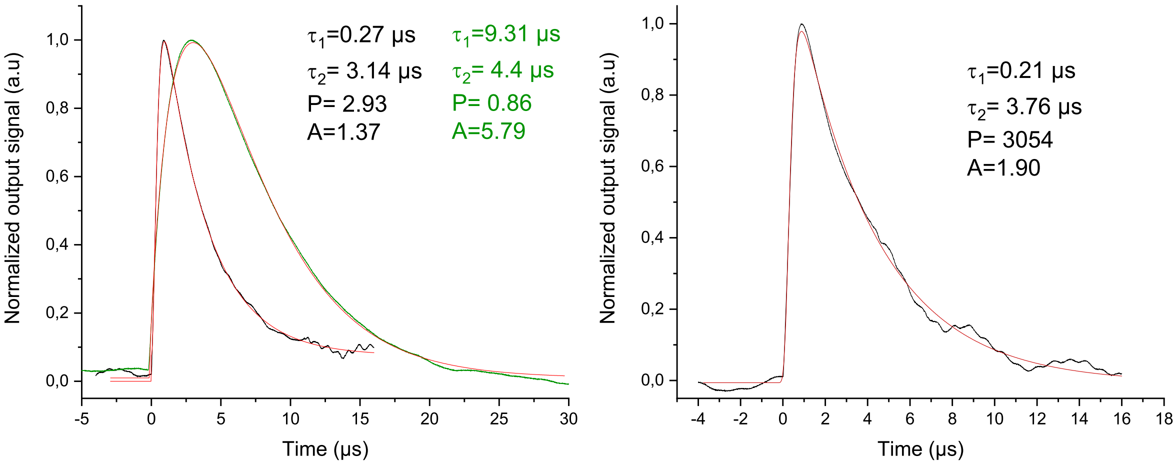

Figure 4.8: Output signal from the preamplifier for a very short input square signal (0.008 µs rising edge, 0.050 µs width). The fitting pulse function is expressed by $y_0 + A \times (1 - e^{-t/\tau_1})^P \times e^{-t/\tau_2}$. Parameters of the pulse function are indicated for the two independent measurements. In the left panel, the output signal of the previous amplifier is also displayed for comparison (corresponding curve and parameters are in green color).

Absorption configuration

FIREFLY can be used to record absorption spectra. The absorption configuration can provide only low resolution spectra because of the low resolution of CVFs but we used it for CVF 1 calibration, the correction of the FHG position and for the determination of the apparatus response function. As mentioned above, when FIREFLY is operating in the emission configuration, the data acquisition system is triggered via the laser pulses. However, there are no light pulses when FIREFLY operates in the absorption configuration. Indeed, in that case, the detected photon signal comes from a continuous blackbody radiance and no more from pulsed IR fluorescence of highly vibrationally cooling molecules. We used a lock-in amplifier system (SIGNAL RECOVERY Model 7225 Digital Signal Processing) for the absorption configuration. Figure 4.9 shows the data acquisition system in the absorption configuration of FIREFLY and the lower panel of figure 4.2 shows the external part of the corresponding setup.

The lock-in detection is operated by setting a fork light chopper (Hi-Tech Detection Systems, CH-10 tuning fork chopper) at the entrance of FIREFLY. This light chopper works at 202 Hz and defines the reference periodic signal for the lock-in amplifier. Very briefly, the light chopper makes the blackbody signal 202 Hz periodic which then contains all the spectral components of the reference signal. These spectral components are subtracted (in Fourier space) by the lock-in amplifier and the output signal from the lock-in amplifier is the signal just before the chopper which is actually the desired signal.

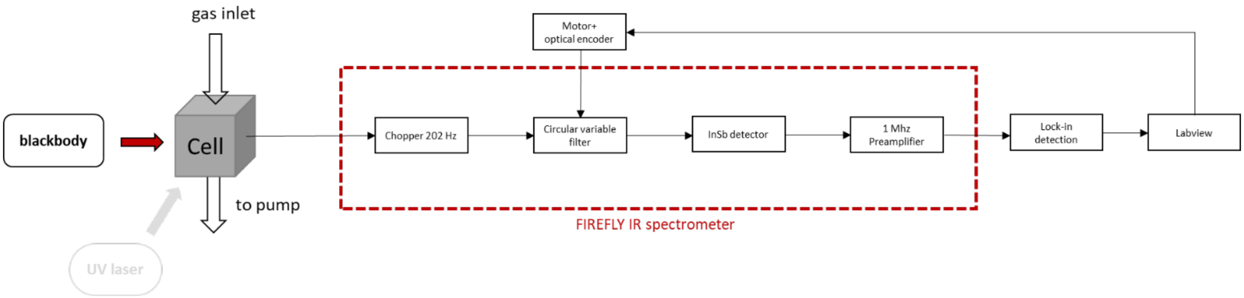

Figure 4.9: Schematic illustration of the acquisition data system when FIREFLY operates in absorption configuration

Figure 4.10 shows the 800°C blackbody emission spectrum recorded with the lock-in amplifier. The cell was vacuumed ($< 10^{-4}$ mbar). The recorded signal presents two large absorption bands. The absorption band at 4.27 µm comes from C-O asymmetric streching vibrational mode of carbon dioxide absorbing along the optical path in the atmosphere. According to the presence of air in the cell (in standard conditions of pressure and temperature), we noticed stronger absorption about 2 mV in the 4.27 µm band (figure 4.10). We also know that the path length crossed the blackbody radiation beam inside the cell is around 14 cm. Thus, the CO_2 absorption signal per unit length is estimated to be 0.14 mV/cm (this will be useful in the next subsection).
The very large 2.9 µm absorption band is attributed to solid water condensed on the sensitive element of the IR detector. Indeed, there is no difference in the 2.9 µm absorption band for the two curves in figure 4.10 which suggest that this band is not due to water vapor of air. Also, the asymmetric and symmetric streching water modes are below 2.7 µm.
The two absorption spectra of figure 4.10 are slightly shifted in wavelength because of non-repeatability of the exact angular position of the filter holder gearwheel.

If we want to record the absorption spectra of a species between 2.5 and 4.5 µm, the absorption spectrum of figure (4.10) can be viewed as a reference signal. Figure 4.11b displays the absorption spectrum of propylbenzene obtained by the ratio of the reference 800°C blackbody signal and the signal obtained when propylbenzene (figure 4.11a) is in the cell (vapor pressure of propylbenzene, ~ 4.5 mbar).
The 3.4 µm absorption is due to C–H aliphatic absorption bands and the 3.3 µm band absorption is due to C–H aromatic absorption bands. Because there can be slight shifting in the wavelength between two blackbody emission signal (figure 4.11 a), the derived absorption spectra can display some parasitic absorption features such as between 2.8 and 2.9 µm for propylbenzene (figure 4.11 b). The relative intensities can also change.

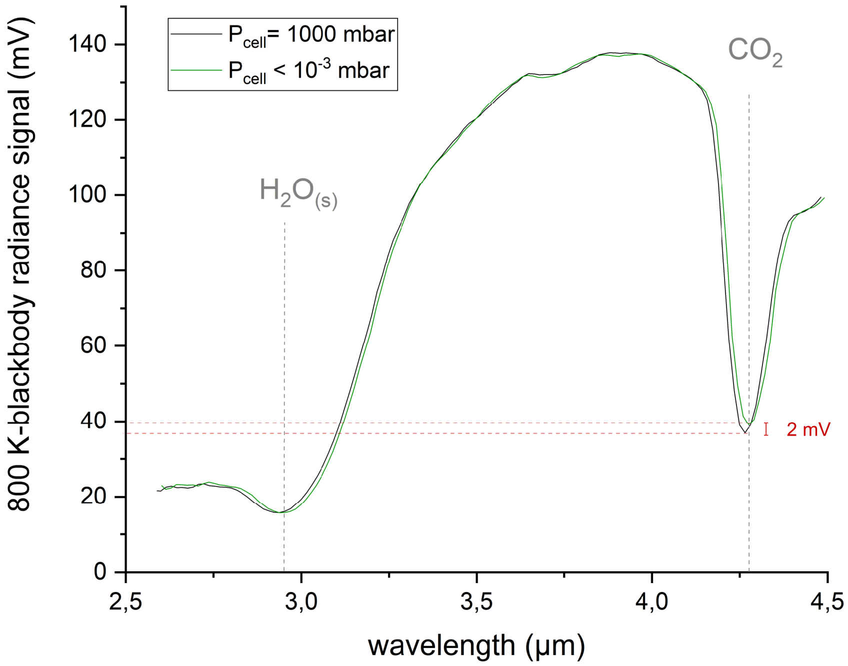

Figure 4.10: Recorded spectra with CVF 1 of a 800°C blackbody radiation by means of a lock-in detection. Two spectra for two different cell conditions: cell in contact with the atmosphere and vacuumed cell ($< 10^{-4}$ mbar).

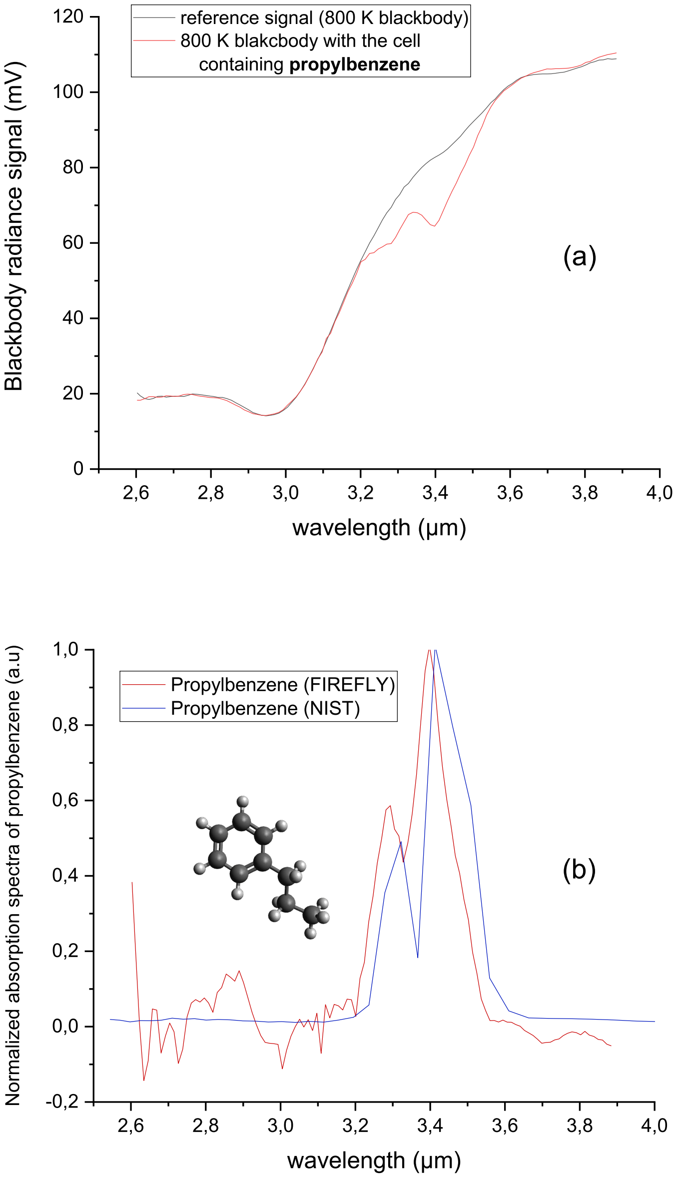

Figure 4.11: (a): spectra with and without propylbenzene in the cell. The C–H aromatic (∼3.3 µm) and aliphatic (∼3.4 µm) bands are visible besides solid water and CO_2 absorptions. (b) In red, the propylbenzene absorption deduced from (a) and in blue the propylbenzene found in the NIST database. Normalization have been done at 3.4 µm. Artifact band appears around 2.85 µm.

Usually, to test the reliability of the absorption spectrum we record it several times and we ensure reproductibility because this kind of artifact are not reproducible from one FHG turn to another.

Some manipulations for the correct operation of FIREFLY

Correction of the FHG angular position

As described above, from one FHG full rotation to the next, the angular position of the FHG is very slightly shifted. This angular shifting correspond to wavelength shifting about 0.2-0.3 µm (figure 4.17). Despite the angular shifting is as small as 0.5°, its influence on recorded spectra is noticeable. Figure 4.12a shows several absorption bands in terms of the motor step position (i.e angular position). Figure 4.13 displays the motor step position for (a) the CO_2 absorption band and (b) the 3.28 µm C-H aromatic streching absorption band of toluene for several FHG turns. For the two wavelengths, the shifting obeys to a periodic evolution which can be approximately described by a sinusoidal function. The successive real motor step positions fluctuates periodically with the FHG full turn number around the correct motor step. We define the correct motor step as being at the middle of the real motor step range. Thus, the correct motor step is $\sim$ 2295 for 4.13a and $\sim$ 3575 for 4.13b. Thus, with that sinusoidal fitting, it is possible to numerically correct the real motor step position and obtain motor step position closer to the correct motor step position (see figure 4.14 and 4.12b). After this correction, shifting still occurs but is reduced to less than 0.1 µm (figure 4.17).

The result on CO_2 absorption spectrum of this kind of correction is shown in figure 4.13 and is the same for emission spectra.
After the correction is done, we can start the CVF calibration.

CVF calibration

CVFs have been made in such a way to have a linear relation between the angular position and the wavelength. Then, we can look for a linear relation between the motor step position and the wavelength.
To do so, we have to select molecules whose absorption bands allow to uniformly span the wavelength range of the CVF 1 (from 2.6 µm to 4.5 µm). The positions of streching modes of carbon dioxide, aromatic C-H stretching modes of toluene, and aliphatic C-H stretching modes of cycloheptatriene are well-known. By associating the motor step position of these absorption bands to their respective wavelengths, we obtain figure 4.15. A linear fit is used to calibrate the CVF 1. With this calibration, the absorption spectra of ethylbenzene and phenylacetylene are displayed and compared to that of the NIST

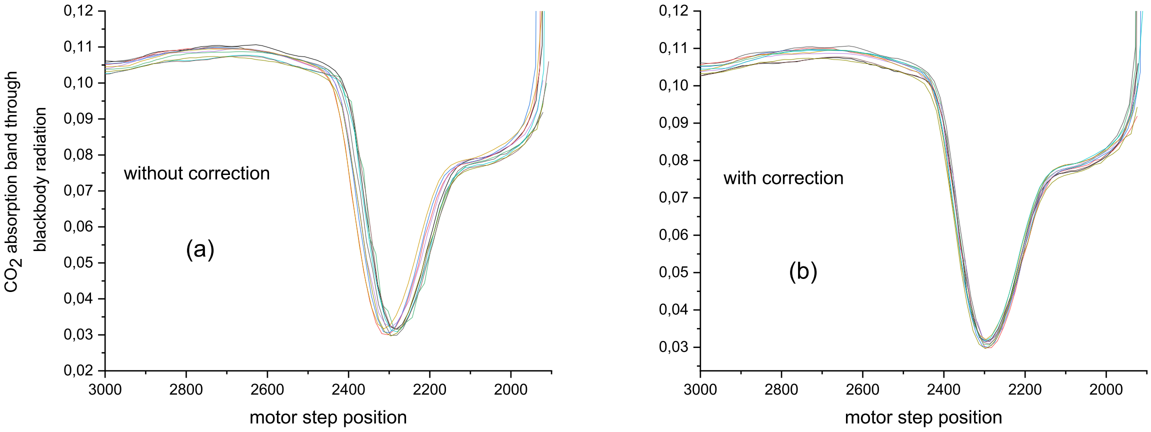

Figure 4.12: Several CO_2 absorption bands irradiated by a 800 K blackbody. (a): without correction. Given that electrical noise, there is an uncertainty on the step motor position of the minimum of absorption bands. (b): The correction is done using the fitting sinusoidal function displayed in figure 4.13a.

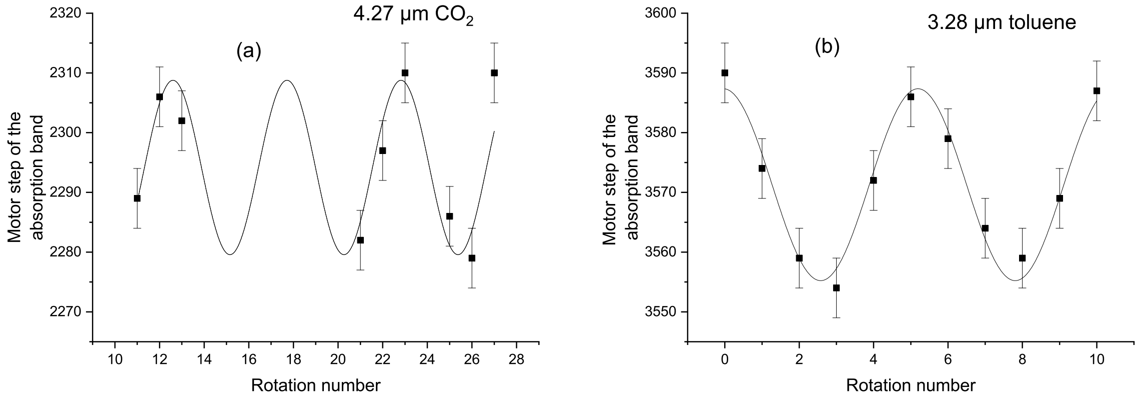

Figure 4.13: Two absorption bands motor step position in terms of the rotation number of the filter holder gearwheel (FHG). The fit function is a sinus function and the period is the same for both fitting, around 5.15. Uncertainty bars are estimated from the uncertainty of the minimum of absorption bands because of electrical noise (see figure 4.12 without correction). (a): 4.27 µm of carbon dioxide and positions are deduced from figure 4.12a (b): 3.28 µm of C-H aromatics of toluene.

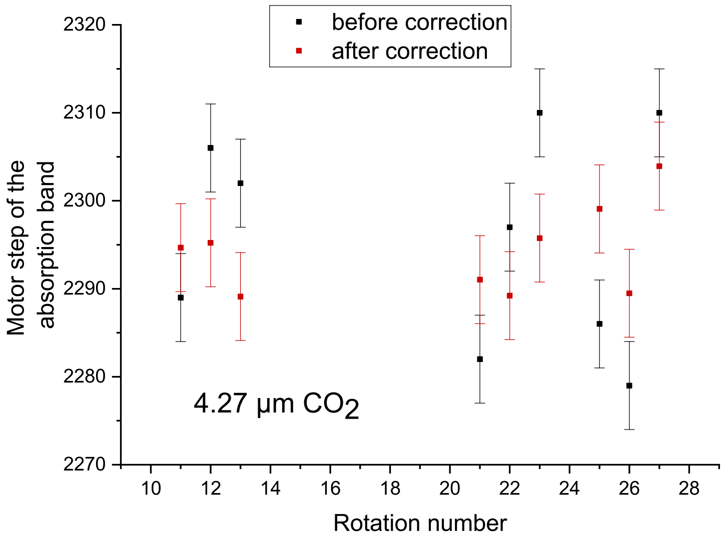

Figure 4.14: Black points are those appearing in figure 4.13a. Red points are the motor step position after the numerical correction. These positions should correspond to that of figure 4.12 b. The dispersion is reduced.

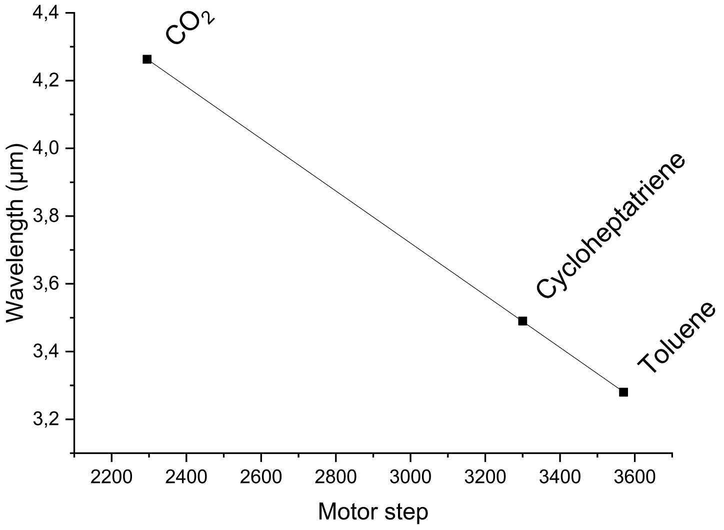

Figure 4.15: Calibration curve of the CVF 1.

figure 4.16. Also, we show in figure 4.17)the absorption bands of figure 4.12 in terms of the wavelength.
Once the calibration is done, we can determine the response function of FIREFLY.

Response function of the apparatus

In this last subsection, we present the estimation of the response function of FIREFLY (CVF 1, InSb detector, preamplifier) and eventually other components outside FIREFLY but contained in the data acquisition system. To determine the response function $\mathscr{F}$, we have to define an input signal $\mathcal{S}_i$ and measure the output signal $\mathcal{S}_o$. Then, the response function $\mathscr{F}$ is defined by

$$\mathcal{S}_o(\lambda) = \mathscr{F}(\lambda) \times \mathcal{S}_i(\lambda)$$

The 800°C blackbody radiation is the input signal $\mathcal{S}_i$ and we suppose that all components upstream on the IR fluorescence region (three golden plane mirrors visible in the lower figure of 4.2 and the blackbody radiation entrance window) have response function equal to the unity. The detected signal is displayed in figure 4.18 (in black) with the theoretical emission profile of the 800°C blackbody (in red). We arbitrarily matched both curves around 4.0 µm. Thus, by dividing $\mathcal{S}_i$ and $\mathcal{S}_o$, we obtain the profile of the response function of our apparatus (violet curve in figure 4.18). Actually, we had to take into account the stronger CO_2 absorption for absorption configuration compared to the emission configuration of FIREFLY because of the additional optical path between the blackbody and the cell whereas the response function will be useful only for emission spectra. As mentioned in section 4, the CO_2 absorption per optical path length unit is estimated to be around 0.14 mV/cm. The excess optical path length is about 95 cm (figure 4.2). From these informations, we estimated the total CO_2 absorption between the IR fluorescence region and the IR detector. We recognize that this is a crude estimation of the CO_2 absorption in FIREFLY emission configuration but this is simplest and fastest way we found. The profile of the response function is enough for our work because we only record relative spectra. The recorded emission spectra have to be divided by $\mathscr{F}(\lambda)$.

The response time of the apparatus has also been estimated. In that case, we cannot fix the input signal to the IR detector as a very short square pulse but we can try to generate a very short IR fluorescence signal. Indeed, if we increase the buffer gas pressure, then collisional cooling will be faster and the IR fluorescence signal will also be faster. Thus, the idea is to increase the buffer gas pressure up to the point where we see no more changes in the time-resolved signal which would indicate that the apparatus cannot distinguish faster IR fluorescence signals. Also, when the buffer gas pressure

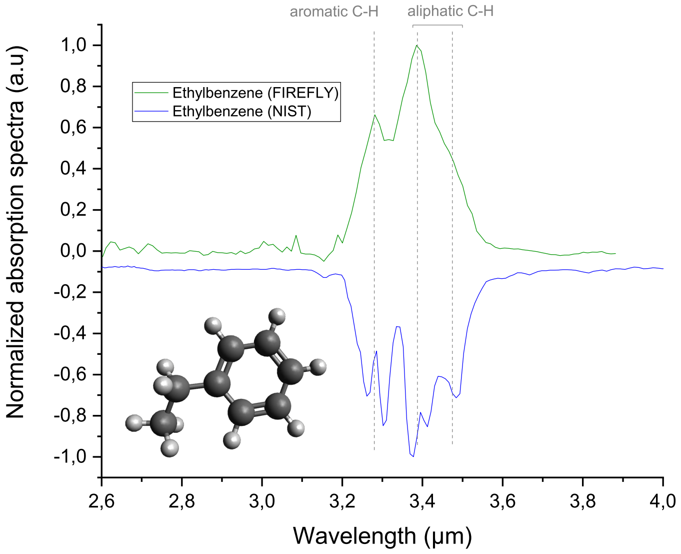

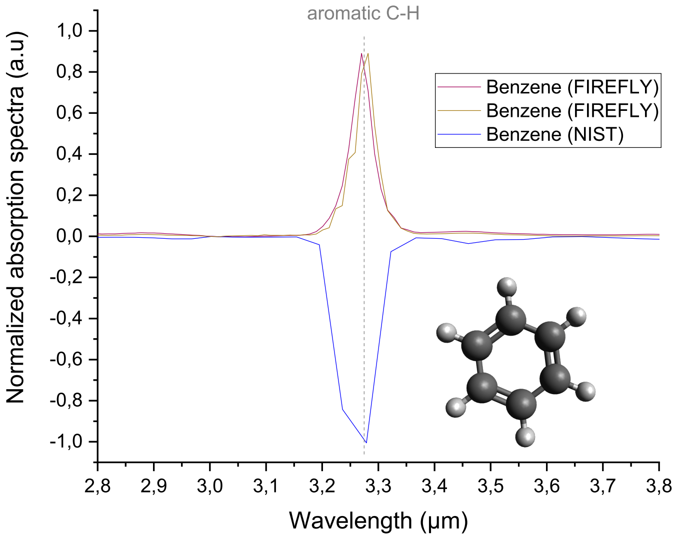

Figure 4.16: Normalized absorption spectra deduced from the calibration of figure 4.15 and compared to NIST spectra.

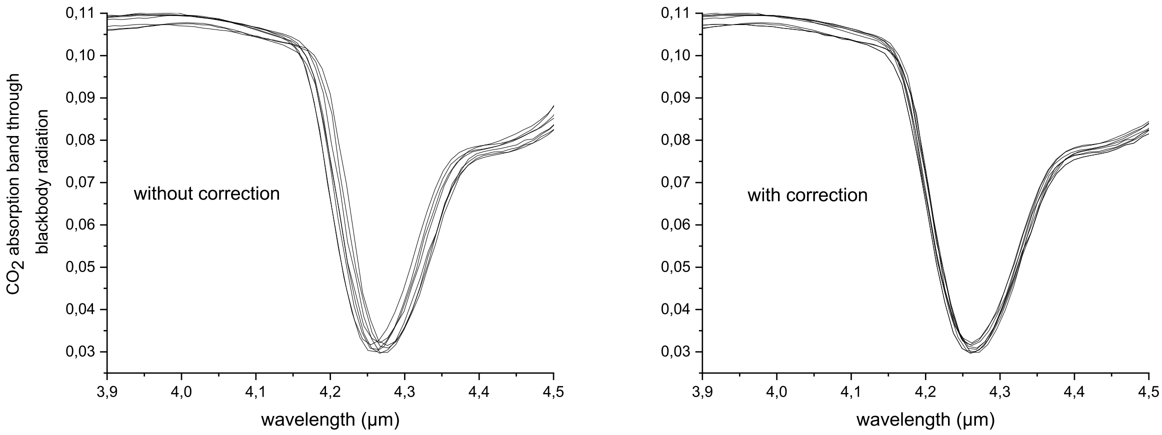

Figure 4.17: Shift of carbon dioxide absorption bands from one rotation of the FHG to an another. The correction reduces these shifts.

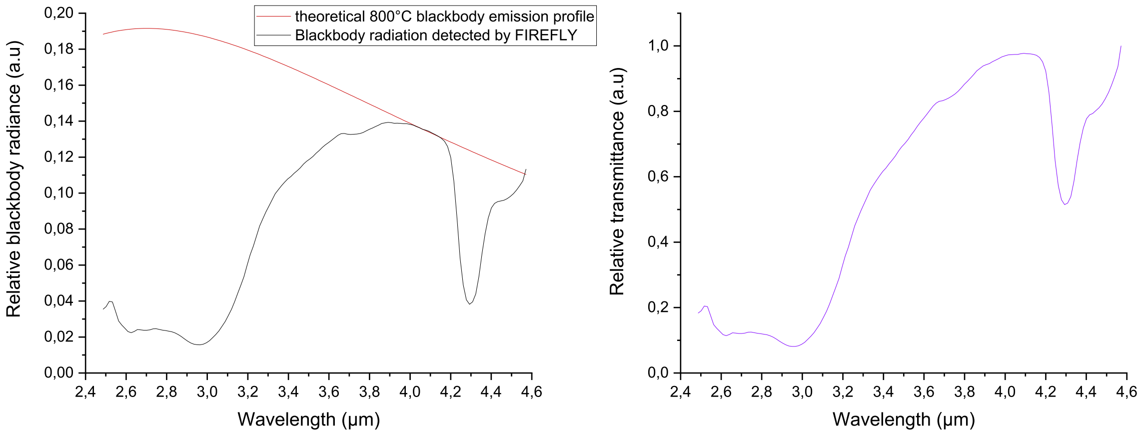

Figure 4.18: (a) In red: the relative 800°C blackbody radiance obtain by the Planck function. In black: the detected signal by FIREFLY when irradiated by 800°C blackbody. In violet: the profile of the response function of the apparatus that have been obtained from the black and red spectra.

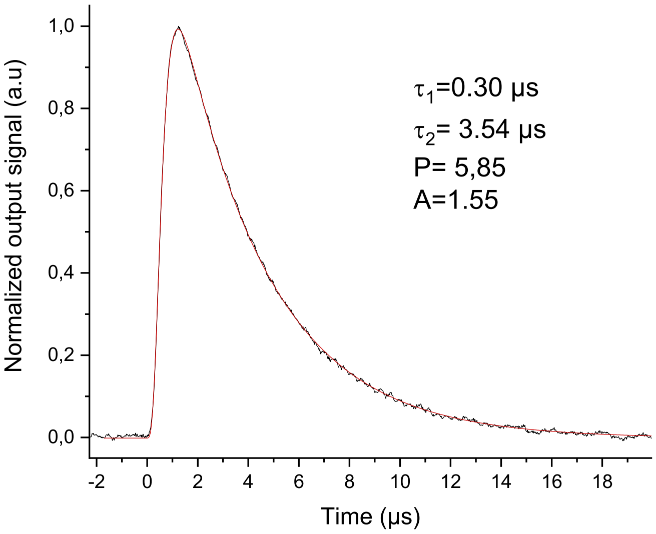

Figure 4.19: IR fluorescence signal of toluene excited at 193 nm. For this record, pressure conditions are approximately known: argon partial pressure around 10 mbar and toluene partial pressure between 1 and 2 mbar.

increases, the IR fluorescence is weaker because the excited species yields energy via collisional transfer (collisional rate is higher). This is why we studied the response time of apparatus with toluene because its IR fluorescence signal is relatively strong. We excited toluene at 193 nm (excimer laser) with total pressure more than 10 mbar. The resulting non-dispersed (no CVF) IR fluorescence signal is displayed in figure 4.19. The pulse function parameters are similar to those obtained for the preamplifier which suggests that the preamplifier is the slowest element of the data acquisition system (the InSb detector should have shorter response time but we cannot measure it).

Conclusion

The FIREFLY home-made IR spectrometer allows to detect IR emission induced by electronic excitation of species in the gas phase by means of three circular variable filters (CVF) with suitable IR detectors. We used only the first CVF, spanning the 2.5 to 4.5 µm wavelength range with resolution power between 35 to 60. CVF calibration and measurement of the apparatus response function are done by using FIREFLY in absorption configuration. Approximately periodical angular position shifting of CVF is reduced thanks to a correction. To detect the IR emission, species are introduced in a gas cell and are continuously pumped.

5. Investigation of toluene to cycloheptatriene isomerization

Contents

Cell and light sources **131**
  Cell description 132
  Physical conditions monitoring inside the cell 132
  Light sources 135
FIREFLY spectrometer **137**
  Constituting components of FIREFLY 138
  Absorption configuration 145
Some manipulations for the correct operation of FIREFLY . . . **149**
  Correction of the FHG angular position 149
  CVF calibration 149
  Response function of the apparatus 152

Description of the studied system

Several studies have shown that the fluorescence quantum yield of toluene decreases as the excitation energy increases, reflecting the fact that the internal conversion becomes very efficient (Otis et al., 1983; Duncan et al., 1981; Farmanara et al., 2001). Toluene is then left very quickly in the electronic ground state after having undergone successive internal conversions and the initial electronic energy (photon energy absorbed by electronic excitation) is mainly converted into vibrational motion and statistically distributed among all vibrational modes (intramolecular vibrational redistribution).
In addition to the vibrational radiative de-excitation, toluene can dissociate or isomerize. For the dissociation, it is now established that 193 nm-excited toluene dissociates

mainly via aliphatic C–H bonds cleavage ($\approx$ 3.8 eV, benzyl radical formation) and in a lesser extent via the C–C bond cleavage linking the benzene ring to the methyl group ($\simeq$ 4.4 eV, phenyl radical formation) (Ikeda et al., 1985; Park et al., 1990; McMillen and Golden, 1982).
Toluene (and benzene derivatives) isomerization, for its part, is generally considered to occur in the same way as for benzene, *i.e.* via fulvene derivatives, benzvalene and prismane. This isomerization mechanism in benzene derivatives is corroborated by the permutation of carbon atoms of the benzene ring and the displacement of functional groups around the ring (Wilzbach and Kaplan, 1964; Wilzbach et al., 1968; Bryce-Smith and Gilbert, 1980). In this isomerization mechanism, carbon atoms of the ring switch with each other without the participation of carbon atoms of the functional groups. However, by studying toluene photodissociation containing aromatic deuteriums (namely, C–D bonds are located on the phenyl ring) and aliphatic hydrogens (namely, C–H bonds are located on the methyl group) after excitation at 193 nm and detecting its dissociation products via a two-dimensional ion imaging detection system, Chi-Kung Ni's group (Lin et al., 2002; Ni* and Lee, 2004; Tseng et al., 2006) noted that hydrogens initially located in the methyl group could be found on the benzene ring, which was unexplained by the isomerisation paths considered so far. In fact, it is also known since the 1960's that cycloheptatriene (CHT), when vibrationally excited to the electronic ground state, isomerizes very quickly to toluene (Srinivasan, 1962; Atkinson and Thrush, 1970; Luu and Troe, 1973, 1974; Astholz et al., 1979) (isomerization rate around $1.8 \cdot 10^8$ s^{-1} at 193 nm (Hippler et al., 1981b,a, 1983a,c)) with a quantum yield close to 1 when CHT is excited at 250 nm (Hippler et al., 1983e). Then, Chi-Kung Ni's group explained their observations as the illustration of the reverse path of CHT to toluene isomerization. Their idea is that when toluene is excited at 193 nm, it isomerizes to CHT which very quickly undergoes several hydrogen scrambling (one hydrogen permutation occurs over less than 10^{-8} s) (Park et al., 1990) before isomerizing back to toluene. These hydrogen scrambling could explain why the methyl dissociation products contain deuterium initially located in the phenyl ring.

Our work is in line with these observations. The general idea is to excite an isotopomer of toluene, labeled as toluene-d_5^{Ar} and indicating that the five deuterium atoms are located on the aromatic ring and three hydrogen atoms are located in the methyl group. The 193 nm excited toluene-d_5^{Ar} in the S_3 excited electronic state will quickly come back (very fast compared to the all relaxation pathways, section 2) in the electronic state S_0 and highly vibrationally excited. During the cooling cascade, among the different pathways of dissociation, collisional relaxation and vibrational emission,

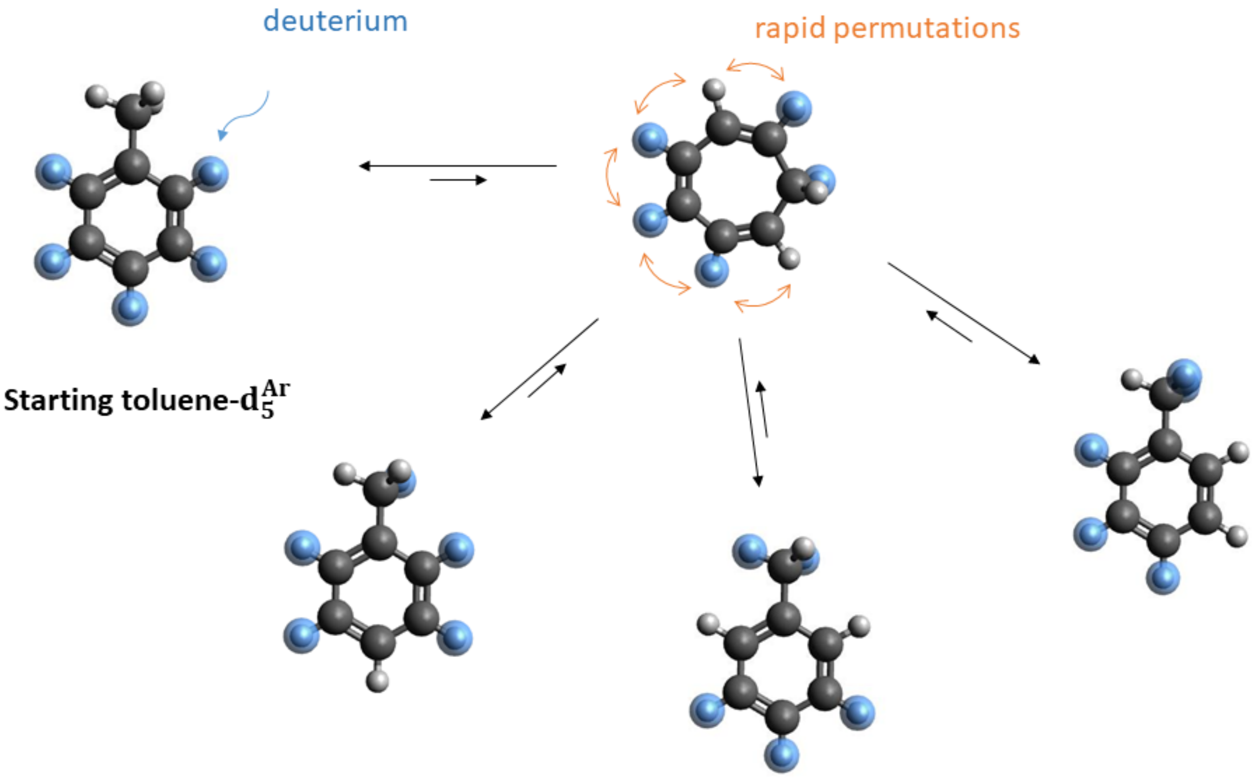

Figure 5.1: Principle of toluene → cycloheptatriene isomerisation study via the vibrational emission process. The initially excited toluene-d_5^{Ar} isomerizes to cycloheptatriene which, before isomerizing back to toluene, undergoes hydrogens/deuteriums scrambling of 7-membered ring carbon atoms. Consequently, a toluene-d_5 isotopologue appears from the cycloheptatriene → toluene isomerisation. The goal is to detect the emission of toluene-d_5 isotopologues through the emergence of aromatic C–H bonds and their vibrational stretching mode. The emergence of aliphatic C–D bonds is not detectable because their vibrational stretching mode emission wavelength is out of the circular variable filter wavelength range (2.5 to 4.5 µm).

the excited toluene-d_5^{Ar} will also isomerize to CHT. The toluene-d_5^{Ar} will emit IR photons via radiative de-excitation of aromatic C–D streching and aliphatic C–H stretching vibrational modes. During the cooling cascade, the isomerisation will cause one or several round trip between toluene and CHT which will therefore involve other toluene isotopologues-d_5 (because of very fast hydrogen scrambling in CHT), in which there are aromatic C–H and aliphatic C–D. These vibrational modes should then appear in the emission spectrum of the radiative relaxation. Figure 5.1 summarizes the isomerisation between toluene and CHT in our study.

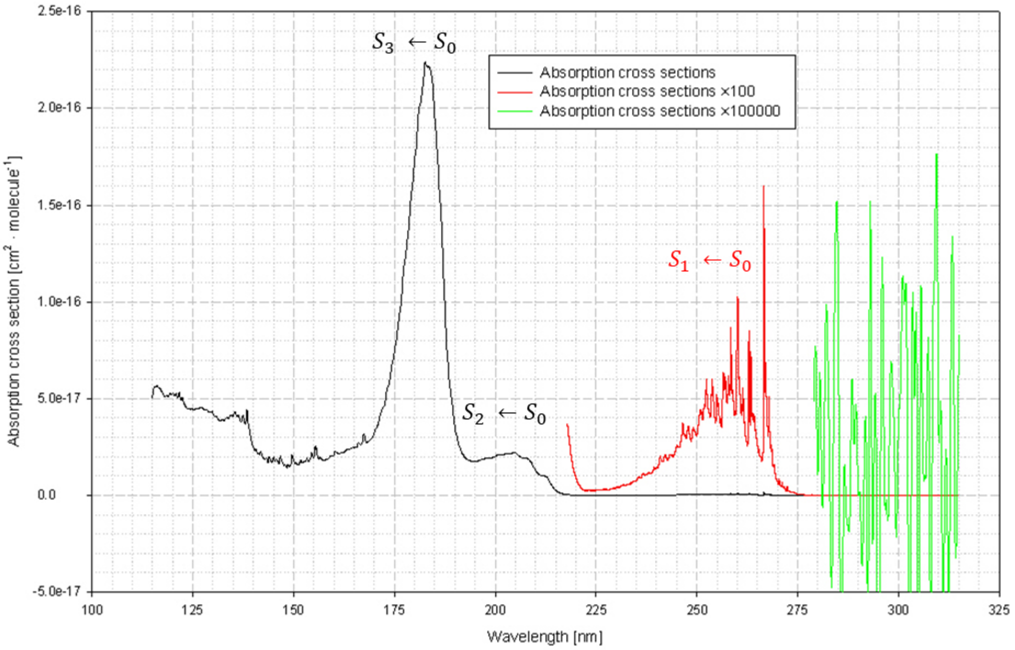

Absorption cross sections of methylbenzene (toluene) $(CH_3)C_6H_5$ at room temperature,
Serralheiro et al., J. Phys. Chem. A 119 (2015) 9059

Figure 5.2: toluene absorption spectra. The figure has been taken from *The MPI-Mainz UV/VIS Spectral Atlas of Gaseous Molecules of Atmospheric Interest* website.

Raw data processing

In this section, we aim to show methods used to process the time traces and emission spectra recorded by the Labview program (raw data). The excimer laser (ArF, 193 nm) employed has a 20 Hz repetition rate which leaves a time interval of 50 ms between two successive pulses. This time delay is long enough for the relaxation of the studied species to be completed. The acquisition card is triggered by a photodiode. The emission spectra recording is processed by a Labview program developed by Julien Vincent (CNRS engineer at Institut des Sciences Moléculaires). The initial and final wavelengths of any acquisition, and the motor step (i.e the wavelength step) can be defined. The i^{th} acquisition stage proceeds as follows:

- The time trace is recorded after each excitation and averaged over several hundred shots (usually between 300 and 500 shots and defined before the acquisition is started). This detection is performed for a fixed wavelength λ_i which is filtered by the interference filter (*i.e* for a given position θ_i of the filter-holder gearwheel).

- An integration of the time trace is performed over k time gates, Δt_i^k. This kind of integration is translated into a value at the λ_i wavelength in the emission spectrum

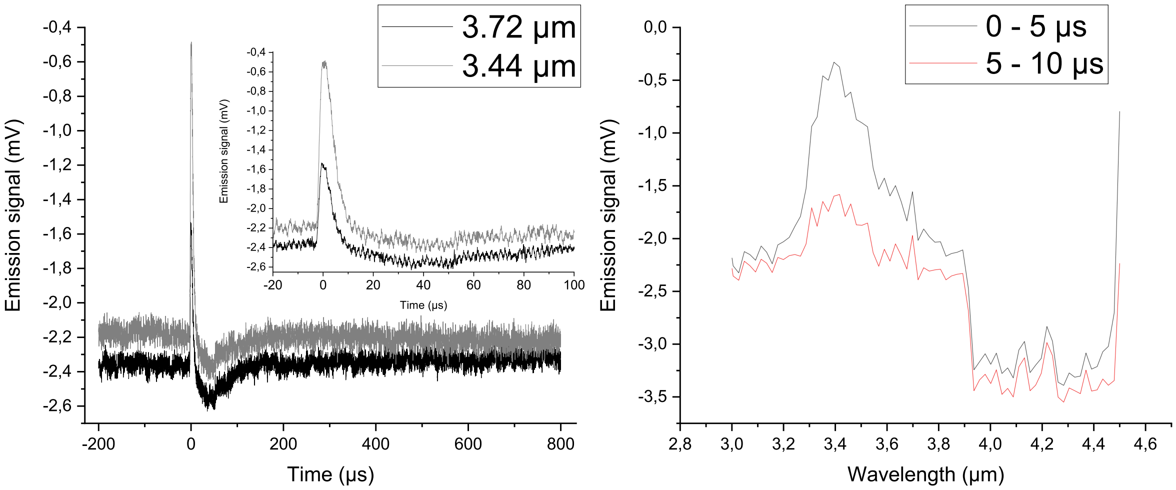

Figure 5.3: Toluene-d_5^{Ar} emission with 1.16 mbar total pressure (P_{Ar}=0.95 mbar and toluene-d_5^{Ar} partial pressure of 0.21 mbar). The laser power at the entrance window was 175 mW (repetition rate is 20 Hz). Left panel: two examples of raw time trace. The inset figure is a zoom between -20 and 100 µs. Right panel: two examples of raw emission spectra

associated with a Δt_i^k time gate.

- After the time trace is recorded and calculations are done for the emission spectra associated with the different time gates, the filter-holder gearwheel moves to the position θ_{i+1} to filter the λ_{i+1} wavelength and the Labview program resumes the recording described in the previous two points.

Acquisitions last between 15 and 45 minutes. Figure 5.3 shows an example of emission spectra and time traces obtained during acquisition (raw data). Since emission spectra are derived from time traces, these must first be treated. The set of algorithms that allowed us to do the processing was coded in Python. The baseline may vary from one time trace to another, which is due to low frequency noise of unknown origin. This noise is then found in emission spectra because of the time trace integration within time gates (right panel of figure 5.3). In addition to their noise, emission spectra in figure 5.3 show an abrupt variation around 3.9 µm. This type of discontinuity in raw emission spectra often occurs and never appear more than twice during an acquisition. We believe that they are due to the acquisition chain.

To extract the physical information from raw emission spectra and minimize the electronic noise, the baseline of each time trace must be set to zero. However, this does not prevent the occurrence of low frequency noise in time traces which results in a slight

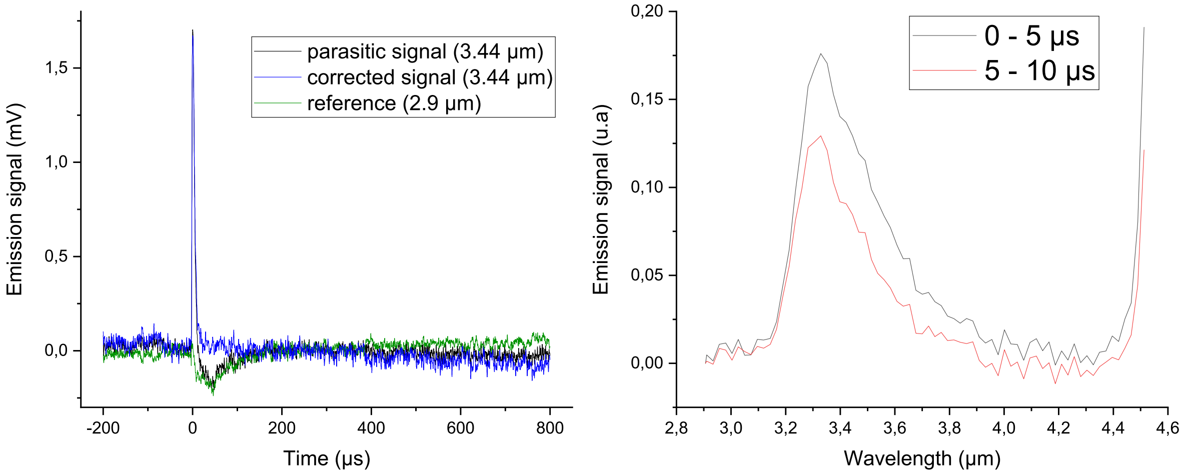

Figure 5.4: Left panel: time trace correction infected with the hollow-shaped parasitic signal between 0 and 100 µs. Right panel: emission spectrum calculated after time traces processing. The sudden increase around 4.5 µm is due to the end of the interference filter and no wavelength is filtered.

upward or downward slope and remains incorrigible (left panel of figure 5.5). This type of slope is not a major problem for processing since it is imperceptible on time gates that we define. After time trace's offset are set to zero, the idea is to get rid of the the hollow shaped parasitic signal between 0 and 100 µs that distorts time traces and constantly appears in each of these traces. It is likely induced by the laser pulse. It is then sufficient to define a reference signal which is devoid of any vibrational emission signal (no emission signal) and remove it from all other temporal traces. An example is given in the left panel of figure 5.5 where the reference is defined by the time trace at 2.9 µm (no transmission signal appears). Time traces being processed, we can then define time gates in our algorithm and calculate and plot emission spectra.

It then remains to correct the emission spectra of figure 5.5 by the response function of the device (section 4). This correction has the effect to increase the noise as the wavelength decreases (figure 4.18). This effect is clearly seen below 3.1 µm where no emission signal is detected (left panel of figure5.5) but where the noise is huge. Of course, at fixed wavelength, signal to noise ratio should not change before and after correction by the response function of the apparatus. Spectra obtained can be slightly smoothed (over 3 points by a polynomial of degree 1). An artificial signal, due to smoothing, appears at 3.0 µm. This kind of artificial signals are not a problem for interpretation because they are not reproducible from one acquisition to another.

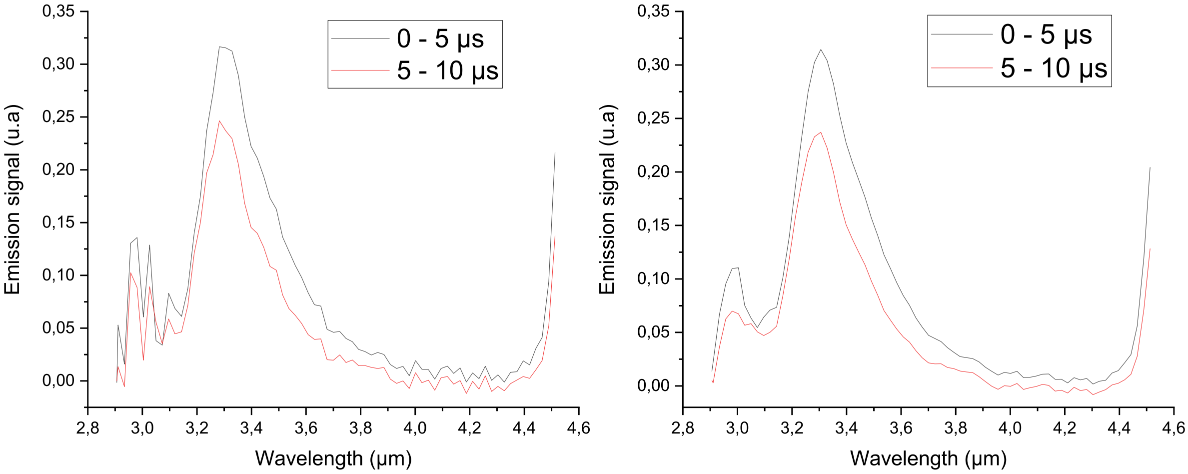

Figure 5.5: Left panel: emission spectra corrected by the response function of the apparatus. Right panel: the same spectra of the left panel smoothed by the Savitsky-Golay algorithm (over three points by a polynome of degree 1).

Infrared emission of toluene $C_6H_5CH_3$

Before starting the study of infrared emission of toluene-d_5^{Ar} and toluene → cycloheptatriene (CHT) isomerization, we will first present the emission of fully hydrogenated toluene excited at 193 nm ($\approx$ 51800 cm^{-1}) which will be useful to better understand the emission spectra of deuterated toluene. This section will allow us to do a proof-of-concept of our experimental method.

Intensity study

To ensure that the IR emission process is induced by single photon absorption at 193 nm, we present in figure 5.6 the intensity study obtained by integrating the temporal trace in total fluorescence (*i.e.* without a filter) over the whole cooling. It is assumed that the photon detection between 2.5 and 4.5 µm does not alter our intensity study which should be done over the entire wavelength range. On the x-axis, we indicated the laser power upstream of the cell entrance window rather than the photon flux because the laser spot area is relatively large ($\sim$ 5 cm^2) and the photon flux is clearly inhomogeneous. The excimer laser has a repetition rate of 20 Hz. In figure 5.6, we noticed that the absorption regime of interest is valid up to 150 mW and is no longer valid above 200 mW. We have deliberately left the range between 150 mW and 200 mW as indeterminated regime because this range corresponds to the transition range between one- and two-photon process.

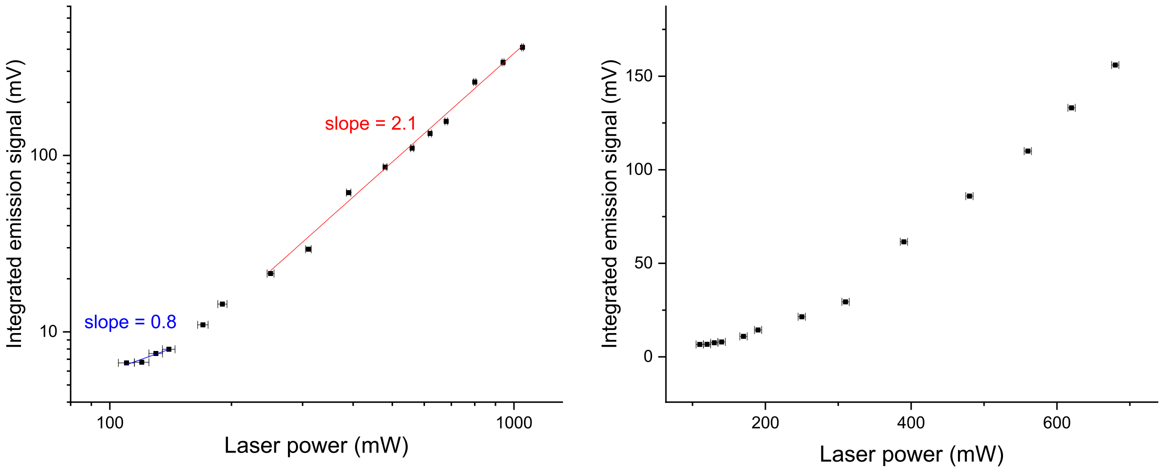

Figure 5.6: Intensity study of toluene excited at 193 nm. Each points of the scatter plot has been deduced by integrating the undispersed vibrational emission signal (all wavelengths between 2.5 and 4.5 µm) over the whole relaxation. Left panel: log scale. Right panel: linear scale to show that between 150 and 200 mW the absorption regime is indeterminate.

We consider that this intensity study is also valid for toluene-d_5^{Ar}. Given that the challenge is to have, simultaneously, one-photon process and high signal-to-noise ratio, we focused on our measurements between 140 and 200 mW laser power. We have incidentally made some acquisitions around 500 mW.

Emission spectra as a function of time

An example of undispersed emission time trace (all wavelengths between 2.5 and 4.5 µm are detected, i.e no interferential filter) is illustrated in figure 5.7. The emission signal rising up to 5 µs is due to the detector response (figure 4.18 in chapter 4) and the decay is dominated by collisional cooling. In addition to this emission signal, it is interesting to plot the emission spectra at a different time window of the cooling cascade. In figure 5.8, we show the emission spectra from 1 µs to 19 µs with the integration performed on 2 µs wide time gates. In accordance with figure 5.7, the emission spectrum over 3−5 µs is more intense than that over 1−3 µs and the subsequent emission spectra are all weaker than their predecessor, which reflects the observed decay in figure 5.7. The noise below 3.2 µm is due to the fact that the emission spectra are corrected by the response function of the apparatus which is particularly low below 3.2 µm. The comparison of the spectra obtained by the two acquisitions clearly shows that below 3.2 µm there is no reproducible emission signal. This is why, from now on, we will limit our analysis between 3.2 and 4 µm.

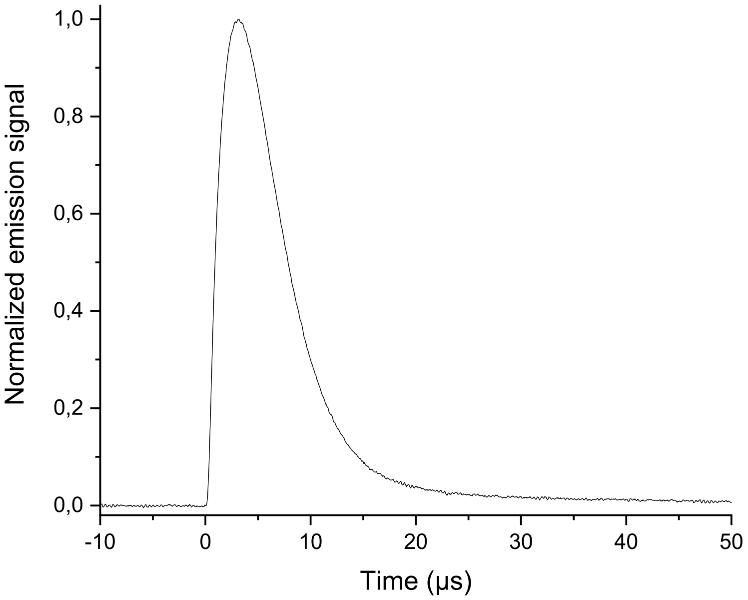

Figure 5.7: Undispersed emission signal of toluene excited at 193 nm.

We also notice that during the relaxation cascade, the emission spectrum profile becomes thinner (figure 5.9) and the whole emission band shifts continuously towards the blue. This effect is due to the anharmonicity of the potential energy surface in which the nuclei move. Given that normal vibrational modes frequency is related to the second derivative of the potential energy surface, the anharmonicity reduces this second derivative (for instance, such as the Morse potential). In fact, harmonic approximation of vibrational motion is less and less valid as the internal energy increases. Thus, when the internal energy and therefore the number of quanta per normal modes increases, the frequency of normal vibrational modes will be lower. This implies that at the end of the relaxation (when the internal energy is relatively low, i.e. when the number of quanta in the interest normal modes is on average 1), the emission spectrum should tend towards the absorption spectrum. We present in figure 5.9, the emission spectrum between 15 and 18 µs.

We know that, in addition to vibrational emission and dissociation, toluene could isomerise to CHT. This raises the question of whether CHT is at the origin of vibrational emission shown in figure 5.8, especially since figure 5.9 seems to show that the two species can be at the origin of the emission between 15 and 18 µs. However, as underlined in the introduction of this chapter, it is now established that highly excited vibrational CHT rapidly isomerizes to Toluene. For example, it has been measured that this isomerization rate is around $8 \cdot 10^8$ s^{-1}, which is at least an order of magnitude above the collision rate usually encountered in our FIREFLY experiments. For this reason, we believe that the observed emission spectrum at the end of the cooling in figure 5.9 is probably due to toluene.

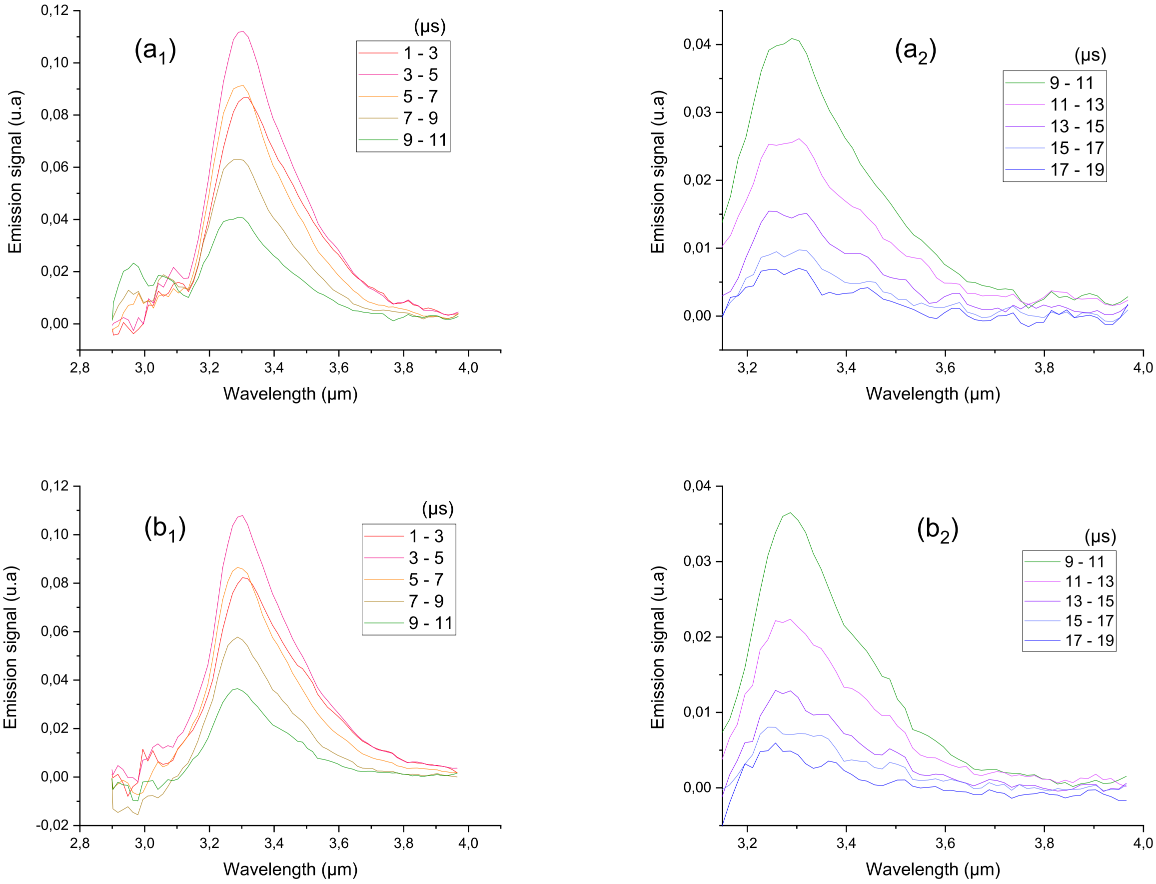

Figure 5.8: (a_1, a_2): two emission spectra above are from the same acquisition. (b_1, b_2): two emission spectra above are from the same acquisition but different from (a_1, a_2) acquisition. In these two acquisitions pressure conditions are identical: total pressure is P= 1.16 mbar and argon partial pressure is 0.93 mbar. The laser power upstream of the entrance UV window is 145 mW. The ultimate vacuum reached is of the order of 10^{-4} mbar.

Time traces as a function of wavelength

Part of the information obtained from emission spectra at different times of the relaxation can be presented as time traces at different wavelengths. In figure 5.10, we show time traces recorded at different wavelengths with wavelengths attributed to the anharmonicity effect appear (3.81, 3.72 et 3.61 µm). Actually, signals from anharmonic effects also occur between 3.5 and 3.4 µm due to the vibrational normal modes of the C–H

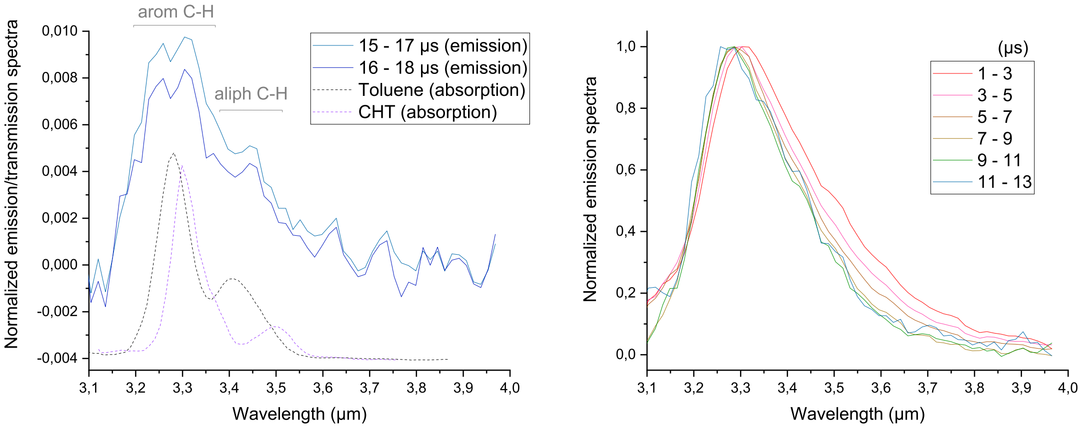

Figure 5.9: Left panel: emission spectra at the end of the cooling cascade of toluene excited at 193 nm. The dotted line shows the absorption spectra of toluene and cycloheptatriene (obtained as described in section 4). The emission band around 3.3 µm is due to aromatic C-H streching and the band around 3.45 µm is due to aliphatic C–H stretching. Right panel: emission spectra are narrower as the internal energy decreases. Broadening of the emission spectra in short times is due to the anharmonicity of the potential energy surface.

aromatic. By normalizing these time traces, we can compare their temporal emission profiles (figure 5.10). We see that the decay is shorter for anharmonic aliphatic C–H wavelengths which emit, as described above, only at internal energies greater than for harmonic aliphatic C–H wavelengths.

Simulation of the cooling cascade

Based on the methodology described in chapter 2, it was possible to simulate the entire relaxation cascade, get more insight in it and possibly provide information that is inaccessible from vibrational emission detection with FIREFLY.

As explained in chapter 2, the relaxation is modelled by a kinetic Monte Carlo algorithm in which rates of different relaxation pathways are known for each value of the internal energy. To calculate vibrational emission rates, the vibrational structure of toluene and CHT must first be known, *i.e.* the 39 normal vibrational modes and their respective IR intensities. This information is obtained via a DFT calculation in the harmonic approximation (CAM-B3LYP/6-311++G(d,p)). We used B3LYP hybrid functional because it is the most popular to calculate absorption spectra of hydrocarbons and we tried CAM-B3LYP (Coulomb-attenuating method) because it is as accurate as B3LYP and better for long-range interactions (Yanai et al., 2004) but CAM-B3LYP proves to be useless for our needs. We deliberately chose the very precise and extended 6-311++G(d,p) basis set. G means that Gaussian functions are used for atomic orbital description and are

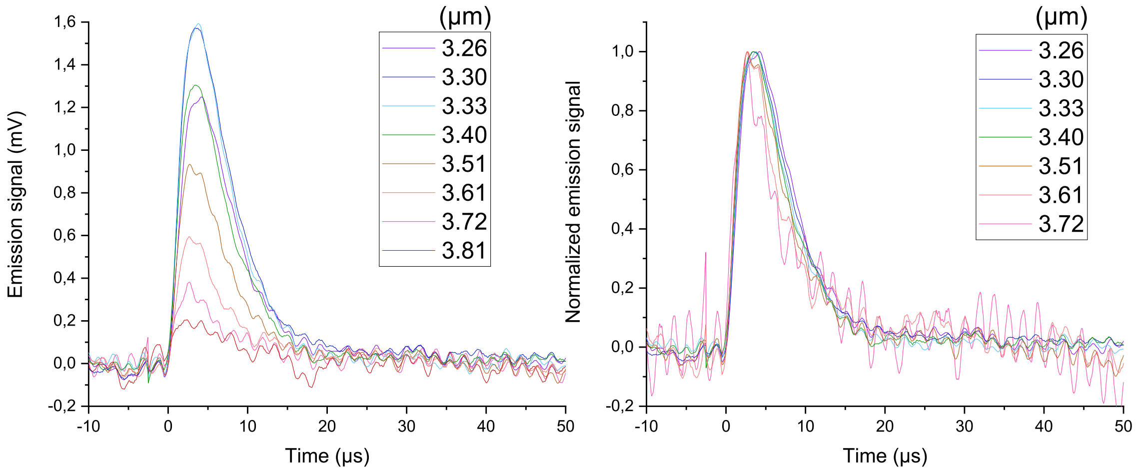

Figure 5.10: Left panel: time traces at different wavelengths from the radiative relaxation of toluene. Right panel: these same normalized temporal traces.

less CPU time consuming but less accurate than Slater functions. Nevertheless, linear combination of Gaussian functions can accurately represent Slater functions and still remain faster to compute than Slater functions. The 6-311++G(d,p) Pople style basis set means that 6 primitive Gaussian functions are used for core atomic orbitals description, a triple split valence basis set is used for each valence orbital functions (three number, 311) with the first function composed of 3 primitive Gaussian functions; the second composed of one primitive Gaussian function and the third function composed of one primitive Gaussian function. The first "+" means that diffuse functions are used (better description of wavefunction tails) on heavy atoms and the second "+" is for hydrogen atoms. (d,p) means that d-type polarization function are used on heavy atoms and p-type on hydrogen atoms (Jensen, 2017).

The main route of toluene dissociation is C–H aliphatic bond cleavage to form benzyl. We obtained its dissociation rates via a RRKM calculation by computing the vibrational structure of its transition state during dissociation. For the transition state, it was supposed that one of the aliphatic C–H bonds is frozen. The dissociation threshold is taken to be equal to 31,400 cm^{-1} (McMillen and Golden, 1982). With this method we obtain k_{disso}(193 nm)$= 3.6 \cdot 10^6$ s^{-1} which is slightly above the experimental values measured in different works but remains of the same order of magnitude (Lin et al., 2002; Park et al., 1990; Ikeda et al., 1985). For Cycloheptatriene, we omitted its dissociation considering that it is probably quenched by isomerisation to toluene. Even if it were not, its influence on our observable (IR emission convoluted by detector response + preamplifier) is negligible as it would occur at very short times (< 0.5 µs).

The collisional energy transfers between excited toluene/non-excited toluene and excited toluene/argon are determined by the α function of the model in exponential (section 2). The α coefficients obtained by Toselli & Barker (valid below 40 000 cm^{-1} internal energy because their photon wavelength excitation is 248 nm) do not allow us to recover the IR emission decay dominated by collisions and a possible difference in measured pressure and real pressure in our cell does not explain this discrepancy between experiment and simulation. A hypothesis to explain this discrepancy is that in their work the decay time of the IR detector response was not taken into account (section 4), which could distort parameters they obtained. Another hypothesis is the possibility that collisions between excited toluene are not negligible. In any case, we know that relaxation is dominated by collisions (except probably for times below 1 µs) and therefore, the dependence of the two α functions (Tol*-Tol et Tol*-Ar) will be decisive for the IR emission signal decay (emission time profile). Based on this observation, we determined the α coefficients in such a way that our simulation of emission time profile agrees with that obtained by measurement. Simulation results with this new set of parameters are shown in figure 5.11. In the same figure, we show the vibrational emission arising simultaneously from the aromatic and aliphatic C–H stretching modes. Indeed, because of the anharmonicity, it is not possible to define aromatic C–H and aliphatic C–H separately as they both emit between 3.3 and 3.5 µm. This is why we systematically work with the sum of these two emission bands. Our observable is therefore the sum of aromatic C–H stretching and aliphatic C–H stretching emissions.

An interesting information obtained with this simulation is the curve giving the value of the internal energy in terms of time (figure 5.12) from which it is possible to plot the emission spectrum as a function of the internal energy. The emission spectrum as a function of time obtained by the simulation is shown in Figure 5.13. We cannot compare the result obtained by our simulation and the emission spectra obtained with FIREFLY given that the effects of anharmonicity were not taken into account in our simulation. In figure 5.13, we see that at high internal energy, toluene emits more via the high frequency modes. This observation is valid for any species that exhibits highly excited vibrational states. Indeed, as underlined in section 2, spontaneous emission increases as ν^3, with ν the vibrational normal modes frequency (a ν^2 contribution originates from the density of states of electromagnetic normal modes in vacuum and a ν contribution originates from the dipolar electric transition moment in the harmonic approximation of vibrational motion). This contribution to emission probability can be seen as a quantum contribution. Another contribution to the emission probability, considered as statistical, is the number of vibrational quanta contained in each mode and favours the vibrational

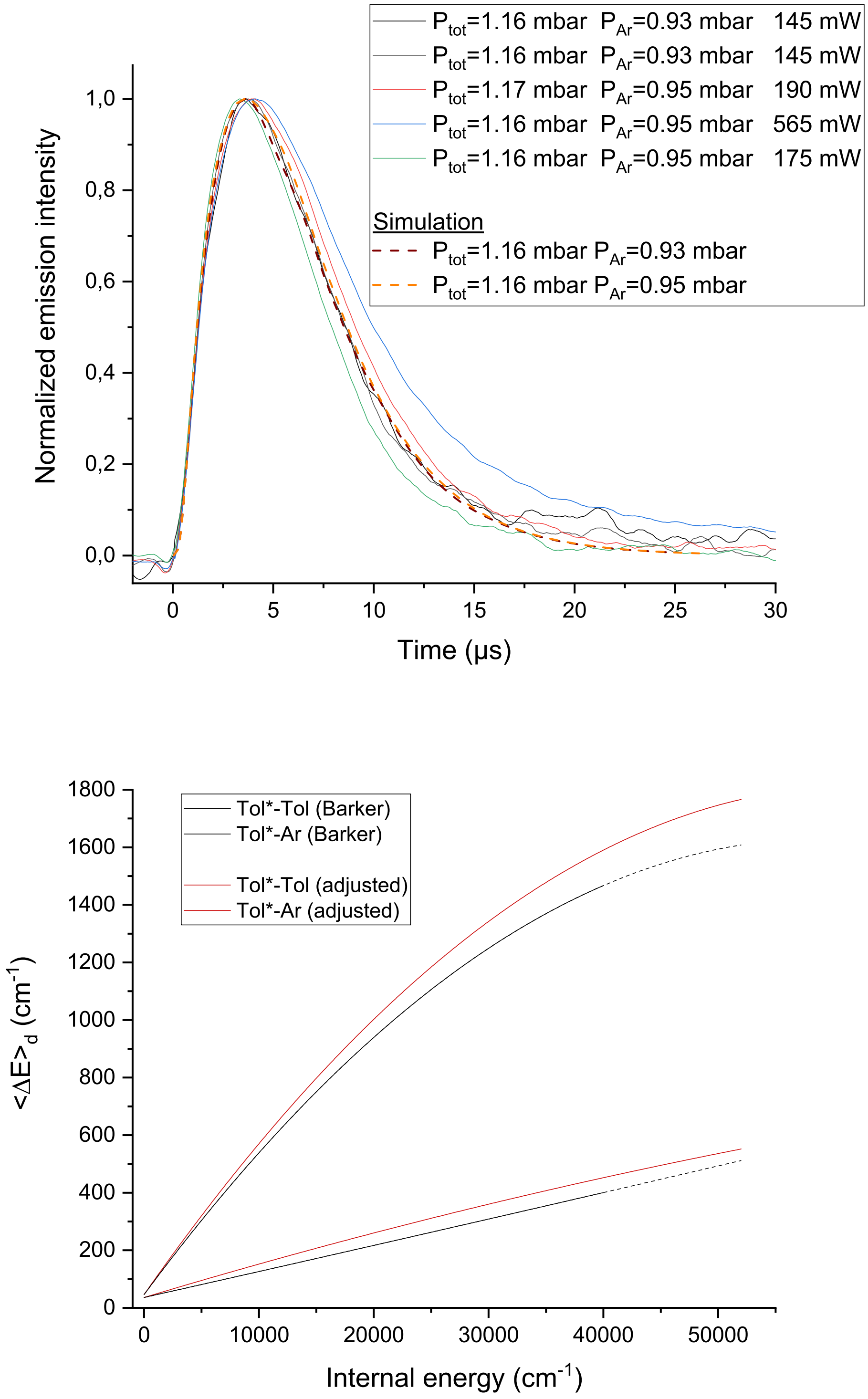

Figure 5.11: Upper panel: sum of the aromatic and aliphatic C–H streching IR emission. The experimental time trace are in solid lines. The simulated time trace are shown in dashed lines. Lower panel: the average energy transferred per down-step collisions (which is equal to α at high internal energies, see section 2) depending on the parameterization used. Dashed lines for Toselli & Barker's parameterization (Barker and Toselli, 1993) indicates extrapolation beyond their measurement. The plot is stopped at 52 000 cm^{-1}= 193 nm.

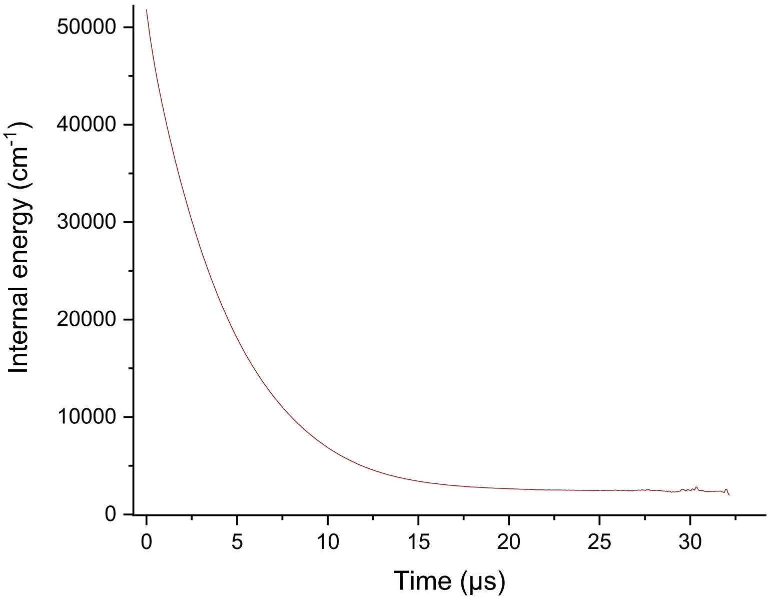

Figure 5.12: Simulated internal energy decay of toluene in terms of time, with P_{Ar}= 0.93 mbar et P_{Tol}= 0.23 mbar. The kMC trajectories were stopped at 1000 cm^{-1} internal energy.

emission via the normal low frequency modes. It turns out, according to our simulation, that the quantum contribution outweighs the statistical one.
At lower internal energy, the emission spectrum should tend towards the absorption spectrum. This is not visible in figure 5.13 because the kMC trajectory number for the calculation (10^9) is not sufficient to account for the emission spectrum in long times. Nevertheless, this kMC trajectory number remains largely sufficient for temporal traces of the aromatic and aliphatic C-H stretching vibrational modes.

Toluene ⟶ cycloheptatriene isomerization

After the observation and simulation of the relaxation of 193 nm excited toluene, we can start to investigate the relaxation of toluene-d_5^{Ar} excited at 193 nm and better understand the isomerisation to CHT which was unobservable with previously studied non-deuterated toluene.

Evidence of isomerization

We want to show in this section that the emission spectrum observed after toluene excitation-d_5^{Ar} at 193 nm suggests that deuterated toluene is the source of the detected

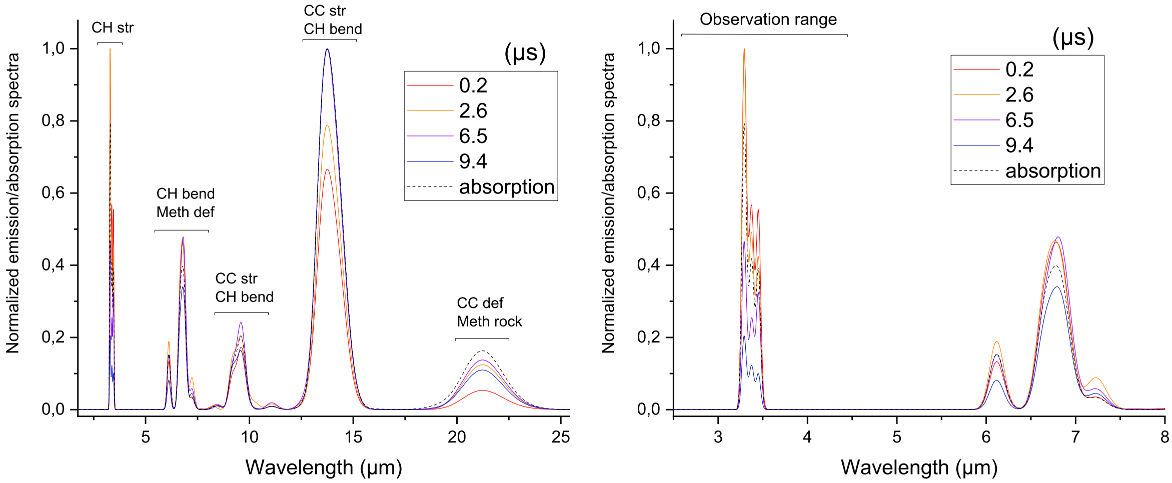

Figure 5.13: Temporal evolution of normalized emission spectra for toluene excited at 193 nm

IR emission and that the benzene ring was populated with hydrogen most likely from the methyl group.

We had the opportunity to record four acquisitions at several laser beam powers (upstream of the entrance UV window). The resulting emission spectra (integrated over the whole relaxation, *i.e.* between 1 and 20 µs) are shown in Figure 5.14 with toluene emission spectra. The dotted line shows the absorption spectra of toluene and toluene-d_5^{Ar}. We can clearly distinguish the emission of aromatic C–H stretching modes (≈ 3.28 µm) and the emission of aliphatic C–H stretching modes (≈ 3.45 µm). Not surprisingly, for toluene, the aromatic C–H band is stronger than the aliphatic C–H band. For toluene-d_5^{Ar}, aliphatic C–H band emission is stronger than that of the aromatic C–H and the latter clearly does not appear in the toluene-d_5^{Ar} absorption spectrum. The emission and absorption band of aromatic C–D appear partially around 4.4 µm. The aromatic C–D absorption band position may be close to reality but, given our method for obtaining the absorption spectra, we doubt its relative intensity (especially since it is not reproducible, unlike the relative intensity of the absorption band around 3.45 µm). The aliphatic C–D band, for its part, is undetectable because it emits around 4.6 and 4.7 µm (out of range). In figure 5.14, we see that the aromatic C–H band appears after excitation of toluene-d_5^{Ar}. Nevertheless, the mere appearance of this emission band does not prove that these aromatic C–H are coming from a toluene isotopologue-d_5^{Ar}. If we assume that the observed emission is due to a stable species, formed by the toluene dissociation-d_5^{Ar}, then its initial internal energy must be 51 800 cm^{-1} subtracted from the dissociation barrier which should be close to that of phenyl formation (because, in this case of dissociation, a C-C bond cleavage should likely occur) which is around 35 000 cm^{-1} (McMillen

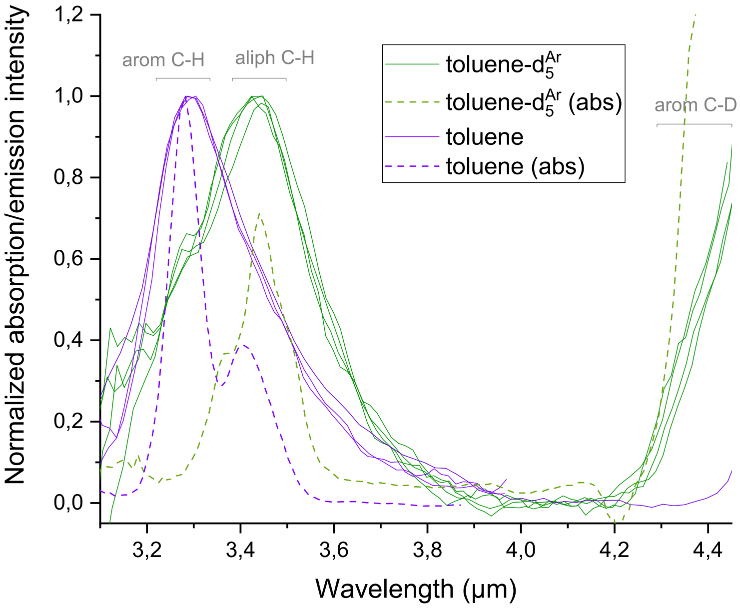

Figure 5.14: For all these spectra, the total pressure is 1.16 mbar with 0.93 mbar argon partial pressure. Green spectra: emission spectra recorded after excitation at 193 nm of toluene-d$_5^{\mathrm{Ar}}$ with laser power varying from one acquisition to another (between 140 et 190 mW). Purple spectra: emission spectra recorded after excitation at 193 nm of CH_5CH_3 toluene with laser power between 145 and 175 mW.

and Golden, 1982). This dissociation would leave the species with a maximum internal energy around 20 000 cm^{-1} and it would be then difficult to explain the strong anharmonicity (figure 5.15) observed before 10 µs and the variation of the emission spectrum profile indicating high initial internal energy (figure 5.15). Another difficulty is to find a species that is formed by dissociation (smaller than toluene) and contains aromatic C–H, aliphatic C–H and aromatic C–D bonds.

Given the proximity of the absorption bands of toluene and CHT in the [3 µm; 4.5 µm] wavelength range and the low resolution of our circular variable filter, we cannot rule out a contribution from CHT to the observed emission spectrum. However, as noted above, previous works show that vibrationally excited CHT rapidly isomerizes to toluene and therefore, its vibrational emission is quenched by isomerization to toluene. It is therefore reasonable to consider that the emission spectra obtained from 193 nm excited toluene-d$_5^{\mathrm{Ar}}$ are due to toluene isotopologues-d$_5$.

We show in figure 5.16 the emission spectra kinetics of excited toluene-d$_5$ from four acquisitions. One way to ensure that there is no emission signal for wavelengths below 3.2 µm is to check the non-reproducibility of detected signals from one acquisition to another. That is indeed the case below 3.2 µm (figure 5.16). We will see later that in

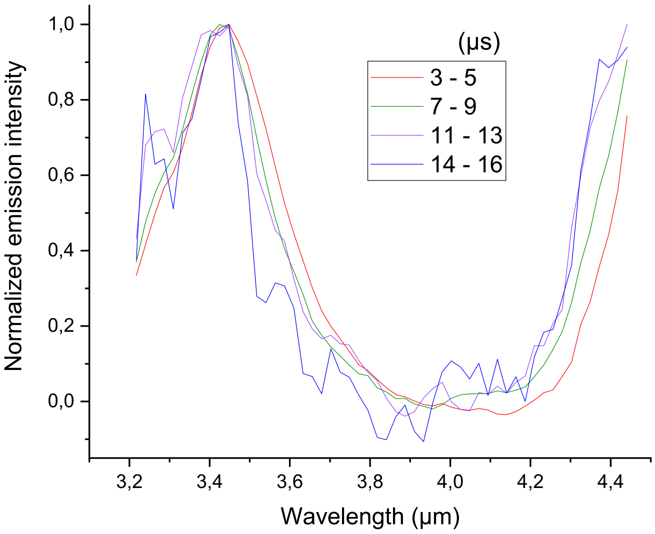

Figure 5.15: Emission spectrum profile variation after excitation at 193 nm of toluene-d_5^{Ar}. We clearly see the redshift in the short times.

the case of phenylacetylene an emission signal appears between 3.1 and 3.2 µm and that confirms the idea that in the toluene and toluene-d_5 cases there is no strong emission signal for wavelengths below 3.2 µm.

Long time emission spectra

We know that the emission spectrum at the end of the relaxation (beyond 10 µs in the case of toluene-d_5, see figure 5.12) should tend towards the absorption spectrum of the emitting species. We show in figure 5.17 emission spectra recorded between 10 and 16 µs from the same acquisitions as in figure 5.16. We see that the ratio between the three emission bands remains roughly the same from one acquisition to the next. Knowing that the emission at the end of the relaxation informs us about the emitting species (absorption spectra), we can try to check whether all the toluene-d_5^{Ar} have isomerized in such a way that species which emit at the end of the relaxation form or do not form a mixture of toluene-d_5 isotopologues. We do not have the means to obtain the experimental absorption spectrum of the toluene-d_5 isotopologue mixture.

To obtain the theoretical emission spectrum of this isopologues mixture, we must first inventory the isotopologues liable to appear after CHT isomerization to toluene-d_5. Once the toluene has isomerized to CHT, we know that hydrogen scrambling in CHT is very fast compared to isomerization of CHT to toluene. We can then assume that when CHT isomerizes back to toluene, any toluene-d_5 isotopologue may appear. Therefore, we can classify the toluene-d_5 isotopologues according to their aromatic hydrogen number.

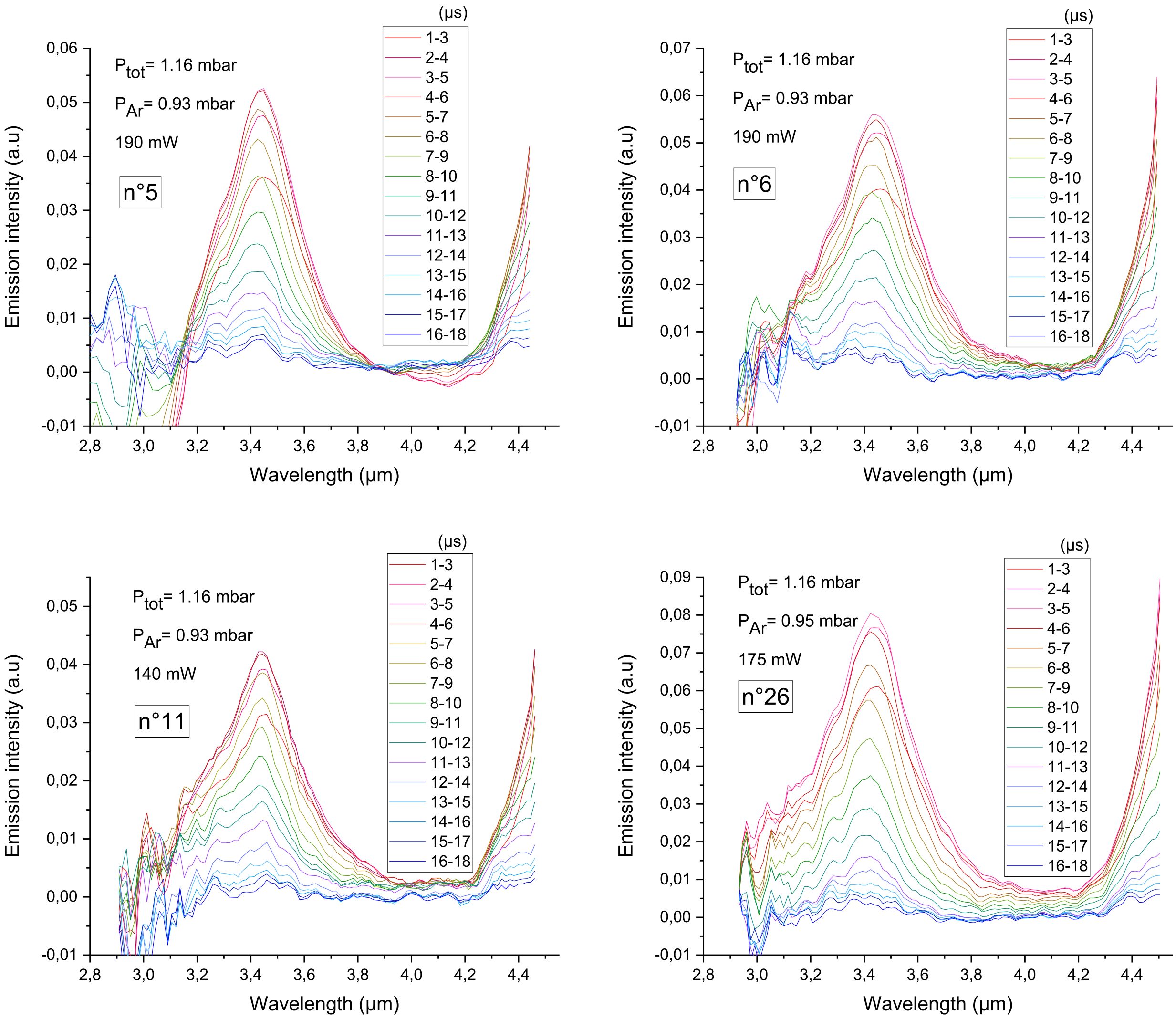

Figure 5.16: Kinetics of the emission spectra obtained for four different acquisitions with approximately the same pressure conditions. The laser power upstream of the entry window is also indicated. From left to right and top to bottom: acquisitions n° 5, 6, 11 et 26.

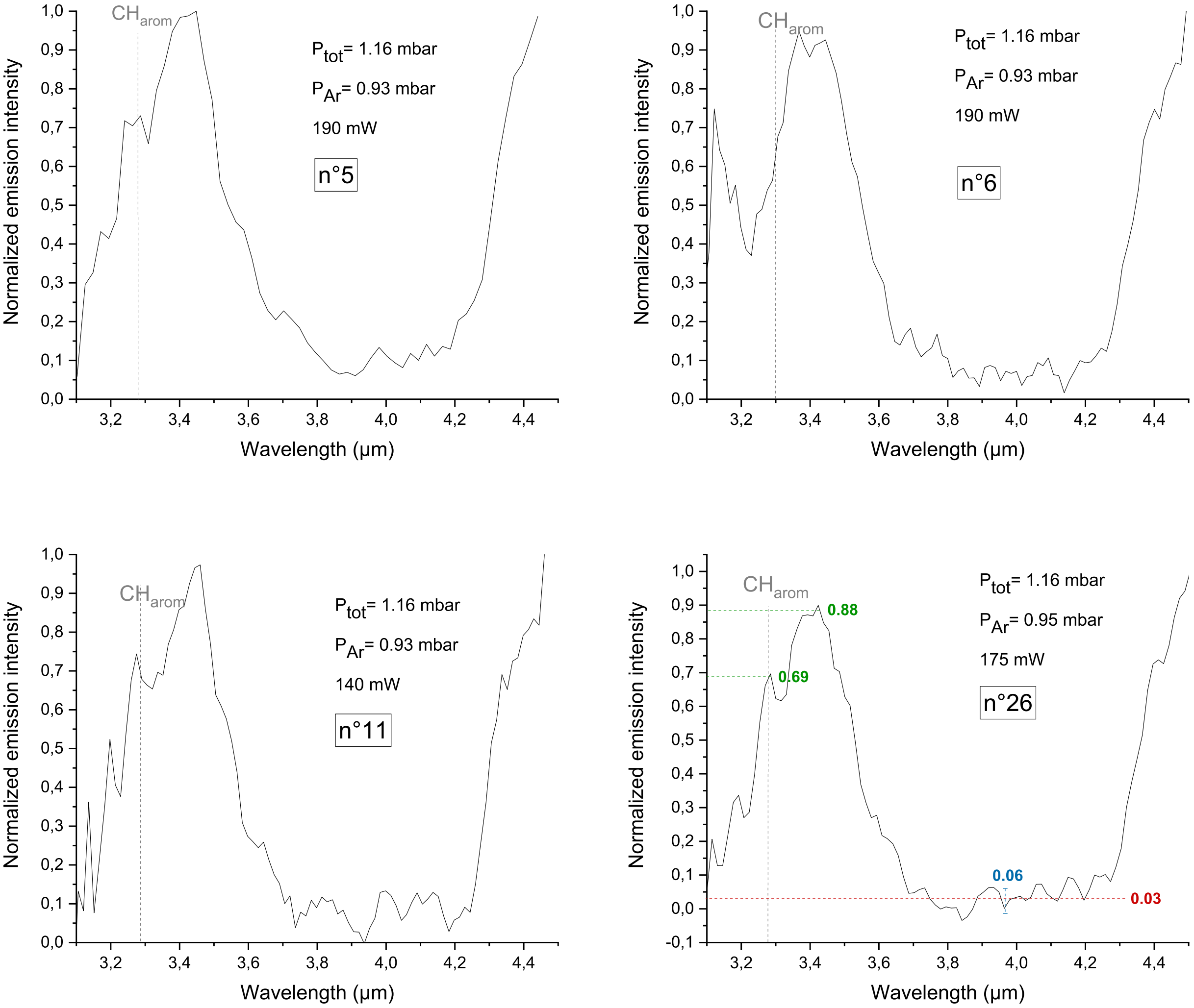

Figure 5.17: Emission spectra with integration between 10 and 16 µs for the 4 acquisitions in the figure 5.16. From left to right and top to bottom: acquisitions n° 5, 6, 11 et 26.

We have 4 classes of isotopologues:

- The class of isotopologues involving no aromatic hydrogen in the phenyl group contains only one species: toluene-d_5^{Ar}.
- The class involving a single aromatic hydrogen contains $5 \times 3 = 15$ isotopologues. The 5 stems from the five possible sites on the phenyl and the 3 stems from the three possible sites for the only deuterium in the aliphatic group.
- The class involving two aromatic hydrogens contains $10 \times 3 = 30$ isotopologues.

The 10 stems from the combinations number of two hydrogens among the 5 phenyl sites and the 3 stems from the combinations number in the methyl group.

- For that involving three aromatic hydrogens, we do the same calculation as for the previous point (we reverse hydrogens and deuteriums in the phenyl). However, we do not multiply by 3 because there are in that class three aliphatic deuteriums, which sets the number of possible arrangements for the methyl group at 1. This makes 10 isotopologues for this last class.

We have a total of 56 isotopologues which can appear equiprobably when deuterated CHT isomerizes to toluene. It is then possible to calculate the absorption spectrum by ab initio calculation (CAM-B3LYP/6-311++G(d,p), in the harmonic approximation) of these 56 isotopologues (flat population distribution). Figure 5.18 shows the absorption spectrum of this isotopologue set and the spectrum of the initially excited species. It was shown, from observed emission spectra (previous section), that isomerization to CHT occurs after excitation of toluene-d_5^{Ar}. However, it was not shown that all excited toluene-d_5^{Ar} isomerized. Ideally, the emission spectrum at the end of the relaxation should be compared with the absorption spectrum of all isotopologues. Figure 5.18 clearly shows that the aromatic C-H band is more intense than the aliphatic C–H band, contrary to what is obtained from the experiment (figure 5.17). Thus, the idea is to take linear combinations of the two absorption spectra (black and red of figure 5.18) to simulate the emitting population which, in that case, divides into two populations: non-isomerized toluene d_5^{Ar} and the mixture of toluene-d_5 isotopologues produced by isomerization.
Actually, toluene-d_5^{Ar} absorption spectrum calculated by DFT and that experimentally measured do not entirely agree. Indeed, Fermi resonances occur (Cavagnat and Lespade, 2001) and maybe also rotational structures (internal rotation of the methyl group) which broaden the vibrational bands. Likely, there are also the same effects on the absorption spectrum of toluene-d_5 isotopologues mixture. However, since we are only interested in ratios between two relatively broad emission bands ($\approx$ 0.2 µm or $\approx$ 200 cm^{-1} around 3.3 µm), the relative intensities of theoretical spectra can be considered to be close to reality.

Proportion of non-isomerized toluene-d_5^{Ar}

In this section, we present the intensity ratio values between the aromatic C–H, aliphatic C–H and aromatic C–D emission bands that we measured at the end of the relaxation. Before giving results of our measurements, we present the way in which these values were deduced with the example of the $I_{3.3}/I_{3.4}$ ratio for acquisition n° 26 (arbitrarily

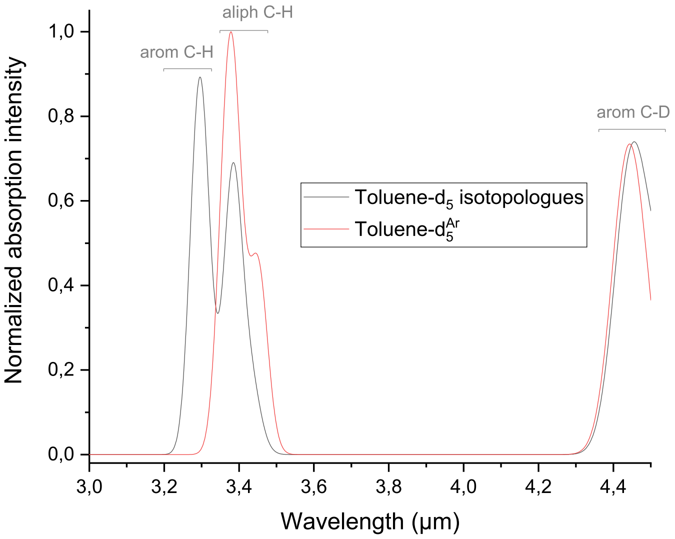

Figure 5.18: Absorption spectra simulated by CAM-B3LYP/6-311++G(d,p) for toluene-d_5^{Ar} and the mixture of all isotopologues liable to appear after the CHT-d_5 → toluene-d_5 isomerisation. A gaussian convolution (fwhm = 70 cm^{-1}, faithful to the resolution of the interference filter) have been applied to the histogram absorption spectra.

chosen). This is the intensity ratio between the aromatic C–H band and the aliphatic C–H band emission. All the following values are in arbitrary units. As detailed in the bottom right (n°26) of figure 5.17, we must first define the zero of the spectrum which is 0.03 in this case. Around 4.0 µm, we define the electronic noise which is estimated to be about 0.06 for the acquisition n°26. However, the electronic noise will vary on our processed spectrum. Indeed, we used a multiplicative factor that is a function of the wavelength and reflects the response function of the apparatus (quantity $\mathscr{F}(\lambda)$ described in section 4). This multiplication factor is 1.25 for the aromatic C–D band (4.4 µm), 1.5 for aliphatic C–H (3.4 µm) and 2 for aromatic C–H (3.3 µm). The noise level is then estimated at 0.12 around the aliphatic C–H band, 0.10 around the aromatic C–H band and 0.08 around the aromatic C–D band.

The following results are obtained for acquisition n° 26:

$$\begin{cases} I_{3.3} = 0.60 \pm 0.06 \\ \\ I_{3.4} = 0.80 \pm 0.05 \end{cases}$$

hence

$$\frac{I_{3.4}}{I_{3.3}} = 1.33 \pm 0.23$$

	$I_{3.4}/I_{3.3}$	$I_{4.4}/I_{3.4}$
acquisition 05	1.52 ± 0.25	1.00 ± 0.11
acquisition 06	1.39 ± 0.14	0.92 ± 0.07
acquisition 11	1.44 ± 0.38	0.85 ± 0.16
acquisition 26	1.33 ± 0.23	1.11 ± 0.12
Average	1.42 ± 0.25	0.97 ± 0.12

Table 5.1: Measured emission bands ratios for the four acquisitions. The average of these values is deduced.

Table 5.1 shows the value of ratios measured for the four acquisitions. From the average of the four measurements, it is then possible to constrain the intensity ratios for the linear combinations of the two theoretical absorption spectra. In the isotopologues mixture absorption spectrum also appears toluene-d_5^{Ar} as this species can reappear after CHT isomerization. Figure 5.19 shows several absorption spectra that should be observed depending on the percentage of initial toluene-d_5^{Ar} that have not isomerized. Our measurements (table 5.1) constrain the possibilities. Figure 5.19 also shows the areas in which the 3.3 µm and 4.4 µm bands should be located (that of 3.4 µm has been fixed to 1). The area delimitations are defined from the two average values given in table 5.1. It can be seen that the percentage of non-isomerized toluene-d_5^{Ar} should be between 20 % et 50 %. It is then assumed that 35 % ± 15 % of toluene-d_5^{Ar} did not isomerize. It is also remarkable that the curve corresponding to 40 % shows the values $I_{3.4}/I_{3.3}$=1.45 and $I_{4.4}/I_{3.4}$= 0.97, both ratios being near averaged measured ratios.

How does the constraint on the proportion of unisomerised toluene-d_5^{Ar} translate into the characteristic amount of the isomerisation reaction ?
To answer this question, it is necessary to go through the simulation of the relaxation cascade which will allow us to obtain, using the constraint discovered above, some information on the isomerisation rate. In order to do so, we must first determine the collisional energy transfer for our isotopologues.

Collision parameters

As in the case of toluene, we have estimated coefficients of the α function which parameterizes the collisional energy transfer. We show in figure 5.20 the aromatic C–H +

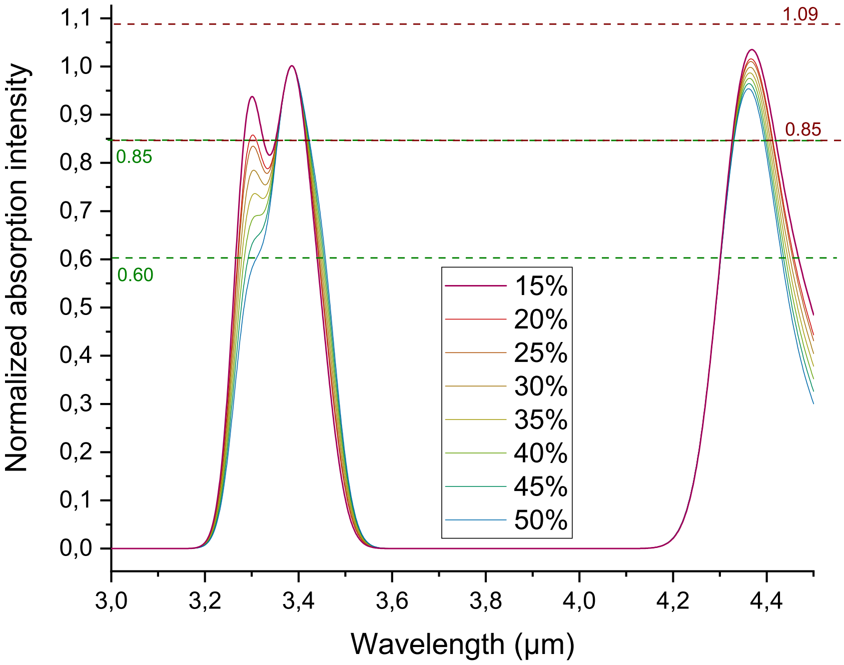

Figure 5.19: Linear combinations of the absorption spectrum of all isotopologues and that of toluene-d_5^{Ar}. Non-isomerised toluene-d_5^{Ar} percentage are shown for all these combinations. Theoretical spectra are obtained by CAM-B3LYP/6-311++G(d,p). The green dotted lines delimit the aromatic C–H band and are determined by the uncertainty of the average ratio of table 5.1. Those in dark red delimit the aromatic C–D band. The aliphatic C–H band is arbitrarily fixed to unity for all spectra.

aliphatic C–H stretching modes emission obtained by the simulation for different sets of collisional parameters, superimposed on the emission signal obtained by FIREFLY. We see that the temporal emission is not very sensitive to the settings shown in figure 5.20. This allows us to arbitrarily choose a parameterization while keeping in mind that we have an uncertainty.
A very important fact for the rest of the work is that the isomerization proportion obtained by the simulation changes very little from one set of parameters to another. Indeed, by arbitrarily fixing the isomerization rates with $A=3 \cdot 10^{19}$ s^{-1} and $E_{\mathrm{iso}}= 28400$ cm^{-1} (the isomerization threshold) we obtain a proportion of non-isomerized toluene-d_5^{Ar} of about 42 % for all settings in the figure 5.20. In the following, we have arbitrarily chosen to work with the settings shown in dark yellow.

Constraints on A and $\mathbf{E_{iso}}$

Now, knowing that the non-isomerised toluene-d_5^{Ar} proportion is between 20 et 50 %, we can simulate the relaxation cascade by changing the pair (A, E_{iso}) and determine the set of pairs that verify this constraint. The result is shown in figure 5.21. The black curve represents all the pairs for which the proportion of non-isomerized species is 20 % and the red curve represents the proportion at 50 %. The result set of (A, E_{iso}) pairs is therefore between these two curves. The evolution with internal energy of the isomerisation rate for different pairs (A, E_{iso}) is shown in figure 5.22. From these k(E; A, E_{iso}) rate curves, we understand why the possibilities may seem endless if the only condition is the isomerized toluene-d_5^{Ar} proportion. Indeed, either the isomerization rate is very high at 193 nm and decreases very rapidly with the internal energy, or it is relatively low at 193 nm and decreases slowly with internal energy (figure 5.22). Unfortunately, it was not possible to find a value for the isomerisation rate at a given internal energy. This would have solved the problem. We will see if the kinetics of the aromatic C–H + aliphatic C–H emission signal can help us to further constrain (A, E_{iso}) pairs.

Relaxation kinetics

Figure 5.23 shows emission signals of the aromatic C–H, aromatic C–D, aliphatic C–H and aliphatic C–D stretching modes for two pairs (A, E_{iso}). These simulated emissions are not convolved by the detector response. The two (A, E_{iso}) pairs chosen are the two extremes of figure 5.21 ($A=3 \cdot 10^{13}$ s^{-1}; $A=3 \cdot 10^{27}$ s^{-1}). The emission signal profile of aromatic C–H and aliphatic C–D stretching modes is the result of the contribution of two processes (figure 5.23). On the one hand, isomerization produces isotopologues that emit via these wavelengths. On the other hand, radiative cooling induce the internal energy

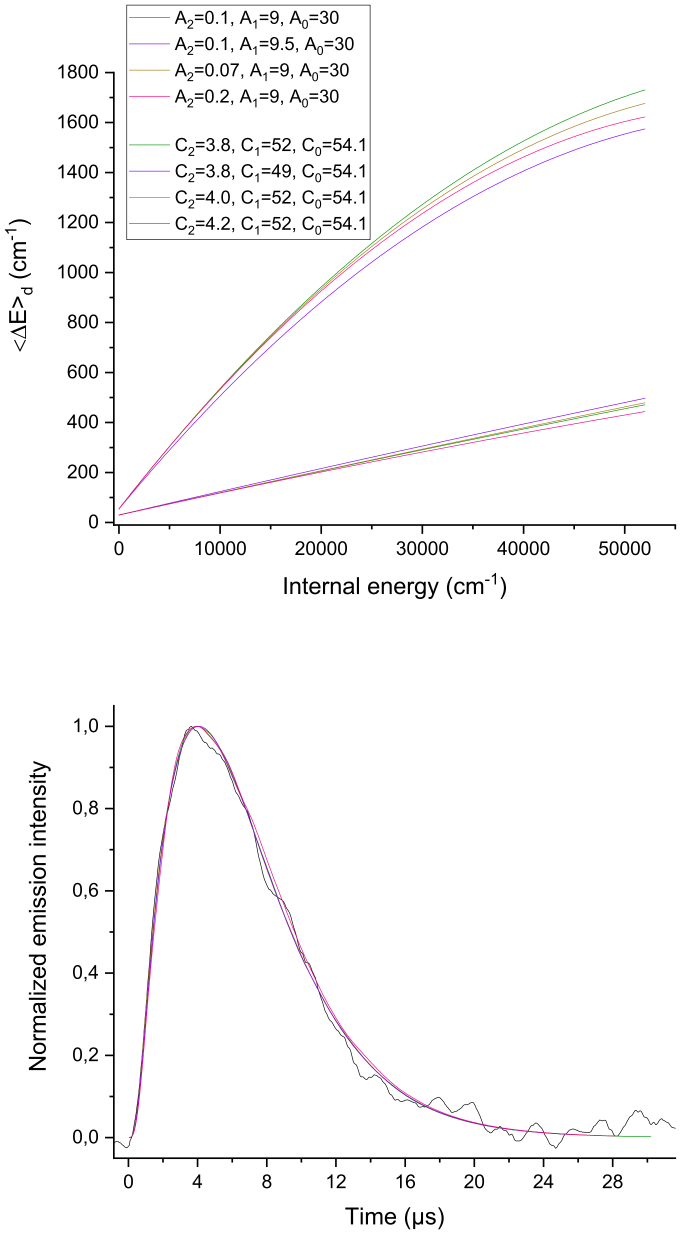

Figure 5.20: Mean energy transferred per down-step collision for several settings. The parameterization is expressed as a second order polynomial such as $A_0 + A_1 \cdot 10^{-3} \times E + A_2 \cdot 10^{-7} \times E^{2}$ for collisions between excited toluene and argon and $C_0 + C_1 \cdot 10^{-3} \times E + C_2 \cdot 10^{-7} \times E^{2}$ for that between excited and non-excited toluene, E is the internal energy. The time traces of aromatic + aliphatic C-H stretching modes from all settings are superimposed on that obtained by the experiment.

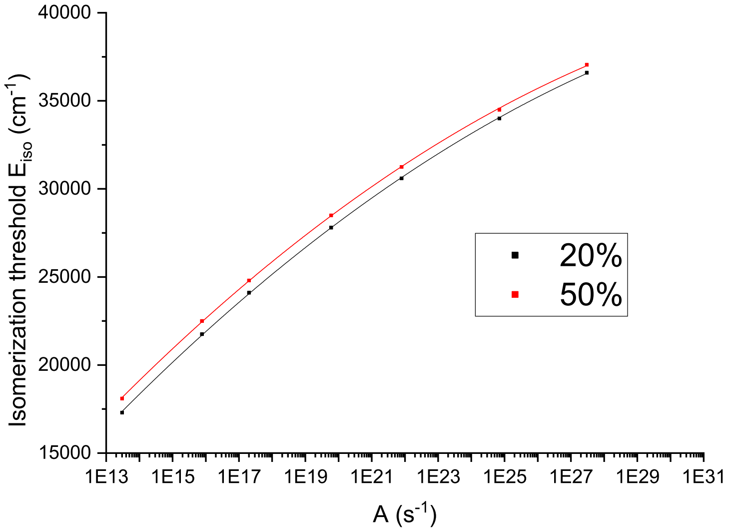

Figure 5.21: Each red dot represents the pairs (A, E_{iso}) giving a proportion of 20% ± 2% non-isomerised toluene-d_5^{Ar}. The same goes for black dots for a proportion of 50% ± 2%. The curves are fits for each set of points.

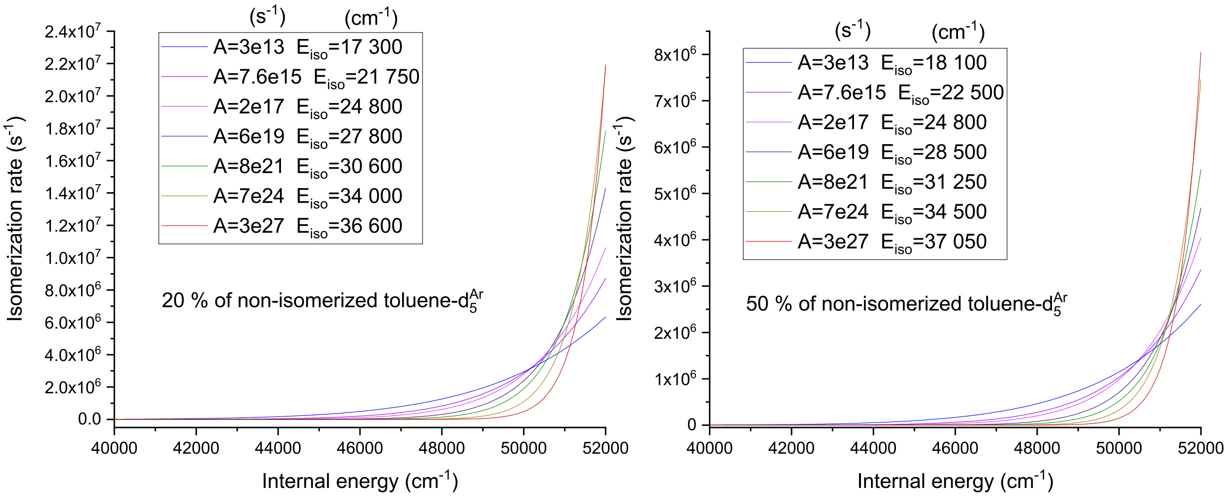

Figure 5.22: Isomerisation rate obtained by RRK for the several (A, E_{iso}) pairs.

decrease of the species, which results in a decrease of the vibrational emission. The emission signal of aromatic C–D and aliphatic C–H stretching modes can only decrease. Two decay regimes can be distinguished, separated around 1 µs. For times before 1 µs, dissociation, isomerisation and collision occur. For the aromatic C–D and aliphatic C–H stretching modes, the decline is very marked, which would be mainly due to isomerisation and marginally due to dissociation. Indeed, in this first regime, the aliphatic C–D and aromatic C–H stretching modes emission increases despite the decrease of the internal energy, which indicates a high rate of isomerisation. The RRKM calculation shows that the dissociation rate of methyl hydrogen is around 10^5 s^{-1} which is negligible compared to the isomerization rate. Otherwise, we would have very little isomerization.

For times beyond 1 µs, the decline is dominated by collisions as evidenced by the similar decline in aromatic C–H and aliphatic C–D stretching modes (figure 5.23 (c) et (d)). We summarize all this by concluding that before 1 µs, the species is in isomerization regime and after 1 µs, it is in collisional regime.

In figures 5.23 (c) and 5.23 (d), we see that the isomerization regime for ($A=3{\cdot}10^{27}$ s^{-1}, $E_{\mathrm{iso}}=36\ 800$ cm^{-1}) is shorter than for ($A=3{\cdot}10^{13}$ s^{-1}, $E_{iso}=17\ 800$ cm^{-1}). This can be seen in particular by comparing the position of the maximum emission of aromatic C-H and aliphatic C-D stretching modes. This can be explained by the evolution of the isomerization rate with the internal energy (figure 5.22). Indeed, for the ($A=3{\cdot}10^{27}$ s^{-1}, $E_{\mathrm{iso}}=36\ 800$ cm^{-1}) pair for which the maximum emission is reached earlier, the isomerization rate also drops very quickly.

One can also try to understand why the aromatic C–H and aliphatic C–D streching modes emission are lower than that of aromatic C–D and aliphatic C–H stretching modes. In the case of the ($A=3{\cdot}10^{13}$ s^{-1}, $E_{\mathrm{iso}}=17\ 800$ cm^{-1}) pair, 34% of toluene-d_5^{Ar} did not isomerize. A probability calculation shows that for the isotopologues mixture there are, on average, two aromatic C–H bonds (and a single aromatic C–H bond) per isotopologue. However, it remains at the end of the relaxation 34% of toluene-d_5^{Ar} which has no aromatic C–H bonds and three aliphatic C–H bonds. A simple calculation then predicts in the case of ($A=3{\cdot}10^{13}$ s, $E_{iso}=17\ 800$ cm^{-1}) that after isomerization (*i.e.* in the collisional regime) 1.7 aliphatic C–H bonds and 1.3 aromatic C–H bonds should emit. Their ratio is 1.3. However, it was noticed from DFT results data that generally, for toluene-d_5 isotopologues, the vibrational intensity strength of aliphatic C–H stretching modes are more than 50 % higher than that of aromatic C-H stretching modes. Thus, the emission ratio between aliphatic C–H and aromatic C–H stretching modes should correspond to the value $(1.5 \times 1.7)/1.3 = 2$ (actually this ratio should be more than 2, see the previous sentence). This value corresponds approximately to the emissions ratio $\frac{70}{30} = 2.3$ measured in figure 5.23 (a). This measurement is carried out in the collisional

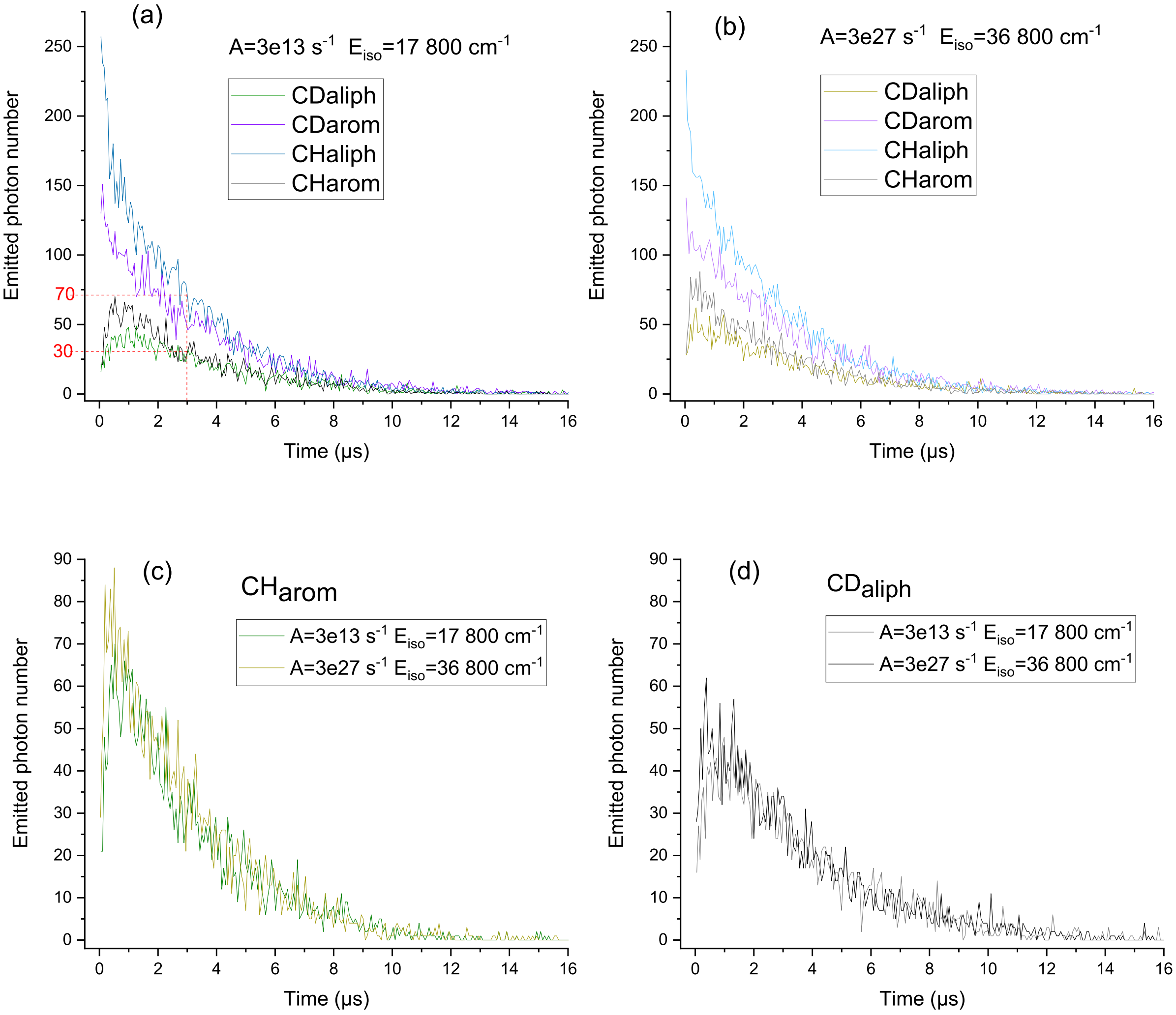

Figure 5.23: (a) et (b): Time emissions for the four bands and two (A, E_{iso}) pairs. (c): Aromatic C–H emissions for both pairs. (d): Aliphatic C–H emissions for both pairs.

regime of the relaxation because the population is established.

To better understand the isomerization regime, we can investigate how the toluene-d_5^{Ar} fraction having undergone its first isomerization decreases (figure 5.24). The first isomerization is the only information that can be detected because it is at the origin of other toluene-d_5 isotopologue appearance. Experimentally, the subsequent isomerizations are indistinguishable because their starting point is the isotopologue mixture. For all (A, E_{iso}) pairs (for which the non-isomerized toluene-d_5^{Ar} proportion is around 30 %) the first isomerizations occur before 1 µs (figure 5.24).

As mentioned above, because of anharmonicity, the only experimental signals that can be compared to our simulation is the sum of aromatic C–H and aliphatic C–H stretching modes emission. Figure 5.25 (a) shows the simulation of aromatic C–H + aliphatic

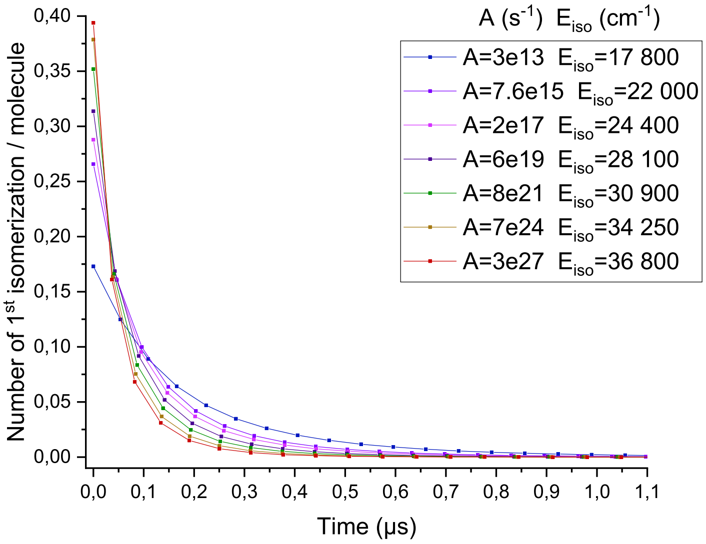

Figure 5.24: Simulation of the number first isomerization per molecule (*i.e* first isomerization proportion) from toluene-d_5^{Ar} to CHT-d_5. The simulation is carried out for (A, E_{iso}) pairs presented in figure 5.22.

C–H stretching modes emission signal normalized and we can see that the rise in the emission signal due to the aromatic C–H (figure 5.23) is embedded in the decreasing emission signal of the aliphatic C–H. The sharp decline in aliphatic C–H (figure 5.23) during the isomerization regime is not visible because it is compensated by the rise of aromatic C–H. It is noticeable that there is no significant difference in aromatic C–H + aliphatic C–H emission profile whatever is the (A, E_{iso}) pair used for the isomerization rate simulation.

In addition, the rising edge of the preamplifier (≈ 0.3 µs, see section 4) prevents us from observing the kinetics before 0.5 µs (figure 5.25 (b)). However, even if we could observe at times shorter than 0.5 µs, it would be necessary to enormously limit the electronic noise to distinguish the difference in the aromatic C–H emission according to the (A, E_{iso}) pair as shown in figure 5.23 (c) et (d).

We show in figure 5.26 the normalized emission signal of aromatic C–H + aliphatic C–H detected after 193 nm excitation of toluene and toluene-d_5^{Ar} and their simulation in dotted lines. Beyond 5 µs, given the difference in collisional energy transfer (slightly lower for toluene-d_5 and this isotopic effect had already been noted in (Barker and Toselli, 1993)), the decline is slightly different for the two species. Before 5 µs, there is no difference between the two spectra and this brought us to mind, for a moment, that isomerization was negligible beyond 0.5 µs (which corresponds to approximately 47 000 cm^{-1}). However, from the simulation, we now know that the difference in the

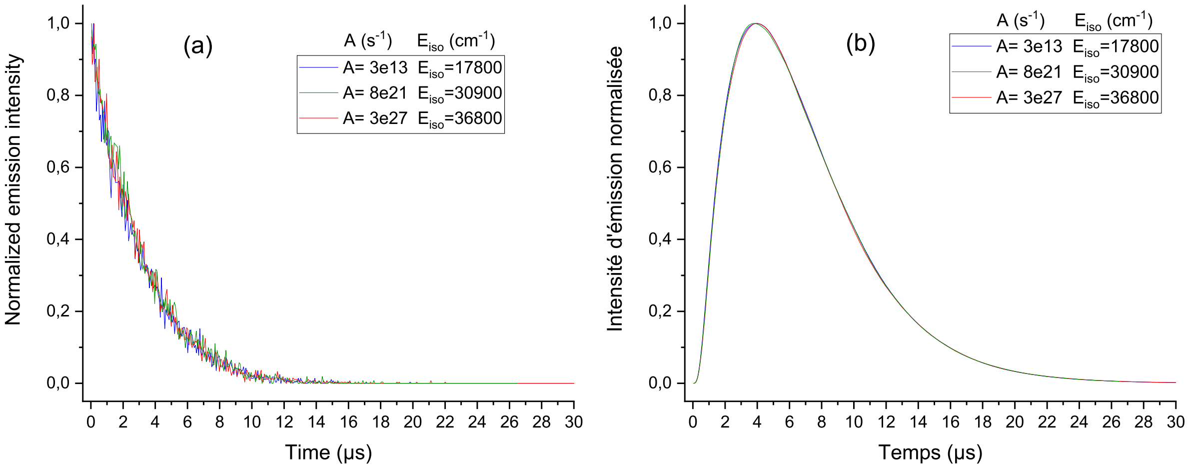

Figure 5.25: Sum of simulated aromatic C–H and aliphatic C–H stretching modes emission. (a): without convolution by the preamplifier response. (b): with convolution by the preamplifier response.

aromatic C–H + aliphatic C–H emission signal between (A,E_{iso}) pairs is experimentally indistinguishable. We therefore concluded that the emission kinetics of aromatic C–H + aliphatic C–H stretching modes do not allow us to obtain any information on the isomerization kinetics because it is too fast for our preamplifier.

Other constraints ?

A first constraint is provided by the result indicating that not all toluene-d_5^{Ar} have isomerized. A maximum of 80 % of the toluene-d_5^{Ar} must be isomerized. The probability of isomerization at 51 800 cm^{-1} is written as follows:

$$P_{\text{iso}}(51800\ \text{cm}^{-1}) = \frac{k_{\text{iso}}}{k_{\text{iso}} + k_{\text{coll}} + k_{\text{disso}} + k_{\text{vib}}^{\text{tot}}} \tag{5.1}$$

For 0.93 mbar argon partial pressure and 0.23 mbar toluene partial pressure, the Lennard-Jones collision rate is $8.8 \cdot 10^6\ \text{s}^{-1}$ (see section 2). The RRKM calculation performed for an aliphatic C–H bond cleavage indicates a rate at the order of $10^5\ \text{s}^{-1}$ at 193 nm and the vibrational emission rate $k_{\text{vib}}^{\text{tot}}$ over all vibrational modes is of the order of $10^2\ \text{s}^{-1}$. Then, in the calculation of P_{iso}(51800 cm^{-1}), the dissociation and vibrational emission rate are neglected compared to the collision rate. As for the isomerization rate k_{iso}(193 nm), we know that some species have isomerized but not all. This assumes that after a certain time the isomerization is quenched by collisions and figure 5.24 suggests that the isomerization proportion is fixed within 1 µs. Since all first isomerizations occur in less than 1 µs (internal energy > 43 000 cm^{-1}), we can state that k_{iso}(193 nm) is not

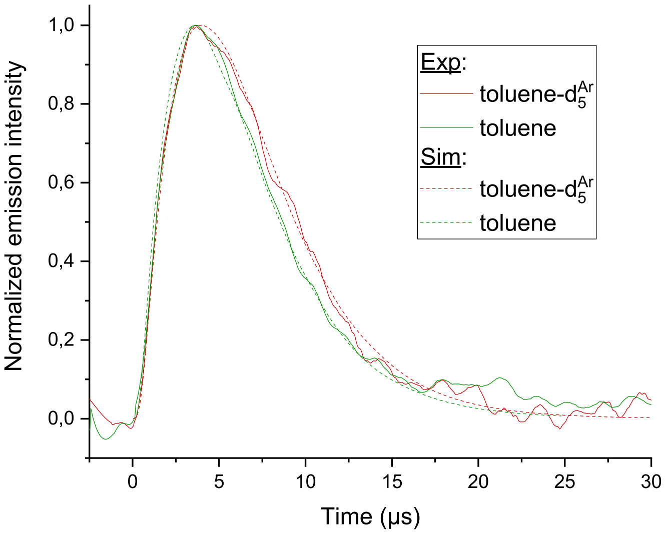

Figure 5.26: Temporal (aromatic C–H + aliphatic C–H) emission signal after excitation at 193 nm from toluene (in green) and toluene-d$_5^{\mathrm{Ar}}$ (in red). The resulting simulations are dotted.

negligible in the expression 5.1.
We write the isomerization probability at 193 nm (*i.e* to isomerize before the first collision occurs) as

$$P_{\mathrm{iso}}(51800\ \mathrm{cm}^{-1}) = \frac{k_{\mathrm{iso}}}{k_{\mathrm{iso}} + k_{\mathrm{coll}}} \tag{5.2}$$

Experimentally, we obtained that over the entire relaxation the isomerized toluene-d$_5^{\mathrm{Ar}}$ proportion is at most 80 %. A constraint is then to fix an upper limit on the isomerization rate so that at 193 nm less than 80% of toluene-d$_5^{\mathrm{Ar}}$ have isomerized , *i.e.* $P_{\mathrm{iso}}(51800\ \mathrm{cm}^{-1}) \leq 0.8$. Hence

$$P_{\mathrm{iso}}(51800\ \mathrm{cm}^{-1}) \leq 0.8 \iff k_{\mathrm{iso}}(51800\ \mathrm{cm}^{-1}) \leq 4 \times k_{\mathrm{coll}} = 3.5 \cdot 10^7 \mathrm{s}^{-1} \tag{5.3}$$

This is translated as a constraint on (A, $\mathrm{E_{iso}}$) pairs by the following inequation

$$A \leq \frac{3.5 \cdot 10^7}{(1 - E_{\mathrm{iso}}/51800)^{38}} \tag{5.4}$$

Figure 5.27 shows how this constraint is added to figure 5.21. All A-prefactors values that respect the inequality 5.4 are to the left of the green curve. We then fix the maximum limit of $\mathrm{E_{iso}}$ at 39 000 cm^{-1}. To decrease this maximum value, a more elaborate probability calculation with credible hypothesis is needed.

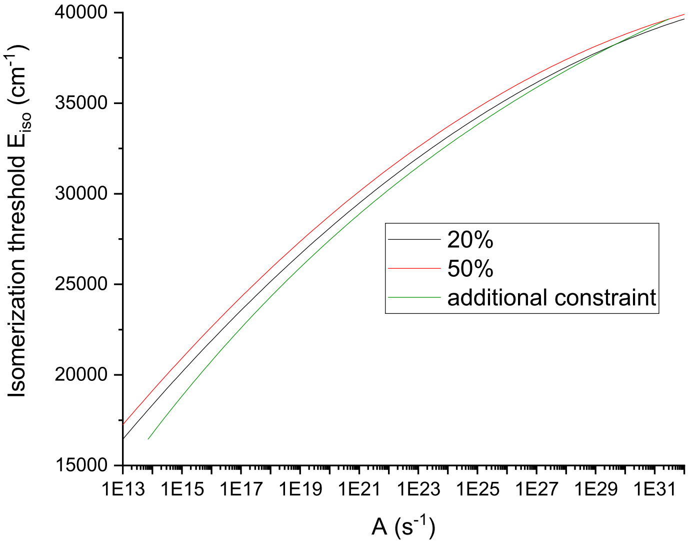

Figure 5.27: Red curve: set of (A, E_{iso}) leaving a proportion of toluene-d_5^{Ar} at 50 %. Black curve: proportion of toluene -d_5^{Ar} at 20 %. In green: for condition 5.4 to be verified, the couple must be on the left of the curve .

According to figure 5.26, we can consider that the system is already in the collisional regime at 3.5 µs, which corresponds to internal energy between 27 000 and 28 000 cm^{-1}. Thus, isomerization rate should be negligible compared to collision rate around 28 000 cm^{-1}. However, this new constraint does not fix a relevant lower limit to E_{iso} as it would be around 10 000 cm^{-1}.

k_{iso}(193 nm) determination

The investigation carried out in Chi-Kung Ni's group consisted in understanding the photodissociation of benzene derivatives via a multimass ion imaging detection system (Lin et al., 2002; Ni* and Lee, 2004; Tseng et al., 2006). Their detection system comprises a mass spectrometer, a two-dimensional ion detector whose axis reflect the mass and the ions recoil velocity. Toluene that undergoes dissociative ionization via a pump-probe system is then unambiguously detected by its signature on the two-dimensional detector. Therefore, it is possible to plot the ion signal in terms of the time period between pump and probe pulses. Using an RRKM simulation, it is then possible to obtain the dissociation rate. During this study, as explained in the introduction to this chapter, they noticed that the deuteriums located in the aromatic cycle were found in methyl dissociation products.

They were able to estimate the isomerization rate from toluene to CHT via a simulation. The potential energy surface was calculated by B3LYP/aug-cc-pVTZ and CCSD/6-

311+G*. The geometry optimization was performed by B3LYP/6-31+G*. The isomerisation threshold from toluene to CHT they obtained is around 29700 cm^{-1} (Lin et al., 2002; Ni* and Lee, 2004). Then, they estimated the isomerization rate at 193 nm to be $(3.4 \pm 0.3) \cdot 10^5$. Assuming this isomerisation barrier, we obtain from figure 5.21 that the isomerisation rate at 193 nm should be $(7.7 \pm 3.8) \cdot 10^6$ s^{-1}. This value is one order of magnitude higher than that estimated by the Chi-Kung Ni's group.
However, in the three articles of this group (Lin et al., 2002; Ni* and Lee, 2004; Tseng et al., 2006), the latest ((Tseng et al., 2006), published in 2006) does not refer to any determination of the isomerization rate, unlike the two others published in 2002 and 2004. They maybe noticed a mistake in their simulation (I did not asked them). According to our work, an isomerization rate of $3.4 \cdot 10^5$ at 51 800 cm^{-1} implies an isomerization threshold around 10 000 cm^{-1} (See figures 5.21 and 5.22). We have no explanation for this discrepancy.

The phenylacetylene-d$_1$ case

As in the previous study, we investigated the radiative emission from deuterated phenylacetylene (or phenylacetylene-d$_1$) excited at 193 nm. The deuterium is located in the acetylenic group and we wonder if the deuterium can also migrate around the phenyl group during the relaxation. The migration mechanism is not necessarily the same than toluene → cycloheptatriene isomerization.
In this section, we show preliminary results on phenylacetylene emission after 193 nm excitation.

Intensity study and absorption spectrum

As for toluene, we tried to detect the phenylacetylene emission signal after excitation at 266, 213 and 193 nm. Contrary to toluene, phenylacetylene does absorb at these wavelengths but the IR emission signal reveals a more than one-photon process for 266 and 213 nm as shown in figure 5.28. Thus, we focused on the emission induced by 193 nm excitation.

The absorption spectrum measured by FIREFLY is shown at the bottom right panel of figure 5.28. In addition to the FIREFLY absorption spectrum, the gas phase absorption spectrum from the NIST and that of obtained by DFT computation are displayed. Acetylenic C–H stretching (around 3.0 µm) and aromatic C–H stretching vibrational modes (around 3.28 µm) are the relevant modes of phenylacetylene between 2.5 and 4.0 µm wavelength range. There are two problems: i) even if the absorption band positions are reproducible, the relative intensities are different with those of obtained by DFT

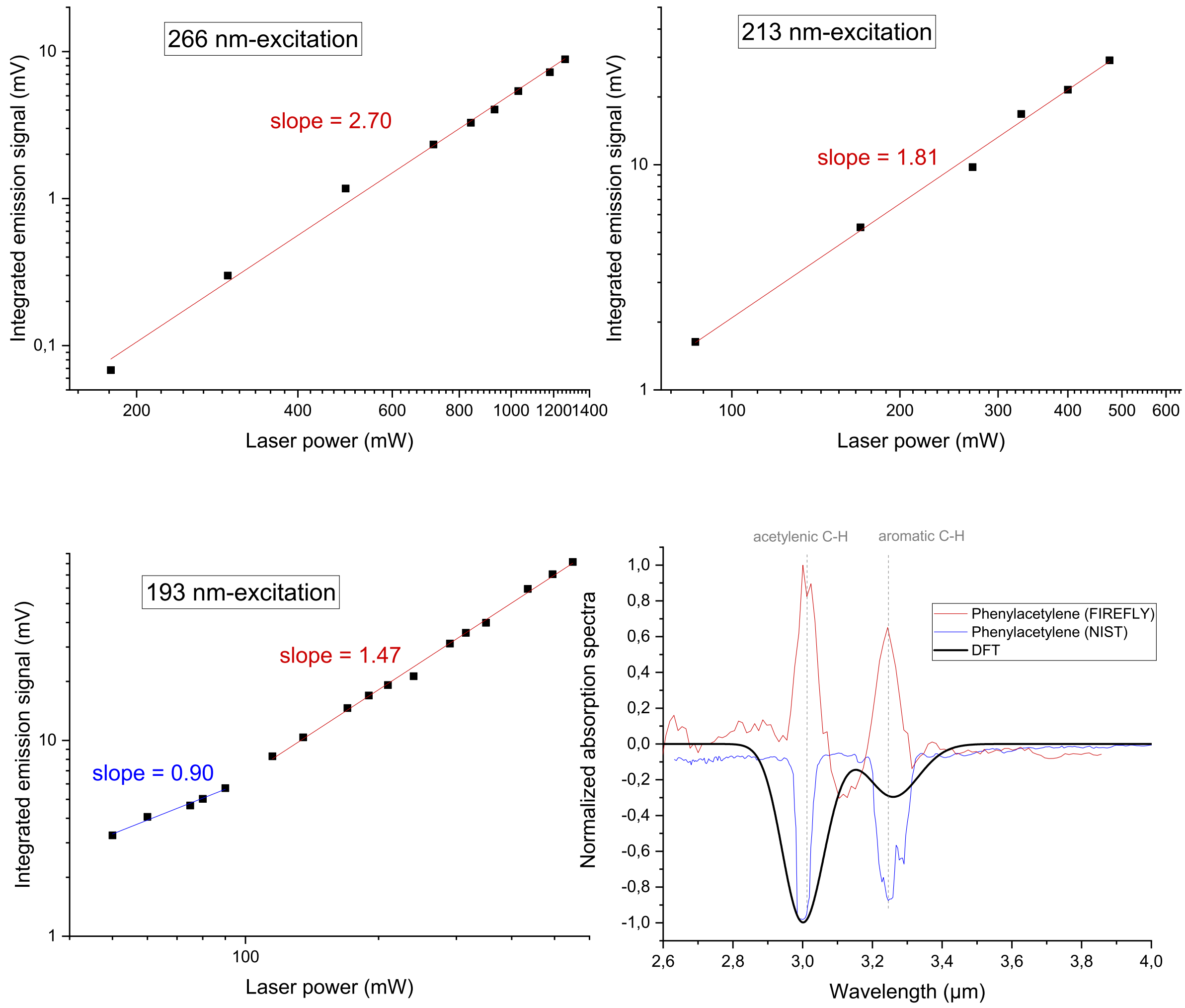

Figure 5.28: Integrated emission signal over the whole relaxation for several laser powers and wavelengths. For 266 and 213 nm excitation, more than one-photon absorption process occurs. For 193 nm, one-photon absorption process occurs up to 100 mW. At the bottom right panel, emission spectra from FIREFLY, NIST and DFT calculation (CAM-B3LYP/6-311++G(d,p)) are displayed. The histogram absorption spectra have been convolved by gaussian function with FWHM = 70 cm^{-1}.

and the quality of the recorded absorption spectra is not reliable because there was a bit of toluene in the cell. We have been able to suppress the toluene contribution but this treatment makes the obtained phenylacetylene absorption spectra not reliable; ii) the acetylenic C–H stretching mode of the NIST absorption spectrum seems to be saturated (see the 3.0 µm acetylenic C–H stretching mode). We did not find other phenylacetylene gas phase absorption spectrum in the literature. Thus, we decided to only take into account the theoretical absorption spectra.

Phenylacetylene relaxation induced by 193 nm excitation

As we proceeded for toluene, we first start with the investigation of $C_6H_5{-}CCH$ phenylacetylene (no deuterium).

The undispersed emission signal is shown in figure 5.29 for three laser powers. For 80 mW laser power irradiation, the relaxation is finished after ≈ 20 µs and negative values do not appears in log scale. For 350 mW laser power, the emission lasts beyond 100 µs and presents at least three relaxation regimes (figure 5.29 in log scale): the first until 20 µs, the second until 150 µs and the third decay regime lasts for several hundreds of µs. For 190 mW laser power, the relaxation does not last as long as for 350 mW but longer than 80 mW. The increasing emission signal beyond 200 µs is likely due to very low frequency noise (section 5). The analysis of the time-dependent emission spectra could give us more information.

Figure 5.30 shows four acquisitions (n° 09, 10, 11 and 12) recorded in the one-photon absorption power range (< 100 mW). The redshift (anharmonic effect) on band positions at high internal energies, as noticed for toluene, is seen for both acetylenic and aromatic C–H stretching modes in phenylacetylene. The broadening of emission bands with the internal energy is also seen, especially with the acetylenic C–H band. However, the aromatic C–H band decreases over time and a possible explanation is given by the statistical distribution of internal energy among vibrational modes. Indeed, the vibrational frequency of both bands is almost the same (the difference is less than 7 %) then the frequency mode dependence of the statistical part of the occupation probability of vibrational modes (equation 2.16 in chapter 2) should not explain this evolution. In fact, there are 5 aromatic C–H bonds and only one C–H acetylenic bond, thus the internal energy dependence of occupation probability of the aromatic C–H band will be 5 times higher compared to the acetylenic C–H band. Hence, the more pronounced emission decrease of C–H aromatic stretching modes.

For the four acquisitions, figure 5.31 shows emission spectra at the end of the relaxation. All of them are similar and the normalized emission spectra seem to be in accordance with the theoretical absorption spectra of phenylacetylene. Figure 5.32 shows two

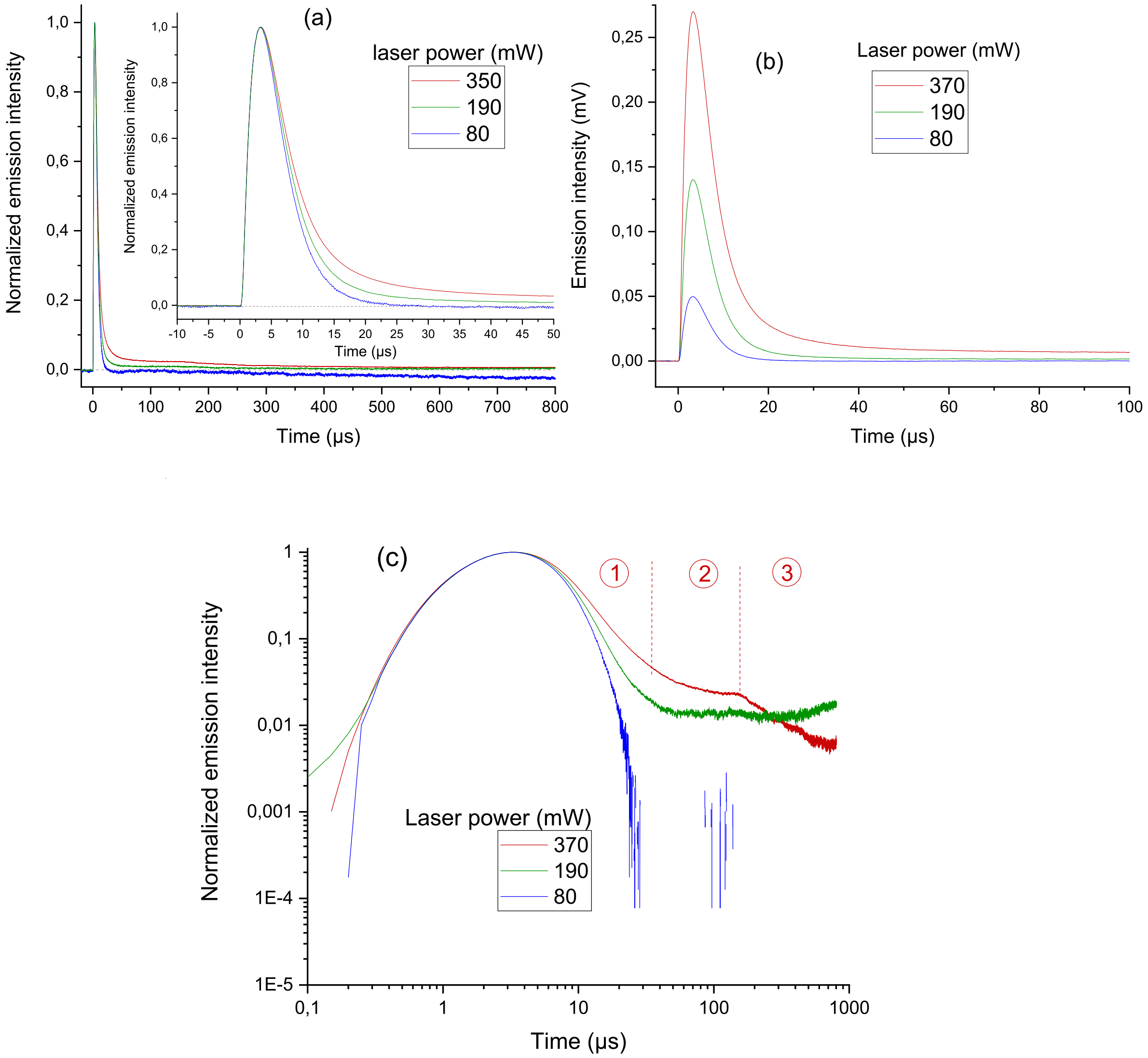

Figure 5.29: (a): normalized undispersed temporal traces (undispersed IR photons between 2.5 and 4.5 µm) of the relaxing phenylacetylene excited at 193 nm for three laser powers. The inset focuses at the beginning of the relaxation. The dotted horizontal grey line indicates the zero value. There is still emission signal after 100 µs for 350 mW laser power. Panel (b): the unnormalized undispersed temporal traces. Panel (c): panel (a) in log scale.

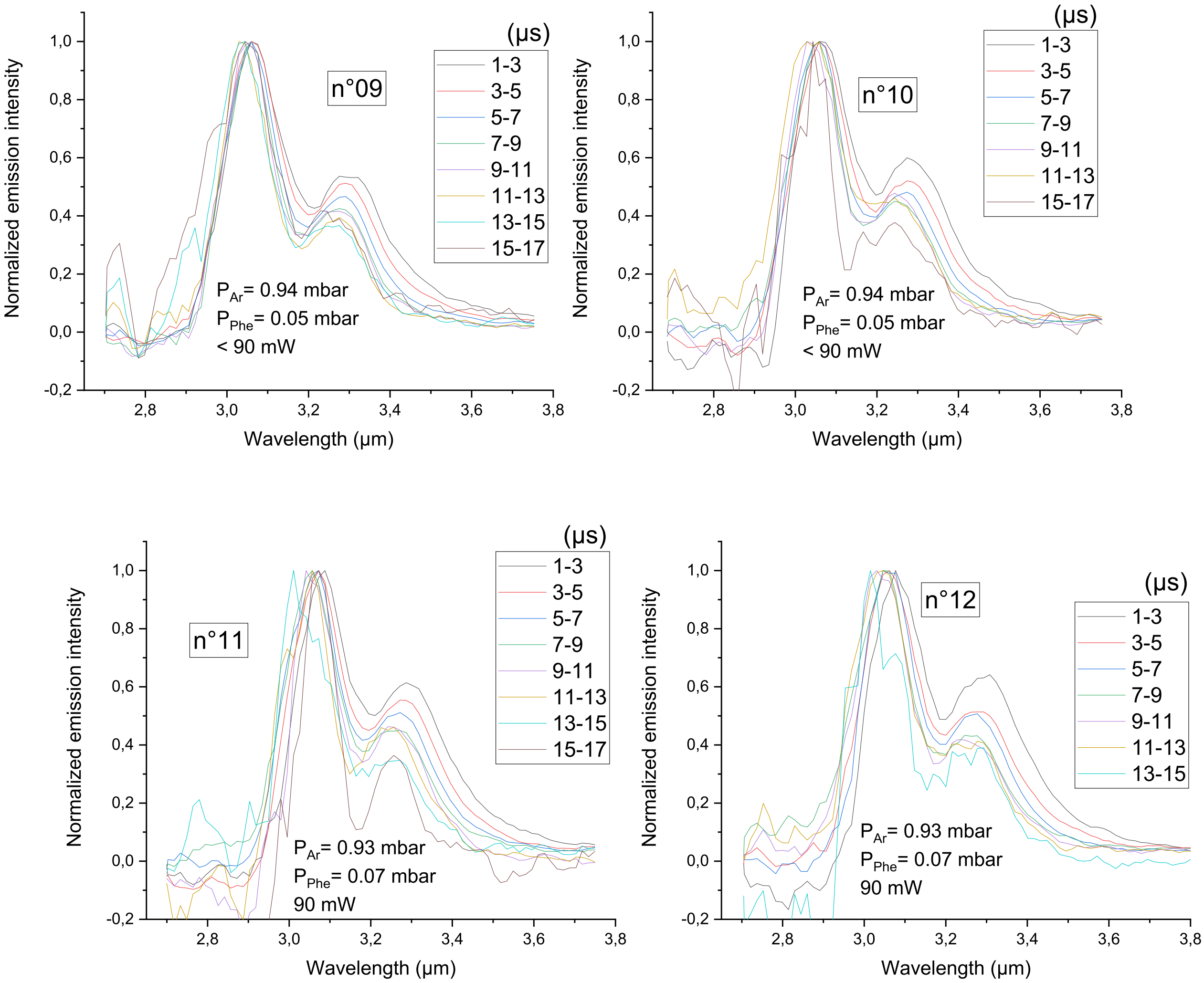

Figure 5.30: Phenylacetylene emission spectra excited at 193 nm for laser power below 100 mW (one-photon absorption process). Pressure conditions and acquisition number are indicated. Temporal gates are 2 µs wide.

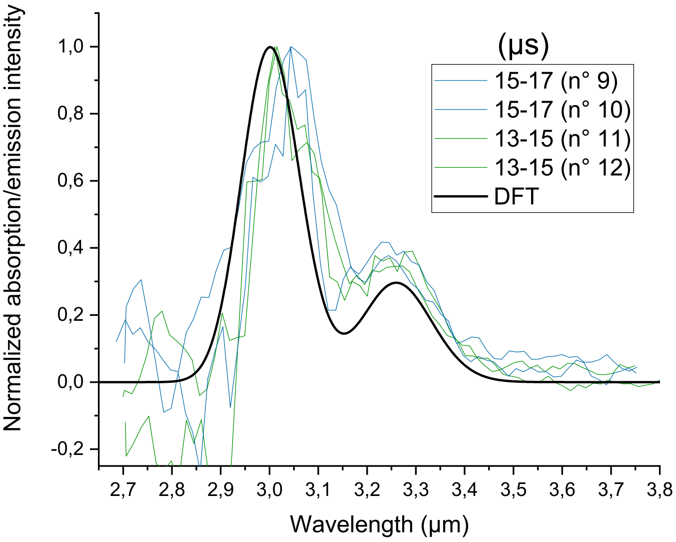

Figure 5.31: Emission spectra of the four acquisitions in figure 5.30 and all have the same emission profile. The theoretical absorption spectra (CAM-B3LYP/6-311++G(d,p), 0.955 scaling factor) is superimposed.

acquisitions (n° 02 and 07) for phenylacetylene irradiated at 370 mW corresponding to more than one-photon absorption. As noticed in figure 5.29, there is still emission beyond 100 µs. The first regime corresponds to emission with changing emission spectrum profile because, as stressed above, it lasts until 20 µs after which the emission spectrum profile does not change anymore. The interesting point is that the emission profile seems to be same than the emission profile displayed in figure 5.31 and thus the carrier of the emission spectra in both cases (80 and 370 mW laser power) are likely the same (e.g phenylacetylene). This lead us to the surprising conclusion that phenylacetylene can survive to more than one-photon absorption. We highlighted three decay regimes (figure 5.29). For the first regime, emission spectra profiles have the same time-evolution than emission spectrum recorded at 80 mW laser power (two upper panels of figure 5.32). The second regime is characterized by a static emission spectra profile (two middle panels of figure 5.32). In the third regime, we cannot conclude if the emission spectra are static or if the relative emission intensity of aromatic C–H band grows over time (two lower panels of figure 5.32). However, this third regime seems to dispute the hypothesis that phenylacetylene is the carrier of observed emission spectra in the second regime. Actually, we tried to record the emission spectra at 720 mW but the total pressure increased rapidly during the acquisition (from 1.09 mbar to 1.24 mbar within 1 minute laser exposure). We believe that this phenomenon occurred, to a less extent, at 370 mW. Thus, it is possible that two mechanisms occur simultaneously: the phenylacetylene emission and phenylacetylene dissociation with radiative emission of products (such as C_2H_2). Phenylacetylene-d_1 could make easier this analysis.

Phenylacetylene-d_1 relaxation induced by 193 nm excitation

As usual, we recorded several absorption spectra of the introduced species in the reservoir to ensure that the phenylacetylene-d_1 has not been damaged. Figure 5.33 shows three acquisition with drift signal at lower wavelength (blue, green and red spectra). The black spectrum is the theoretical phenylacetylene-d_1 obtained via DFT calculation and the Gaussian convolution has been done with a full width at half maximum of 50 cm^{-1}. This fwhm value is lower than previous 70 cm^{-1} because fwhm changes along the circular variable filter (see table 4.2 in chapter 4). All measured phenyacetylene-d_1 absorption spectra (also those no displayed in figure 5.33) have an artifact drift signal that we cannot correct. This comes from our method to obtain absorption spectra with FIREFLY, namely the fact to divide the raw phenyacetylene-d_1 absorption spectra by the reference absorption spectra (chapter 4 section 4). However, as indicated in figure 5.33, it is possible to estimate the relative aromatic C–H stretching mode absorption band (around 3.25 µm) by defining, in a crude way, the bottom of absorption bands (solid straight lines). Then, the bands height are estimated (dotted lines) and turn out to be similar to that of the black curve. Moreover, although there is only one acetylenic C–D bond and five aromatic C–H bonds, the acetylenic C–D absorption band is stronger because the vibrational oscillator strength is stronger.

The relaxation cascade of phenylacetylene-d_1 has been recorded at 90, 200 and 370 mW laser powers. Figure 5.34 shows two acquisitions (n° 18 and 19) for irradiation at 90 mW. No acetylenic C–H bond emits during the whole relaxation and we deduce that the acetylenic deuterium has not been exchanging its position with a hydrogen atom. The relative emission intensity of acetylenic C–D stretching mode (around 3.9 µm) increases over time and is lower than aromatic C–H stretching mode emission. Indeed, although the vibrational oscillator strength of the acetylenic C–D mode is ≈ 2.5 times higher than that of aromatic C–H (figure 5.33), the spontaneous emission increases as the cub of the vibrational frequency. The aromatic C-H stretching frequency mode is 1.2 (around 3.25 µm) higher than that of the acetylenic C–D stretching mode and the cubic is then 1.7 times higher compared to the acetylenic C–D. It results that the acetylenic C–D spontaneous emission is 1.5 times higher. Then, the explanation to the higher aromatic C-H emission is to find in the energy distribution among vibrational modes. Indeed, aromatic C–H band contains 5 vibrational modes (with different vibrational oscillator strength) and the acetylenic C–D contains one. Thus, at fixed internal energy, there are more aromatic C–H vibrational states and the occupation probability is higher. Also, given

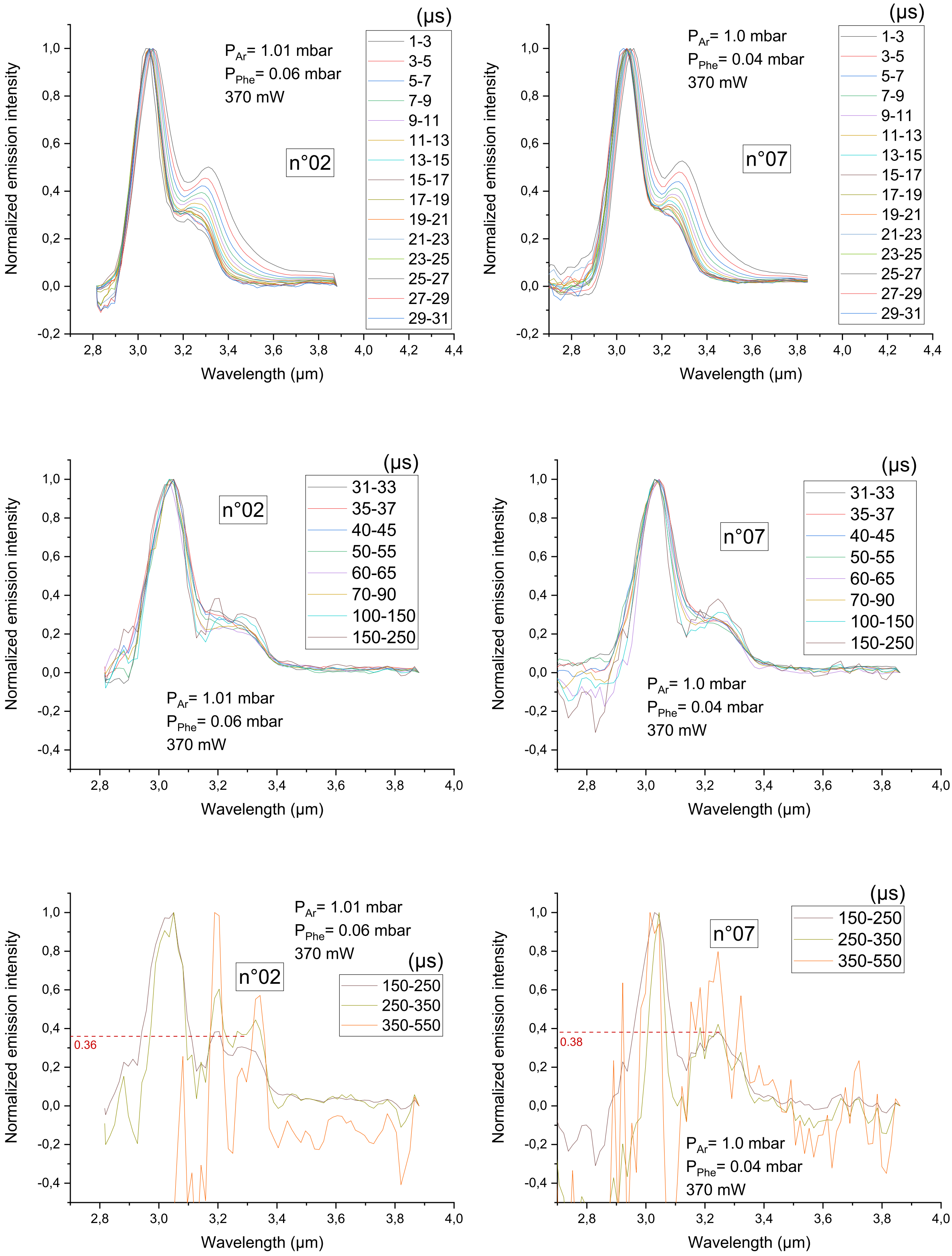

Figure 5.32: Phenylacetylene emission spectra excited at 193 nm for 370 mW laser power (more than one-photon absorption process). Pressure conditions and acquisition numbers are indicated. Temporal gates are 2 µs wide but are wider at long times to have a better signal-to-noise ratio.

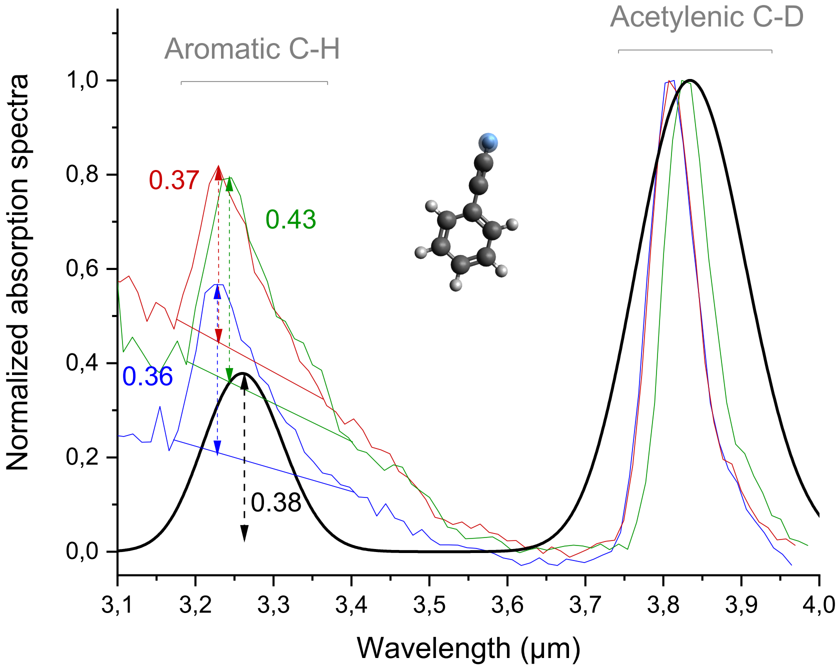

Figure 5.33: Three absorption spectra of phenyacetylene-d1 recorded with FIREFLY (blue, green and red). For all spectra, there is systematically an artifact drifting signal growing toward short wavelength and stems from our method to obtain absorption spectra that can generate artifact signal (chapter 4 section 4). The theoretical spectra is shown in black (CAM-B3LYP/6-311++G(d,p)) with a Gaussian convolution (FWMH= 50 cm^{-1}) and 0.955 scaling factor.

that the vibrational density of states increases faster with the internal energy, occupation probability of aromatic C–H will be higher at the beginning of the relaxation.
However, it seems from figure 5.35 that the phenylacetylene-d$_1$ relaxation lasts longer than the phenylacetylene relaxation. The phenylacetylene-d$_1$ emission spectra integrated between 13 and 19 µs do not match its own absorption spectra whereas this is the case for phenylacetylene at this time (figure 5.31). Figure 5.36 shows that the phenylacetylene-d$_1$ is slower but not enough to explain the observation that emission spectra does not match the absorption spectrum between 13 and 19 µs. Emission spectra beyond 20 µs are too weak to infer reliable information (right panel of figure 5.35). The slower relaxation of phenylacetylene-d$_1$ cannot be explained in a qualitative way because even if acetylenic C–H has a higher frequency mode (thus higher spontaneous emission), its occupation probability should be lower than acetylenic C–D because, at fixed internal energu, the higher the frequency mode, the lower the vibrational density of states. A kMC simulation could be useful to explain the relaxation speed between these two species.
It is puzzling to detect, at 90 mW laser power, that phenylacetylene emission spectra matches its own absorption spectra but not phenylacetylene-d$_1$. It could be interesting to compute the radiative relaxation of these species to see if the phenylacetylene-d$_1$ anharmonicity is more important at lower internal energy than for phenylacetylene (this calculation does not requires collisional parametrization). If so, maybe phenylacetylene-d$_1$ emission spectra is too faint to see its matching with its own absorption spectra (right panel of figure 5.35).
In any event, we undoubtedly observe that acetylenic C–H bond does not appear at 193 nm excitation of phenylacetylene-d$_1$. In conjunction with phenylacetylene observation at long times (figure 5.31), it is likely that only usual relaxation pathways (vibrational emission, collisional relaxation) or also dissociation (H loss) take place. No major isomerization is detected. But to be sure of this conclusion, we have to clarify the phenylaetylene emission spectrum profile at long times.

Emission spectra obtained at 370 and 200 mW irradiation are displayed in figure 5.37 for acquisition n°21 and 22. For these laser powers, the acetylenic C–H appears and its relative intensity increases over time. The relative intensity of aromatic C–H band decreases constantly. That of acetylenic C–D increases and starts to decrease between 15 and 20 µs. If a species similar to phenylacetylene with the deuterium located in the phenyl was the carrier of these emission spectra, then the aromatic C–H should also appear in emission spectra at the end of the relaxation. Indeed, a weak aromatic C–H emission band around 3.2 µm is noticed and its vibrational intensity compared to acetylenic C–D band is similar to that of phenylacetylene-d$_1$ (figure 5.33).
We noticed for acquisition n°21 (390 mW laser power) that the total pressure in the

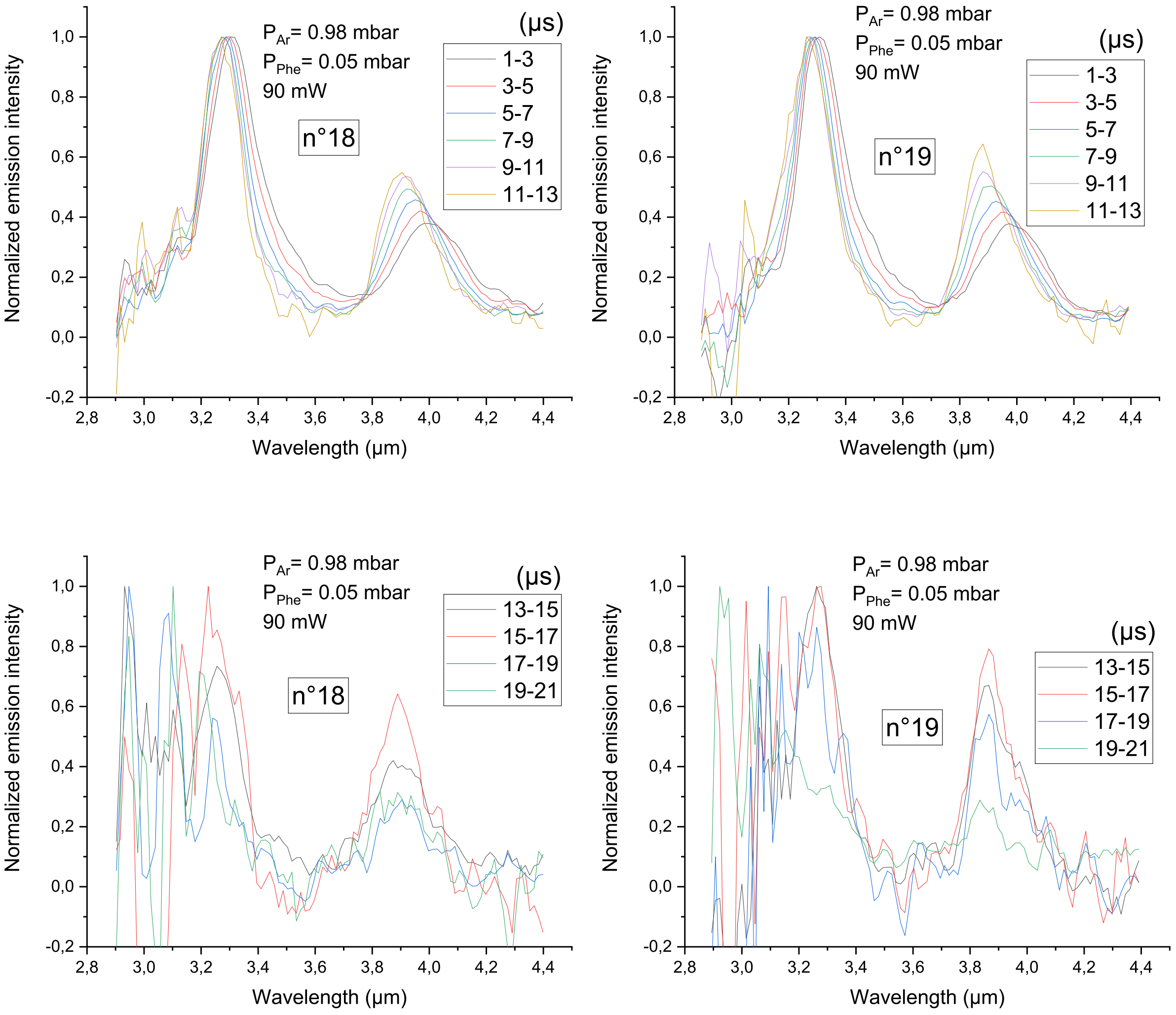

Figure 5.34: Phenylacetylene-d_1 emission spectra excited at 193 nm at 90 mW laser power.

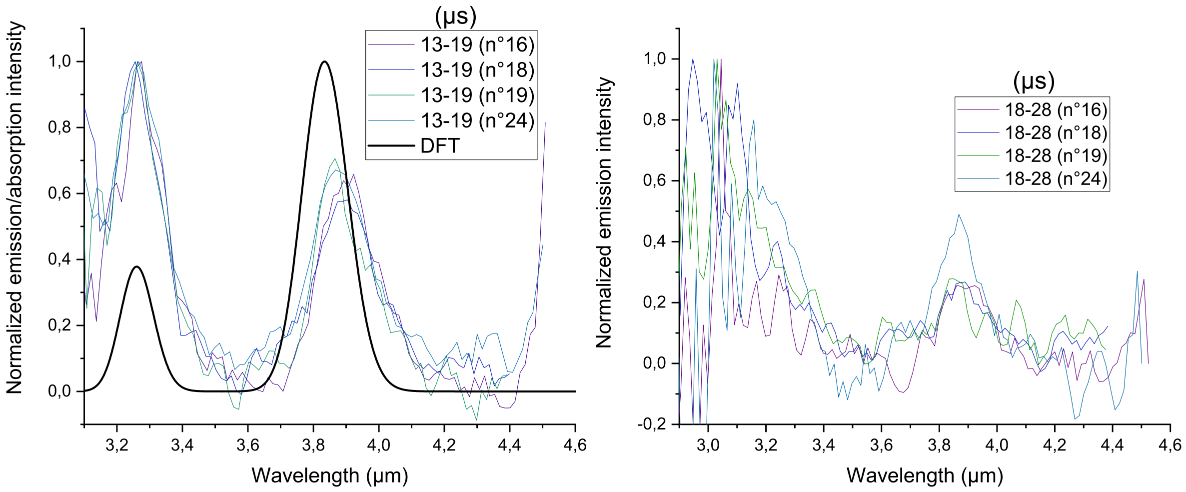

Figure 5.35: Left panel: emission spectra integrated within 13-19 µs temporal gates, at the end of the relaxation. In black line, the theoretical absorption spectra of phenylacetylene-d$_1$. Right panel: emission spectra integrated within 18-28 µs temporal gates.

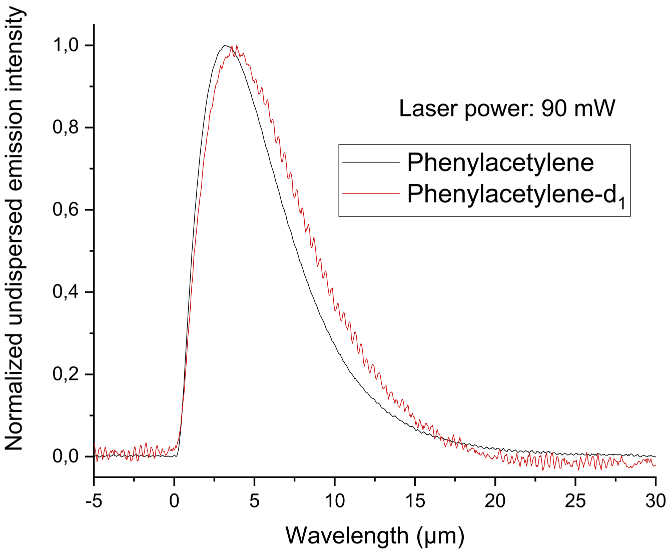

Figure 5.36: Normalized total emission (between 2.5 and 4.5 µm) of phenylacetylene and phenylacetyelene-d$_1$ after 193 nm excitation at 90 mW laser power. The phenylacetylene-d$_1$ is slightly lower. The weaker signal-to-noise ratio of phenylacetyelene-d$_1$ signal is due to the fact that the aperture was smaller than for phenylacetylene.

gas cell was increasing at a moderate speed and this is why pressure conditions are not indicated for this acquisition. The total pressure at the beginning of the acquisition was 1.15 mbar and 1.23 mbar at the end (the acquisition lasted around 30 minutes). This total pressure increase is due to laser excitation process because it occurs as soon as laser pass through the Ar-phenylacetylene mixture in the gas and for high laser power (acquisition n°21, 390 mW). The increase of the total pressure in the cell stops when the laser is off. Then, we suspect that pyrolysis occurs at 390 mW laser power. Emission spectra from acquisition n°22 (200 mW laser power) displays same profiles than those of acquisition n°21 although we did not notice pressure increase. However, this does not mean there is no pyrolysis also at 200 mW. At 200 mW laser power, pyrolysis rate could be lower than at 390 mW but still create emitting fragments. As mentioned above, total pressure increase occured for phenylacetylene at 720 mW laser power but much less at 370 mW compared to phenylacetylene-d_1 at 370 mW.

Actually, the emission profile at 200 mW and 370 mW are different at times below 10 µs. Indeed, the relative intensity of acetylenic C–H increases faster at 390 mW irradiation. To have a better understanding, we computed the emission bands intensity in terms of the laser power. Figure 5.38 shows that the acetylenic C–H emission a two-photon absorption process.
If the emission spectra of figure 5.32 is only due to fragments, then all emission bands had to be two-photon process. If there is only an isomerization process at the origin of the acetylenic C–H apparition, then all emission bands had to be two-photon process also. It is possible that at these laser power irradiation, two mechanism occurs simultaneously. The acetylenic C–H emission band could stem from C_2H_2 and 3-hexene-1,5-yne (HC–C=C–CH) radical dissociation product (Sorkhabi et al., 2001) and one-photon absorption of phenylacetylene may be at the origin aromatic C–H and acetylenic C–D emission bands.

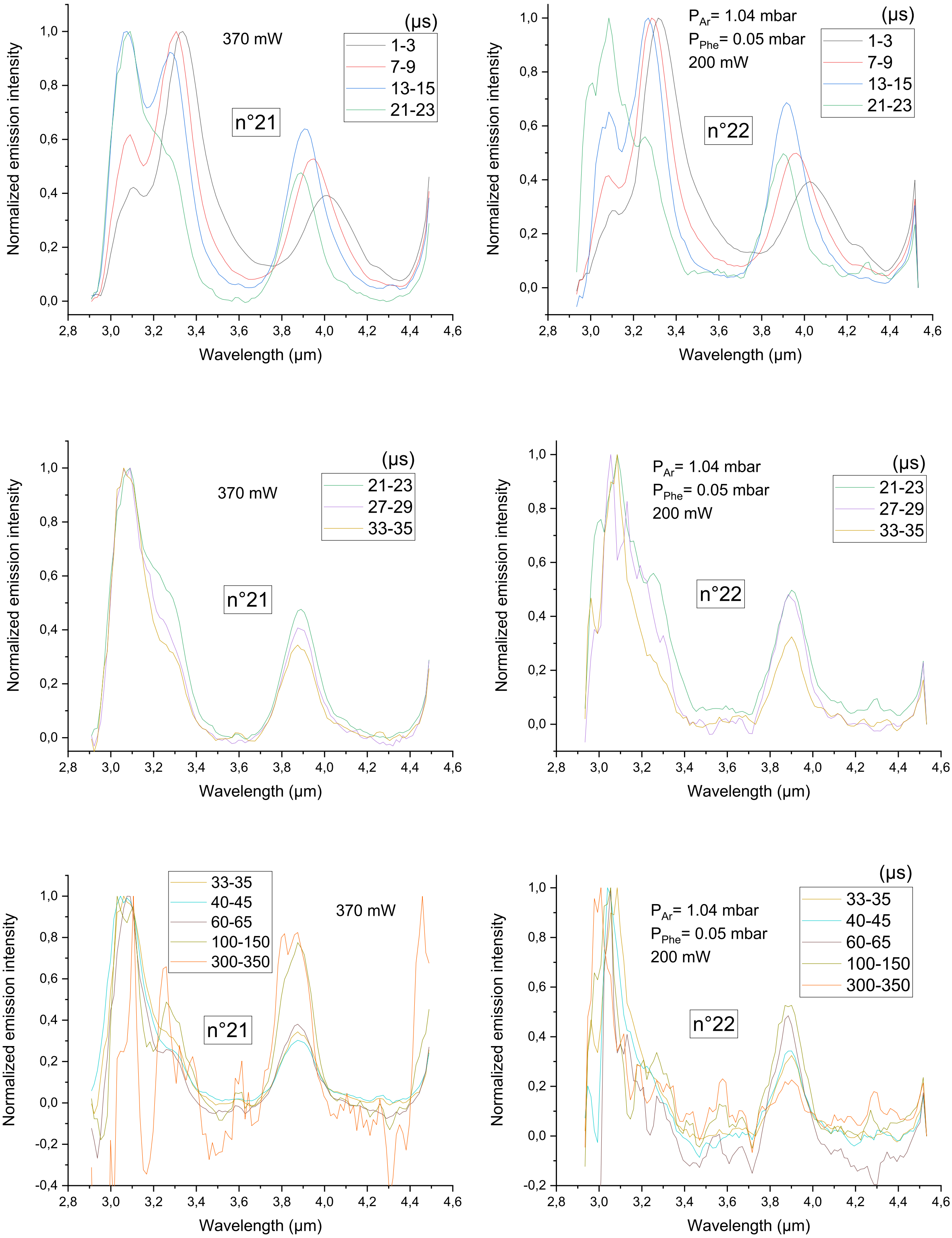

Figure 5.37: Phenylacetylene-d$_1$ emission spectra excited at 193 nm for 370 and 200 mW laser power. Pressure conditions are indicated only for the acquisition n°22 because during the acquisition n°21 total pressure was cosntantly increasing (see the text). Temporal gates are 2 µs but are wider at long delay time to have a better signal-to-noise ratio.

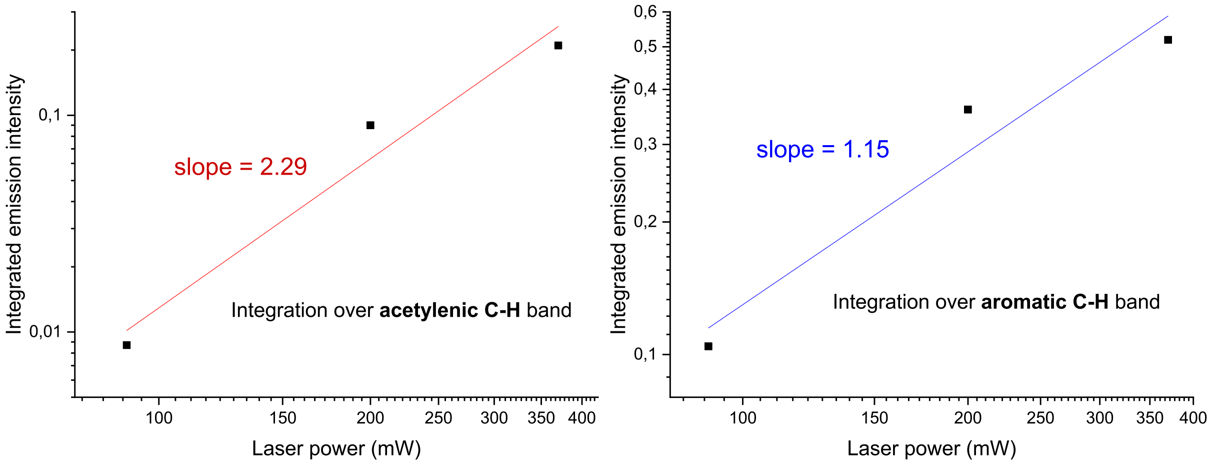

Figure 5.38: Intensity emission study for each emission bands. Left panel: two-photon absorption process for the acetylenic C–H band. Right panel: one-photon process for the aromatic C–H band. The same slope is obtained for the acetylenic C–D band.

Conclusion

Our investigation on the toluene → cycloheptatriene isomerization did not allow us to deduce the isomerization threshold and A-prefactor. We dealt with several problems.

• Firstly, the aromatic C–H stretching modes emission that appears before 1 or 2 µs is redshifted (anharmonicity). Then, it takes place in the same wavelength range of aliphatic C–H streching modes emission. We therefore do not have access to the aromatic C–H emission in the isomerization regime. Aliphatic C–D stretching modes wavelength is out of range of our circular variable filter.

• Secondly, the sum of aromatic C–H and aliphatic C–H emission (which is our observable) is dominated by aliphatic C–H emission. This is partly due to the fact that aliphatic C–H has more than 50% more vibrational activity than aromatic C–H. The presence of significant amount (between 20% and 50%) of toluene-d_5^{Ar} after the isomerization regime intensify the prevalence of aliphatic C–H emission in our observable.

• Thirdly, the simulation revealed that the isomerization regime ends before 1 µs for all realistic (A, E_{iso}) pairs considered. The rising edge of the preamplifier is not fast enough to probe the isomerisation kinetics.

• Fourthly, the simulation revealed that the difference in aromatic C–H + aliphatic C–H emissions from one (A, E_{iso}) pair to another is small. Assuming we have a fast preamplifier, electronic noise would prevent us from concluding. In this case, we could, at best, constrain possibilities on (A, E_{iso}) but we doubt about that.

An additional investigation to go further would be to electronically excite toluene -

d_5^{Ar} at several wavelengths. In this case, we would have constraints similar (but difference values) to the one shown in figure 5.21 which would be added to constraints obtained with excitation at 193 nm. Without considering isomerization kinetics issues as mentioned above, we would then achieve a great step forward on the determination of (A, E_{iso}). However, this study assumes that several problems have been overcome. Indeed, if we take an excitation wavelength greater than 193 nm, the system will then have a lower initial internal energy than in the current study described in this chapter. It is necessary to ensure that there is sufficient emission signal and that the isomerization rate at the initial energy is large enough to compete with collisions. If we take a shorter wavelength, we must ensure that the dissociation does not limit the number of emitting species (if no, it would result in a drastic decrease in the emission signal even if the initial energy is higher than 52 000 cm^{-1}). It is also necessary to ensure that the isomerization rate is not very important compared to the collision rate because in this case we would only have 100% of toluene-d_5^{Ar} which would prevent us from drawing a curve similar to that of figure 5.21. Also, 100% of isomerized toluene-d_5^{Ar} would leave us only with the kinetics of isomerization as the only way to derive any information. Moreover, in the high internal energy case, the kinetics would be very fast.
We attempted to measure vibrational emission at 266 nm and 213 nm. Neither of these wavelengths was absorbed by toluene.

Another idea is to vary the pressure for the same excitation energy. In this case, it would only be a matter of changing the argon partial pressure because any change in the toluene partial pressure reduces the emission signal. For this new argon partial pressure, it would be possible to draw a curve similar to the one in Figure 5.21. If this study is well conducted, we can do this for several pressures and therefore further constrain (A, E_{iso}) pairs. It must be ensured that for new argon partial pressure values, the emission signal does not vary much and, simultaneously, the non-isomerized toluene-d_5^{Ar} proportion has varied appreciably.
We did not have the presence of mind to make these manipulations at the time. The two partial pressures were fixed so as to maximize the toluene-d_5 emission signal. We did not anticipate that pressure variation could be useful.

It may also be interesting to take the experimental methodology described in this chapter and apply it to the toluene-d_3^{Ar} case instead of toluene-d_5^{Ar}. In this case, the three deuteriums would initially be methylic and aromatic C–D and aliphatic C–H bonds would appear after isomerization to CHT. The presence of aromatic C–D would be seen at the end of the relaxation because its red shift is undetectable by FIREFLY. However, aliphatic C–H anharmonicity would be accessible and not contaminated by aromatic C–

H. The emission intensity of aromatic C–H would be similar to aliphatic C–H emission intensity as the latter have at least 50% lower infrared intensities.

We could also collaborate with Daniel Pelaéz-Ruiz from our group, for a more precise calculation of the potential energy surface (via Multi-configuration time-dependent Hartree, MCTDH) than that of the Chi-Kung Ni's group. It is possible that they misjudged the transition state of the isomerization.

The preliminary work on phenylacetylene-d_1 vibrational emission excited at 193 nm indicates that there is no deuterium migration from the ethynyl to the phenyl group. However, at more than one-photon absorption, acetylenic C–H emission bands is detected and could assigned to main dissociation products which are acetylene and 3-hexene-1,5-yne. Thus, even if there were deuterium/hydrogen permutation as a secondary pathway, we could not detect it because dissociation products emit around 3.0-3.1 µm wavelength range.

6. Conclusion and perspectives

We aimed to extend the PAH hypothesis photophysics mechanism to C_n (n=24, 42, 60) carbon clusters and benzene derivatives in the gas phase. Miscellaneous detections of buckminsterfullerene in the ISM and carbon clusters in flames support the investigation of carbon clusters emission spectra in ISM and combustion context. The home-made FIREFLY IR spectrometer, originally developed for Aromatic Infrared Bands investigations, has been used in this thesis work to explore if IR emission spectral analysis could be valuable for isomerization reaction studies.

The theoretical study on radiative relaxation of carbon clusters has been motivated by their low-lying electronic states and thus, possible high recurrent fluorescence rate in competition with vibrational fluorescence. Thousands of carbon clusters for each size were generated by our colleagues Bonnin et al. (2019) and their electronic and vibrational structures were explored Dubosq et al. (2019, 2020). The recurrent and vibrational fluorescence competition has been investigated in terms of size, internal energy and family (cage, flake, pretzel, branched) for archetype isomers 3. Emission spectra from overall radiative relaxation at a given initial internal energy revealed the exponential decay of the recurrent fluorescence part of the emission spectra. This exponential decay is explained by the exponential decay dependence of recurrent fluorescence rate with the electronic energy (similarity with Energy Gap Law, section 3). This study led us to investigate the correlation between recurrent or vibrational fluorescence and carbon clusters structural parameters (compacity, sp^2 carbon percentage, gyration radius, etc) Bonnin et al. (2019) but we couldn't rigorously prove any correlation although this kind of correlation is highly suspected (especially between recurrent or vibrational fluorescence and compacity and/or sp^2 percentage). Further work could be to search for a structural parameter witnessing the presence of aromatic cells and their size in our carbon cluster isomers. This should allow us to see if carbon clusters containing large aromatic cells (i.e polycyclic aromatic regions) display or not any spectroscopic signature in their emission spectra.

Emission spectra simulation of large sets of carbon clusters for each family irradiated by spectral energy distributions simulating those of 20 000 K star-like blackbody spectrum or the standard interstellar radiation field is useful in an interstellar context 3. For all family and sizes, recurrent fluorescence emits mainly in the near-IR wavelength range (below 5 µm) much more than vibrational emission. Even if it is difficult to exploit the vibrational emission in far and mid-IR emission for astrophysical issues, the recurrent fluorescence influence on vibrational emission bands have been rationalized. The large set of C_{60} cages near-IR emission turns out to reproduce the exponential profile detected by K.Sellgren in several reflection nebulae Sellgren (1984); Sellgren et al. (1983) (section 3). To test further the hypothesis of C_{60} (or similar carbon cluster size) cages carriers of the near-IR continuum via their recurrent fluorescence, we calculated the spectral flux density that should be emitted from NGC 7023 and detected on Earth. Comparison with K.Sellgren detection indicates that C_{60} cages should contain around 0.1% of the elemental carbon in that region (assuming 10^{-4}:1 carbon to hydrogen ratio in NGC 7023). This value does not rule out the assumption that C_{60} cages could be the carriers of the K.Sellgren's near-IR continuum via recurrent fluorescence. We could do the same study for hydrogenated fullerenes (fulleranes) which are highly suspected to be present in interstellar medium Cataldo and Iglesias-Groth (2010). The first step is to generate $C_{60}^{+}H_{n}$ carbon cluster isomers by our colleagues (in progress). We could generalize our simulation to rotational radiative de-excitation Mulas (1998) and consider $C_{60}^{+}H_{n}$ isomers rotational emission besides vibrational emission and recurrent fluorescence. We could compare the simulation result to the astrophysically observed anomalous microwave emission Draine and Lazarian (1998); Zhang et al. (2020); Iglesias-Groth (2006). We could go further by investigating recurrent fluorescence and vibrational emission in large PAHs. To do so, it could be useful to first use large PAHs in theoretical spectral database of PAHs Malloci et al. (2007) containing 20 large PAHs (from coronene $C_{24}H_{12}$ to circumovalene $C_{66}H_{20}$) and evaluate the 3.3 µm C-H stretching mode intensity to near-IR continuum ratio. This evaluation would be approximate because we cannot obtain a near-IR continuum from 20 PAHs Malloci et al. (2007). We could also consider Draine & Li's dust model Li and Draine (2001); Draine and Li (2001) to simulate the radiative relaxation of dust containing large amount of carbon atoms (> 100). However, in this model, the electronic cross section is given without the electronic density of states. So, for this study, some assumptions are required for the electronic density of states of dust. These assumptions will give us the electronic energies and their electronic oscillator strength, necessary for the kMC computation. For the extended red emission, it could be possible to assume the electronic density of states and simulate the recurrent fluorescence emission spectra that should result. Then, we can search for the electronic density of states and size distribution that matches the extended red emission profile via

recurrent fluorescence through molecular carriers hypothesis.
In this thesis work, we also considered large carbon clusters at fixed high temperature (2000 K−3000 K) which is interesting for laser-induced fluorescence experiments. Here, we assume the electronic density of states over a large set of carbon clusters rather than their vibrational structure. This simulation allowed us to calculate the mean total emissivity of carbon clusters for each C_{42} and C_{60} family and found a value around 10^{-4}. Their emissivity increases quadratically with photon frequency. This fixed temperature study could be used for a crude determination of the previously mentioned electronic density of states over a large set of carbon clusters for Draine & Li's dust model by assuming the emissivity index. Indeed, from astrophysical observations, the emissivity index β varies usually between 1 and 2.5 Galliano et al. (2018).

The setup of the new preamplifier (bandwidth: 1.5Hz - 1 MHz) allowed us to reduce the electrical noise thanks to a better connection to the electrical ground compared to the previous preamplifier (bandwidth: 1.5Hz - 1 MHz). The experimental study of isomerization reaction by UV-laser induced infrared emission has been carried out for toluene → cycloheptatriene isomerization by spanning the [2.5 µm; 4.5 µm] wavelength range. This isomerization has been described by RRK and we aimed to determine the A-prefactor and the isomerization threshold. Thanks to vibrational radiative emission at the end of the relaxation (> 10-15 µs), we have been able to relate these two quantities. However, it turned out that the A-prefactor and the isomerization threshold are not measurable because the isomerization regime is too fast for recording. Assuming the 29 700 cm^{-1} isomerization threshold (calculated via ab-initio method in Lin et al. (2002)), we estimated the isomerization rate at 193 nm to be $(7.7 \pm 3.8) \cdot 10^6$ s^{-1} whereas Lin et al. (2002) estimation is $(3.4 \pm 0.3) \cdot 10^5$ s^{-1}. We did not find any explanation to this inconsistency so far.
We concluded that phenylacetylene does not undergo isomerization associated to its phenyl ring at 193 nm excitation. Indeed, the deuterium initially located at the ethynyl group did not permute with an aromatic hydrogen because no acetylenic C-H stretching mode were observed. However, at more than one-photon absorption process of phenylacetylene, we observed acetylenic C-H stretching mode through emission of dissociation products containing acetylenic C-H bonds. Modeling could help understanding the main reaction channels that lead to the appearance of the CH acetylenic bond.
With this experimental study, we showed how vibrational fluorescence could be employed for isomerization reactions while the species is relaxing. The species must be complex enough to have efficient internal conversion (> 10 atoms) and small enough so that their vapor pressure is higher than about 0.1 mbar for studies in the cell. As mentioned in the introduction of section 4, vibrational fluorescence induced by UV-excitation ex-

periments have been carried out for collisional energy transfer and for PAH hypothesis investigations. We carried out this kind of experiment to follow isomerization reactions. We focused our efforts on 6-membered to 7-membered ring isomerization for carefully chosen deuterated benzene derivatives with the likely assumption of efficient scrambling in the 7-membered ring isomer (toluene, ethylbenzene, propylbenzene, styrene, cumene, phenylacetylene, cycloheptatriene, aniline and benzonitrile). Yet, we believe that this experimental method can be extended to consider other unimolecular reactions. The interesting point is that, while the unimolecular reaction operates, the internal energy is decreasing (due to collisional or vibrational relaxation) which dramatically drops the unimolecular reaction rate. Those can be dissociation or other types of isomerization but all must be slow enough to be detected or at least to see their effect on the vibrational emission at the end of the cooling. Simulating the relaxation kinetics can be useful to go further in the characterization but reliable collisional parametrization is required to describe the collisional cooling. Unfortunately, these parametrizations are available only for very few benzene derivatives.

The collisional parametrization constraint could be avoided by using a molecular beam. In that case, emitting species are less numerous compared to experiments with the cell but, with a photon collector designed especially for FIREFLY, it is possible to detect as intensity as in cell experiments and there will be no more collisional regime and collisional quenching. Thus, this is interesting for slow unimolecular reactions in competition with vibrational emission (e.g our observable) and for observation of these reactions at very long times (> 5 µs).

Bibliography

Abramowitz, M. and Stegun, I. A. (1964). Handbook of mathematical functions with formulas, graphs, and mathematical tables, volume 55. US Government printing office.

Ahrens, J., Bachmann, M., Baum, T., Griesheimer, J., Kovacs, R., Weilmünster, P., and Homann, K.-H. (1994). Fullerenes and their ions in hydrocarbon flames. International Journal of Mass Spectrometry and Ion Processes, 138:133–148.

Allain, T., Leach, S., and Sedlmayr, E. (1996a). Photodestruction of pahs in the interstellar medium. i. photodissociation rates for the loss of an acetylenic group. Astronomy and Astrophysics, 305:602.

Allain, T., Leach, S., and Sedlmayr, E. (1996b). Photodestruction of pahs in the interstellar medium. ii. influence of the states of ionization and hydrogenation. Astronomy and Astrophysics, 305:616.

Allamandola, L., Tielens, A., and Barker, J. (1985). The Astrophysical Journal, 290:L25–L28.

Allamandola, L., Tielens, A., and Barker, J. (1989). Interstellar polycyclic aromatic hydrocarbons-the infrared emission bands, the excitation/emission mechanism, and the astrophysical implications. The Astrophysical Journal Supplement Series, 71:733–775.

Anacleto, J. F., Perreault, H., Boyd, R. K., Pleasance, S., Quilliam, M. A., Sim, P. G., Howard, J. B., Makarvovsky, Y., and Lafleur, A. L. (1992). C60 and c70 fullerene isomers generated in flames. detection and verification by liquid chromatography/mass spectrometry analyses. Rapid communications in mass spectrometry, 6(3):214–220.

Andersson, B., Lazarian, A., and Vaillancourt, J. E. (2015). Interstellar dust grain alignment. Annual Review of Astronomy and Astrophysics, 53:501–539.

Astholz, D., Troe, J., and Wieters, W. (1979). Unimolecular processes in vibrationally highly excited cycloheptatrienes. i. thermal isomerization in shock waves. The Journal of Chemical Physics, 70(11):5107–5116.

Atkinson, R. and Thrush, B. A. (1970). Photochemical studies of unimolecular processes i. the photoisomerization of cycloheptatriene and cycloheptatriene-d8. Proceedings of the Royal Society of London. A. Mathematical and Physical Sciences, 316(1524):123–130.

Baba, H., Nakajima, A., Aoi, M., and Chihara, K. (1971). Fluorescence from the second excited singlet state and radiationless processes in pyrene vapor. The Journal of Chemical Physics, 55(5):2433–2438.

Barker, J. R. (1983). Monte carlo calculations on unimolecular reactions, energy transfer, and ir-multiphoton decomposition. Chemical Physics, 77(2):301–318.

Barker, J. R. (2009). Energy transfer in master equation simulations: A new approach. International Journal of Chemical Kinetics, 41(12):748–763.

Barker, J. R. and Golden, R. E. (1984). Temperature-dependent energy transfer: direct experiments using azulene. The Journal of Physical Chemistry, 88(5):1012–1017.

Barker, J. R. and Toselli, B. M. (1993). Infrared emission studies of the vibrational deactivation of benzene derivatives. International Reviews in Physical Chemistry, 12(2):305–338.

Barran, P., Firth, S., Stace, A., Kroto, H., Hansen, K., and Campbell, E. (1997). International journal of mass spectrometry and ion processes, 167:127–133.

Basire, M., Parneix, P., Pino, T., Bréchignac, P., and Calvo, F. (2011). in PAHs and the Universe, edited by C. Joblin and A. G. G. M. Tielens, EAS Publication Series, 46:95–101.

Beck, R. (2009). Galactic and extragalactic magnetic fields–a concise review. Astrophysics and Space Sciences Transactions, 5(1):43–47.

Bernard-Salas, J., Cami, J., Peeters, E., Jones, A., Micelotta, E., and Groenewegen, M. (2012). On the excitation and formation of circumstellar fullerenes. The Astrophysical Journal, 757(1):41.

Bernath, P. F., Hinkle, K. H., and Keady, J. J. (1989). Detection of c5 in the circumstellar shell of irc+ 10216. Science, 244(4904):562–564.

Berné, O., Cox, N., Mulas, G., and Joblin, C. (2017). Detection of buckminsterfullerene emission in the diffuse interstellar medium. Astronomy & Astrophysics, 605:L1.

Berné, O., Fuente, A., Goicoechea, J., Pilleri, P., González-García, M., and Joblin, C. (2009a). Mid-infrared polycyclic aromatic hydrocarbon and h2 emission as a probe of physical conditions in extreme photodissociation regions. The Astrophysical Journal Letters, 706(1):L160.

Berné, O., Joblin, C., Fuente, A., and Ménard, F. (2009b). What can we learn about protoplanetary disks from analysis of mid-infrared carbonaceous dust emission? Astronomy & Astrophysics, 495(3):827–835.

Berné, O., Montillaud, J., and Joblin, C. (2015). Top-down formation of fullerenes in the interstellar medium. Astronomy & Astrophysics, 577:A133.

Berne, O., Mulas, G., and Joblin, C. (2013). Interstellar c60+. Astronomy & Astrophysics, 550:L4.

Berné, O. and Tielens, A. G. (2012). Formation of buckminsterfullerene (c60) in interstellar space. Proceedings of the National Academy of Sciences, 109(2):401–406.

Bernstein, L., Shroll, R., Lynch, D., and Clark, F. (2017). A small fullerene (c24) may be the carrier of the 11.2 μm unidentified infrared band. The Astrophysical Journal, 836(2):229.

Beyer, T. and Swinehart, D. (1973). Algorithm 448: number of multiply-restricted partitions. Communications of the ACM, 16(6):379.

Birks, J. B. (1970a). Aromatic Molecules, volume 704. Wiley, New York.

Birks, J. B. (1970b). Photophysics of aromatic molecules. Wiley Monographs in Chemical Physics.

Bixon, M. and Jortner, J. (1968). Intramolecular radiationless transitions. The Journal of chemical physics, 48(2):715–726.

Bondybey, V. (1984). Relaxation and vibrational energy redistribution processes in polyatomic molecules. Annual Review of Physical Chemistry, 35(1):591–612.

Bonnin, M. A., Falvo, C., Calvo, F., Pino, T., and Parneix, P. (2019). Physical Review A, 99(4):042504.

Brenner, D. W., Shenderova, O. A., Harrison, J. A., Stuart, S. J., Ni, B., and Sinnott, S. B. (2002). A second-generation reactive empirical bond order (rebo) potential energy expression for hydrocarbons. J. Phys. Cond. Mat., 14:783.

Brenner, J. and Barker, J. R. (1992). Infrared emission spectra of benzene and naphthalene-implications for the interstellar polycyclic aromatic hydrocarbon hypothesis. The Astrophysical Journal, 388:L39–L43.

Bryce-Smith, D. and Gilbert, A. (1980). Rearrangements of the benzene ring. In Organic Chemistry: A Series of Monographs, volume 42, pages 349–379. Elsevier.

Burkhardt, A. M., Lee, K. L. K., Changala, P. B., Shingledecker, C. N., Cooke, I. R., Loomis, R. A., Wei, H., Charnley, S. B., Herbst, E., McCarthy, M. C., et al. (2021). Discovery of the pure polycyclic aromatic hydrocarbon indene (c-c9h8) with gotham observations of tmc-1. The Astrophysical Journal Letters, 913(2):L18.

Cami, J. (2014). Can fullerene analogues be the carriers of the diffuse interstellar bands? Proceedings of the International Astronomical Union, 9(S297):370–374.

Cami, J., Bernard-Salas, J., Peeters, E., and Malek, S. E. (2010). Science, 329(5996):1180–1182.

Cami, J., Bernard-Salas, J., Peeters, E., and Malek, S. E. (2011). Fullerenes in circumstellar and interstellar environments. Proceedings of the International Astronomical Union, 7(S280):216–227.

Campbell, E. K., Holz, M., Gerlich, D., and Maier, J. P. (2015). Laboratory confirmation of c 60+ as the carrier of two diffuse interstellar bands. Nature, 523(7560):322–323.

Castellanos, P., Berné, O., Sheffer, Y., Wolfire, M. G., and Tielens, A. G. (2014). C60 in photodissociation regions. The Astrophysical Journal, 794(1):83.

Cataldo, F. and Iglesias-Groth, S. (2010). Fulleranes: the hydrogenated fullerenes, volume 2. Springer Science & Business Media.

Cavagnat, D. and Lespade, L. (2001). Ch-stretching overtone spectra of a fast rotating methyl group. i. toluene c 6 d 5 ch 3. The Journal of Chemical Physics, 114(14):6030–6040.

Cernicharo, J., Agúndez, M., Cabezas, C., Tercero, B., Marcelino, N., Pardo, J., and de Vicente, P. (2021). Pure hydrocarbon cycles in tmc-1: Discovery of ethynyl cyclopropenylidene, cyclopentadiene and indene. arXiv preprint arXiv:2104.13991.

Cesarsky, C. and Sargent, A. (1996). Isocam in flight. Astronomy and Astrophysics, 315(2):L32–L37.

Chandrasekaran, V., Kafle, B., Prabhakaran, A., Heber, O., Rappaport, M., Rubinstein, H., Schwalm, D., Toker, Y., and Zajfman, D. (2014). The Journal of Physical Chemistry Letters, 5(23):4078–4082.

Chang, Y., Zhang, J., Sun, H., Hong, B., An, Z., and Wang, R. (2005). International journal of quantum chemistry, 105(2):142–147.

Cherchneff, I. and Barker, J. R. (1989). Infrared emission from a polycyclic aromatic hydrocarbon (pah) excited by ultraviolet laser. The Astrophysical Journal, 341:L21–L24.

Chihara, K. and Baba, H. (1977). Quenching of dual fluorescences of pyrene vapor by high-pressure oxygen or nitric oxide. Chemical Physics, 25(2):299–306.

Clar, E. and Schoental, R. (1964). Polycyclic hydrocarbons, volume 2. Springer.

Cohen-Tannoudji, C., Diu, B., and Laloë, F. (2021). Mécanique Quantique-Tome 2. EDP Sciences.

Cook, D. and Saykally, R. (1998). Simulated infrared emission spectra of highly excited polyatomic molecules: a detailed model of the pah-uir hypothesis. The Astrophysical Journal, 493(2):793.

Cook, D., Schlemmer, S., Balucani, N., Wagner, D., Harrison, J., Steiner, B., and Saykally, R. (1998). Single photon infrared emission spectroscopy: a study of ir emission from uv laser excited pahs between 3 and 15 μm. The Journal of Physical Chemistry A, 102(9):1465–1481.

Cook, D., Schlemmer, S., Balucani, N., Wagner, D., Steiner, B., and Saykally, R. (1996). Infrared emission spectra of candidate interstellar aromatic molecules. Nature, 380(6571):227–229.

Cordiner, M., Linnartz, H., Cox, N., Cami, J., Najarro, F., Proffitt, C., Lallement, R., Ehrenfreund, P., Foing, B., Gull, T., et al. (2019). Confirming interstellar c60+ using the hubble space telescope. The Astrophysical Journal Letters, 875(2):L28.

Dartois, E. (2019). Interstellar Carbon Dust. C - Journal of Carbon Research, 5(4):80.

De Vries, J., Steger, H., Kamke, B., Menzel, C., Weisser, B., Kamke, W., and Hertel, I. (1992). Single-photon ionization of c60-and c70-fullerene with synchrotron radiation: determination of the ionization potential of c60. Chemical physics letters, 188(3-4):159–162.

Donn, B. (1968). Polycyclic hydrocarbons, platt particles, and interstellar extinction. The Astrophysical Journal, 152:L129.

Douin, S., Gronowski, M., Lamarre, N., Phung, V.-T., Boyé-Péronne, S., Crépin, C., and Kolos, R. (2015). Cavity ring down spectroscopy measurements for high-overtone vibrational bands of hc3n. The Journal of Physical Chemistry A, 119(36):9494–9505.

Draine, B. and Lazarian, A. (1998). Electric dipole radiation from spinning dust grains. The Astrophysical Journal, 508(1):157.

Draine, B. and Li, A. (2001). Infrared emission from interstellar dust. i. stochastic heating of small grains. The Astrophysical Journal, 551(2):807.

Dreier, T. and Ewart, P. (2002). Applied combustion diagnostics, k. kohse-höinghaus and j. b. jeffries.

Dubosq, C., Calvo, F., Rapacioli, M., Dartois, E., Pino, T., Falvo, C., and Simon, A. (2020). Quantum modeling of the optical spectra of carbon cluster structural families and relation to the interstellar extinction uv bump. Astronomy & Astrophysics, 634:A62.

Dubosq, C., Falvo, C., Calvo, F., Rapacioli, M., Parneix, P., Pino, T., and Simon, A. (2019). Mapping the structural diversity of c60 carbon clusters and their infrared spectra. Astronomy & Astrophysics, 625:L11.

Duley, W. (2009). The Astrophysical Journal, 705(1):446.

Duley, W. (2019). Carbonaceous grains. In Dust and chemistry in astronomy, pages 71–102. Routledge.

Duley, W. and Williams, D. (1981). The infrared spectrum of interstellar dust: Surface functional groups on carbon. Monthly Notices of the Royal Astronomical Society, 196(2):269–274.

Duncan, M., Dietz, T., Liverman, M., and Smalley, R. (1981). Photoionization measurement of the triplet lifetime of benzene. The Journal of Physical Chemistry, 85(1):7–9.

Dunk, P. W., Adjizian, J.-J., Kaiser, N. K., Quinn, J. P., Blakney, G. T., Ewels, C. P., Marshall, A. G., and Kroto, H. W. (2013). Metallofullerene and fullerene formation from condensing carbon gas under conditions of stellar outflows and implication to stardust. Proceedings of the National Academy of Sciences, 110(45):18081–18086.

Dunk, P. W., Kaiser, N. K., Hendrickson, C. L., Quinn, J. P., Ewels, C. P., Nakanishi, Y., Sasaki, Y., Shinohara, H., Marshall, A. G., and Kroto, H. W. (2012a). Closed network growth of fullerenes. Nature communications, 3(1):1–9.

Dunk, P. W., Kaiser, N. K., Mulet-Gas, M., Rodríguez-Fortea, A., Poblet, J. M., Shinohara, H., Hendrickson, C. L., Marshall, A. G., and Kroto, H. W. (2012b). The smallest stable fullerene, m@ c28 (m= ti, zr, u): stabilization and growth from carbon vapor. Journal of the American Chemical Society, 134(22):9380–9389.

Durana, J. F. and McDonald, J. (1976). Infrared chemiluminescence studies of chlorine substitution reactions with brominated unsaturated hydrocarbons. The Journal of Chemical Physics, 64(6):2518–2527.

Ebara, Y., Furukawa, T., Matsumoto, J., Tanuma, H., Azuma, T., Shiromaru, H., and Hansen, K. (2016). Detection of recurrent fluorescence photons. Physical review letters, 117(13):133004.

Ebert, L. B. (1990). Is soot composed predominantly of carbon clusters? Science, 247(4949):1468–1471.

Einstein, A. (2016). 7 on the quantum theory of radiation. The Old Quantum Theory: The Commonwealth and International Library: Selected Readings in Physics, page 167.

Elmegreen, B. G. and Scalo, J. (2004). Interstellar turbulence i: observations and processes. Annu. Rev. Astron. Astrophys., 42:211–273.

Elstner, M., Porezag, D., Jungnickel, G., Elsner, J., Haugk, M., Frauenheim, T., Suhai, S., and Seifert, G. (1998). Self-consistent-charge density-functional tight-binding method for simulations of complex materials properties. Phys. Rev. B, 58(11):7260.

Englman, R. and Jortner, J. (1970). Molecular Physics, 18(2):145–164.

Ermolaev, V. L. (2001). Ultrafast nonradiative transitions between higher excited states in organic molecules. Russian Chemical Reviews, 70(6):471–490.

Falvo, C., Calvo, F., and Parneix, P. (2012). Probing the spin multiplicity of gas-phase polycyclic aromatic hydrocarbons through their infrared emission spectrum: A theoretical study. The Journal of chemical physics, 137(6):064303.

Falvo, C., Friha, H., Pino, T., Dhaouadi, Z., Parneix, P., Calvo, F., and Bréchignac, P. (2013). Effects of hydrogen dissociation on the infrared emission spectra of naphthalene: theoretical modeling. Physical Chemistry Chemical Physics, 15(25):10241–10250.

Farmanara, P., Stert, V., Radloff, W., and Hertel, I. (2001). Ultrafast internal conversion in highly excited toluene monomers and dimers. The Journal of Physical Chemistry A, 105(23):5613–5617.

Federman, S., Strom, C., Lambert, D., Cardelli, J. A., Smith, V., and Joseph, C. (1994). Chemical transitions for interstellar c2 and cn in cloud envelopes. The Astrophysical Journal, 424:772–792.

Féraud, G., Pino, T., Falvo, C., Parneix, P., Combriat, T., and Bréchignac, P. (2014). Intramolecular processes revealed using uv-laser-induced ir-fluorescence: A new perspective on the "channel three" of benzene. The journal of physical chemistry letters, 5(7):1083–1090.

Fichthorn, K. A. and Weinberg, W. H. (1991). Theoretical foundations of dynamical monte carlo simulations. The Journal of chemical physics, 95(2):1090–1096.

Flagey, N., Boulanger, F., Verstraete, L., Deschênes, M. M., Crespo, A. N., and Reach, W. (2006). Spitzer/irac and isocam/cvf insights on the origin of the near to mid-ir galactic diffuse emission. Astronomy & Astrophysics, 453(3):969–978.

Forst, W. (2012). Theory of unimolecular reactions. Elsevier.

Freed, K. F. and Jortner, J. (1970). Multiphonon processes in the nonradiative decay of large molecules. The Journal of Chemical Physics, 52(12):6272–6291.

Frenklach, M. and Feigelson, E. D. (1989). Formation of polycyclic aromatic hydrocarbons in circumstellar envelopes. The Astrophysical Journal, 341:372–384.

Frenklach, M. and Mebel, A. M. (2020). On the mechanism of soot nucleation. Physical Chemistry Chemical Physics, 22(9):5314–5331.

Galliano, F., Galametz, M., and Jones, A. P. (2018). The interstellar dust properties of nearby galaxies. Annual Review of Astronomy and Astrophysics, 56:673–713.

García-Hernández, D., Iglesias-Groth, S., Acosta-Pulido, J., Manchado, A., García-Lario, P., Stanghellini, L., Villaver, E., Shaw, R. A., and Cataldo, F. (2011). The formation of fullerenes: Clues from new c60, c70, and (possible) planar c24 detections in magellanic cloud planetary nebulae. The Astrophysical Journal Letters, 737(2):L30.

García-Hernández, D., Manchado, A., García-Lario, P., Stanghellini, L., Villaver, E., Shaw, R., Szczerba, R., and Perea-Calderón, J. (2010). Formation of fullerenes in h-containing planetary nebulae. The Astrophysical Journal Letters, 724(1):L39.

García-Hernández, D. A., Villaver, E., García-Lario, P., Acosta-Pulido, J. A., Manchado, A., Stanghellini, L., Shaw, R. A., and Cataldo, F. (2012). Infrared study of fullerene planetary nebulae. The Astrophysical Journal, 760(2):107.

Gavilan, L., Le, K. C., Pino, T., Alata, I., Giuliani, A., and Dartois, E. (2017). Polyaromatic disordered carbon grains as carriers of the uv bump: Far-uv to mid-ir spectroscopy of laboratory analogs. Astronomy & Astrophysics, 607:A73.

Gerhardt, P., Löffler, S., and Homann, K. (1989). The formation of polyhedral carbon ions in fuel-rich acetylene and benzene flames. In Symposium (International) on Combustion, volume 22, pages 395–401. Elsevier.

Giddings, J. C. and Eyring, H. (1954). Equilibrium theory of unimolecular reactions. The Journal of Chemical Physics, 22(3):538–542.

Gielen, C., Cami, J., Bouwman, J., Peeters, E., and Min, M. (2011). Carbonaceous molecules in the oxygen-rich circumstellar environment of binary post-agb stars-c60 fullerenes and polycyclic aromatic hydrocarbons. Astronomy & Astrophysics, 536:A54.

Gilbert, R. G. and King, K. D. (1980). Gas/gas and gas/wall average energy transfer from very low-pressure pyrolysis. Chemical Physics, 49(3):367–375.

Gillespie, D. T. (2007). Stochastic simulation of chemical kinetics. Annu. Rev. Phys. Chem., 58:35–55.

Gillett, F., Forrest, W., and Merrill, K. (1973). 8-13-micron spectra of ngc 7027, bd+ 30 3639, and ngc 6572. The Astrophysical Journal, 183:87–93.

Gillett, F., Forrest, W., Merrill, K., Capps, R. W., and Soifer, B. (1975). The 8-13 micron spectra of compact h ii regions. The Astrophysical Journal, 200:609–620.

Handschuh, H., Ganteför, G., Kessler, B., Bechthold, P. S., and Eberhardt, W. (1995). Stable configurations of carbon clusters: Chains, rings, and fullerenes. Phys. Rev. Lett., 74:1095–1098.

Hansen, K. and Campbell, E. (1998). Thermal radiation from small particles. Physical Review E, 58(5):5477.

Hansen, K. and Echt, O. (1997). Physical review letters, 78(12):2337.

Heath, J. R., Curl, R. F., and Smalley, R. E. (1987). The uv absorption spectrum of c60 (buckminsterfullerene): A narrow band at 3860 å. J. Chem. Phys., 87(7):4236–4238.

Hedén, M., Hansen, K., Jonsson, F., Rönnow, E., Gromov, A., Campbell, E., Taninaka, A., and Shinohara, H. (2005). Thermal radiation from cn+ and la@ cn+. The Journal of chemical physics, 123(4):044310.

Hilborn, R. C. (1982). Einstein coefficients, cross sections, f values, dipole moments, and all that. American Journal of Physics, 50(11):982–986.

Hilborn, R. C. (2002). Einstein coefficients, cross sections, f values, dipole moments, and all that. arXiv preprint physics/0202029.

Hippler, H., Luther, K., Troe, J., and Wendelken, H. (1983a). Unimolecular processes in vibrationally highly excited cycloheptatrienes. iii. direct k (e) measurements after laser excitation. The Journal of Chemical Physics, 79(1):239–246.

Hippler, H., Schubert, V., Troe, J., and Wendelken, H. (1981a). Direct observation of unimolecular bond fission in toluene. Chemical Physics Letters, 84(2):253–256.

Hippler, H., Troe, J., and Wendelken, H. (1981b). Direct observation of collisional deactivation of highly excited toluene. Chemical Physics Letters, 84(2):257–259.

Hippler, H., Troe, J., and Wendelken, H. (1983b). Collisional deactivation of vibrationally highly excited polyatomic molecules. ii. direct observations for excited toluene. The Journal of Chemical Physics, 78(11):6709–6717.

Hippler, H., Troe, J., and Wendelken, H. (1983c). Collisional deactivation of vibrationally highly excited polyatomic molecules. ii. direct observations for excited toluene. The Journal of Chemical Physics, 78(11):6709–6717.

Hippler, H., Troe, J., and Wendelken, H. (1983d). Collisional deactivation of vibrationally highly excited polyatomic molecules. iii. direct observations for substituted cycloheptatrienes. The Journal of Chemical Physics, 78(11):6718–6724.

Hippler, H., Troe, J., and Wendelken, H. (1983e). Uv absorption spectra of vibrationally highly excited toluene molecules. The Journal of Chemical Physics, 78(9):5351–5357.

Hold, U., Lenzer, T., Luther, K., Reihs, K., and Symonds, A. C. (2000). Collisional energy transfer probabilities of highly excited molecules from kinetically controlled selective ionization (kcsi). i. the kcsi technique: Experimental approach for the determination of p (e, e) in the quasicontinuous energy range. The Journal of Chemical Physics, 112(9):4076–4089.

Homann, K.-H. (1998). Fullerenes and soot formation—new pathways to large particles in flames. Angewandte Chemie International Edition, 37(18):2434–2451.

Howard, J. B. (1992). Fullerenes formation in flames. In Symposium (International) on Combustion, volume 24, pages 933–946. Elsevier.

Iglesias-Groth, S. (2006). Hydrogenated fulleranes and the anomalous microwave emission of the dark cloud ldn 1622. Monthly Notices of the Royal Astronomical Society, 368(4):1925–1930.

Ikeda, N., Nakashima, N., and Yoshihara, K. (1985). Photochemistry of toluene vapor at 193 nm. direct measurements of formation of hot toluene and the dissociation rate to benzyl radical. The Journal of chemical physics, 82(11):5285–5286.

Ito, G., Furukawa, T., Tanuma, H., Matsumoto, J., Shiromaru, H., Majima, T., Goto, M., Azuma, T., and Hansen, K. (2014). Cooling dynamics of photoexcited c 6- and c 6 h-. Physical review letters, 112(18):183001.

Itoh, T. (2012). Fluorescence and phosphorescence from higher excited states of organic molecules. Chemical reviews, 112(8):4541–4568.

Jensen, F. (2017). Introduction to computational chemistry. John wiley & sons.

Joblin, C., Tielens, A. G. G. M., and Cherchneff, I. (2011). The formation of polycyclic aromatic hydrocarbons in evolved circumstellar environments. European Astronomical Society Publications Series, 46:177–189.

Jones, A., Tielens, A., and Hollenbach, D. (1996). Grain shattering in shocks: The interstellar grain size distribution. The Astrophysical Journal, 469:740.

Jones, B. M., Zhang, F., Kaiser, R. I., Jamal, A., Mebel, A. M., Cordiner, M. A., and Charnley, S. B. (2011). Formation of benzene in the interstellar medium. Proceedings of the National Academy of Sciences, 108(2):452–457.

Kim, H. L., Kulp, T., and McDonald, J. (1987). Infrared fluorescence study on the threshold of intramolecular vibrational state mixing. The Journal of chemical physics, 87(8):4376–4382.

Kim, H.-S., Wagner, D., and Saykally, R. (2001). Single photon infrared emission spectroscopy of the gas phase pyrene cation: support for a polycyclic aromatic hydrocarbon origin of the unidentified infrared emission bands. Physical review letters, 86(25):5691.

Kim, S. G. and Tománek, D. (1994). Melting the fullerenes: A molecular dynamics study. Phys. Rev. Lett., 72:2418–2421.

King, K. D. and Barker, J. R. (2019). Experiments on collisional energy transfer. In Comprehensive Chemical Kinetics, volume 43, pages 3–62. Elsevier.

Klots, C. E. (1991). Systematics of evaporation. Zeitschrift für Physik D Atoms, Molecules and Clusters, 20(1):105–109.

Kolodney, E., Budrevich, A., and Tsipinyuk, B. (1995). Unimolecular rate constants and cooling mechanisms of superhot c 60 molecules. Physical review letters, 74(4):510.

Krätschmer, W., Lamb, L. D., Fostiropoulos, K., and Huffman, D. R. (1990). Solid c 60: a new form of carbon. Nature, 347(6291):354–358.

Kroto, H. and Jura, M. (1992). Circumstellar and interstellar fullerenes and their analogues. Astronomy and Astrophysics, 263:275–280.

Kroto, H. W., Heath, J. R., O'Brien, S. C., Curl, R. F., and Smalley, R. E. (1985). C 60: buckminsterfullerene. nature, 318(6042):162–163.

Kwok, S. and Zhang, Y. (2011). Mixed aromatic–aliphatic organic nanoparticles as carriers of unidentified infrared emission features. Nature, 479(7371):80–83.

Lai, S. K., Setiyawati, I., Yen, T. W., and Tang, Y. H. (2016). Studying lowest energy structures of carbon clusters by bond-order empirical potentials. Theor. Chem. Acc., 136:20.

Lai, T. S., Witt, A. N., Alvarez, C., and Cami, J. (2020). Monthly Notices of the Royal Astronomical Society, 492(4):5853–5864.

Lai, T. S.-Y., Witt, A. N., and Crawford, K. (2017). Monthly Notices of the Royal Astronomical Society, 469(4):4933–4948.

Léger, A., Boissel, P., and d'Hendecourt, L. (1988). Predicted fluorescence mechanism in highly isolated molecules: the poincaré fluorescence. Physical review letters, 60(10):921.

Leger, A. and Puget, J. (1984). Astronomy and Astrophysics, 137:L5–L8.

Lequeux, J. (2012). Le milieu interstellaire. EDP sciences.

Li, A. and Draine, B. (2001). Infrared emission from interstellar dust. ii. the diffuse interstellar medium. The Astrophysical Journal, 554(2):778.

Lifshitz, C. (2000a). International Journal of Mass Spectrometry, 200(1-3):423–442.

Lifshitz, C. (2000b). C2 binding energy in c60. International Journal of Mass Spectrometry, 198(1-2):1–14.

Lin, C.-K., Huang, C.-L., Jiang, J.-C., Chang, A., Lee, Y. T., Lin, S., and Ni, C.-K. (2002). Photoisomerization and photodissociation of toluene in molecular beam. Journal of the American Chemical Society, 124(15):4068–4075.

Long, B. A., Rodriguez, D. J., Lau, C. Y., Schultz, M., and Anderson, S. L. (2019). Thermal emission spectroscopy of single, isolated carbon nanoparticles: Effects of particle size, material, charge, excitation wavelength, and thermal history. The Journal of Physical Chemistry C, 124(2):1704–1716.

Luu, S. and Troe, J. (1973). Intermolecular energy transfer in the photoisomerization of cycloheptatriene. Berichte der Bunsengesellschaft für physikalische Chemie, 77(5):325–331.

Luu, S. and Troe, J. (1974). Photoisomerization of cycloheptatriene. ii: Temperature dependence of collisional energy transfer. Berichte der Bunsengesellschaft für physikalische Chemie, 78(8):766–773.

Lykhin, A. O., Ahmadvand, S., and Varganov, S. A. (2018). Electronic transitions responsible for c60+ diffuse interstellar bands. The journal of physical chemistry letters, 10(1):115–120.

Maier, J. P. and Campbell, E. K. (2017). Fullerenes in space. Angewandte Chemie International Edition, 56(18):4920–4929.

Maier, J. P., Lakin, N. M., Walker, G. A., and Bohlender, D. A. (2001). Detection of c3 in diffuse interstellar clouds. The Astrophysical Journal, 553(1):267.

Malloci, G., Joblin, C., and Mulas, G. (2007). On-line database of the spectral properties of polycyclic aromatic hydrocarbons. Chemical physics, 332(2-3):353–359.

Malloci, G., Mulas, G., Cecchi-Pestellini, C., and Joblin, C. (2008). Dehydrogenated polycyclic aromatic hydrocarbons and uv bump. Astronomy & Astrophysics, 489(3):1183–1187.

Mandich, M. and Flynn, G. (1980a). Collisional relaxation of vibrationally excited ocs in rare gas mixtures. The Journal of Chemical Physics, 73(8):3679–3687.

Mandich, M. and Flynn, G. (1980b). Vibrational energy transfer map for ocs. The Journal of Chemical Physics, 73(3):1265–1279.

Martin, S., Bernard, J., Brédy, R., Concina, B., Joblin, C., Ji, M., Ortega, C., and Chen, L. (2013). Fast radiative cooling of anthracene observed in a compact electrostatic storage ring. Physical review letters, 110(6):063003.

Martin, S., Ji, M., Bernard, J., Brédy, R., Concina, B., Allouche, A.-R., Joblin, C., Ortega, C., Montagne, G., Cassimi, A., et al. (2015). Fast radiative cooling of anthracene: Dependence on internal energy. Physical Review A, 92(5):053425.

Martini, P., Sellgren, K., and DePoy, D. (1999). Near-infrared spectroscopy of molecular hydrogen emission in four reflection nebulae: ngc 1333, ngc 2023, ngc 2068, and ngc 7023. The Astrophysical Journal, 526(2):772.

Mathis, J., Mezger, P., and Panagia, N. (1983). Interstellar radiation field and dust temperatures in the diffuse interstellar matter and in giant molecular clouds. Astronomy and Astrophysics, 128:212–229.

Matsugi, A. (2018). Collision frequency for energy transfer in unimolecular reactions. The Journal of Physical Chemistry A, 122(8):1972–1985.

McGuire, B. A., Burkhardt, A. M., Kalenskii, S., Shingledecker, C. N., Remijan, A. J., Herbst, E., and McCarthy, M. C. (2018). Detection of the aromatic molecule benzonitrile (c-c6h5cn) in the interstellar medium. Science, 359(6372):202–205.

McMillen, D. F. and Golden, D. M. (1982). Hydrocarbon bond dissociation energies. Annual Review of Physical Chemistry, 33(1):493–532.

Medvedev, E. S. and Osherov, V. I. (1995). Radiationless transitions in polyatomic molecules. Springer Series in Chemical Physics.

Micelotta, E. R., Jones, A. P., Cami, J., Peeters, E., Bernard-Salas, J., and Fanchini, G. (2012). The formation of cosmic fullerenes from arophatic clusters. The Astrophysical Journal, 761(1):35.

Mitzner, R. and Campbell, E. E. (1995). Optical emission studies of laser desorbed c60. The Journal of chemical physics, 103(7):2445–2453.

Montagnon, L. and Spiegelmann, F. (2007). Euro. Phys. J. D, 43:7–10.

Mulas, G. (1998). Astronomy and Astrophysics, 338:243–261.

Nakai, Y., Kambara, T., Itoh, A., Tsuchida, H., and Yamazaki, Y. (2001). Production of singly charged fullerenelike fragment ions in a fast he 2+- c 60 collision. Physical Review A, 64(4):043205.

Nesbitt, D. J. and Field, R. W. (1996). Vibrational energy flow in highly excited molecules: Role of intramolecular vibrational redistribution. The Journal of Physical Chemistry, 100(31):12735–12756.

Ni*, C.-K. and Lee, Y. T. (2004). Photodissociation of simple aromatic molecules in a molecular beam. International Reviews in Physical Chemistry, 23(2):187–218.

Niehaus, T. A., Suhai, S., Della Sala, F., Lugli, P., Elstner, M., Seifert, G., and Frauenheim, T. (2001). Tight-binding approach to time-dependent density-functional response theory. Phys. Rev. B, 63:085108.

Nitzan, A. and Jortner, J. (1978). Inverse electronic relaxation. Chemical Physics Letters, 60(1):1–4.

Nitzan, A. and Jortner, J. (1979). Theory of inverse electronic relaxation. The Journal of Chemical Physics, 71(8):3524–3532.

Onaka, T., Nakamura, T., Sakon, I., Wu, R., Ohsawa, R., Kaneda, H., Lebouteiller, V., and Roellig, T. L. (2018). Near-infrared to mid-infrared observations of galaxy mergers: Ngc 2782 and ngc 7727. The Astrophysical Journal, 853(1):31.

Otis, C., Knee, J., and Johnson, P. (1983). The identification of channel three in isolated benzene. The Journal of Chemical Physics, 78(4):2091–2092.

Otsuka, M., Kemper, F., Cami, J., Peeters, E., and Bernard-Salas, J. (2014). Physical properties of fullerene-containing galactic planetary nebulae. Monthly Notices of the Royal Astronomical Society, 437(3):2577–2593.

Otsuka, M., Kemper, F., Hyung, S., Sargent, B. A., Meixner, M., Tajitsu, A., and Yanagisawa, K. (2013). The detection of c60 in the well-characterized planetary nebula m1-11. The Astrophysical Journal, 764(1):77.

Park, J., Bersohn, R., and Oref, I. (1990). Unimolecular decomposition of methylsubstituted benzenes into benzyl radicals and hydrogen atoms. The Journal of chemical physics, 93(8):5700–5708.

Parmenter, C. S. (1982). Vibrational energy flow within excited electronic states of large molecules. The Journal of Physical Chemistry, 86(10):1735–1750.

Parneix, P., Basire, M., and Calvo, F. (2013). J. Phys. Chem. A, 117:3954–3959.

Peeters, E., Spoon, H., and Tielens, A. (2004). Polycyclic aromatic hydrocarbons as a tracer of star formation? The Astrophysical Journal, 613(2):986.

Pilleri, P., Montillaud, J., Berné, O., and Joblin, C. (2012). Evaporating very small grains as tracers of the uv radiation field in photo-dissociation regions. Astronomy & Astrophysics, 542:A69.

Pino, T., Carpentier, Y., Féraud, G., Friha, H., Kokkin, D., Troy, T., Chalyavi, N., Bréchignac, P., and Schmidt, T. (2021). Electronic spectroscopy of pahs. In PAHs and the Universe, pages 355–372. EDP Sciences.

Pino, T., Chabot, M., Béroff, K., Godard, M., Fernandez-Villoria, F., Le, K., Breuer, L., Herder, M., Wucher, A., Bender, M., et al. (2019). Release of large polycyclic aromatic hydrocarbons and fullerenes by cosmic rays from interstellar dust-swift heavy ion irradiations of interstellar carbonaceous dust analogue. Astronomy & Astrophysics, 623:A134.

Platt, J. R. (1949). The Journal of chemical physics, 17(5):484–495.

Platt, J. R. (1956). On the optical properties of interstellar dust. The Astrophysical Journal, 123:486.

Pogodin, M. A., Miroshnichenko, A. S., Tarasov, A. E., Mitskevich, M. P., Chountonov, G. A., Klochkova, V. G., Yushkin, M. V., Manset, N., Bjorkman, K. S., Morrison, N. D., et al. (2004). A new phase of activity of the herbig be star hd 200775 in 2001: Evidence for binarity. Astronomy & Astrophysics, 417(2):715–723.

Pope, C. J., Marr, J. A., and Howard, J. B. (1993). Chemistry of fullerenes c60 and c70 formation in flames. The Journal of Physical Chemistry, 97(42):11001–11013.

Puget, J. and Léger, A. (1989). A new component of the interstellar matter: Small grains and large aromatic molecules. Annual review of astronomy and astrophysics, 27(1):161–198.

Quack, M. (1990). Spectra and dynamics of coupled vibrations in polyatomic molecules. Annual Review of Physical Chemistry, 41(1):839–874.

Reid, R. C. and Sherwood, T. K. (1966). The Properties of Gases of Liquids: Their Estimation and Correlation. 2d Ed. McGraw-Hill.

Roberts, K. R., Smith, K. T., and Sarre, P. J. (2012). Detection of c60 in embedded young stellar objects, a herbig ae/be star and an unusual post-asymptotic giant branch star. Monthly Notices of the Royal Astronomical Society, 421(4):3277–3285.

Robertson, J. and O'reilly, E. (1987). Physical Review B, 35(6):2946.

Robertson, S. H. (2019). Parametric models. In Comprehensive Chemical Kinetics, volume 43, pages 273–295. Elsevier.

Robinson, P. J. and Holbrook, K. A. (1972). Unimolecular reactions. Wiley-interscience.

Rohlfing, E. A. (1988). Optical emission studies of atomic, molecular, and particulate carbon produced from a laser vaporization cluster source. The Journal of chemical physics, 89(10):6103–6112.

Rossi, M. J. and Barker, J. R. (1982a). Infrared fluorescence and collisional energy transfer parameters for vibrationally excited azulene*(so): dependence on internal energy (evib). Chemical Physics Letters, 85(1):21–26.

Rossi, M. J. and Barker, J. R. (1982b). Infrared fluorescence and collisional energy transfer parameters for vibrationally excited azulene*(so): dependence on internal energy (evib). Chemical Physics Letters, 85(1):21–26.

Rossi, M. J., Pladziewicz, J. R., and Barker, J. R. (1983). Energy-dependent energy transfer: Deactivation of azulene (s 0, e vib) by 17 collider gases. The Journal of Chemical Physics, 78(11):6695–6708.

Rotello, V. M., Howard, J. B., Yadav, T., Conn, M. M., Viani, E., Giovane, L. M., and Lafleur, A. L. (1993). Isolation of fullerene products from flames: structure and synthesis of the c60-cyclopentadiene adduct. Tetrahedron letters, 34(10):1561–1562.

Roueff, E. and Lique, F. (2013). Molecular excitation in the interstellar medium: Recent advances in collisional, radiative, and chemical processes. Chemical reviews, 113(12):8906–8938.

Russell, R., Soifer, B., and Willner, S. (1977). The 4 to 8 micron spectrum of ngc 7027. The Astrophysical Journal, 217:L149–L153.

Saito, M., Kubota, H., Yamasa, K., Suzuki, K., Majima, T., and Tsuchida, H. (2020a). Direct measurement of recurrent fluorescence emission from naphthalene ions. Phys. Rev. A, 102:012820.

Saito, M., Kubota, H., Yamasa, K., Suzuki, K., Majima, T., and Tsuchida, H. (2020b). Direct measurement of recurrent fluorescence emission from naphthalene ions. Physical Review A, 102(1):012820.

Schlemmer, S., Cook, D., Harrison, J., Wurfel, B., Chapman, W., and Saykally, R. (1994). The unidentified interstellar infrared bands: Pahs as carriers? Science, 265(5179):1686–1689.

Sellgren, K. (1984). The Astrophysical Journal, 277:623–633.

Sellgren, K., Werner, M., and Dinerstein, H. (1983). Extended near-infrared emission from visual reflection nebulae. The Astrophysical Journal, 271:L13–L17.

Sellgren, K., Werner, M. W., Ingalls, J. G., Smith, J., Carleton, T., and Joblin, C. (2010). The Astrophysical Journal Letters, 722(1):L54.

Shan, J., Suton, M., and Lee, L. (1991). 3.3 micron emission from ultraviolet excitation of some aromatic molecules. The Astrophysical Journal, 383:459–465.

Shi, J. and Barker, J. R. (1988). Energy-dependent collisional deactivation of vibrationally excited azulene. The Journal of chemical physics, 88(10):6219–6227.

Shipley, H. V., Papovich, C., Rieke, G. H., Brown, M. J., and Moustakas, J. (2016). A new star formation rate calibration from polycyclic aromatic hydrocarbon emission features and application to high-redshift galaxies. The Astrophysical Journal, 818(1):60.

Siegmann, K., Sattler, K., and Siegmann, H. (2002). Clustering at high temperatures: carbon formation in combustion. Journal of Electron Spectroscopy and Related Phenomena, 126(1-3):191–202.

Smith, G. P. and Barker, J. R. (1981). Energy transfer rates for vibrationally excited gas-phase azulene in the electronic ground state. Chemical Physics Letters, 78(2):253–258.

Snow, T. P. and Bierbaum, V. M. (2008). Ion chemistry in the interstellar medium. Annu. Rev. Anal. Chem., 1:229–259.

Sorkhabi, O., Qi, F., Rizvi, A. H., and Suits, A. G. (2001). The ultraviolet photochemistry of phenylacetylene and the enthalpy of formation of 1, 3, 5-hexatriyne. Journal of the American Chemical Society, 123(4):671–676.

Srinivasan, R. (1962). Photoisomerization of 1, 3, 5-cycloheptatriene and its relation to internal conversion of electronic energy. Journal of the American Chemical Society, 84(18):3432–3436.

Steglich, M., Bouwman, J., Huisken, F., and Henning, T. (2011). Can neutral and ionized polycyclic aromatic hydrocarbons be carriers of the ultraviolet extinction bump and the diffuse interstellar bands? The Astrophysical Journal, 742(1):2.

Steglich, M., Jäger, C., Rouillé, G., Huisken, F., Mutschke, H., and Henning, T. (2010). Electronic spectroscopy of medium-sized polycyclic aromatic hydrocarbons: implications for the carriers of the 2175 å uv bump. The Astrophysical Journal Letters, 712(1):L16.

Stock, D., Choi, W.-Y., Moya, L., Otaguro, J., Sorkhou, S., Allamandola, L., Tielens, A., and Peeters, E. (2016). Polycyclic aromatic hydrocarbon emission in spitzer/irs maps. i. catalog and simple diagnostics. The Astrophysical Journal, 819(1):65.

Terral, P. (2016). Structure du champ magnétique interstellaire dans le disque et le halo de notre galaxie. PhD thesis, Université de Toulouse, Université Toulouse III-Paul Sabatier.

Tielens, A. (2013). The molecular universe. Reviews of Modern Physics, 85(3):1021.

Tielens, A. G. (2005). The physics and chemistry of the interstellar medium. Cambridge University Press.

Tielens, A. G. (2008). Interstellar polycyclic aromatic hydrocarbon molecules. Annu. Rev. Astron. Astrophys., 46:289–337.

Tielens, A. G. (2021). Molecular astrophysics. Cambridge University Press.

Tomita, S., Andersen, J., Hansen, K., and Hvelplund, P. (2003). Stability of buckminsterfullerene, c60. Chemical physics letters, 382(1-2):120–125.

Toselli, B. M. and Barker, J. R. (1991). Excitation of co2 by energy transfer from highly vibrationally excited benzene derivatives. The Journal of chemical physics, 95(11):8108–8119.

Toselli, B. M., Brenner, J. D., Yerram, M. L., Chin, W. E., King, K. D., and Barker, J. R. (1991). Vibrational relaxation of highly excited toluene. The Journal of chemical physics, 95(1):176–188.

Troe, J. (1973). Collisional energy transfer in thermal unimolecular reactions. Berichte der Bunsengesellschaft für physikalische Chemie, 77(9):665–674.

Troe, J. (1977). Theory of thermal unimolecular reactions at low pressures. ii. strong collision rate constants. applications. The Journal of Chemical Physics, 66(11):4758–4775.

Tseng, C.-M., Dyakov, Y. A., Huang, C.-L., Lee, Y. T., Lin, S.-H., and Ni, C.-K. (2006). The role of seven-membered ring in the photoisomerization and photodissociation of small aromatic molecules. Journal of the Chinese Chemical Society, 53(1):33–40.

Van den Ancker, M., Djie, T. A., Catala, C., de Winter, D., Blondel, P., Waters, L., et al. (1997). Hipparcos data on herbig ae/be stars: an evolutionary scenario. Astronomy and Astrophysics, 324:L33–L36.

Van Orden, A. and Saykally, R. J. (1998). Small carbon clusters: Spectroscopy, structure, and energetics. Chem. Rev., 98:2313–2358.

Wakelam, V., Bron, E., Cazaux, S., Dulieu, F., Gry, C., Guillard, P., Habart, E., Hornekaer, L., Morisset, S., Nyman, G., et al. (2017). H2 formation on interstellar dust grains: The viewpoints of theory, experiments, models and observations. Molecular Astrophysics, 9:1–36.

Wakelam, V., Smith, I., Herbst, E., Troe, J., Geppert, W., Linnartz, H., Öberg, K., Roueff, E., Agúndez, M., Pernot, P., et al. (2010). Reaction networks for interstellar chemical modelling: improvements and challenges. Space science reviews, 156(1):13–72.

Williams, R. M. and Leone, S. R. (1995). Laboratory studies of 3.3 micron emission from naphthalene induced by 193 and 248 nanometer excitation. The Astrophysical Journal, 443:675–681.

Willner, S., Puetter, R., Russell, R., and Soifer, B. (1979). Unidentified infrared spectral features. Astrophysics and Space Science, 65(1):95–101.

Wilzbach, K. E., Harkness, A. L., and Kaplan, L. (1968). Photochemical rearrangement of benzene-1, 3, 5-tri deutrium. Journal of the American Chemical Society, 90(5):1116–1118.

Wilzbach, K. E. and Kaplan, L. (1964). Photoisomerization of dialkylbenzenes. Journal of the American Chemical Society, 86(11):2307–2308.

Witt, A. N. and Lai, T. S.-Y. (2020). Extended red emission: observational constraints for models. Astrophysics and Space Science, 365(3):1–9.

Yanai, T., Tew, D. P., and Handy, N. C. (2004). A new hybrid exchange–correlation functional using the coulomb-attenuating method (cam-b3lyp). Chemical physics letters, 393(1-3):51–57.

Yerram, M. L., Brenner, J. D., King, K. D., and Barker, J. R. (1990). Collisional deactivation of highly vibrationally excited benzene pumped at 248 nm. Journal of Physical Chemistry, 94(16):6341–6350.

Zamirri, L., Ugliengo, P., Ceccarelli, C., and Rimola, A. (2019). Quantum mechanical investigations on the formation of complex organic molecules on interstellar ice mantles. review and perspectives. ACS Earth and Space Chemistry, 3(8):1499–1523.

Zhang, F., Parker, D., Kim, Y. S., Kaiser, R. I., and Mebel, A. M. (2011). On the formation of ortho-benzyne (o-c6h4) under single collision conditions and its role in interstellar chemistry. The Astrophysical Journal, 728(2):141.

Zhang, Q.-L., O'Brien, S. C., Heath, J. R., Liu, Y., Curl, R. F., Kroto, H. W., and Smalley, R. E. (1986). Reactivity of large carbon clusters: spheroidal carbon shells and their possible relevance to the formation and morphology of soot. The Journal of Physical Chemistry, 90(4):525–528.

Zhang, Y. and Kwok, S. (2011a). Detection of c60 in the protoplanetary nebula iras 01005+ 7910. The Astrophysical Journal, 730(2):126.

Zhang, Y. and Kwok, S. (2011b). Detection of c60 in the protoplanetary nebula iras 01005+ 7910. The Astrophysical Journal, 730(2):126.

Zhang, Y., Sadjadi, S., and Hsia, C.-H. (2020). Hydrogenated fullerenes (fulleranes) in space. Astrophysics and Space Science, 365(4):1–8.

Zhao, L., Kaiser, R. I., Xu, B., Ablikim, U., Ahmed, M., Joshi, D., Veber, G., Fischer, F. R., and Mebel, A. M. (2018). Pyrene synthesis in circumstellar envelopes and its role in the formation of 2d nanostructures. Nature Astronomy, 2(5):413–419.

Zhen, J., Castellanos, P., Paardekooper, D. M., Linnartz, H., and Tielens, A. G. (2014). Laboratory formation of fullerenes from pahs: Top-down interstellar chemistry. The Astrophysical Journal Letters, 797(2):L30.

université PARIS-SACLAY
ÉCOLE DOCTORALE
Ondes et Matière
(EDOM)

Titre: IR radiative relaxation of benzene derivatives and large carbon clusters in the gas phase

Mots clés: recurrent fluorescence, Poincaré fluorescence, carbone clusters, benzene derivatives, interstellar medium, combustion

Abstract: This thesis is in line with investigations started after the statement of the PAH hypothesis. According to this hypothesis, the carriers of ubiquitously observed emission features in the mid-infrared wavelength range in the interstellar medium regions are species similar to aromatic hydrocarbons (with an aliphatic component). These species undergo a radiative relaxation induced by the absorption of a stellar UV photon by emitting in the mid-infrared by vibrational radiative de-excitation.

The radiative relaxation after electronic excitation of benzene derivatives highly excited vibrationally in gas phase is detected via an infrared spectrometer (FIREFLY) developed in the laboratory. The temporal analysis of the emission spectrum (between 2.5 and 4.5 µm) can give information on the relaxation dynamics. This analysis can eventually be extended if it is supported by a vibrational emission simulation in competition with other pathways during the radiative cascade (collision, photodissociation, photoisomerization). This method has been applied to the isomerization dynamics of toluene (partially deuterated) to cycloheptatriene (isomerization from a 6-ring to a 7-ring) while trying to characterize it (isomerization barrier, A-prefactor). Although the isomerization dynamics proved to be too fast to be fully probed, this first study allowed to see the possibilities and limitations of the analysis of the radiative emission during cooling for this type of isomerization. This method of analysis was extended, without simulation, to the study of other isomerizations of the same type in the case of phenylacetylene and aniline (both partially deuterated). Recurrent fluorescence phenomenon (or Poincaré fluorescence) in Cn carbon clusters (n= 24, 42, 60) in competition with vibrational emission has been theoretically investigated. The simulation of the radiative cooling in the experiment described above has been adapted to this context where only radiative processes are in competition. In this work, the vibrational and electronic structures of several thousands of isomers of carbon clusters are known beforehand. This allows to draw conclusions on the emission spectrum of a large set of carbon clusters. Indeed, a large number of isomers are suspected to be present in the interstellar medium (ISM) and in burning media. It turned out that the competition between recurrent fluorescence vibrational emission depends on the internal energy, the size and the family of clusters. The emission spectrum simulation of carbon clusters in ISM conditions (irradiation by a 20 000 K star or the standard radiation field of the ISM) has shown that the C60 cages emission in the near-IR (< 4 µm) could explain astrophysical observations. The resulting abundance of C60 cages in NGC 7023 has been estimated. The emission of a large set of carbon clusters in temperature fixed conditions has been simulation (still by a molecular approach) and indicates that the spectrum is blackbody-like. The average carbon clusters emissivity is then deduced.

In this work, IR radiative relaxation processes have been employed as observable for experimental investigation of isomerization mechanism in benzene derivatives. Theoretically, the recurrent fluorescence and vibrational emission in large Cn (n= 24, 42, 60) carbon clusters have been studied in interstellar and temperature fixed context.

Title: Relaxation radiative dans l 'infrarouge des dérivés de benzène et de gros agrégats de carbone en phase gazeuse

Keywords: fluorescence récurrente, de Poincaré, agrégats de carbone, dérivés de benzène, milieu interstellaire, combustion

Résumé: Ce travail de thèse s'inscrit dans la lignée des travaux entamés depuis l'énoncé de l'hypothèse PAH stipulant que les pics d'émissions observés et omniprésents dans l'IR moyen dans le milieu interstellaire seraient dus à des espèces semblables aux hydrocarbures aromatiques polycycliques (avec éventuellement une composante aliphatique). Ces espèces émettraient dans l'IR moyen par désexcitation radiative vibrationnelle induite par l'absorption d'un photon UV stellaire. C'est dans ce contexte que nous avons effectué un travail expérimentale et théorique.

La relaxation radiative après excitation électronique des dérivés de benzène en phase gazeuse très excités vibrationnellement a pu être détecté via un spectromètre infrarouge (FIREFLY) développé dans l'équipe. L'analyse des spectres d'émission (entre 2.5 et 4.5 µm) en fonction du temps peuvent donner des informations sur la dynamique de relaxation. Cette analyse peut éventuellement être appronfondie si elle est appuyée par une simulation Monte Carlo cinétique de l'émission vibrationnelle en compétition avec d'autres voies lors de la cascade de relaxation (collision, photodissociation, photoisomérisation). Cette méthode a été appliquée à la dynamique d'isomérisation du toluène (partiellement deutérée) vers le cycloheptatriène (isomérisaton d'un cycle à 6 à un cycle à 7) en essayant de la caractériser (barrière d'isomérisation, préfacteur A). Bien que la dynamique d'isomérisation s'est avérée trop rapide pour être entièrement sondée, cette première étude a permis de voir les possibilités et les limites de l'analyse de la dynamique d'isomérisation via les processus de relaxation radiative. Cette méthode d'analyse a été étendu, sans simulation, à d'autres isomérisations du même type dans le cas du phénylacétylène et l'aniline (les deux partiellement deutérés).

Le phénomène de fluorescence récurrente (ou fluorescence de Poincaré) dans les agrégats de carbone C_n (n= 24, 42, 60) en compétition avec l'émission vibrationnelle a été étudié par simulation. La simulation de l'expérience décrite plus haut a été adaptée à ce contexte où seules les processus radiatifs sont en compétition. Nous avions à notre disposition les structures vibrationnelles et électroniques de plusieurs milliers d'isomères d'agrégats carbonés, ce qui nous a permis de tirer des conclusions sur le spectre d'émission d'un grand ensemble d'agrégats de carbone. Dans ce travail, les strucutres vibrationnelles et électroniques de plusieurs milliers d'isomères d'agrégats carbonés sont au préalable connus. Ceci permet de tirer des conclusions sur le spectre d'émission d'un grand ensemble agrégats carbonés. En effet, c'est un grand nombre d'isomères qui sont susceptés d'être présents dans le milieu interstellaire et dans les milieux en combustion. Il s'est avéré que la compétition entre la fluorescence récurrente et vibrationnelle dépend de l'énergie interne, de la taille et de la famille des agrégats.

La simulation du spectre d'émission des agrégats de carbones dans les conditions du milieu interstellaire (irradiés par une étoile à 20000 K ou par le champ de radiation standard du milieu interstellaire) a montré que l'émission des cages C_{60} dans le proche IR ($<$ 4 µm) pourrait expliquer le continuum d'émission dans le proche IR observés dans certaines sources astrophysiques.

L'émission d'un grand nombre d'agrégats de carbone à température fixée a aussi été simulée (toujours par une approche moléculaire) et indique que le spectre d'émission est de type corps noir. L'émissivité moyenne des agrégats de carbone a alors été déduite.

Dans ce travail, les processus de relaxation radiative dans l'infrarouge ont été employé en tant qu'observable pour l'étude expérimentale du mécanisme d'isomérisation dans les dérivés du benzène. Sur le plan théorique, la fluorescence récurrente et l'émission vibrationnelle dans les gros agrégats de carbone C_n (n = 24, 42, 60) ont été étudiées dans le contexte du milieu interstellaire et dans un contexte d'environnement à température fixe.

Université Paris-Saclay
Espace Technologique / Immeuble Discovery
Route de l'Orme aux Merisiers RD 128 / 91190 Saint-Aubin, France